THE SPECTRA OF

TRANSITION-METAL IONS IN SOLIDS

A thesis submitted in partial fulfilment
of the requirements for the Degree of
Doctor of Philosophy in Physics
in the University of Canterbury
Christchurch, New Zealand

by

I.W. Johnstone

1975

To

Marjorie

ABSTRACT

The results of an investigation of the Raman and infrared spectra of cobaltous ions in cadmium-chloride, cadmium-bromide, and manganese-chloride, and of cobalt-chloride are presented. The cobalt ions substitute for the cation in these crystals and experience a trigonal crystal-field which splits the lowest $^4T_{1g}(^4F)$ cubic-field term into six Kramers doublets with energies in the range 0-1200 cm^{-1}. The Raman spectra, measured as a function of temperature and of cobalt concentration show all five single ion electronic transitions together with several lines due to cobalt ion pairs. The infrared spectra comprise both magnetic-dipole allowed electronic transitions and electric-dipole allowed vibronic lines and bands. They confirm the identity of the electronic transitions seen by Raman scattering and also yield information concerning the lattice modes of the host and the possible interactions within cobalt ion pairs. The strong field matrices of the trigonal crystal-field and Zeeman interactions are calculated for the $d^3(d^7)$ configuration and quantitatively explain the experimental data. The crystal-field analysis provides single ion wavefunctions for further calculations which successfully explain the spectra of antiferromagnetic $CoCl_2$ and exchange coupled cobalt ion pairs in $CdCl_2(Co^{2+})$ and $CdBr_2(Co^{2+})$. A preliminary investigation of the infrared absorption of an oxygen-induced impurity site in $CdCl_2$-type crystals is also presented.

ACKNOWLEDGEMENTS

During the course of this work many staff and fellow research students have given me helpful guidance and encouragement. I am particularly indebted to my supervisor, Dr Glynn D. Jones, for his friendship, unfailing optimism, and sustained interest in this project. I would also like to thank Drs John Campbell, Rod Syme and Karel Zdansky for many stimulating discussions and advice, especially during my supervisor's study leave, and Professors A.G. McLellan, B.G. Wybourne and W. Jones for their sincere interest in my progress throughout the last three years. The frustrations with equipment have been alleviated by the skill of Bob Tyree, Terry Rowe, Ross Ritchie and Dave Grieg of the Physics Department technical staff together with the assistance of my postgraduate companion, John Christie.

I am also very grateful to Mrs Margaret Sewell for the typing of this thesis and to Laurie Hunter for the excellent photographic work appearing in it.

The Royal Society of New Zealand kindly offered a travel grant to undertake research in Sydney, Australia and the New Zealand University Grants Committee provided a Post Graduate Scholarship.

Finally, I would like to thank my family and wife for their continued support and understanding.

Ivan Johnstone

9 November 1975.

CONTENTS

Page

CHAPTER I: INTRODUCTION

1.1 Transition-Metal Ions in Crystals 1

1.2 Ligand Field Theory 1

1.3 Cobalt (II) d^7 Spectra 5

1.4 The Structure of This Work 6

CHAPTER II: THE THEORY OF SINGLE COBALTOUS ION SPECTRA

2.1 Introduction 8

2.2 The Trigonal Crystal-Field 8

2.3 Previous Energy Level Calculations 11

2.3.1 The Model of Lines 12

2.3.2 The Model of Robson 13

2.3.3 The Model of Hsu and Stout 14

2.3.4 Summary 15

2.4 Energy Calculations: This Work 15

2.4.1 Formulation of Crystal-Field Operators . 16

2.4.2 Matrix Elements of the Trigonal Crystal-Field and Zeeman Interactions 19

CHAPTER III: EXPERIMENTAL TECHNIQUES

3.1 The Crystals, Their Growth and Preparation . . 26

3.2 Raman Measurements 30

3.2.1 Instrumentation 30

3.2.2 Technical Improvements 33

3.2.3 Measurement Techniques 34

3.3 Infrared Measurements 36

3.3.1 Instrumentation 36

3.3.2 Technical Improvements 37

3.3.3 Measurement Techniques 40

Page

CHAPTER IV: THE RAMAN SCATTERING SPECTRA OF $CdCl_2(Co^{2+})$, $CdBr_2(Co^{2+})$, $MnCl_2(Co^{2+})$ AND $CoCl_2$

4.1 Introduction 41

4.2 General Description of the Spectra 44

4.3 Results 48

4.3.1 $CdCl_2(Co^{2+})$ 48

4.3.2 $CdBr_2(Co^{2+})$ 53

4.3.3 $MnCl_2(Co^{2+})$ 56

4.3.4 $CoCl_2$ 59

4.3.5 Summary 62

4.4 Fitting of the Experimental Data 63

4.5 Interpretation of the Crystal-Field Parameters Obtained 68

4.6 Molecular Field Analysis of $CoCl_2$ Spectra below $25^{o}K$ 72

CHAPTER V : THE INFRARED ABSORPTION SPECTRA OF $CdCl_2(Co^{2+})$, $CdBr_2(Co^{2+})$, $MnCl_2(Co^{2+})$ AND $CoCl_2$

5.1 Introduction 76

5.2 General Description of the Spectra 77

5.3 Results 80

5.3.1 $CdCl_2(Co^{2+})$ 80

5.3.2 $CdBr_2(Co^{2+})$ 87

5.3.3 $MnCl_2(Co^{2+})$ 92

5.3.4 $CoCl_2$ 94

5.4 Analysis of Single Co^{2+} Ion Electronic Spectra 97

5.5 Analysis of the Co^{2+} Ion Vibronic Spectra. . 102

5.5.1 Sharp Lines 102

5.5.2 Broad Bands 106

Page

CHAPTER VI: THE SPECTRA OF EXCHANGE-COUPLED COBALT ION-PAIRS IN $CdBr_2$ AND $CdCl_2$

6.1 Introduction 109

6.2 Cobalt Concentration Theory 111

6.3 Theoretical Review 115

6.4 Real Spin Exchange Model 121

6.5 Zeeman Splitting of the Pair States 126

6.6 Results. 126

6.6.1 $CdCl_2(Co^{2+})$ 127

6.6.2 $CdBr_2(Co^{2+})$ 135

6.6.3 Summary 141

6.7 Spin Hamiltonian Model 142

6.8 The Results of Bailey et al. for $CdBr_2(Co^{2+})$ Crystals 146

CHAPTER VII: OVERALL SUMMARY AND CONCLUSIONS 151

CHAPTER VIII: THE POLARISED INFRARED ABSORPTION SPECTRA OF AN OXYGEN-INDUCED SITE IN $CdCl_2$-TYPE CRYSTALS

8.1 Introduction 153

8.2 The Crystals 155

8.3 Results. 156

8.3.1 $CdCl_2(CdO)$ and $CdCl_2(NiO)$ 156

8.3.2 $CdBr_2(CdO)$ and $CdBr_2(NiO)$ 160

8.4 Analysis of Results to Date 163

8.5 Conclusions and Further Work 170

REFERENCES 172

Page

APPENDIX I: MATRIX ELEMENTS OF THE TRIGONAL CRYSTAL-FIELD BETWEEN STATES OF THE $3d^3(3d^7)$ CONFIGURATION 178

APPENDIX II: MATRIX ELEMENTS OF THE ZEEMAN INTERACTION BETWEEN STATES OF THE $3d^3(3d^7)$ CONFIGURATION 189

APPENDIX III: REQUIRED MATRIX ELEMENTS OF THE OPERATOR S_x DESCRIBING THE MOLECULAR FIELD APPROPRIATE TO $CoCl_2$. 209

APPENDIX IV: REQUIRED MATRIX ELEMENTS OF THE OPERATORS S_z, S_x, S_y, L_z and L_x APPROPRIATE TO $CdCl_2(Co^{2+})$:5 wt.% 211

APPENDIX V: REQUIRED MATRIX ELEMENTS OF THE OPERATORS S_z, S_x and S_y APPROPRIATE TO $CdBr_2(Co^{2+})$: 5 wt.% 216

APPENDIX VI: PUBLICATIONS 218

LIST OF FIGURES

Figure		Page
1-1	Tanabe-Sugano diagram for the d^7 configuration . . .	5
2-1	Structure of $CdCl_2$-type crystals	9
2-2	Splitting of the cubic-field groundstate energy level by spin-orbit coupling and the trigonal crystal-field.	11
3-1	The dry-box.	28
3-2	The crystal polishing-jig	29
3-3	Schematic diagram of the Raman Spectrometer	31
3-4	Backward Raman scattering optical arrangement . . .	35
3-5	The new helium dewar	39
4-1	Polarised, first order Raman phonon spectrum of $CdBr_2$(Co):1 wt.%	45
4-2	Raman scattering spectra of $CdCl_2$(Co):5 wt.%	49
4-3	Polarised, Raman spectrum of $CdCl_2$(Co):5 wt.% (900-1000 cm^{-1}).	51
4-4	Raman spectra of $CdBr_2$(Co):0,3,5, and 10 wt.% . . .	54
4-5	Raman spectra of $MnCl_2$(Co):5 and 10 wt.%	57
4-6	Raman spectrum of $MnCl_2$(Co):10 wt.% recorded at 300^oK.	58
4-7	Raman spectra recorded at 30, 83 and 300^oK of $CoCl_2$ in its paramagnetic state	60
4-8	Raman spectra of $CoCl_2$ in its paramagnetic ($T = 83^oK$) and antiferromagnetic ($T = 15^oK$) states .	61
4-9	Energy-level calculations for a Co^{2+} ion in a trigonal crystal-field	70

Figure		Page
4-10	Calculated and observed energy levels within the $^4T_{1g}(^4F)$ term of a cobalt ion in a trigonal, and trigonal plus exchange field.	74
5-1	Axial infrared absorption spectrum of $CdCl_2$(Co): 7.5 wt.% (1.32 mm) recorded at 15°K between 400 and 1500 cm^{-1}	79
5-2	Axial infrared absorption spectra of $CdCl_2$(Co): 1.0, 2.5, 5.0, 7.5 and 10 wt.%	81
5-3	Polarised infrared absorption spectra of $CdCl_2$(Co): 0.5 wt.%	84
5-4	Polarised infrared absorption spectra of $CdBr_2$(Co):5 wt.% and $CdCl_2$(Co):5 wt.%	85
5-5	Axial infrared absorption spectra of $CdBr_2$(Co); 1.0, 2.5, 5.0, 7.5 and 10.0 wt.%	88
5-6	Polarised infrared absorption spectra of $CdBr_2$(Co):1.0 wt.%	91
5-7	Axial infrared absorption spectra of $CoCl_2$ recorded at 300, 78, 30 and 15°K between 800 and 1450 cm^{-1} .	95
6-1	Raman and infrared axial spectra of $CdCl_2$(Co): 10 wt.% recorded at 15°K in the region 850-1150 cm^{-1} . . .	110
6-2	Co^{2+} ion environment in $CdCl_2$ type crystals viewed normal to the c-axis	112
6-3	Polarised infrared spectra of $CdCl_2$(Co):5.0 wt.% recorded at 30, 15 and 5°K between 875 and 1075 cm^{-1}	128
6-4	Far infrared spectrum of $CdCl_2$(Co):10.0 wt.% showing the position and magnetic field dependence of the cobalt pair line at 8.55 cm^{-1}	130

Figure		Page
6-5	Calculated and observed energy levels for an exchange coupled Co^{2+} ion pair in $CdCl_2$ and $CdBr_2$ crystals	132
6-6	Prediced Zeeman splittings of observed pair lines for fields parallel and perpendicular to the c-axis	133
6-7	Polarised infrared spectra of $CdBr_2$(Co):5.0 wt.% recorded at 78, 30, 15 and 5°K between 800 and 1000 cm^{-1}	136
6-8	Cobalt concentration dependence of the electronic lines in the infrared spectra of $CdBr_2$(Co) crystals	137
6-9	Predicted energy level scheme for the upper exchange split states of $CdBr_2$(Co):5wt.%	139
8-1	Polarised infrared absorption spectra of $CdCl_2(NiO^{16})$:0.5 wt.% recorded at 15°K	157
8-2	Infrared axial absorption spectrum of $CdBr_2$(CdO):0.1 wt.% recorded at 78°K	160
8-3	Temperature dependence of the second-harmonic infrared absorption line near 1400 cm^{-1} in $CdBr_2$(CdO), $MnCl_2$(MnO), $MgCl_2$(MgO) and $CdCl_2$(CdO)	162

LIST OF TABLES

Table		Page
2-I	Energies of the low-lying electronic levels of Co^{2+} ions in $CoCl_2$, $CdCl_2$ and $CdBr_2$	14
2-II	Possible $t_{2g}^m e_g^n$ configurations and $^{(2S+1)}\chi_r$ terms of the $3d^3$ configuration	16
2-III	The unitary matrices $\langle \gamma_t \ell \mid \Gamma_n m \rangle$	24
4-I	Christie and Lockwood's Raman data[41,58,59] (1973)	43
4-II	Selection rules for electronic Raman transitions .	47
4-III	Classification by nearest-neighbour cation environment of the Co^{2+} electronic lines of $CdCl_2$(Co) in the 1000 cm^{-1} region	53
4-IV	Frequencies and assignments of the six Kramers levels of the $^4T_{1g}(^4F)$ term	63
4-V	Calculated and observed energies of the six Kramers degenerate electronic lines of the $^4T_{1g}(^4F)$ term .	65
4-VI	Calculated and observed g-values for $CdCl_2$(Co) and $CdBr_2$(Co) crystals.	66
4-VII	Predicted g-values for the levels of the $^4T_{1g}(^4F)$ manifold in $CdCl_2$(Co) and $CdBr_2$(Co) crystals . . .	68
5-Ia	Infrared axial spectra of $CdCl_2$(Co) recorded at 15°K between 400 and 1500 cm^{-1}	82
5-Ib	Infrared axial spectra of $CdCl_2$(Co) recorded at 78°K between 400 and 1500 cm^{-1}	83
5-II	Polarised intensities of selected infrared absorptions in $CdCl_2$(Co):0.5 wt.%, 5 wt.% and $CdBr_2$(Co):1 wt.%, 5 wt.% at 15°K	86

Table		Page
5-IIIa	Infrared axial spectra of $CdBr_2$(Co) recorded at 15°K between 400 and 1200 cm^{-1}	89
5-IIIb	Infrared axial spectra of $CdBr_2$(Co) recorded at 78°K between 400 and 1200 cm^{-1}	90
5-IV	Infrared axial spectra of $MnCl_2$(Co) recorded at 15 and 78°K between 650 and 1350 cm^{-1}	93
5-V	Axial infrared absorption spectra of $CoCl_2$ recorded at 78, 30 and 15°K between 400 and 1450 cm^{-1}	96
5-VI	Calculated and experimental oscillator strengths for assigned transitions in $CdCl_2$(Co):0.5 wt.% and $CdBr_2$(Co):1.0 wt.%	100
5-VII	Frequencies of sharp acoustic phonons observed in $CoCl_2$ and $CdCl_2$(Co), $CdBr_2$(Co) and $MnCl_2$(Co) . .	103
5-VIII	Analysis of vibronic bands in $CdCl_2$(Co):1 wt.% and $CdBr_2$(Co):1.0 wt.%	107
6-I	Relative percentage probabilities for the occurrence of single, pair and triple cobalt ion centres	113
6-II	Labelling of the $^4T_{1g}(^4F)$ states used in the real spin exchange model for Co^{2+} ion pairs	122
6-III	Comparison of the spin Hamiltonian and real spin exchange models	144
8-I	Spectral data for the crystals studied by Upsall and Driver	154
8-II	Polarised infrared absorption spectra of $CdCl_2(CdO^{16})$ and $CdCl_2(NiO^{16})$:0.5 wt.%	158

Table		Page
8-III	Polarised infrared absorption spectra of $CdBr_2$(CdO):0.5 wt.%	161
8-IV	Infrared absorption spectra of $MnCl_2$(MnO) and $MgCl_2$(MgO).	163
8-V	Anharmonic shifts of combination modes observed in oxide doped $CdCl_2$-type crystals	166

C H A P T E R I

INTRODUCTION

1.1 TRANSITION-METAL IONS IN CRYSTALS

Many studies have been made of the electronic spectra of cobalt (II) compounds[1-3] as part of a more general investigation into the strong optical absorption of solids containing transition-metal ions. The use of solids, rather than solutions, in such studies has the advantage of restricting the metal ion to a reasonably well-defined geometry. This allows a more precise measurement of the spectra at low temperatures since then the vibrational structure can be either removed, or resolved, and bands otherwise obscured can be observed. The main features of the observed spectra can be interpreted by the application of ligand field theory to the appropriate d^n configuration. Since the d^n electronic energies are sensitive to the surrounding ions in the lattice a study of the electronic Raman scattering and absorption spectra may also shed light on the structure, magnetic interactions, and other physical properties of the crystal.

1.2 LIGAND FIELD THEORY

The characterisation of the electronic levels of a complex is the main aim of ligand field theory. This theory is the result of a considerable refinement of the original electrostatic crystal field theory developed by Bethe[4] and Van Vleck[5-8] and is essentially a hybridization of the pure

electrostatic model and Mulliken's molecular-orbital approach[9]. A comprehensive account of these developments is given in the book by Griffith[10] and in papers by Tanabe and Sugano[11-13] and Orgel[14-16]. Of particular interest is the case of a $3d^n$ ion surrounded by six ligands with approximately octahedral symmetry. These ligands may be molecular groups (e.g. H_2O) or just single ions (e.g. Cl^-) and are assumed to provide a static crystal field. Whereas in the free-ion the electrons move in a spherically symmetric electrostatic field, in a complex the local symmetry of the ion is dependent on the arrangement of ligands surrounding it given by the appropriate point group symmetry of the site. Since the ligands have a filled shell configuration their effect is represented to within a first approximation by a classical electrostatic field of the same symmetry. In the present ligand field theory the partly filled d-shell of the central metal ion is not considered to be composed of pure atomic d-orbitals but rather, orbitals having the same transformation properties under the site symmetry group. Thus, their angular dependence is the same for d-orbitals but allowance is made for the modification of the free-ion radial wavefunctions in the presence of the ligands and the accompanying reduction of the free-ion electrostatic and spin-orbit parameters.

The Hamiltonian for a many electron ion in a complex may be written as an extension of the free-ion case[17] by adding the ligand field term $\mathcal{H}_3$ to the usual free-ion terms $\mathcal{H}_0$, $\mathcal{H}_1$, and $\mathcal{H}_2$. This gives:

$$\mathcal{H} = \sum_k \left[\frac{p_k^2}{2m} + \frac{Ze^2}{r_k}\right] + \sum_{j>k} \frac{e^2}{r_{jk}} + \zeta \sum_j s_j \cdot \ell_j + V_c \qquad (1.1)$$

$$= \mathcal{H}_0 + \mathcal{H}_1 + \mathcal{H}_2 + \mathcal{H}_3$$

$\mathcal{H}_0$: central field; $\mathcal{H}_1$: electrostatic repulsion; $\mathcal{H}_2$: spin-orbit coupling; $\mathcal{H}_3$: ligand field

where the summation is over all electrons outside closed shells. $\mathcal{H}_0$ shifts all levels of a given configuration equally and so does not affect the relative energies within a configuration and may be therefore ignored. For $3d^n$ ions, the magnitude of the electrostatic repulsion $\mathcal{H}_1$ and ligand field $\mathcal{H}_3$ terms is comparable but both are much greater than that of the spin-orbit coupling $\mathcal{H}_2$ term. Thus, two alternative coupling schemes arise depending on which of $\mathcal{H}_1$ and $\mathcal{H}_3$ is considered first. In the weak-field scheme $\mathcal{H}_3$ is considered as a perturbation on the free-ion angular momentum states while for strong-field coupling $\mathcal{H}_1$ is treated as a perturbation of the strong-field terms labelled by the irreducible representations of the symmetry group of $\mathcal{H}_3$.

An a priori calculation of the energy levels using the above hamiltonian is an extremely difficult problem since it requires an explicit form for the radial part of the wave-functions describing the d-orbitals of the complex. Although the function's transformation properties are known from symmetry considerations the quantitative splittings of states depend on numerical radial integrals which can be evaluated by the use of suitable models. The attempts to calculate these have been reviewed by Sugano and Shulman[18], whose work shows that a full molecular-orbital treatment is necessary even for

the simplest of compounds. Hence, group theoretical methods are used to determine the angular symmetry properties of operators and eigenstates while the radial parts are treated as empirically determined parameters.

For example, the cubic component of the ligand field may be parametrized by the splitting of the t_{2g} and e_g orbitals of a single d-electron by:

$$\Delta = 10D_q = E(e_g) - E(t_{2g}) \qquad (1.2)$$

Because of the lack of experimental data the Coulombic and spin-orbit terms cannot usually be treated with full generality and approximations are made to reduce the number of necessary parameters. In a completely general analysis there are ten possible parameters describing the electrostatic repulsion, one cubic-field, and two spin-orbit parameters ζ and ζ'. However, when considering intraconfigurational transitions the electrostatic interaction is almost always represented by the two Racah parameters B and C, following Tanabe and Sugano[12] who have derived energy level diagrams for all d^n configurations in an octahedral field. The energy levels of many complexes can be predicted with reasonable accuracy using such a model (B, C, Δ, ζ and ζ'). However, the spectra are frequently complicated by vibrational modes and splittings induced by low-symmetry components of the ligand field, strains within the crystal, or by possible magnetic interactions between the metal ion and its neighbours. Consequently, additional parameters describing these effects may be introduced where necessary.

1.3 COBALT (II) d^7 SPECTRA

In this thesis attention is restricted to transitions within the cubic-field split levels. These are considered to be essentially d-d transitions of the cobalt ion and have energies typically less than 30,000 cm^{-1}. Since they are electric-dipole forbidden they are of low intensity having oscillator strengths (f) 10^2 weaker than those of the more intense charge transfer bands which usually predominate for energies greater than 30,000 cm^{-1}. Further, these transitions may be either spin-allowed (with f approximately 10^{-4}) or spin-forbidden (with f usually less than 10^{-5})[12].

We have investigated the lowest lying electronic transitions of the cobalt (II) ion in $CoCl_2$, and as a substitutional impurity in $CdCl_2$, $CdBr_2$ and $MnCl_2$. On replacing the appropriate cation in any of these the Co^{2+} ion experiences a crystalline field that is of predominantly cubic symmetry. The resulting spectrum is characterised by the $3d^7$ Tanabe and Sugano diagram[12] which shows, as in Figure 1-1, three

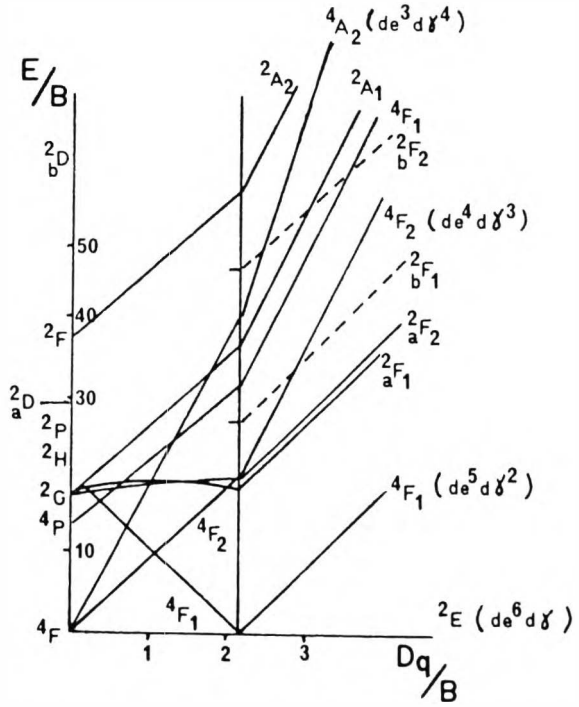

Figure 1-1: Tanabe-Sugano diagram for the d^7 configuration

possible quartet-quartet transitions:

$$^4T_{1g}(^4F) \rightarrow {}^4T_{2g}(^4F),\ {}^4A_{2g}(^4F),\ {}^4T_{1g}(^4P)$$

together with several spin-forbidden quartet-doublet transitions. Of these, the A level is orbitally non-degenerate while the T levels (labelled F by Tanabe and Sugano) have three-fold orbital degeneracy and all have (2s+1) spin degeneracy. These degeneracies may be raised by the combined effects of spin-orbit coupling and the trigonal component of the crystal-field. In particular, the cubic $^4T_{1g}(^4F)$ groundstate manifold splits to give six Kramers doublets with energies in the range 0-1200 cm^{-1}. These may be observed by electronic Raman scattering or infrared absorption experiments when using suitable crystals (Chapter 3.1).

1.4 THE STRUCTURE OF THIS WORK

Chapter II of this thesis will give a detailed account of the theory of single cobaltous ion spectra. It includes a description of the crystal-field and energy level scheme appropriate for the crystals under investigation and gives a brief review of the attempts to calculate their cobalt energy levels to date. The development of a more complete model is discussed and matrix elements of the trigonal crystal-field and Zeeman interactions are obtained for the entire d^7 configuration.

Experimental techniques, and instrumentation are discussed in Chapter III.

The Raman spectra of $CoCl_2$ and $CdCl_2$, $CdBr_2$ and $MnCl_2$ containing cobaltous ions have been partially measured by

previous workers. At the commencement of this work the analysis of each was therefore still incomplete. The measurements have been repeated and extended in Chapter IV. They are interpreted using the complete d^7 crystal-field analysis described in Chapter II.

Chapter V includes the experimental results and complete electronic and vibronic analysis of the single cobaltous ion infrared spectra of the four crystals. These are assigned using the results of Chapter IV.

A quantitative description of the infrared spectra of cobaltous ion pairs in $CdCl_2$ and $CdBr_2$ is given in Chapter VI. Also included is a brief review of the current theories of exchange coupled ions, a model of cobalt ion concentration effects, and an outline of the exchange model developed to explain the spectra. The wavefunctions of the pair states are derived from the single ion wavefunctions obtained in Chapter IV.

Finally, a preliminary analysis of the polarised infrared spectra of an oxygen induced impurity site in $CdCl_2$, $CdBr_2$, $MnCl_2$, $MgCl_2$ and $CoCl_2$ is discussed in Chapter VIII.

The Appendices include the matrix elements of the trigonal crystal-field and Zeeman interactions calculated in Chapter II, the molecular field appropriate to antiferromagnetic $CoCl_2$, and the real-spin exchange and Zeeman operators defined in Chapter VI.

C H A P T E R I I

THE THEORY OF SINGLE COBALTOUS ION SPECTRA

2.1 INTRODUCTION

The electronic Raman and infrared lines observed comprise transitions between the energy levels of the $3d^7$ configuration. Their frequencies and relative intensities are determined by the energy levels and states of this configuration. Since this work has established the positions of all the energy levels for the lowest cubic crystal field term of cobalt it was considered worthwhile to calculate the energies of these levels for the case of a site of D_{3d} symmetry. Because previous attempts[3,19-21] to fit observed frequencies have not been very successful, this calculation was extended to include all 120 states of the $3d^7$ configuration.

2.2 THE TRIGONAL CRYSTAL-FIELD

The divalent cobalt ion has an unfilled 3d shell containing seven electrons. The ion environment in $CdCl_2$-type crystals has been given by Ono et al.[22] The structure belongs to the D_{3d}^5 space group with one molecular unit per primitive cell[23]. Figure 2-1 shows the crystal to be made up of layers of chloride ions which are nearly cubic close packed, with cadmium ions sandwiched between alternate chloride layers. These layers are perpendicular to the c axis of the crystal. "The smaller cadmium ion fits snugly inside the cage of chlorine ions, as the sum of the cadmium and chlorine ionic radii very nearly equals their separation

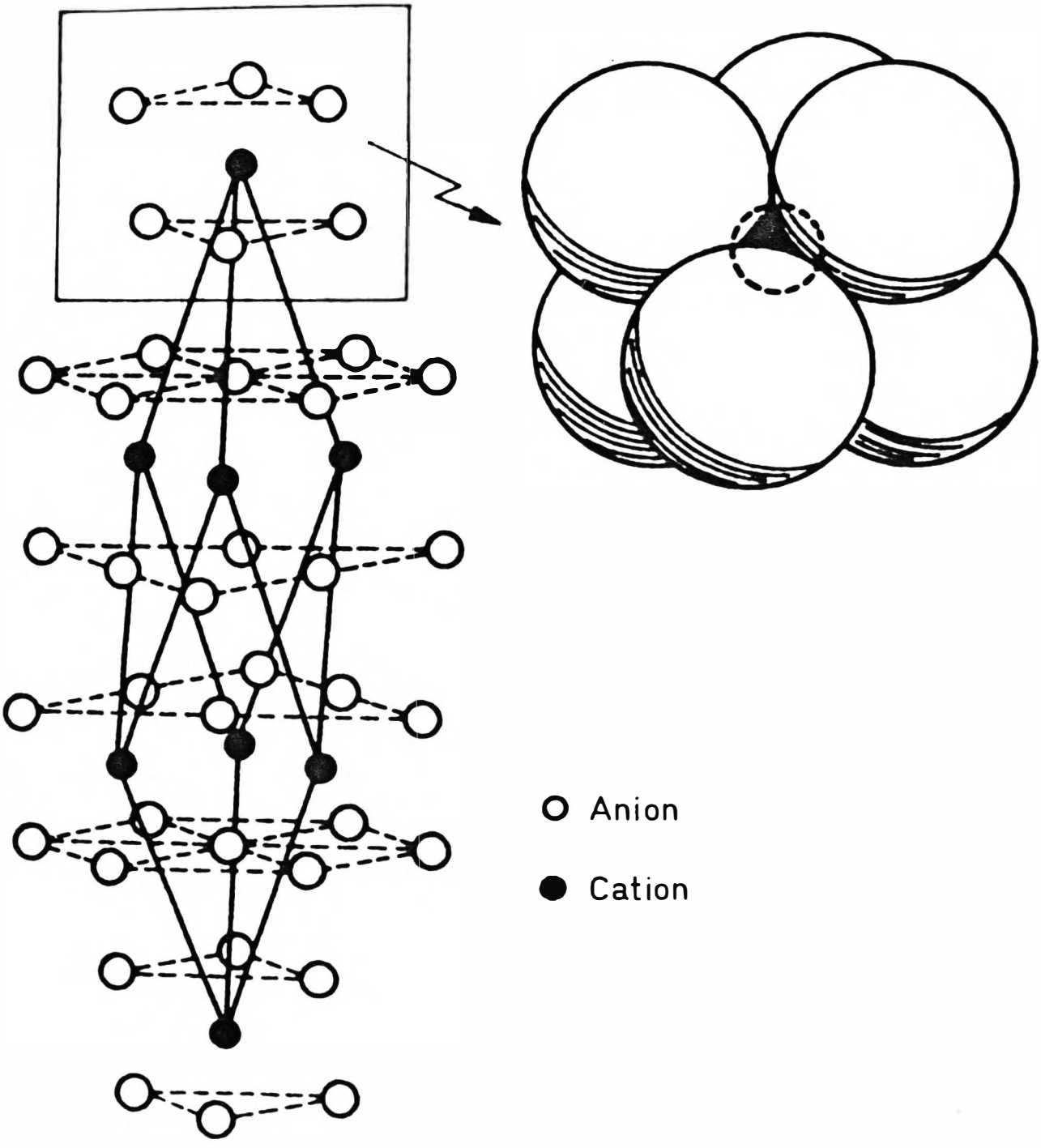

Figure 2-1: Structure of $CdCl_2$-type crystals.

distance"[23]. On substitution for the cation the Co^{2+} ion is surrounded by a nearly octahedral arrangement of anions, the octahedron being slightly expanded along one of its trigonal axes in the cubic {111} direction. Thus, the Co^{2+} ion experiences a crystalline field that has only a small trigonal distortion from octahedral symmetry. However, it is sufficient to raise the degeneracies of the cubic electronic states.

The cubic field causes splitting and mixing of the free-ion multiplets to give terms labelled by $^{(2S+1)}\chi_r$ which are the irreducible representations (A_{1g}, A_{2g}, E_g, T_{1g} and T_{2g}) of the single cubic group with (2S+1) spin multiplicity. The ^4F, and lowest free-ion multiplet is split into $^4T_{1g}$, $^4T_{2g}$ and $^4A_{2g}$ terms with the $^4T_{1g}$ lowest in energy while the ^4P free-ion multiplet is a single $^4T_{1g}$ term. The two $^4T_{1g}$ terms are mixed by the cubic field. The spin-orbit interaction splits these into levels, labelled by the irreducible representations (Γ_6^+, Γ_7^+, Γ_8^+) of the cubic double group. The trigonal crystal field further splits these into states labelled by the γ_4^+ and $\gamma_5^+ + \gamma_6^+$ irreducible representations of the trigonal double group. Here, the γ_5^+ and γ_6^+ irreducible representations are complex conjugates and are degenerate in the absence of a magnetic field, being labelled $\gamma_{5,6}^+$.

The energy level scheme for cadmium-chloride-type crystals containing cobalt is shown in Figure 2-2. The cubic crystal field ground state is a $^4T_{1g}(^4F)$ term, which is split by the spin-orbit interaction into four spin-orbit levels, one each of Γ_6^+ and Γ_7^+ symmetry and two of Γ_8^+ symmetry. The latter are distinguished as $^{(1)}\Gamma_8^+$ and $^{(2)}\Gamma_8^+$ (or Γ_8 and Γ_8').

The trigonal field splits these Γ_8^+ quartets into two levels of γ_4^+ and $\gamma_{5,6}^+$ symmetry, while the Γ_6^+ and Γ_7^+ doublets transform as γ_4^+ levels. The combined effect of this and the spin-orbit interaction is to split the $^4T_{1g}(^4F)$ term into a manifold of six Kramers doublet levels with an overall splitting of approximately 1000 cm^{-1}.

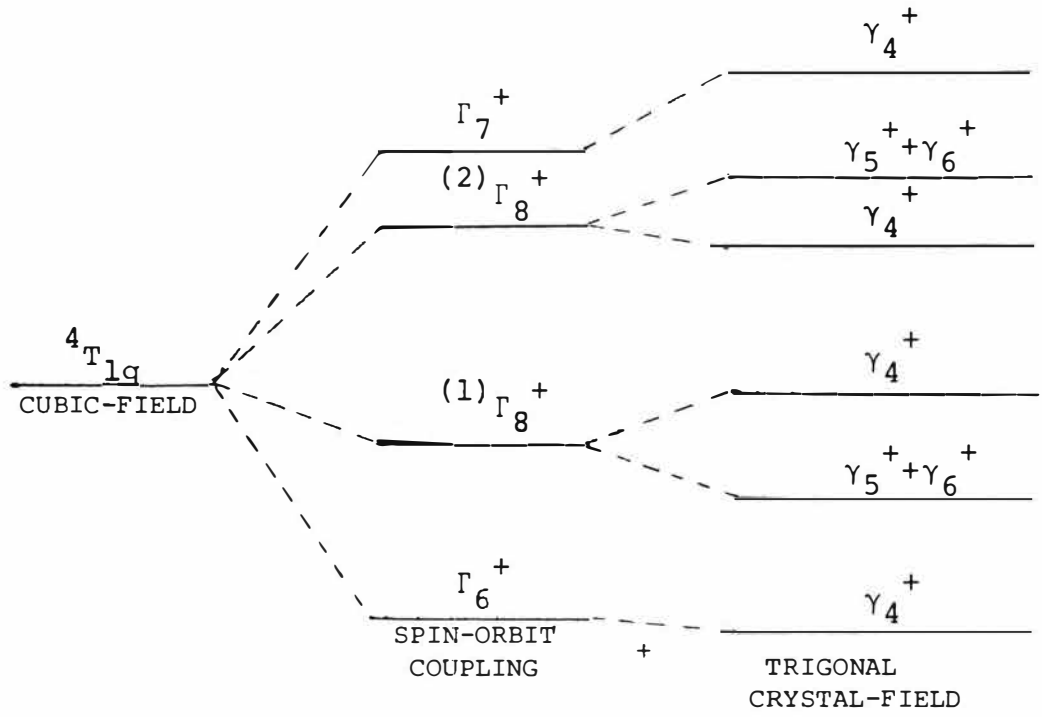

Figure 2-2: Splitting of the cubic-field groundstate energy level by spin-orbit coupling and the trigonal crystal-field.

2.3 PREVIOUS ENERGY LEVEL CALCULATIONS

The energies of the spin-orbit and trigonal-field split $^4T_{1g}(^4F)$ states have been calculated by Lines[19] for Co^{2+} ions in $CdCl_2$ and $CoCl_2$ and by Robson[20] for Co^{2+} ions in $CdCl_2$ and $CdBr_2$. More recently, Hsu and Stout[21] have

performed similar calculations to interpret the infrared spectra of $CoCl_2$ in both its paramagnetic and antiferromagnetic phases. In Table 2-I the energies of the low lying energy levels of Co^{2+} in these lattices are listed for each. The states are labelled by their symmetries under the trigonal double group with their cubic parent levels in brackets.

2.3.1 The Model of Lines[19]

Lines's calculation is performed on the isolated $^4T_{1g}(^4F)$ groundstate using the ^4F cubic wavefunctions of Bleaney and Stevens[24]. Only the admixture of the $^4T_{1g}(^4P)$ term into the $^4T_{1g}(^4F)$ ground-term is taken into account. All other contributions are neglected. By using the structural isomorphism which exists between $^4T_1$ and ^4P states[10] Lines characterizes the cubic groundstate as an effective P state of spin 3/2 and evaluates the matrix elements of the trigonal-field and spin-orbit coupling using the Hamiltonian:

$$\mathcal{H} = -\frac{3}{2} k\lambda \mathbf{L}\cdot\mathbf{S} - \delta(L_z^2 - \frac{2}{3}) \qquad (2.1)$$

between the twelve $|m_L m_S\rangle$ states. This Hamiltonian may be solved to give the energies of the six Kramers doublets as functions of δ/λ', where $\lambda' = k\lambda$. Approximate values for these parameters are obtained from experimentally determined g-values for $CdCl_2(Co^{2+})$, which are assumed to also be appropriate for $CoCl_2$, and from magnetic susceptibility measurements on $CoCl_2$.

2.3.2 The Model of Robson[20]

Robson refines Lines's calculation to include the effects of the cubic and trigonal crystal fields within a basis expanded to include all states of the ^4P and ^4F free-ion manifolds and essentially follows the method of Abragaham and Pryce[1]. The spin-orbit interaction is still restricted to the states of the $^4T_{1g}(^4F)$ term. The cubic field and electrostatic parameters are determined by fitting the optical absorption spectra of $CdCl_2(Co^{2+})$ and $CdBr_2(Co^{2+})$[20] using crystal field matrices formed from the Δ, B, C matrices of Tanabe and Sugano[11] and the spin-orbit matrices of Runciman and Schroeder[25]. With $D_q = \zeta = 0$ the electrostatic matrices may be diagonalised to give the energy separation, E_p, of the ^4P and ^4F terms in the crystal. This, together with the cubic-field parameter $21D_q$, as labelled by Abragaham and Pryce[1], gives the admixture of $^4T_{1g}(^4P)$ character into the $^4T_{1g}(^4F)$ groundstate and hence the second order correction to the spin-orbit interaction within this term. The resulting energies of the lowest lying states are characterised by one trigonal field (δ), one spin-orbit (ζ), and two admixture parameters (α and α'). The energy level scheme obtained using all these parameters is overspecified. Hence, the levels are given in terms of δ/ζ for fixed $\alpha = \alpha' = 1.5$. Additional experimental data is available in the form of known groundstate g-values for $CdCl_2(Co^{2+})$[26-28] and $CdBr_2(Co^{2+})$[26,29] crystals which give alternative values of δ/ζ, and allow a refinement of the fitting.

2.3.3 The Model of Hsu and Stout[21]

The theoretical model of Hsu and Stout for $CoCl_2$ is similar to that of Lines but does include the effect of spin-orbit coupling connecting the $^4T_{1g}$ ground level with the higher crystal field quartet levels. To allow for the splitting of the six fold degenerate $^4T_{1g}$ (J = 5/2) term into two levels $U_g'(\Gamma_8^+)$ and $E_g'(\Gamma_7^+)$ by spin-orbit coupling a separation of 75 cm^{-1} is chosen for their calculations. The trigonal crystal-field will also contribute to this splitting but Hsu and Stout do not take any explicit account of such effects.

TABLE 2-I

Energies of the low-lying electronic levels of Co^{2+} ions in $CoCl_2$, $CdCl_2$ and $CdBr_2$†

	$CoCl_2$[a]	$CoCl_2$[b]	$CdCl_2$[a]	$CdCl_2$[c]	$CdBr_2$[c]
$\gamma_4^+(\Gamma_6^+)$	0	0	0	0	0
$\gamma_5^+ + \gamma_6^+(^{(1)}\Gamma_8^+)$	278	275	310	-	-
$\gamma_4^+(^{(1)}\Gamma_8^+)$	446	452	536	-	-
$\gamma_4^+(^{(2)}\Gamma_8^+)$	918	956	949	928	825
$\gamma_5^+ + \gamma_6^+(^{(2)}\Gamma_8^+)$	976	986	1037	988	890
$\gamma_4^+(\Gamma_7^+)$	1059	1113	1134	1063	968

a Calculation based on theory of Lines[19]

b Calculated by Hsu and Stout[21]

c Calculated by Robson[20]

† All units are wavenumbers.

2.3.4 Summary

All the above calculations are not very successful in predicting the positions and splittings of the energy levels of Co^{2+} ions in these crystals. The experimental results obtained in this work could not be adequately interpreted by any of the above models and consequently a more complete model has been adopted. The contributions from doublet states, ignored above, are included and found to be of significance.

2.4 ENERGY LEVEL CALCULATIONS: THIS WORK

For the calculation of the energy levels for divalent cobalt, the strong-field approach of Sugano, Tanabe and Kamimura[30] is used. In this, the splitting of the orbital of a single d-electron by the cubic crystal field into a t_{2g} and e_g orbital is first considered, and then all seven electrons are accommodated in these split orbitals to obtain configurations $t_{2g}^{m}e_g^{n}$ where m+n = 7. Matrices of the electrostatic, spin-orbit interaction, cubic-field and trigonal crystal-field need to be calculated for all states of these $t_{2g}^{m}e_g^{n}$ configurations. The electron-hole isomorphism[31] allows the calculation to be performed for the $3d^3$ configuration provided changes of sign are made to the parameters characterising the cubic crystal-field and spin-orbit interaction. Using the $3d^3$ configuration the allowed configurations and terms are shown in Table 2-II.

The terms of $t_{2g}^{m}e_g^{n}$ are simply derived by combining the allowed terms of t_{2g}^{m} with those of e_g^{n} in all possible ways.

TABLE 2-II

Possible $t_{2g}^{m}e_{g}^{n}$ configurations and $^{(2s+1)}\chi_{r}$ terms of the $3d^{3}$ configuration.

Configurations $t_{2g}^{m}e_{g}^{n}$	Allowed terms $^{(2s+1)}\chi_{r}$
e_g^3	^2E
$t_{2g}e_g^2$	$2(^2T_1) + {}^4T_1 + 2(^2T_2)$
$t_{2g}^2e_g$	$^2A_1 + {}^2A_2 + 2(^2E) + 2(^2T_1) + {}^4T_1 + 2(^2T_2) + {}^4T_2$
t_{2g}^3	$^4A_2 + {}^2E + {}^2T_1 + {}^2T_2$

2.4.1 Formulation of Crystal-Field Operators

In the strong field coupling scheme a wavefunction may be represented as

$$|t_{2g}^{m}e_{g}^{n},\alpha,{}^{(2s+1)}\chi_{r},\Gamma_{i}^{+},\gamma_{t}^{+},\ell\rangle \qquad (2.2)$$

where ℓ identifies the basis functions of the trigonal double group, and α is an additional label to distinguish wavefunctions when there is more than one with the same group theoretical labels in any configuration. Here, α is taken as the irreducible representation of states of the parent $t_{2g}^{m}e_{g}^{n-1}$ configuration.

For these strong cubic field wavefunctions, the cubic crystal-field matrix elements are necessarily diagonal and are characterised by the cubic crystal-field parameter $\Delta = 10D_q$ and:

$$\langle t_{2g}^{m}e_{g}^{n}|V_{cubic}|t_{2g}^{m}e_{g}^{n}\rangle = n\Delta \qquad (2.3)$$

where m+n = 3. The energy matrices of the electrostatic and spin-orbit interactions have already been calculated in the strong-field coupling scheme for the $3d^3$ configuration by Sugano[11] and Schroeder[25] respectively. The electrostatic interaction has non-zero matrix elements only between levels belonging to the same $^{(2s+1)}\chi_r$ terms and is expressed in terms of two Racah parameters B and C. The spin-orbit interaction is characterised by two parameters ζ and ζ'. We thus only need to calculate the energy matrices of the trigonal crystal-field and for the Zeeman interaction in the strong-field coupling scheme to obtain both the position of the energy levels and their g factors for divalent cobalt ions in this symmetry crystal field.

The operator for the trigonal field interaction is given by:

$$V_T = A_2(xy + yz + zx) + A_4[yz(r^2-7x^2) + xz(r^2-7y^2) + xy(r^2-7z^2)] \quad (2.4)$$

for a trigonal distortion along the cubic {111} axis[32]. Both terms in brackets are the sum of three functions transforming as the cubic representation T_2. The general form is thus:

$$V(T_2) = \frac{1}{\sqrt{3}}(V_\xi + V_\eta + V_\zeta) \quad (2.5)$$

where the V_ξ, V_η, V_ζ, transform like the $\eta\zeta(yz)$, $\xi\zeta(xz)$, and $\xi\eta(xy)$ basis functions of the cubic T_2 representation and where the ξ,η,ζ are the cubic axes. For a single d-electron this interaction has non-zero matrix elements between two t_{2g}

orbital states and between t_{2g} and e_g orbital states. Use of the Wigner-Eckart theorem yields:

$$\langle t_2\gamma|V(T_2)|t_2\gamma'\rangle = \frac{1}{\sqrt{3}}\langle t_2 \|V(T_2)\| t_2\rangle \sum_{\bar{\gamma}} \langle t_2\gamma|t_2\gamma' T_2\bar{\gamma}\rangle$$
$$\langle t_2\gamma|V(T_2)|e\gamma'\rangle = \frac{1}{\sqrt{3}}\langle t_2 \|V(T_2)\| e\rangle \sum_{\bar{\gamma}} \langle t_2|e\gamma' T_2\bar{\gamma}\rangle \qquad (2.6)$$

where the γ, γ' and $\bar{\gamma}$ denote particular components of the t_2, e, and T_2 representations[30]. The reduced matrix elements are used to define the two trigonal crystal-field parameters:

$$v = \frac{1}{\sqrt{2}} \langle t_2 \|V(T_2)\| t_2\rangle$$
$$v' = \frac{1}{\sqrt{6}} \langle t_2 \|V(T_2)\| e\rangle \qquad (2.7)$$

The numerical factors in these definitions were chosen to make these parameters identical with the weak crystal-field parameters defined by Pryce and Runciman[33]. The trigonal crystal-field is thus expressed in terms of two parameters v and v'. The operator for this interaction is a one-electron kind and so for a system of n d-electrons, it is summed over all electrons:

$$V_{trig} = \frac{1}{\sqrt{3}} \sum_{i=1}^{n} (V_\xi + V_\eta + V_\zeta) \qquad (2.8)$$

and is calculated between the various terms of the multi-electron configurations.

In an analogous way, the operators for the z and x components of the Zeeman interaction (kL + 2S), where k is the

orbital reduction parameter (typically 0.9), may be developed in terms of one d-electron reduced matrix elements as parameters. The orbital part L of the Zeeman operator has T_1 cubic symmetry, its z and x components being expressed in terms of the operators U_α, U_β, U_γ which transform like the α,β,γ basis functions of the cubic T_1 representation by:

$$U_z(T_1) = \frac{1}{\sqrt{3}}(U_\alpha+U_\beta+U_\gamma), \quad U_x(T_1) = \frac{1}{\sqrt{6}}(U_\alpha+U_\beta-2U_\gamma) \tag{2.9}$$

There are two orbital reduction parameters defined by:

$$\sqrt{6}ik = \langle t_2 \| V(T_1) \| t_2 \rangle \quad -2\sqrt{3}ik' = \langle t_2 \| V(T_1) \| e \rangle \tag{2.10}$$

which are related to those of the spin-orbit interaction by:

$$k = \zeta/\zeta_0, \qquad k' = \zeta'/\zeta_0 \tag{2.11}$$

where ζ_0 is the free-ion spin-orbit coupling constant. The S_z and S_x components of the spin operator S transform in an identical manner and have matrix elements that involve no adjustable parameters.

2.4.2 Matrix Elements of the Trigonal Crystal-Field and Zeeman Interactions

There are 120 states in the $d^3(d^7)$ configuration and matrix elements of the trigonal crystal-field and Zeeman interaction are required of all of these.

Since there are no non-zero matrix elements of either the trigonal crystal-field or the z component of the Zeeman operator between γ_4^+ and $\gamma_{5,6}^+$ states, the 120-dimension matrices

for these interactions can be reduced to two matrices of dimension 78 and 42, respectively, by using basis states having either Υ_4^+ or $\Upsilon_{5,6}^+$ symmetry. However, the basis states used for the published calculations of the cubic-field, electrostatic, and spin-orbit interaction transform as the irreducible representations of the cubic double group referred to a cubic system of axes while the Υ_4^+ and $\Upsilon_{5,6}^+$ states appropriate for a site of D_{3d} symmetry refer to a trigonal system of axes, with the principal axis along the diagonal {111} direction of the set of cubic axes. A rotation of the double cubic group basis states was then performed to obtain basis states of Υ_4^+ or $\Upsilon_{5,6}^+$ symmetry referred to a trigonal system of axes. With these basis states the Υ_4^+ matrices of the trigonal crystal field and the z component of the Zeeman operator simplify further into two 39-dimension matrices corresponding to the two components of the Υ_4^+ states. The x component of the Zeeman operator has non-zero matrix elements between Υ_4^+ and $\Upsilon_{5,6}^+$ states and it is necessary to diagonalise the full 120-dimension energy matrix for this interaction.

The calculation proceeds as follows: The matrix elements of a given interaction are first evaluated between the single cubic group wavefunctions $|t_{2g}^m e_g^n, S, M, \chi_r, \rho\rangle$ where M denotes the particular components of the spin S, and the ρ denotes the components of the particular χ_r irreducible representation of the single cubic group. The Wigner-Eckart theorem is used to obtain:

$$\langle SM\chi_r\rho | V(\bar{\chi}\bar{\rho}) | S'M'\chi_r'\rho' \rangle$$

$$= \frac{1}{\sqrt{\chi_r}} \langle \chi_r\rho | \chi_r'\rho'\bar{\chi}\bar{\rho} \rangle \langle SM\chi_r \| V(\bar{\chi}) \| S'M'\chi_r' \rangle$$

where the Clebsch Gordon coefficients $\langle \chi_r \rho | \chi_r' \rho' \bar{\chi} \bar{\rho} \rangle$ are tabulated by Tanabe et al.[34].

(i) Evaluation of the Reduced Matrix Elements

These have been calculated using the formulae and tables published by Tanabe and Kamimura[35]. The appropriate results are given here for completeness and the reader is referred to their paper for further details.

The reduced matrix elements diagonal in a strong field configuration $t_{2g}^m e_g^n$ are given by:

$$\begin{aligned}
&\langle t_2^m(S_1\Gamma_1) e^n(S_2\Gamma_2) S\Gamma \,\|V(\bar{\Gamma})\|\, t_2^m(S_3\Gamma_3) e^n(S_4\Gamma_4) S\Gamma' \rangle \\
&\quad = \langle t_2^m S_1\Gamma_1 \,\|V(\bar{\Gamma})\|\, t_2^m S_3\Gamma_3 \rangle \delta(S_1S_3)\delta(S_2S_4)\delta(\Gamma_2\Gamma_4) \\
&\qquad\qquad \times (\Gamma_1\Gamma_2\Gamma\{\bar{\Gamma}_a\}\Gamma_3\Gamma_2\Gamma') \\
&\quad + \langle e^n S_2\Gamma_2 \,\|V(\bar{\Gamma})\|\, e^n S_4\Gamma_4 \rangle \delta(S_1S_3)\delta(S_2S_4)\delta(\Gamma_1\Gamma_3) \\
&\qquad\qquad \times (\Gamma_1\Gamma_2\Gamma\{\bar{\Gamma}_6\}\Gamma_1\Gamma_4\Gamma') \qquad (2.13) \\
&\qquad\qquad\qquad\qquad\qquad\qquad\qquad\qquad (2.25)\text{T\&K}
\end{aligned}$$

Tanabe and Kamimura show how the elements $\langle t_2^m S_1\Gamma_1 \,\|V(\bar{\Gamma})\|\, t_2^m S_3\Gamma_3 \rangle$ and $\langle e^n S_2\Gamma_2 \,\|V(\bar{\Gamma})\|\, e^n S_4\Gamma_4 \rangle$ are related to the one-electron matrix elements $\langle t_2 \,\|V(\bar{\Gamma})\|\, t_2 \rangle$ and $\langle t_2 \,\|V(\bar{\Gamma})\|\, e \rangle$ which are usually treated as parameters.

For elements not diagonal in m and n we have:

$$\langle t_2^m(S_1\Gamma_1)e^n(S_2\Gamma_2)S\Gamma \,\|V(\bar{\Gamma})\|\, t_2^{m-1}(S_3\Gamma_3)e^{n+1}(S_4\Gamma_4)S\Gamma'\rangle$$

$$= \sqrt{M(2S_1+1)(\Gamma_1)}\ (t_2^m S_1\Gamma_1\{|t_2^{m-1}(S_3\Gamma_3)t_2) \qquad (2.14)$$

$$\times\ (ee^n(S_2\Gamma_2)|\}e^{n+1}S_4\Gamma_4)\sqrt{(n+1)(2S_4+1)(\Gamma_4)} \qquad (2.35)\text{T\&K}$$

$$\times\ \langle t_2\,\|V(\bar{\Gamma})\|\,e\rangle[S_1S_2S|S_3S_4S][\Gamma_1\Gamma_2\Gamma\{\bar{\Gamma}\}\Gamma_3\Gamma_4\Gamma']$$

The coefficients of fractional parentage, $(t_2^m S_1\Gamma_1\{|t_2^{m-1}(S_3\Gamma_3)t_2)$ are tabulated in Tanabe and Sugano[11] while the remaining factors in (2.13) and (2.14) are listed in Tanabe and Kamimura[35].

Since the ligand-field operator is a one-electron operator all elements between configurations $t_2^m e^n$ and $t_2^{m'} e^{n'}$ for which $|m-m'| + |n-n'| > 2$ (with $m+n = m'+n'$) are zero. Other selection rules are implied in (2.13) and (2.14) and these reduce the necessary computation.

Using the equations above, the reduced matrix elements for $\bar{\Gamma} = T_2$ and T_1 have been calculated for all configurations $t_2^m e^n$ with $m+n = 3$, these being the reduced matrix elements for the trigonal crystal-field and Zeeman interactions. They are listed in Appendix I and II. The reduced matrix elements of $V(T_2)$ and $V(T_1)$ for t_2^3 and t^2e configurations have already been published by Sugano and Peter[36] and for the common configurations our results are in agreement with theirs.

(ii) Transformation to a $|\gamma_t \ell\rangle$ scheme

The $|SM\chi_r\rho\rangle$ wavefunctions are transformed to wavefunctions of the double cubic group $|\Gamma_n m\rangle$ by:

$$|\Gamma_n m\rangle = \sum_{M\,\rho} \langle SM\chi_r\rho|\Gamma_n m\rangle |SM\chi_r\rho\rangle \qquad (2.15)$$

where the Wigner coefficients $\langle SM\chi_r\rho|\Gamma_n m\rangle$ are tabulated by Schroeder[37]. These wavefunctions are then rotated to the trigonal system of axes by the transformation:

$$|\gamma_t \ell\rangle = \sum_m \langle\Gamma_n m|\gamma_t \ell\rangle|\Gamma_n m\rangle \qquad (2.16)$$

The coefficients of this unitary transformation were derived from the rotation matrices for the $s = \frac{1}{2}$, $s = \frac{3}{2}$ spin functions[38] and are listed in Table 2-III.

(iii) Computation and Checking

The final expression for the matrix element is:

$$\langle\gamma_t'\ell'|V(\bar{\chi}\bar{\rho})|\gamma_t\ell\rangle$$

$$= \langle\tau'S'\chi_r'\,\|V(\bar{\chi}\bar{\rho})\|\,\tau S\chi_r\rho\rangle$$

$$\times \{\sum_{mm'}\Big[\sum_{\rho\rho'}\langle\Gamma_n'm'|S'\chi_r'\rho'\rangle\frac{1}{\sqrt{\chi_r}}\langle\chi_r'\rho'|\chi_r\rho\bar{\chi}_r\bar{\rho}\rangle\langle S\chi_r\rho|\Gamma_n m\rangle\Big]$$

$$\times \langle\Gamma_n m|\gamma_t\ell\rangle\langle\gamma_t'\ell'|\Gamma_n'm'\rangle\} \qquad (2.17)$$

where the sum over m,m',ρ,ρ' can be considered as decomposed into two matrices $A_{m'm}$ and $B_{mm'}$. The first, is that part of (2.17) contained in auxiliary brackets, and the second is the product of the last two terms. Thus,

$$\langle\gamma_t'\ell'|V(\bar{\chi}\bar{\rho})|\gamma_t\ell\rangle = \langle\tau'S'\chi_r'\,\|V(\bar{\chi}\bar{\rho})\|\,\tau S\chi_r\rho\rangle$$

$$\times \sum_{mm'} A_{m'm} \times B_{mm'} \qquad (2.18)$$

where this sum is the trace of the product $A_{m'm} \times A_{mm'}$, and can be calculated directly as a sum of the product of corresponding

TABLE 2-III: The Unitary Matrices $\langle \gamma_t \ell | \Gamma_n m \rangle$

$\langle \gamma_4 \ell | \Gamma_6 m \rangle$

γ_4 \ Γ_6	$\frac{1}{2}$	$-\frac{1}{2}$
$\frac{1}{2}$	$ce^{i\alpha/2}$	$se^{-i\alpha/2}$
$-\frac{1}{2}$	$-se^{i\alpha/2}$	$ce^{-i\alpha/2}$

where: $c = \cos \beta/2$

$s = \sin \beta/2$

$\alpha = \frac{\pi}{4}$

$\langle \gamma_4 \ell | \Gamma_7 m \rangle$

γ_4 \ Γ_7	$\frac{1}{2}$	$-\frac{1}{2}$
$\frac{1}{2}$	$-ce^{-i3\alpha/2}$	$se^{i3\alpha/2}$
$-\frac{1}{2}$	$-se^{-i3\alpha/2}$	$-ce^{3i\alpha/2}$

and β is such that:

$\cos \beta = 1/\sqrt{3}$

$\sin \beta = \sqrt{2}/\sqrt{3}$

$\langle \gamma_4 \ell | \Gamma_8 m \rangle$

γ_4 \ Γ_8	$\frac{3}{2}$	$\frac{1}{2}$	$\frac{-1}{2}$	$\frac{-3}{2}$
$\frac{1}{2}$	$\sqrt{3}c^2se^{i3\alpha/2}$	$(-c^3+2cs^2)e^{i\alpha/2}$	$(s^3-2c^2s)e^{-i\alpha/2}$	$-\sqrt{3}cs^2e^{-3i\alpha/2}$
$-\frac{1}{2}$	$\sqrt{3}cs^2e^{i3\alpha/2}$	$(s^3-2c^2s)e^{i\alpha/2}$	$(c^3-2cs^2)e^{-i\alpha/2}$	$\sqrt{3}c^2se^{-i3\alpha/2}$

$\langle \gamma_{5,6} \ell | \Gamma_8 m \rangle$

$\gamma_{5,6}$ \ Γ_8	$\frac{3}{2}$	$\frac{1}{2}$	$\frac{-1}{2}$	$\frac{-3}{2}$
$\frac{3}{2}$	$c^3e^{i3\alpha/2}$	$\sqrt{3}c^2se^{i\alpha/2}$	$\sqrt{3}cs^2e^{-i\alpha/2}$	$s^3e^{-i3\alpha/2}$
$-\frac{3}{2}$	$-s^3e^{i3\alpha/2}$	$\sqrt{3}cs^2e^{i\alpha/2}$	$-\sqrt{3}c^2se^{-i\alpha/2}$	$c^3e^{-i3\alpha/2}$

elements in the m'-row and m-column of A with those of the m-row and m'-column of B. The result obtained from evaluating the auxiliary brackets is then multiplied by the appropriate reduced matrix element $<||\ ||>$.

The complete matrices of the trigonal crystal-field are given in Appendix I. Because of their dimension, those for the Zeeman interaction are listed in Appendix II in a more compact form as follows: The terms in the summation in (2.18) are listed according to the spin multiplicity (2s+1 = 2 - doublets, 2s+1 = 4 - quartets) and need only be multiplied by the appropriate reduced matrix element $<||V(T_1)||>$ which are also listed there.

Because of the large amount of numerical calculation involved in evaluating the matrix elements it is necessary to carry out checks on the final results. All matrices were checked to within a phase by numerical diagonalisation. Incorrect elements were located by examining the form of the eigenvectors. The trigonal crystal-field matrices were further checked by examining the eigenvalues when each parameter is separately set to zero. These values are necessarily identical with those obtained by distributing three electrons over the trigonally split levels of a single d-electron taking account of the Pauli Exclusion principle. The Zeeman matrices were checked in the same way. Further checks were made by comparison of the eigenvalues with the results for $MgO:Cr^{3+}$ and $Al_2O_3:Cr^{3+}$ obtained by Macfarlane[39] using his weak-field $d^3(d^7)$ matrices.

CHAPTER III

EXPERIMENTAL TECHNIQUES

3.1 THE CRYSTALS, THEIR GROWTH, AND PREPARATION

Cadmium-chloride-type crystals were chosen as hosts for these investigations for the following reasons:

(i) They contain relatively heavy atoms and form anhydrous crystals possessing no molecular groups. Consequently, samples a few millimetres thick are transparent down to 400 cm^{-1} for the chlorides and to 250 cm^{-1} in the case of cadmium-bromide.

(ii) The metal cations are located in sites which have only a slight trigonal distortion from cubic symmetry.

(iii) Cadmium-chloride, cadmium-bromide, manganese-chloride, and cobalt-chloride are all isomorphic and spectral changes caused by the variation of either the cation or anion in a given crystal structure can be readily investigated.

(iv) The $\vec{k} = 0$ lattice phonon spectra of all four crystals have been previously determined by infrared absorption[40] and Raman scattering experiments[41].

(v) The crystals containing cobalt are generally blue/green in colour and can be examined by Raman scattering with argon-ion laser excitation with the possibility of resonance enhancement due to the proximity of the cobalt absorption bands to the argon-ion laser frequencies.

(vi) The cobalt ion concentration may be varied over a wide range to distinguish spectra of both single cobalt ions

and of cobalt ion clusters. Cobalt-chloride itself becomes antiferromagnetically ordered below 24.71^{o}K and the effects of such magnetic ordering on the spectra can also be determined.

However, all the crystals used are hygroscopic and care must be taken in their preparation and mounting in order to prevent contamination by moisture.

The crystals were grown from the melt using the Stockbarger method by Mr Ross Ritchie of this department. Analar-grade powders of the hydrated salts were first dehydrated, under vacuum, in a furnace maintained at 200^{o}C, for several days. They were purified of oxide and residual water by passing dry hydrogen-chloride or hydrogen-bromide (as appropriate) through the materials for several hours as they were heated to the melting point and then bubbling the gas through the melt for an additional hour. The purified melt was filtered through a sintered quartz sieve into a quartz tube which was sealed off. The crystals were grown by slowly lowering the sealed quartz ampoules through a sharp temperature gradient. The resulting crystal-boules were typically of dimension 8 mm diam. by 20 mm long and comprised a single crystal if the tip of the ampoule was pointed to allow the growth of only one crystal from the initial seed crystals. If, in addition, the ampoule was necked 5 mm above the tip single crystals were consistently obtained. A typical crystal ampoule is shown in an inset of Figure (6-4).

Cadmium-chloride and -bromide crystals are optically clear while manganese-chloride is pink. Introduction of cobalt results in a blue/green colouration which becomes progressively

more intense with increased doping. The crystals containing either negligible or high cobalt-dopings were not usually as perfect in structural quality as the lightly doped samples, which were excellent.

The quartz ampoules were opened and the crystal specimens prepared and mounted in a dewar all inside a dry-box. This was constructed in this department by Mr Ross Ritchie and is shown in Figure 3-1. By continually recirculating the air through molecular sieves (B.D.H. Molecular Sieves type 4A) the atmosphere of the box was maintained at better than 14% humidity. The dewar to be used was evacuated immediately after its removal from the box to prevent possible crystal rehydration. Subsequent infrared measurements showed no absorptions due to water[42], confirming that the crystals prepared as above had no contamination introduced during either growth or transfer to the dewar.

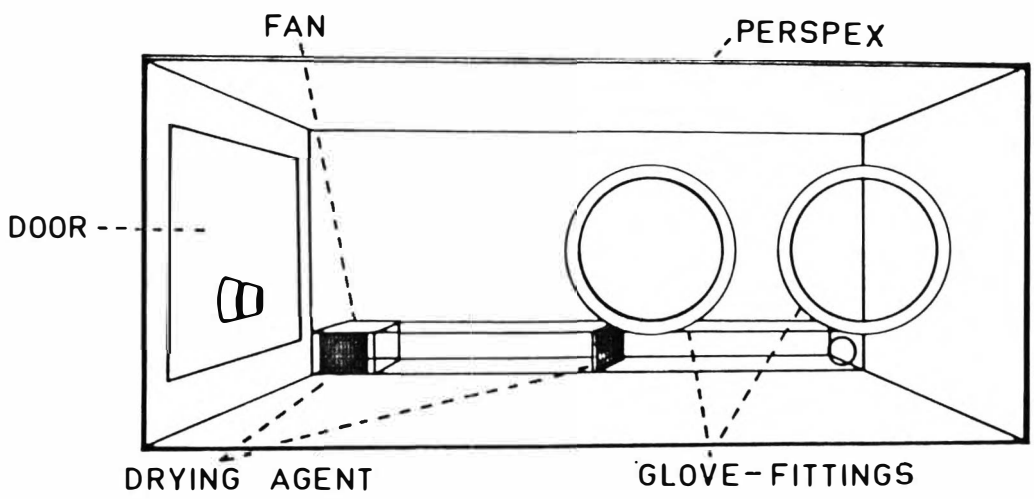

Figure 3-1: The dry-box.

Cadmium-chloride-type crystals have a layered structure with weak bonding between the chlorine or bromine ions (Figure 2-1). Hence, the crystals cleave easily along the layers, which are perpencidular to the crystal c-axis. However, samples suitable for polarised measurements required the polishing of faces perpendicular to these natural cleavage planes. This was accomplished by the use of a polishing jig which was constructed in the department and was suitable for the preparation of specimens for both Raman and infrared polarised spectra. The device is shown below in Figure 3-2.

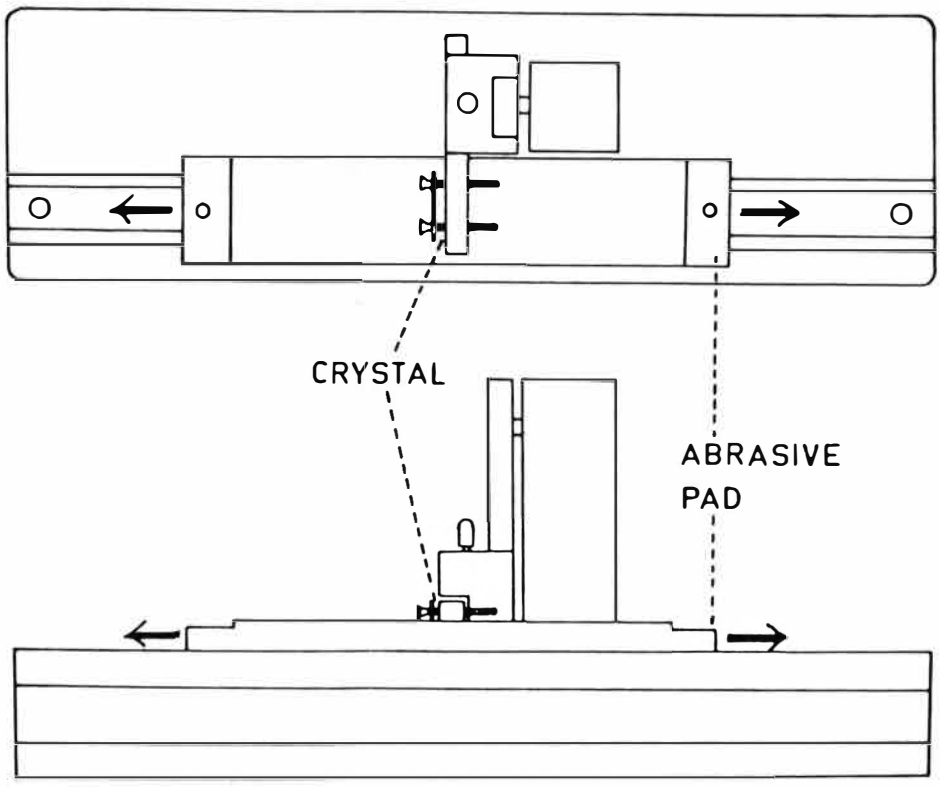

Figure 3-2: The crystal polishing-jig.

To use it, the crystal was first clamped so that its cleaved surface was in contact with the machined surface of the steel bar. The bar was then fixed into a metal support on the vertical slide. The weight of the bar and its support was sufficient to hold the crystal in continuous contact with the abrasive pad which may be drawn forward and back beneath it. Successively finer grades (350, 400, 600 ...) of Silicon-Carbide paper were used to grind a pair of parallel faces. A final, high-lustre finish was obtained by using (0-3) emery paper and soft leather.

3.2 RAMAN MEASUREMENTS

3.2.1 Instrumentation

The Raman system was originally assembled by Lockwood[43] and Christie[44] and was inherited by the author. A schematic diagram of the equipment is given in Figure 3-3.

Raman spectra were excited by using the argon ion laser lines at 457.9, 476.5, 488.0, 496.5 and 514.5 nm provided by a Space Rays Inc. model 5600 argon ion laser. The output power is nominally 1 watt and 80% of this is shared between the 488.0 and 514.5 nm lines. More power could be obtained by using high quality quartz flats as Brewster windows in place of the glass ones supplied and these were used throughout this work. Selection of a single wavelength is achieved by a reflecting prism which can be rotated accurately with micrometer screwgauges. The emerging laser beam is filtered, largely by the prism already mentioned, and by a simple interference filter which may be rotated to match the laser frequency. This effectively removes all argon ion plasma

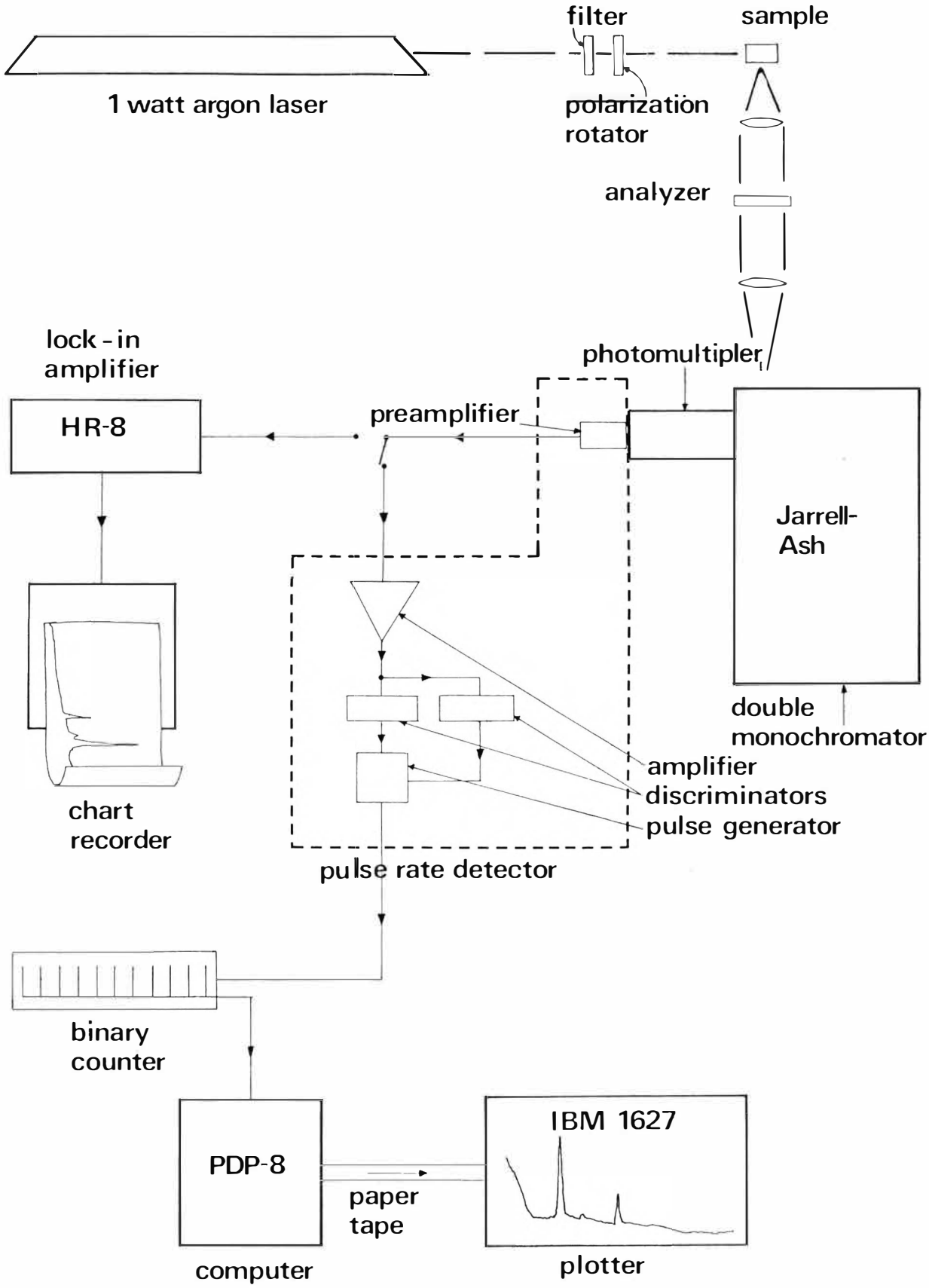

Figure 3-3: Schematic diagram of the Raman spectrometer.

light scattered elastically into the spectrometer. Polarisation of the incident laser beam on the crystal was set using a half-wave plate coupled to a Glan Thomson prism. The scattered light was analysed by a large Nicol prism. The light was then dispersed with a Jarrell-Ash model 25-103 double monochromator of one-metre focal length and detected photoelectrically with a thermoelectrically cooled E.M.I. 6255 S.A. photomultiplier.

There are two signal processing systems that can be used: namely, phase-sensitive detection or photon-counting. The phase-sensitive detector is a Princeton Applied Research model HR-8 lock in amplifier which detects only those signals modulated at the reference frequency. A mechanical chopper, positioned in front of the reflecting prism modulated the emerging laser light, and hence the Raman signal, and provided the necessary reference signal for the amplifier.

For more detailed work the more sensitive photon-counting system is used in which a pulse-rate detector records the photo-multiplier signal in digital form by counting the number of photon-induced pulses produced by the photomultiplier in a given time. This is in contrast to the analogue method used by the phase-sensitive detector. The initial electronic circuitry has been described by Lockwood[43] and the later modifications by Christie[44]. The pulses are amplified and fed into a remote, unidirectional, 11-bit binary counter controlled by a DEC PDP-8 computer. The computer is operated on a timeshare-basis with other experiments and reads the counter either at constant time-intervals or in the event of an overflow interrupt. The counter also has a twelfth bit

which is incremented by calibration pulses from the Raman spectrometer permitting accurate frequency calibration of recorded spectra. The data thus collected is stored and punched onto paper tape on command. This tape output may be processed later using an IBM 360/44 computer and plotted by an IBM 1627 plotter. More recently the computing facilities have been replaced by a Burroughs B6700 machine.

3.2.2 Technical Improvements

The following improvements have been made to the system during this work:

(i) The previous digital detection system has been augmented with a direct chart recorder output using a ratemeter constructed in this department by Mr Ray Borrell. This has the advantage of giving immediate visual data in conjunction with the computer recording system. The electronic circuitry has been described in a department report[45]. The photomultiplier pulses are fed into a monostable through either an Edge- or Schmitt-trigger input depending on their waveform. The latter is used for pulses with rise-times less than 1 volt per micro-second. The monostable generates regular pulses of fixed height but of variable width depending on the number of pulses entering per second. This number-range may be preset and has upper and lower limits of 3.0×10^4 and 10^2 pulses per second respectively. These pulses are then averaged over a preset time interval of between 0.1 and 30 seconds, depending on the spectrometer scanning speed, to give a d.c. voltage proportional to the number of

pulses received which is then displayed on a chart recorder.

(ii) For the early polarisation measurements, a 1/3-metre monochromator was attached to the double monochromator to produce a triple monochromator. This was not coupled to the frequency drive of the spectrometer but was operated instead as a fixed-frequency premonochromator with the double spectrometer scanning through the "fixed-frequency window". This arrangement was useful for reducing stray light in cases where the Raman lines were very weak.

(iii) Finally, the laser described above has been recently replaced by a Spectra-Physics Model 171 argon ion laser together with a Model 370 tunable dye laser. However, this facility was not operational before the completion of the research work described in this thesis.

3.2.3 Measurement Techniques

Crystal specimens for most of the Raman spectra were cleaved and positioned so that the laser beam entered the crystal in a direction perpendicular to the c-axis while the scattered light was viewed along the direction of the c-axis itself. This is the usual right-angled scattering geometry. For cobalt-chloride crystals, the absorption by the crystal for all the argon ion laser frequencies used was sufficiently high to require the use of a backward scattering technique. In this, the laser light is incident on a polished crystal surface and that scattered off this same surface is collected by the spectrometer. This surface scattering technique was also used for obtaining the polarisation of the Raman lines as

it has the advantage of requiring only one polished surface on the crystal for which there is less depolarisation of the incident and scattered laser beam. The optical arrangement is shown in Figure 3-4.

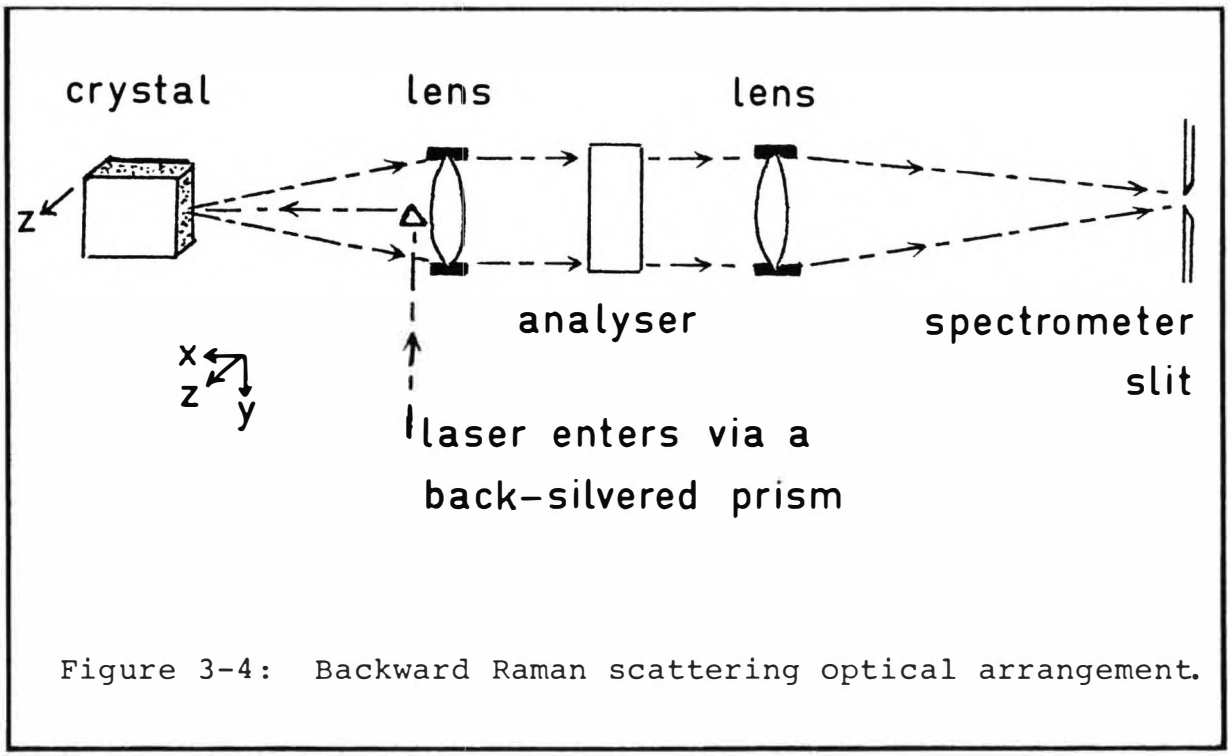

Figure 3-4: Backward Raman scattering optical arrangement.

For low temperature spectra, the crystals were clamped to a sample block, using Indium foil to ensure maximum thermal contact between the crystal and block. The copper block was fixed to the base of the liquid helium reservoir of a Hofman optical dewar. The crystals were cooled by conduction and achieved a temperature somewhat higher than that of the refrigerant. For liquid helium, crystal temperatures of approximately $15^{o}K$ were obtained. The observation of the onset of antiferromagnetic ordering in cobalt-chloride confirms that

the crystal temperature goes below 24.71°K while the difference in vibronic spectra observed by infrared spectroscopy (as described in Chapter 5.5) allowed the actual crystal temperatures to be measured.

3.3 INFRARED MEASUREMENTS

3.3.1 Instrumentation

All absorption spectra in the range 200-4000 cm^{-1} were obtained using a Beckman IR12 double beam spectrophotometer. This instrument can measure lines to an accuracy of ±0.25 cm^{-1} at 923 cm^{-1}. Its overall wavenumber accuracy was maintained to better than ±0.5 cm^{-1} by use of the calibration lines of water-vapour, ammonia, and polystyrene films. The machine uses a Nernst glower as the infrared source and employs the double beam optical null method where the light is passed alternately through the sample and reference compartments by a pair of synchronous choppers. On recombination the two beams are dispersed by a filter/grating monochromator and then focussed through slits onto a vacuum thermocouple detector. The slit-widths are programmed to give approximately constant energy. During the recording of low-temperature spectra the second chopper frequently had to be stopped in order to prevent thermal emission effects from producing a spurious spectral signal causing 0% transmission below 800 cm^{-1}. This is caused by the detector comparing the thermal emission from the reference channel with the absence of it from the cold sample.

To reduce the effect of atmospheric water-band absorption on the spectra and protect the hygroscopic thermocouple window, the complete spectrophotometer was continually purged with dry air.

Polarisation spectra were recorded using either a Beckman silver chloride polariser or a Cambridge grid wire polariser. Increased slit widths were needed for these spectra to compensate for the transmission loss in the polariser which is located in the combined beam, after the monochromator. The axial spectra were recorded without the polariser in place and consequently narrower spectrophotometer slit-widths were possible which allowed more accurate line-shapes, frequencies, and widths to be obtained.

3.3.2 Technical Improvements

For most of this work the crystals were cooled in a Hofman conduction type dewar, as in the Raman experiments, except now equipped with caesium-bromide or caesium-iodide windows. However, recently a new low-temperature dewar has been constructed by Messrs Bob Tyree and Terry Rowe of this department so that spectra may be recorded for temperatures below that of the previous limit of $15^{o}K$.

For cooling, this dewar employs two small jets which spray liquid helium directly onto the sample rather than relying on the conventional copper conduction block. The crystal temperature may be varied either by pumping on the helium outlet line, throttling the valve controlling helium flow through the jets, or by an electrical heater wound around the sample holder. Crystal temperatures as low as $4^{o}K$ were consistently obtained. In addition to reducing helium consumption, samples were able to be changed without recycling the apparatus to room temperature. The design of the dewar-tail was necessarily restricted by the dimensions of the Beckman beam condenser, in which the sample must be placed,

while the design of the whole assembly had to allow for frequent servicing of the deliquescent caesium-bromide windows. The dewar design is outlined in Figure 3-5.

The outer can was constructed of argon-welded stainless steel while the inner can and internal piping is copper. The tail-section is brass. To assist with pre-cooling and cryo-pumping the vacuum space the inner can has two compartments. The first is a helium-outlet-line cooling space at the base while the second, contained charcoal in brass wire cages which were designed to fit snugly around all inner piping. For extra thermal insulation the inside can's outer surface was wound with alternate layers of fibre-glass and aluminium foil.

Both sets of windows were Caesium-bromide. The three outer ones were held in their recesses by wire-clips and sealed by rubber "O"-rings. Because of the differing thermal expansions of caesium-bromide, copper, and brass the inner windows had to be mounted on a flexible support if they were to survive recycling between 300 and 4^{o}K. In the most satisfactory method for this, the windows were glued to a thin copper ring which was soldered to the brass sample compartment with Wood's metal. A die was used to press the holders (Inset, Figure 3-5) from a 0.002" thick annealed copper sheet which had been cleaned in a 10% Sulphuric acid solution. The contact surfaces of the window and copper ring were wetted with Araldite A.U.1 glue, fixed, and then cured for three hours at 150^{o}C. For periodic cleaning the copper-brass joint was unsoldered and the windows polished with a Tin-oxide/methanol paste.

Figure 3-5: The new helium dewar.

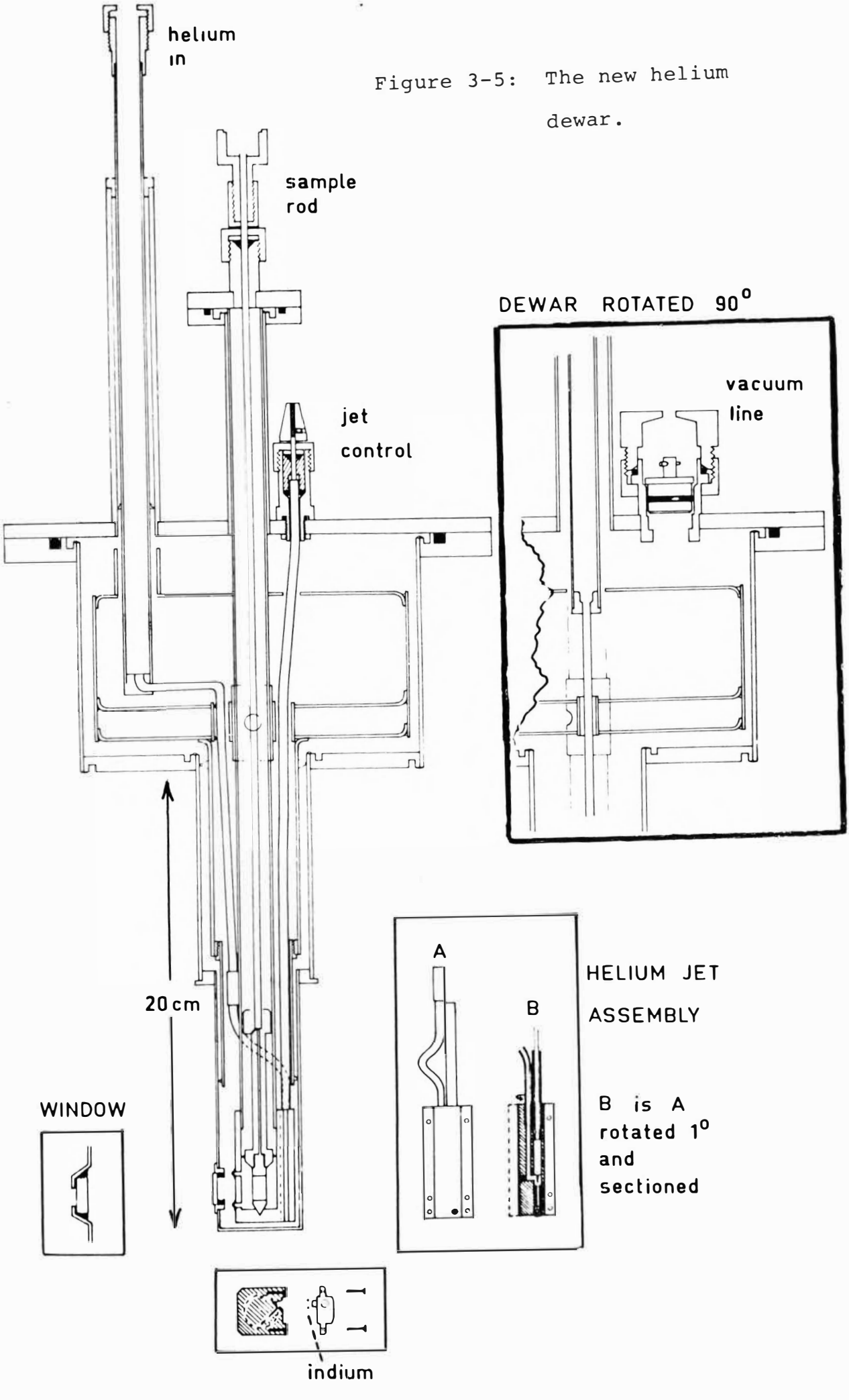

The copper sample holder was screwed into a heater bobbin at the end of a hollow inserting rod which could be located in a countersunk recess in the base of the sample chamber to facilitate optical alignment and maintain cold contact. The rod's hollow centre also served to accommodate all electrical leads which simplified the interchanging of sample tips. The crystal temperature was continuously monitored by a 1 kΩ Alan Brady resistor whose calibration curve has been given by Rose[46] as:

$$\log_{10}R = a + b\left(\frac{\log_{10}R}{T}\right)^{\frac{1}{4}} \qquad (3.1)$$

with a = 2.85 and b = 1.60. For sustained accuracy however, the resistor was recalibrated at $4^{o}K$ before each experiment.

3.3.3 Measurement Techniques

The crystal specimens for the axial spectral measurements were obtained by cleaving the crystals to the desired thickness and having the infrared radiation propagating perpendicular to the cleavage planes. For the polarisation spectra, it was necessary to mount the crystals so that the light propagated along the cleavage planes and surfaces perpendicular to the cleavage planes were obtained by polishing the crystals for these directions.

CHAPTER IV

THE RAMAN SCATTERING SPECTRA OF $CdCl_2(Co^{2+})$, $CdBr_2(Co^{2+})$, $MnCl_2(Co^{2+})$ AND $CoCl_2$

4.1 INTRODUCTION

Traditionally, Raman scattering has been concerned with the measurement of the vibrational and rotational behaviour of solids, liquids and gases. However, more recently it has also been successfully applied to the study of electronic[47-52] and magnetic[47,53-56] behaviour in solids. Several properties of the laser have made this possible. Firstly, the high intensity and narrow linewidths of the laser have enabled Raman scattering of materials to be observed under higher resolution. Secondly, the collimated and plane-polarised characteristics of the laser radiation permit the measurement of the separate polarisability components of the scattered light, which in principle, gives the symmetries of the electronic states in addition to their energies.

Raman and infrared spectra often yield complementary information. Although Raman spectra are weak, since they rely on a second-order process, they are frequently less complicated than infrared spectra and have narrower spectral lines. Further, the low-lying electronic levels of interest have a common free-ion parent (namely ^4F) and thus have the same parity. Since the Raman operator has even parity all transitions between these levels are Raman allowed while they are parity forbidden for electric-dipole transitions. In contrast, the

infrared electronic lines are magnetic-dipole in character, very weak, and easily confused with their associated vibronics or other impurity activated lines.

In this work polarised Raman spectra of divalent cobalt ions in cobalt-chloride and as a substitutional impurity in cadmium-chloride, cadmium-bromide and manganese-chloride are reported for concentrations ranging from 2.5 to 10.0 wt.% and for temperatures of 15, 77 and 300^{o}K. All five electronic transitions from the lowest to the upper spin-orbit and trigonal crystal-field split levels of the $^{4}T_{1g}(^{4}F)$ cubic-field ground term have been identified for each crystal. A general description of the spectra observed is outlined in Section 4.2 while specific results are documented in Section 4.3. The spectra of single cobalt ions are analysed in Section 4.4 using a crystal-field model involving all 120 states of the $3d^{7}$ configuration. Parameters describing the trigonal crystal-field and spin-orbit interaction are obtained and interpreted in Section 4.5. The spectra of cobalt ion clusters are also described but due to the paucity of data compared to that obtained by infrared absorption investigations of the same lines their assignment is left to Chapter VI. The antiferromagnetic ordering of $CoCl_2$, below 25^{o}K, is quantitatively interpreted in Section 4.6 using a molecular field model for the exchange split electronic levels.

Some Raman spectra have been already reported for these lattices. The phonon spectra of the pure lattices were measured by Lockwood[40]. Similar work by Nakashima et al.[57] was restricted to $CdCl_2$, $CdBr_2$, and CdI_2 crystals. The Raman spectra of the first four hosts containing Co^{2+} ions have

already been reported by Christie and Lockwood[41,58,59]. Their initial work was extended by Christie[44] whose results were still largely incomplete at the commencement of this thesis work. The data available then is summarised in Table 4-I and was interpreted using Robson's[20] crystal-field analysis.

TABLE 4-I

Christie and Lockwood's Raman data[41,58,59] (1973)†

$CdCl_2(Co^{2+})$: 3 wt.%	$CdBr_2(Co^{2+})$: 3 wt.%	$MnCl_2(Co^{2+})$: 3 wt.%	$CoCl_2$[a] (P.M.)	$CoCl_2$[a] (A.F.M.)
-	284	(206)	221	233
500	-	529	545	549
923	-	936	968	961.5
953	894	967	987	983
-	995	-	-	1014
				-

†. All measurements in wavenumbers (cm^{-1})

a. Results for both paramagnetic and antiferromagnetic phases.

The agreement obtained was only qualitative, since the spectra indicated that the lower pair of excited states should be much more widely split than predicted while of the expected upper triplet only two lines were visible. Consequently, the uppermost $\gamma_4^+(\Gamma_7^+)$ line had not been correctly identified in any of the crystals and no overall spectral pattern was evident. Further, since no spectra of Ni^{2+}-doped hosts were available there was no surety that some of the features observed were in

fact Co^{2+} electronic lines and not impurity activated second-order phonon lines. Also, because of the lack of polarisation spectra no assignment of transitions to specific crystal-field states of the $^4T_{1g}(^4F)$ manifold could be made.

4.2 GENERAL DESCRIPTION OF THE SPECTRA

The Raman spectra observed for the three chloride crystals were very similar to each other, while that for the bromide differed in some respects. All the spectra showed two narrow and intense lines due to the Raman active $\vec{k} = 0$ phonons of the host lattices. For crystals containing a low concentration of cobalt the positions of these lines were identical to those of the undoped hosts. As the cobalt concentration was increased, the lines exhibited one-mode behaviour by shifting to higher frequencies, towards those of the corresponding lines observed in cobalt-chloride and cobalt-bromide[60]. Since these crystals possess a centre of inversion the infrared and Raman active phonons necessarily have odd and even parity respectively. Factor group analysis predicts that the possible symmetries of the Raman active phonons are one A_{1g} and one doubly degenerate E_g mode for each crystal. Of these, Lockwood has shown that the A_{1g} mode has the higher frequency and this has been confirmed by polarisation measurements in this work. A polarised phonon spectrum, representative of all the crystals examined, is presented in Figure 4-1.

In the high frequency region of the Raman spectra additional lines were observed. Those due to electronic transitions of cobalt were identified by their correlation

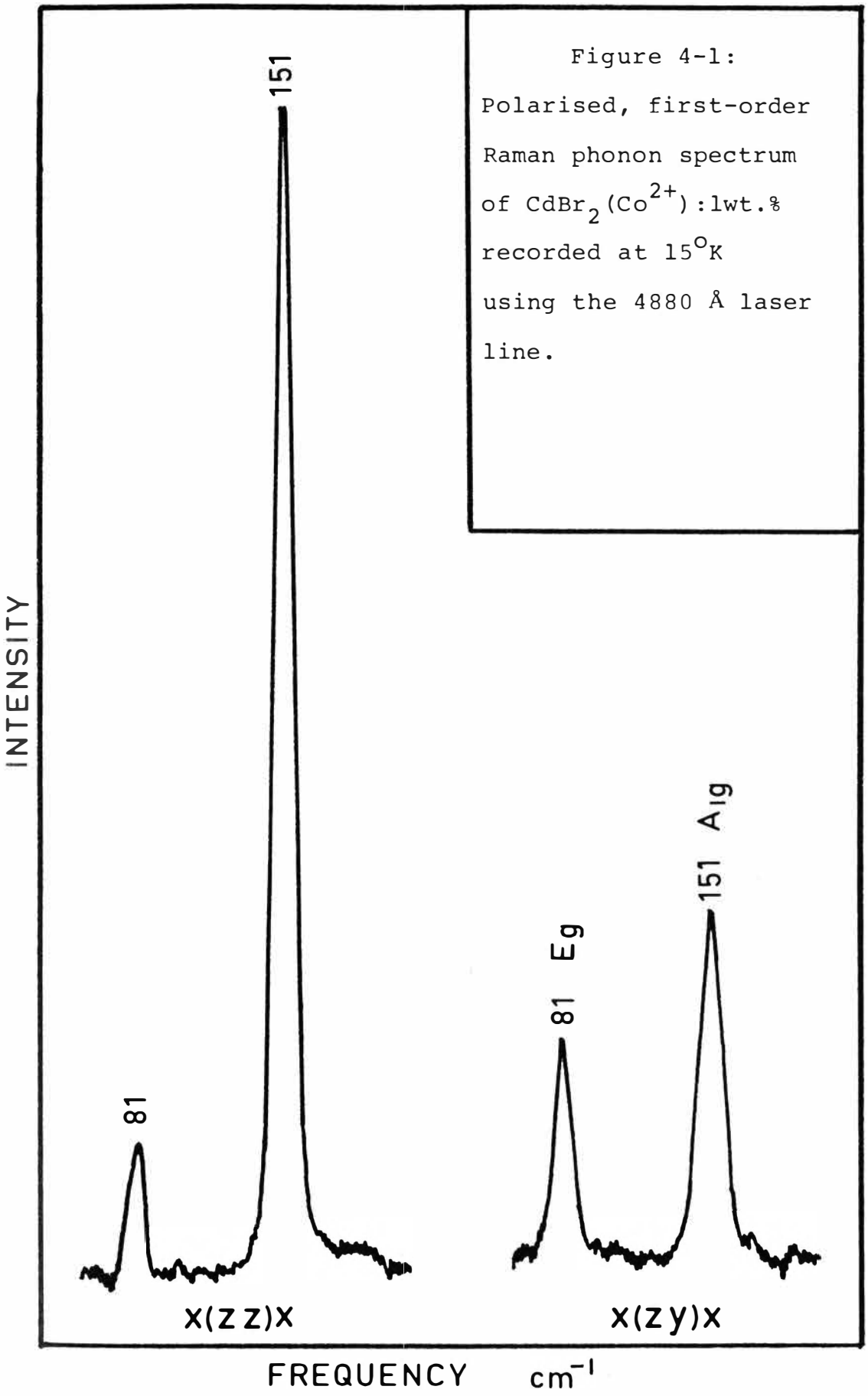

Figure 4-1:
Polarised, first-order Raman phonon spectrum of $CdBr_2(Co^{2+})$:1wt.% recorded at 15°K using the 4880 Å laser line.

with the cobalt concentration - the lines due to isolated cobalt ions have an intensity linearly related to the cobalt concentration while the intensity of lines associated with cobalt ion clusters showed a more rapid increase. Raman lines due to two-phonon processes were also present. These have an intensity which is enhanced by the presence of impurities in the crystals. However, they can be distinguished from the cobalt electronic lines by their presence in the same host crystals doped with other ions. In particular, $CdBr_2(Ni^{2+})$ crystals were examined. Fluorescence lines also occur for some crystals but these can be distinguished in the usual way by comparison of the spectra for two different laser excitation frequencies: Raman lines have a fixed displacement from the exciting line while fluorescence lines have the same absolute frequencies irrespective of the excitation frequency.

The identification of the electronic Raman lines due to single cobalt ions from their concentration dependence was confirmed by their polarisation properties which are consistent with the selection rules for Raman active transitions between γ_4^+ and $\gamma_{5,6}^+$ electronic states. These may be derived[44] from the multiplication table for representations of the point group D_{3d} together with the symmetry properties of the relevant Raman scattering tensors. The Raman scattering efficiencies for the two transitions $\gamma_4^+ \rightarrow \gamma_4^+$, and $\gamma_4^+ \rightarrow \gamma_5^+ + \gamma_6^+$ are obtained by adding and squaring the irreducible Raman tensors as shown in Table 4-II. Of the two types of transitions then, $\gamma_4^+ \rightarrow \gamma_5^+ + \gamma_6^+$ transitions will be absent in **x(zz)x** polarisation while $\gamma_4^+ \rightarrow \gamma_4^+$ transitions will occur in all polarisations. They may also be distinguished by comparing the

xx and xy polarisation spectra since the xx and xy components of the tensors below may differ for transitions to γ_4^+ final states but not for transitions to $\gamma_5^+ + \gamma_6^+$ final states.

TABLE 4-II†

Selection rules for Raman transitions among the low-lying energy levels of the Co^{2+} ion in a trigonal crystal field.

Representation Multiplication Table for D_{3d}:

$$\gamma_4^+ \times \gamma_4^+ = \gamma_1^+ + \gamma_2^+ + \gamma_3^+$$

$$\gamma_4^+ \times (\gamma_5^+ + \gamma_6^+) = 2\gamma_3^+$$

$$(\gamma_5^+ + \gamma_6^+) \times (\gamma_5^+ + \gamma_6^+) = 2\gamma_1^+ + 2\gamma_2^+$$

Transformation Properties of Raman Scattering Tensors:

Symmetry	Raman Tensor	Allowed Transitions
γ_1^+	$\alpha_{xx}=\alpha_{yy}=a;\ \alpha_{zz}=b$	$\gamma_4^+ \to \gamma_4^+;\ (\gamma_5^+ + \gamma_6^+) \to (\gamma_5^+ + \gamma_6^+)$
γ_2^+	$\alpha_{xy}=-\alpha_{yx}=c$	$\gamma_4^+ \to \gamma_4^+;\ (\gamma_5^+ + \gamma_6^+) \to (\gamma_5^+ + \gamma_6^+)$
γ_3^+	$-\alpha_{xx}=\alpha_{yy}=\alpha_{xy}=\alpha_{yx}=d$ $\alpha_{yz}=-\alpha_{xz}=e$ $\alpha_{zx}=-\alpha_{zy}=f$	$\gamma_4^+ \to \gamma_4^+;\ \gamma_4^+ \to (\gamma_5^+ + \gamma_6^+)$

Raman Scattering Efficiencies:

$$\gamma_4^+ \to \gamma_4^+ \quad \begin{bmatrix} a'^2 & c'^2 & f'^2 \\ c'^2 & a'^2 & f'^2 \\ e'^2 & e'^2 & b'^2 \end{bmatrix} \quad ; \quad \gamma_4^+ \to \gamma_5^+ + \gamma_6^+ \quad \begin{bmatrix} a''^2 & a''^2 & c''^2 \\ a''^2 & a''^2 & c''^2 \\ b''^2 & b''^2 & 0 \end{bmatrix}$$

† reproduced from J.H. Christie[44].

The basic similarity of the Raman spectra of all hosts was helpful in determining the complete spectra in all the crystals. For cadmium- and manganese-chloride crystals, one of the electronic lines was obscured by a Raman-active phonon line while another was of weak intensity. Comparison of their spectra with those of other crystals revealed their presence. Firstly, the electronic Raman spectra of cobalt-chloride is relatively intense because of the 100% cobalt concentration and this established the pattern of electronic levels and indicated the position of the lowest $(^{(1)}\Gamma_8^+, \gamma_{5,6}^+)$ electronic line. The presence of this line under the $\vec{k} = 0$ Raman A_{1g} phonon line in cadmium- and manganese-chloride was then demonstrated in their high temperature spectra by the presence of Raman active transitions from the first excited electronic level to higher electronic levels. These transitions vanish at low temperature due to thermal depopulation of the first excited electronic level. The Raman spectrum of cadmium-bromide showed the high frequency (Γ_7^+, γ_4^+) electronic Raman line at relatively high intensity compared to those in the chloride crystals and enabled the position of the corresponding lines in the chlorides to be inferred. They were subsequently observed directly at liquid helium temperatures by operating the Raman spectrometer at its highest sensitivity.

4.3 RESULTS

4.3.1 $CdCl_2(Co^{2+})$

The Raman spectra of crystals containing 0, 2.5, 5.0, 10.0 and 100% by weight of cobalt were measured at both room and low temperatures. Figure 4-2 depicts the main features of the

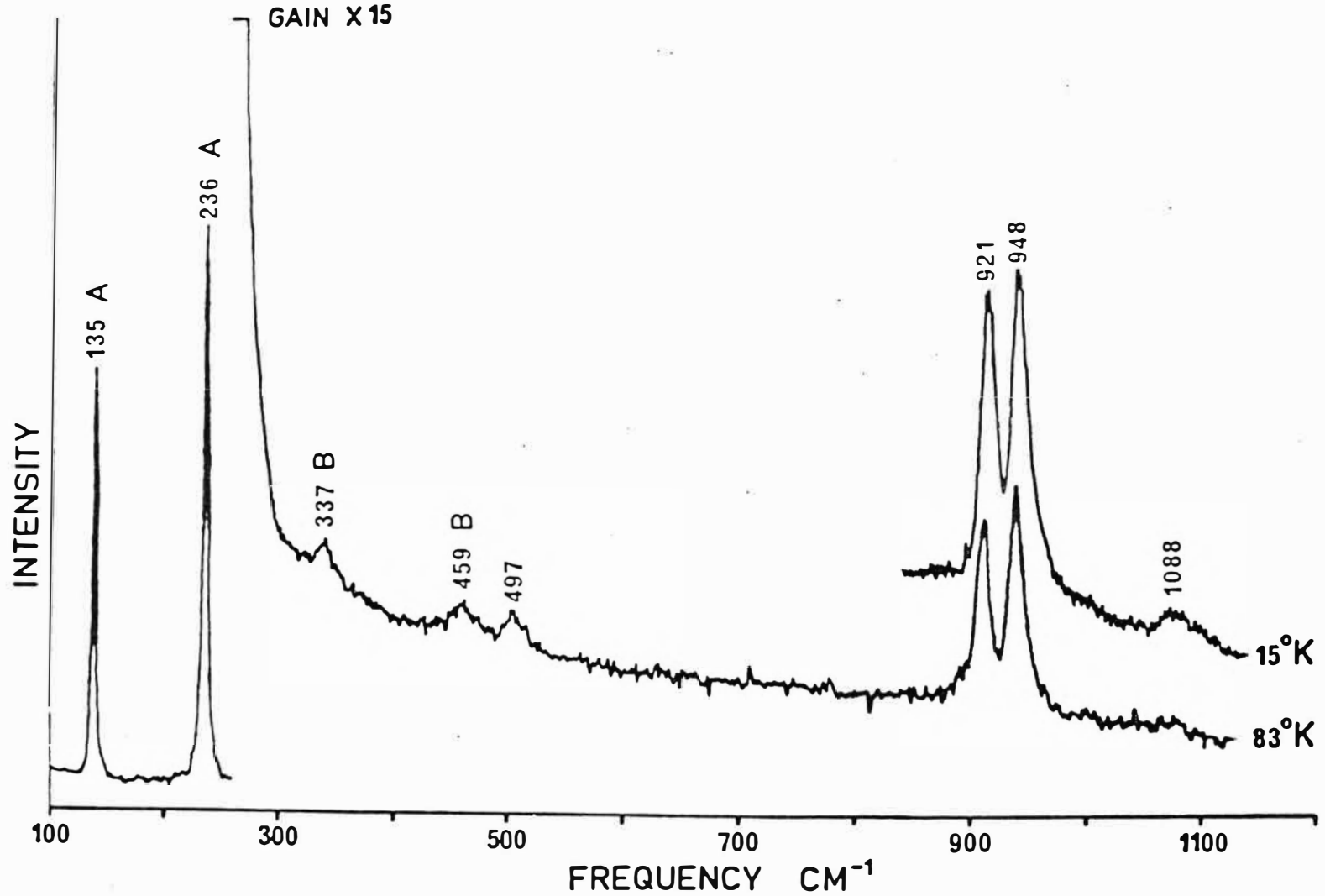

Figure 4-2: Raman spectrum of $CdCl_2$(Co):5 wt% recorded with spectral slit widths of 1.5 cm^{-1} (100-300 cm^{-1}) and 6.0 cm^{-1} (300-1150 cm^{-1}). First and second-order phonon features are labelled A and B.

observed spectra. The two intense, narrow lines at 135±1 cm^{-1} and 236±1 cm^{-1} are the E_g and A_{1g} lattice phonon lines while other lines were observed at 337, 459, 499, 923, 953 and 1088 cm^{-1} for the lowest concentration (viz. 2.5 wt.%) cobalt crystal. Of these, the two lines at 337 and 459 cm^{-1} also appeared in undoped cadmium-chloride and have already been attributed to the second-order phonon spectrum of the host crystal[44]. The other four lines correlate with cobalt ion concentration and are assigned as electronic Raman lines due to cobalt.

A broad Raman line appears at 715±5 cm^{-1} in the room temperature spectra and is not present at low temperatures. It is assigned to be a transition from the lowest excited electronic level, thermally populated at room temperature, to the broadened and overlapping pair of lines at 950±5 cm^{-1}. This gives the energy of the lowest excited electronic level of cobalt as 235±10 cm^{-1}.

Polarisation studies of the lines at 948 and 921 cm^{-1} in $CdCl_2(Co^{2+})$:5 wt.% spectra showed that the 948 cm^{-1} line decreases markedly in intensity for the x(zz)x polarisation direction while the 921 cm^{-1} line shows little change (Figure 4-3). The 948 and 921 cm^{-1} lines are, therefore, assigned as transitions from a γ_4^+ groundstate to electronic states of $\gamma_{5,6}^+$ and γ_4^+ symmetries respectively.

As the cobalt concentration is increased additional Raman lines appear due to the formation of cobalt ion clusters. These can be seen by comparing Figures 4-2, 4-3, and 6-1. The main trends are an increase in intensity of all the electronic Raman lines and an overall shift of the spectra to higher frequencies as the cobalt cluster lines become dominant. The

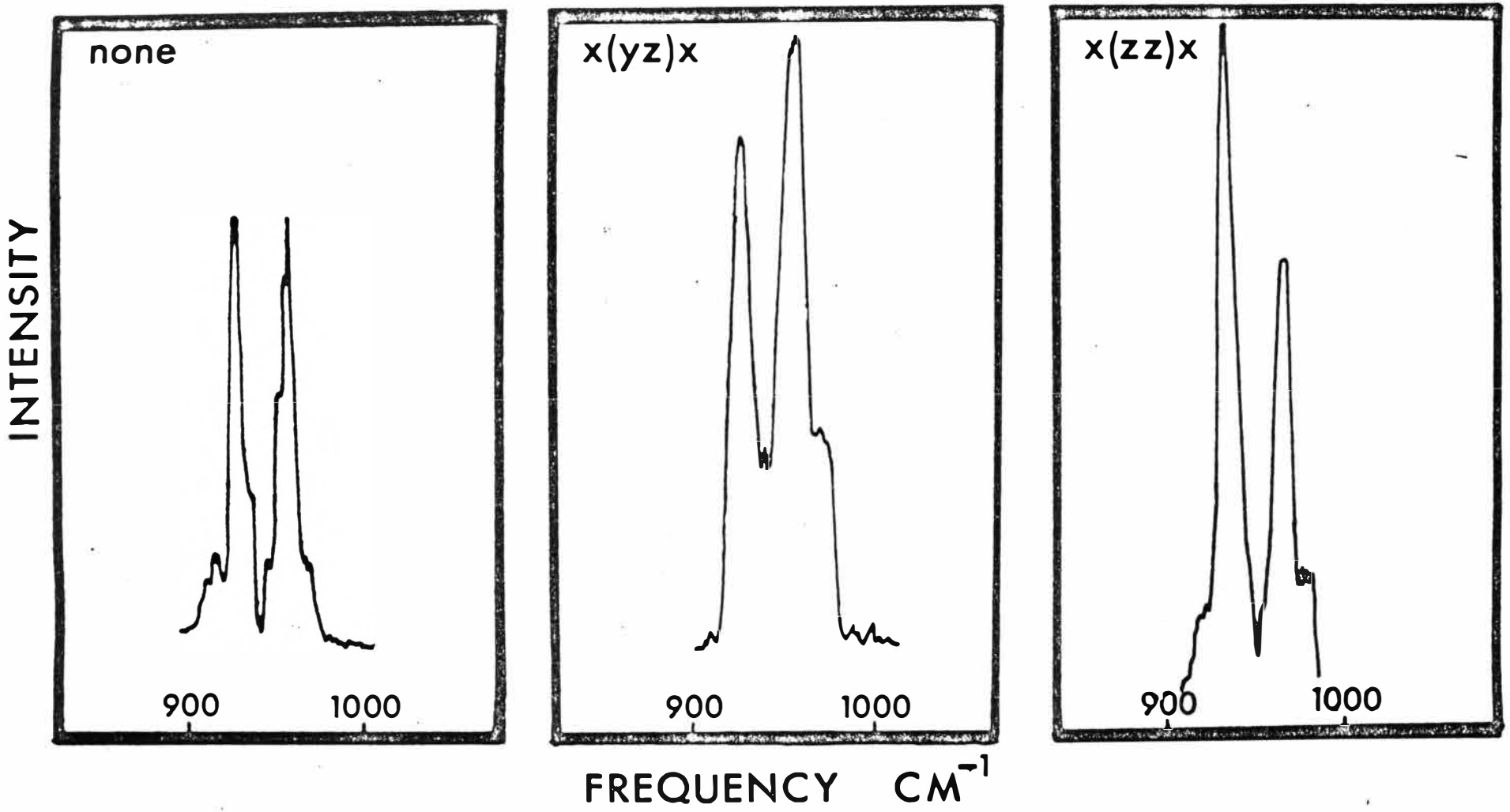

Figure 4-3: Polarized Raman spectrum of $CdCl_2$(Co): 5 wt.%, recorded at 78°K (900-1000 cm^{-1}).

frequencies of the single cobalt ion lines decrease slightly. The cluster lines are broader due to exchange effects between the paramagnetic ions. As the cobalt ion concentration increases, so too does the number and variety of possible cluster sites which, together with the greater width of the lines causes the Raman spectra to become less well defined. For a cobalt concentration of 50 wt.% the spectra are broad and featureless[61]. For cobalt-chloride, with a 100% cobalt concentration there is again only one situation of each cobalt ion being entirely surrounded by identical ions and the overall width of the Raman spectra is consequently lower. Table 4-III gives the spectral data for the 1000 cm^{-1} region, together with an assignment of the lines due to cobalt pairs in the cadmium planes. The data, though not consistent with Christie's[44] earlier measurements, is in complete agreement with the infrared absorption results obtained for the identical crystals and presented in the next chapter.

TABLE 4-III[†]

Classification by nearest-neighbour (n.n.) cation environment of the Co^{2+} electronic lines of $CdCl_2(Co^{2+})$ in the 1000 cm^{-1} region.

Number of n.n. Co^{2+} ions	2.5(wt.%)	5.0(wt.%)	10.0(wt.%)	100.0(wt.%)
	499±2	497±2	495±2	
0	923±1	921±1	918±1	
	953±1	948±1	944±1	
	1088±3	1088±2	1088±2	
1	517±1	513±1	508±1	
	937±3		929±1	
	969±2	966±2	961±1	
6				963±4
				992±4

[†] all frequencies in wavenumbers (cm^{-1}).

4.3.2 $CdBr_2(Co^{2+})$

The liquid helium temperature Raman spectra of cadmium-bromide crystals containing 0, 3, 5, and 10% by weight of cobalt-bromide are given in Figure 4-4. These spectra are confused by a multiplicity of impurity activated Raman lines due to second-order phonons and fluorescence lines. The fluorescence lines have been tabulated by Christie[(44)] together with the concentration dependence of the cobalt doped host and for the most part his work is confirmed. The

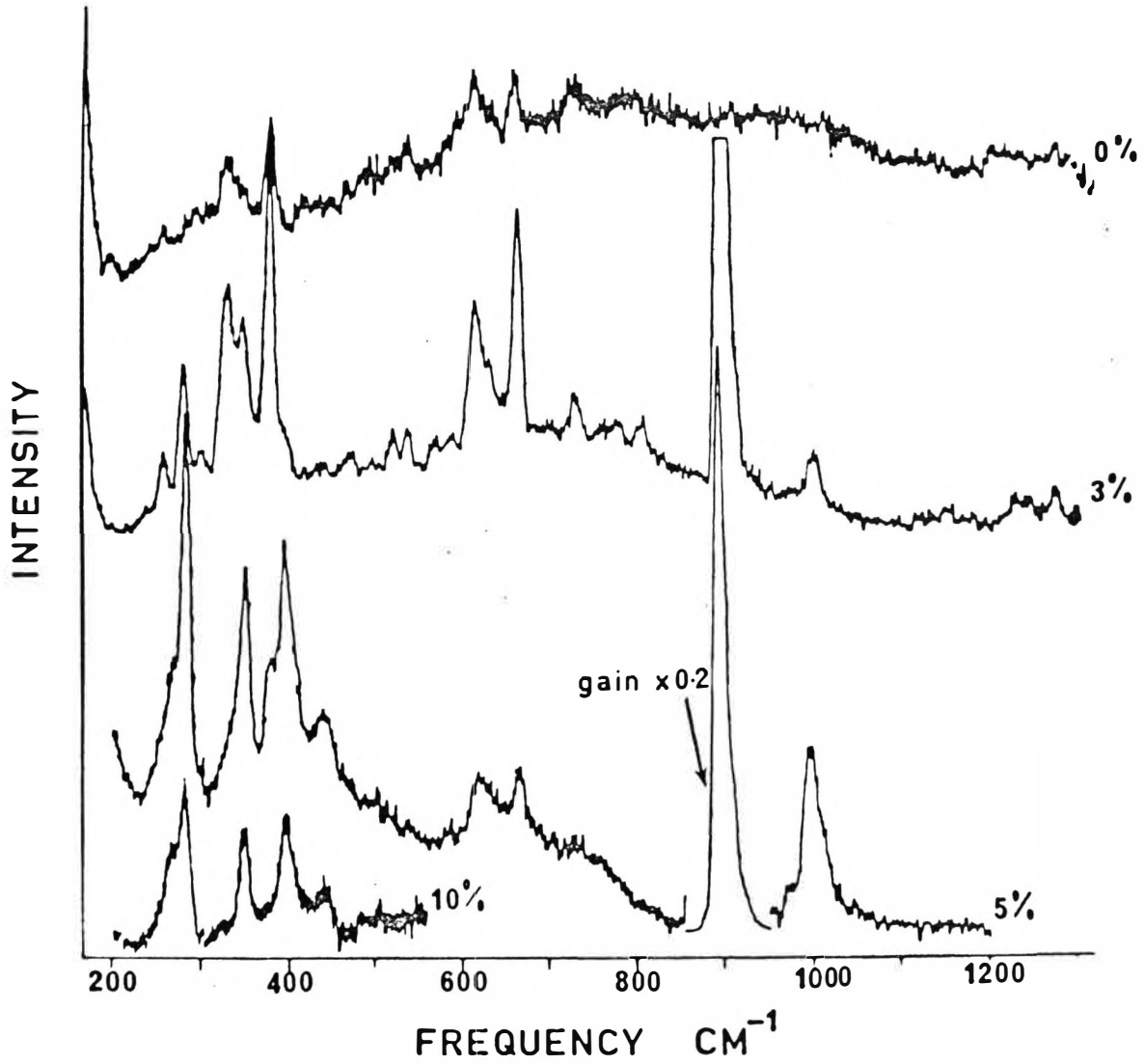

Figure 4-4: Raman spectra $CdBr_2$(Co): 0, 3, 5, and 10 wt%, all recorded at 15°K with a spectral width of 6.0 cm^{-1}.

spectrum of the 3.0 wt.% crystal has many weak lines, all of which, except those at 282, 394, 893 and 995 cm^{-1} appear also in the pure (0 wt.%) cadmium-bromide. In the 5.0 wt.% crystal analogous lines appear together with those at 268, 439, 903 and 1007 cm^{-1}. The 10.0 wt.% crystal shows all these lines at slightly shifted frequencies.

By comparison of the Raman spectra excited by the argon ion laser lines at 476.5 and 514.5 nm. The only Raman lines that correlate with the presence of cobalt in the 5.0 wt.% crystals have frequencies of 282, 394, 893 and 995 cm^{-1}. The previous ambiguity in the assignment of the line at 351 cm^{-1} is removed by examining cadmium-bromide crystals containing 5.0 wt.% Ni^{2+} ions. It is assigned to be a second-order phonon and not a possible feature of the cobalt electronic spectrum. A high resolution spectral scan shows that the 893 cm^{-1} line is a doublet with line components at 889 and 894 cm^{-1}. Their separation of 5 cm^{-1} is much less than the 27 cm^{-1} splitting of the analogous lines in cadmium-chloride.

Polarisation studies show that the 889 cm^{-1} line is largely unpolarised, the 894 cm^{-1} line has weak intensity in the x(zz)x polarisation direction and the 282 cm^{-1} line is reduced in intensity by 30% for this direction. The 889, 894 and 282 cm^{-1} lines are, therefore, assigned to be transitions from a γ_4^+ groundstate to electronic states of γ_4^+, $\gamma_{5,6}^+$ and $\gamma_{5,6}^+$ symmetries respectively. Depolarisation effects due to the imperfect crystal surfaces caused only reduced, rather than zero intensity to be observed for the $\gamma_{5,6}^+$ levels in the x(zz)x polarisation direction.

As the cobalt concentration is increased, additional lines appear, analogous to the case of cadmium-chloride. Due to the much smaller separation of the single cobalt ion lines in the 900 cm^{-1} region it is more difficult to analyse the superposed pair spectra and the data is consequently less complete. In the 5.0 wt.% crystal the lines observed at 268, 439, 903 and 1007 cm^{-1} are associated with cobalt ion pairs.

4.3.3 $MnCl_2(Co^{2+})$

The spectra of $MnCl_2(Co^{2+})$ are very similar to those of $CdCl_2(Co^{2+})$. The lines are less intense than for the other crystals studied, partially because of the absorption of laser light by the pink coloured host crystal and partially because of the greater width of the lines. For these reasons no attempts were made to determine the polarisation spectra of the electronic Raman lines. The spectra of 0, 5.0 and 10.0 wt.% crystals were measured and are shown in Figure 4-5. In addition to the strong phonon lines at 150 and 242 cm^{-1}, lines were observed at 461, 524, 938, 972 and 1108 cm^{-1}. Of these the line at 1108 cm^{-1} was only observed at liquid helium temperatures because of its weak intensity. The line at 461 cm^{-1} appears in undoped manganese-chloride, while the remaining lines correlate in intensity with the cobalt ion concentration. They are therefore assigned as electronic transitions of the cobalt ion using the similarity of the line positions, and polarisation of the $CdCl_2(Co^{2+})$ spectra as a guide. The greater width of these lines compared to those in the cadmium-halide crystals is attributed to the dipolar broadening by the neighbouring paramagnetic manganese ions.

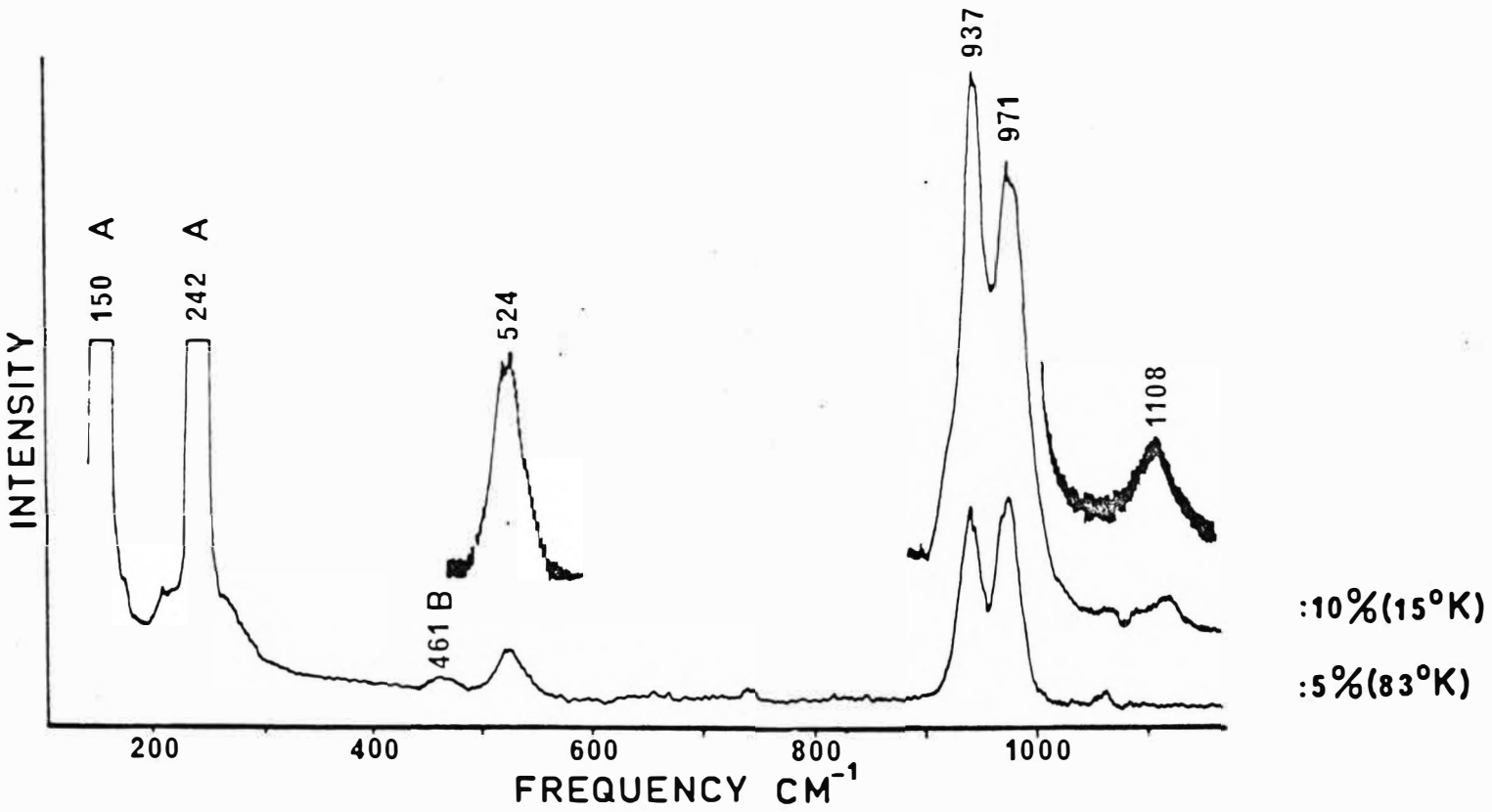

Figure 4-5: Raman spectra of $MnCl_2$(Co): 5 and 10 wt%, both recorded with a spectral width of 6.0 cm^{-1}. First and second order phonons are labelled A and B respectively.

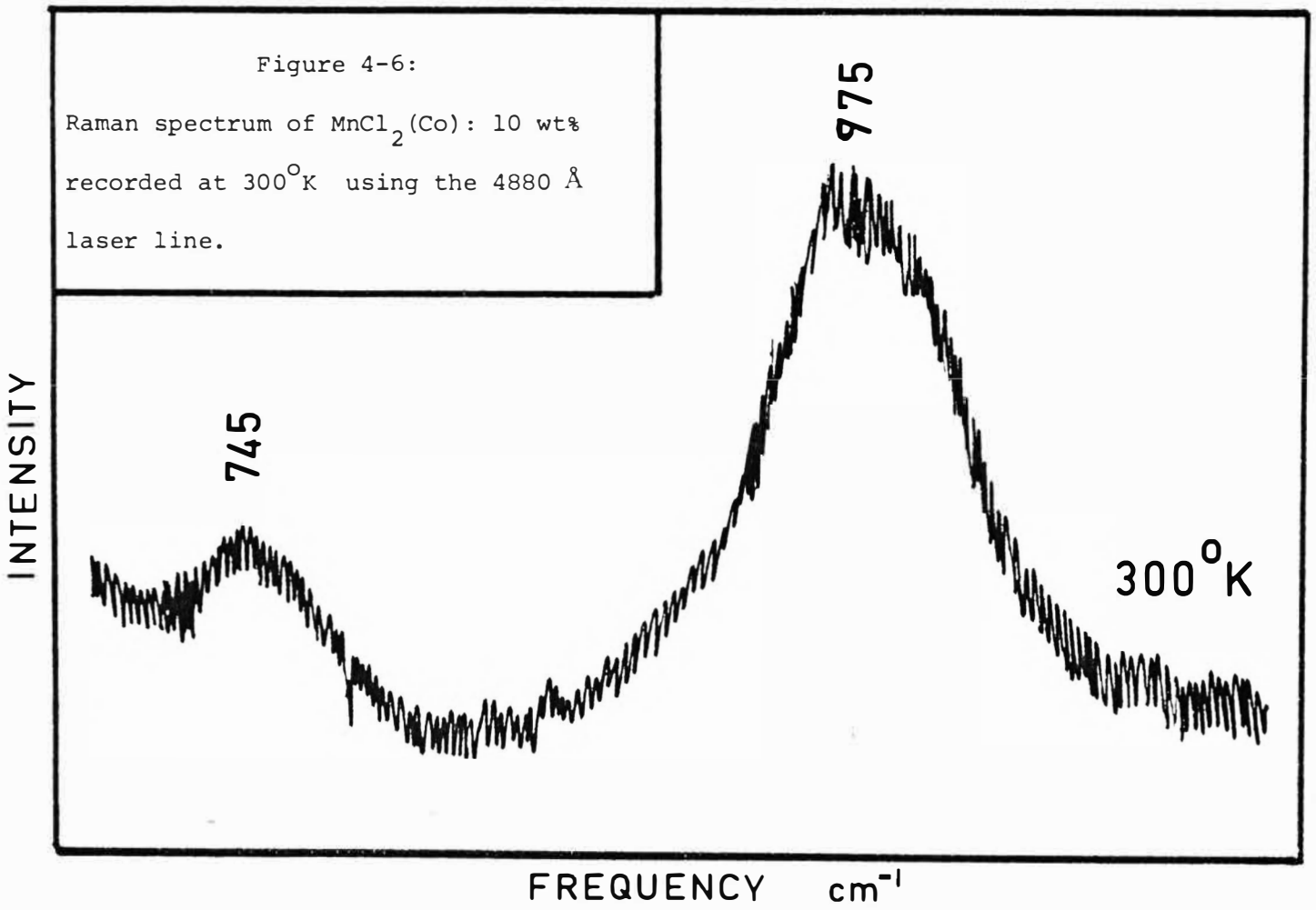

Figure 4-6:

Raman spectrum of $MnCl_2$(Co): 10 wt% recorded at 300°K using the 4880 Å laser line.

Figure 4-6 shows the room temperature spectrum of the 10.0 wt.% crystal. In it there is a line at 745±10 cm^{-1} which indicates the lowest excited electronic level of the cobalt ion is 230±13 cm^{-1}.

As the cobalt ion concentration is increased the Raman lines become asymmetric on their high frequency sides due to additional scattering by cobalt ion clusters. The large width of the Raman lines prevented the observation of distinct line peaks due to these and consequently their spectra could not be investigated in any further detail.

4.3.4 $\underline{CoCl_2}$

The dark blue cobalt-chloride crystals absorbed the laser light to a considerable extent, and only surface scattering techniques were found to give satisfactory results.

Spectra were recorded at room, liquid-nitrogen and liquid helium temperatures and these are shown in Figures 4-7 and 4-8. Comparison of the two demonstrates the presence of hot lines in the spectrum. These bands are approximately 220 cm^{-1} below the corresponding low temperature lines and, in addition, a line exists at 220 cm^{-1} in both the room and low temperature spectra. This confirms the identification of the hot line spectra and fixes the position of the lowest excited level of cobalt.

At low temperature, there are two broad lines at 545 and 978 cm^{-1}. A high resolution scan on the high frequency side of the latter revealed a weak line at 1115 cm^{-1} which is assigned to be the electronic transition to the uppermost level in analogy with the other crystals examined. As in the

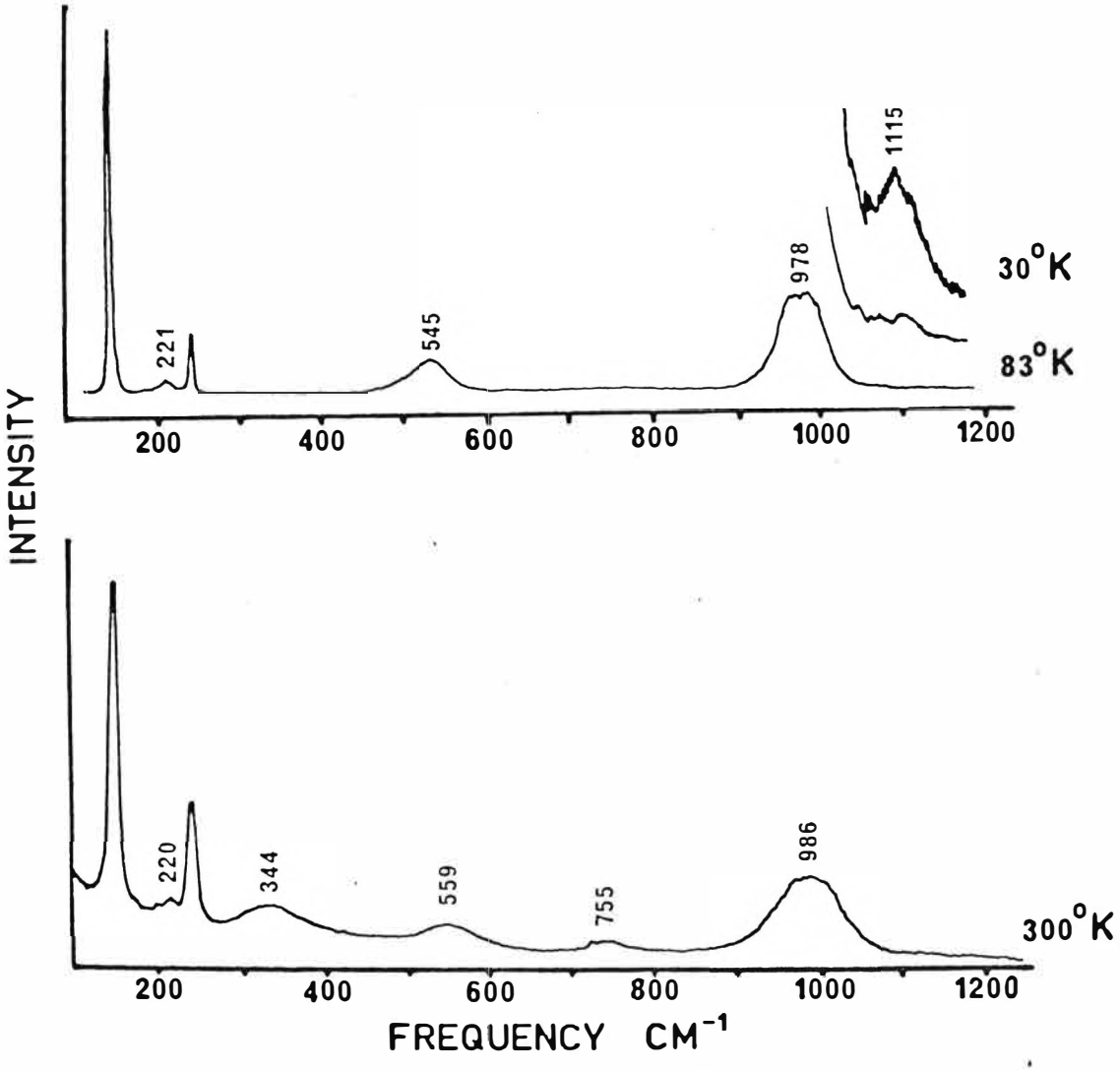

Figure 4-7: Raman spectra recorded at 30°, 83°, and 300°K of $CoCl_2$ in its paramagnetic state.

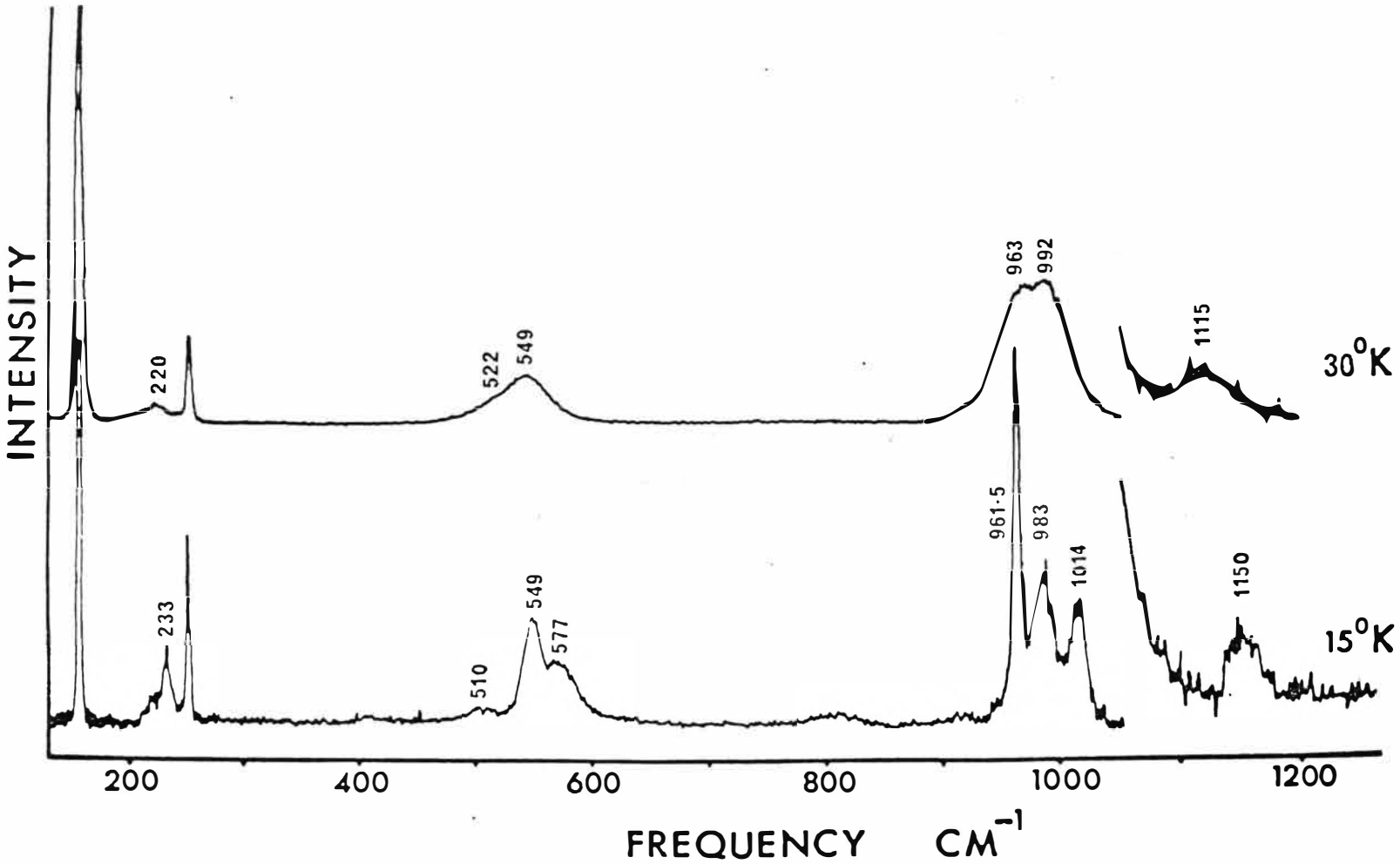

Figure 4-8: Raman spectra of $CoCl_2$ in its paramagnetic (T = 83°K) and antiferromagnetic (T = 15°K) states. The latter is constructed from several part spectra as follows: 130-270 cm^{-1} using the 4880-Å laser line and a spectral slit width of 1.5 cm^{-1}; 270-460 cm^{-1}, 4579-Å, 3 cm^{-1}; 460-650 cm^{-1}, 4579-Å, 6 cm^{-1}; 650-900 cm^{-1}, 4765-Å, 6 cm^{-1}; 900-1050 cm^{-1}, 4880-Å, 1.5 cm^{-1}; 1050-1270 cm^{-1}, 4880-Å, 10.5 cm^{-1}.

case of manganese-chloride, the widths of these Raman lines are attributed to dipolar broadening by the neighbouring paramagnetic cations. The 545 cm^{-1} line exhibits definite asymmetry, while the 978 cm^{-1} line comprises more than one line. The profiles of both of these were analysed by a least squares fitting procedure, described by Christie[44], to give two overlapping components for each.

Of these, the lines at 549, 963 and 992 cm^{-1} are assigned to be the remaining electronic transitions of cobalt, while the 522 cm^{-1} line has been assigned as a second-order phonon band whose intensity is enhanced by its proximity to the 545 cm^{-1} electronic line. This assignment is supported by measurements on the antiferromagnetic ordered cobalt-chloride crystals below $24.7^{o}K$[44] where the three electronic lines shift to higher frequencies while the 522 cm^{-1} line becomes a broad, weak line at 510 cm^{-1} (Figure 4-8). Three sharp lines appear in the 1000 cm^{-1} region of which the line at 963 cm^{-1} is clearly sharpest suggesting it is the 992 cm^{-1} line that has been split by the antiferromagnetic ordering. A detailed search has been made for the lowest lying, magnon level without success but these experiments are to be repeated with the new laser facility (Chapter 3.3.2).

4.3.5 Summary

The Raman measurements on the electronic levels of cobalt in the above crystals is summarised in Table 4-IV.

TABLE 4-IV

Frequencies (cm^{-1}) and assignments of the six Kramers degenerate electronic levels of the $^4T_{1g}(^4F)$ term

Assignment	$CdBr_2(Co^{2+})$ 3.0 wt.%	$CdCl_2(Co^{2+})$ 2.5 wt.%	$MnCl_2(Co^{2+})$ 5.0 wt.%	$CoCl_2$
$\gamma_4^+(\Gamma_6^+)$	0	0	0	0
$\gamma_5^+ + \gamma_6^+(^{(1)}\Gamma_8^+)$	282±1	235±10	230±13	220±3
$\gamma_4^+(^{(1)}\Gamma_8^+)$	394±1	499±2	524±3	549±4
$\gamma_4^+(^{(2)}\Gamma_8^+)$	889±1	923±1	938±2	963±4
$\gamma_5^+ + \gamma_6^+(^{(2)}\Gamma_8^+)$	894±1	953±1	972±2	992±4
$\gamma_4^+(\Gamma_7^+)$	995±1	1088±3	1108±3	1115±5

4.4 FITTING OF THE EXPERIMENTAL DATA

With the implicit assumption of a pure $3d^7$ configuration there are seven parameters which determine all the energy levels for a trigonal site. These are the cubic-field parameter $\Delta(= 10\ D_q)$, the two electrostatic parameters B and C, the two spin-orbit parameters ζ and ζ', and the two trigonal crystal-field parameters v and v'. The five observed electronic Raman lines are transitions between the six spin-orbit and trigonal crystal-field levels of the $^4T_{1g}(^4F)$ cubic crystal-field term, and, therefore do not depend directly on the values for the cubic crystal-field or electrostatic parameters. These were, therefore, set at values obtained from the cubic crystal-field analysis of the optical spectra of cobalt-chloride and of cadmium-chloride and -bromide containing cobalt carried out by Ferguson et al.[2] and Robson[20]. The

values appropriate to manganese-chloride containing cobalt were taken as the same as those for cobalt-chloride because these two crystals have closely similar dimensions.

The frequencies, (E_i), of the electronic Raman lines were then fitted by a least-squares routine to the (E_i^0) of the appropriate transitions within the states of the $3d^7$ configuration by adjusting the four parameters ζ, ζ', v, v' to make the quantity:

$$\sum_{i=1}^{5} w_i (E_i - E_i^0)^2 \qquad (4.1)$$

a minimum. The weighting factors, w_i, were chosen to be proportional to the reciprocal of the uncertainty in the measured frequencies. This least-squares fitting procedure was iterated until agreement to within experimental accuracy was obtained and the results are listed in Table 4-V. For all four crystals this could be achieved with four parameters fitting the five observed frequencies.

In the case of cadmium-chloride and -bromide crystals the g-values for the ground state are known from e.p.r. measurements[26-29] and the set of parameters obtained above could be tested by comparing these g values with those calculated using these parameters. These are shown in Table 4-VI. The least-squares routine was modified to include the deviation of the observed value for $g_{\parallel}$ from the calculated one. This was done in the expectation that only slight adjustments in the parameter values may allow an exact fit of the observed g values without significantly degrading the energy fit. No new parameters need be introduced since the parameters k and

Table 4-V Calculated and observed energies of the six Kramers degenerate electronic of the $^4T_{1g}(^4F)$ term. †

	$CdBr_2$(Co):3%		$CdCl_2$(co):2.5%		$MnCl_2$(Co):5%		$CoCl_2$	
	Expl.	Calc.	Exptl.	Calc.	Exptl.	Calc.	Exptl.	Calc.
	282±1	282	235±10	225	230±13	217	220±3	217
	394±1	394	499±2	497	524±3	522	549±4	546
	889±1	889	923±1	923	938±2	939	963±4	965
	894±1	894	953±1	953	972±2	972	992±4	991
	995±1	995	1088±3	1091	1108±3	1108	1115±5	1115
PARAMETERS OF ENERGY MATRIX								
Dq	-610		-670		-690		-690	
B	790		790		780		780	
C	3090		3320		3432		3432	
ζ	-544		-512		-516		-533	
ζ'	-432		-513		-515		-503	
v	129		57		124		440	
v'	-227		-345		-433		-694	

† all measurements and parameters in units of wavenumbers (cm^{-1})

k' characterising the orbital part of the Zeeman interaction are related to the spin-orbit parameters ζ and ζ' by equation (2.11). The corresponding $g_\perp$ deviation was not included since this would necessitate diagonalising the entire 120-dimension energy matrices. The $g_{||}$ deviation was weighted heavily because of the greater experimental precision in its value.

TABLE 4-VI

Calculated and observed g-values for the $\gamma_4^+(\Gamma_6^+)$ level in $CdCl_2(Co^{2+})$ and $CdBr_2(Co^{2+})$ crystals

	$CdBr_2(Co^{2+})$		$CdCl_2(Co^{2+})$	
	Expt.	Calc.	Expt.	Calc.
$g_{||}$	3.74±0.1[a]	3.59	3.06±0.05[a]	3.02
	2.71±0.05[b]		3.06±0.02[b]	
			3.04±0.02[c]	
$g_\perp$	4.67±0.1[a]	4.66	4.96±0.05[a]	5.07
	4.99±0.05[b]		4.98±0.02[b]	
			4.95±0.02[c]	

a A. Edgar (Ref. 28,29)

b K. Morigaki (Ref. 26)

c J.W. Orton (Ref. 27)

For $CdCl_2(Co^{2+})$, the g-value fit was initially found to be very good and it did not prove possible to improve the agreement without seriously degrading the energy fit.

For $CdBr_2(Co^{2+})$, the experimentally observed g-values[26] were very different from those calculated and it was not possible to find any set of parameters that would bring the calculated values close to the experimental values. To resolve this discrepancy, the e.p.r. measurements on $CdBr_2(Co^{2+})$: 0.1 wt.% and $CdCl_2(Co^{2+})$:0.1 wt.% were repeated for us by Dr A. Edgar[28,29] using the department's Q band e.p.r. spectrometer. The results are given in Table 4-VI which shows the previous e.p.r. results for $CdBr_2(Co^{2+})$ are in error. These new g-values are similar to the initially calculated values and, as for $CdCl_2(Co^{2+})$ the inclusion of the $g_{\shortparallel}$ deviation did not result in a significantly better fitting. In both $CdCl_2(Co^{2+})$ and $CdBr_2(Co^{2+})$ this is due to the relative insensitivity of the g-values to small parameter variations about the optimum set obtained from the energy fit above. The final energy fit obtained is within the experimental accuracy of measurement for the observed lines, while the g-values are obtained to within ±0.15. The g-values predicted for the upper levels are listed in Table 4-VII.

Previous calculations (Chapter 2.3) of the spin-orbit and trigonal crystal-field energy levels of the $^4T_{1g}(^4F)$ cubic-field groundstate have included an admixture, α, of the $^4T_{1g}(^4P)$ term into these levels and yield an energy level scheme which approximates that obtained here using all states of the $3d^3(3d^7)$ configuration (Figure 4-9). The principle difference is in the splitting of the upper levels in the more exact calculation. The 100 cm^{-1} splitting is apparent in the observed spectra as the separation of the $(^{(2)}\Gamma_8^+, \Upsilon_4^+)$ and $(^{(2)}\Gamma_8^+, \Upsilon_{5,6}^+)$ levels from the uppermost $(\Gamma_7^+, \Upsilon_4^+)$ level. The

absence of such a splitting in the earlier calculations prevented a good energy fit to all observed levels. In order to reproduce this it is essential to include all doublet and quartet states in the crystal-field analysis since inclusion of the quartet states alone yields a splitting of only 50 cm^{-1}.

TABLE 4-VII

Predicted g-values for the levels of the $^4T_{1g}(^4F)$ manifold in $CdCl_2(Co^{2+})$ and $CdBr_2(Co^{2+})$ crystals

	$CdCl_2(Co^{2+})$		$CdBr_2(Co^{2+})$	
energy-level	$g_{\parallel}$	$g_{\perp}$	$g_{\parallel}$	$g_{\perp}$
$\gamma_4^+(\Gamma_6^+)$	3.02	5.07	3.59	4.66
$\gamma_5^+ + \gamma_6^+(^{(1)}\Gamma_8^+)$	0	2.38	0	2.31
$\gamma_4^+(^{(1)}\Gamma_8^+)$	4.47	1.84	4.87	2.16
$\gamma_4^+(^{(2)}\Gamma_8^+)$	0.39	0.33	0.07	0.08
$\gamma_5^+ + \gamma_6^+(^{(2)}\Gamma_8^+)$	0	0.83	0	0.44
$\gamma_4^+(\Gamma_7^+)$	0.27	0.22	0.08	0.10

4.5 INTERPRETATION OF THE CRYSTAL FIELD PARAMETERS OBTAINED

The very close fits to the experimental data achieved with the complete $3d^7$ crystal field matrices indicate that the crystal-field theory is perfectly adequate for the cases examined here. However, the exact values obtained for the trigonal crystal-field are not physically significant because of the sensitivity of these parameters to the experimental accuracy of the data. It was found that relative variations of a few wavenumbers (cm^{-1}) in the measured energy levels

could alter the parameters by 15%. In comparison, the spin-orbit parameters were insensitive to such changes. In view of this, further refinements in the fit by remeasuring the optical absorption spectra of each crystal in greater detail and refitting the cubic-field and electrostatic parameters is not justified.

The values obtained for the two spin-orbit parameters are closely equal in the case of the chlorides and the data could have been fitted equally well by using only one spin-orbit parameter ($\zeta = \zeta'$), as is usually done in the weak-field calculations[62]. On the other hand, the data for the bromide requires distinctly different values for the two parameters and it is not possible to obtain either a good energy fit or g-value shift if the two parameters are set to the same value. In all cases, the spin-orbit parameter values are close to the free ion spin-orbit coupling constant $\zeta_0 = -535\ cm^{-1}$ and there is little covalency reduction. This may be expected from the intraconfigurational nature of the transitions which are all between states of the $t_{2g}^5 e_g^2$ configuration.

While too much significance should not be placed on the particular values obtained for the trigonal crystal-field parameters obtained for each crystal they do have a similarity which one would expect bearing in mind the crystals' isomorphic structure. Their d^3 configuration values are characterised by a positive v and a negative v' with $v'/v \approx -3$. Their magnitudes are small compared to those usually obtained for trigonally distorted crystals[39], consistent with the small trigonal distortion of the cadmium-chloride lattice.

Figure 4-9: Energy level calculations for Co^{2+} in a trigonal crystal field: (a) Robson's calculation (20) (δ and ζ are the trigonal and spin-orbit parameters respectively); (b) the full $3d^3$ calculation for Dq = - 690, B = 780. C = 3430; spin-orbit parameters: ζ = - 510, ζ' = - 540 (all cm^{-1}); trigonal parameters: v/v' = - 0.323.

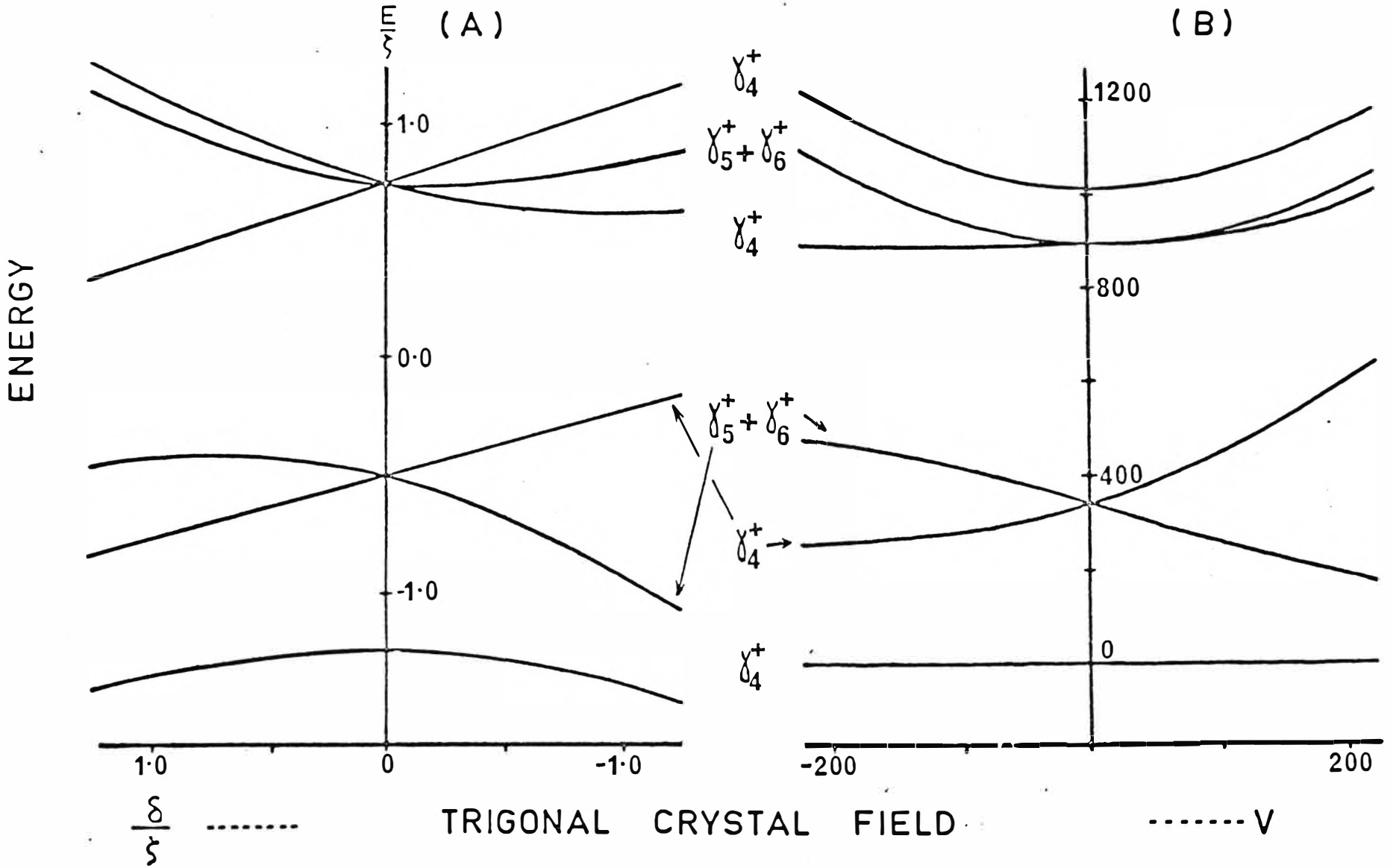

The electrostatic contributions to the trigonal crystal-field for these lattices come from the small departure from cubic symmetry of the octahedron of nearest neighbour chloride ions, the non-cubic arrangement of the next-nearest neighbour cadmium ions, and the electric dipole moments induced on the chloride ions, by the cadmium ions[63]. The main part of the trigonal crystal-field comes from the non cubic arrangement of the cadmium ions and the induced chlorine dipole moments. Kanamori[63] has calculated the trigonal crystal-field for cobalt-chloride due to these two contributions and found that the contribution due to the non-cubic arrangement of cadmium ions was sufficient to split the $^4T_{1g}(^4F)$ term into two levels, $^4A_{1g}$ and ^4E_g, separated by 1000 cm^{-1}. Inclusion of the contribution from the chloride dipole moments modified this energy-level separation and for large induced dipole moments, the level scheme was reversed. A calculated splitting of 1000 cm^{-1} is large compared to that actually observed hence these electrostatic contributions can more than account for the magnitude of the trigonal crystal-field parameters obtained from the analysis of the spectra. A quantitative calculation is not possible at present as it would require knowledge of the magnitude of the induced dipole moments on the chloride ions and the inclusion of the effects of covalency, overlap and other nonelectrostatic contributions. A discussion of the role of these effects and the interpretation of crystal-field parameters has been given by Newman[78] and the reader is referred to his paper for further details.

4.6 MOLECULAR-FIELD ANALYSIS OF $CoCl_2$ SPECTRA BELOW 25°K

The Raman spectra of cobalt-chloride below 24.71°K shows splitting of the single ion levels due to exchange interactions between the cobalt ions. When the lattice becomes antiferromagnetic the single ion electronic excitations of the paramagnetic phase are transformed into magnetic excitations of the lattice as a whole and are generally termed, excitons. Where such an electronic excitation only involves a change in spin parameters the excitation is known as a magnon.

In view of the calculation of Hsu and Stout[21] it is worthwhile attempting a revised calculation to fit the additional levels observed in this work.

Below 24.71°K, cobalt-chloride becomes antiferromagnetically ordered and forms a two sublattice antiferromagnet with layers of ferromagnetically coupled cobalt ions which are weakly coupled by an antiferromagnetic interaction between the layers. The spins of the cobalt ions lie in the plane of the layers and are perpendicular to the c-axis of the crystals, with alternate layers having oppositely directed spins. There is also a domain structure which may be modified by applying magnetic fields of up to 0.3T[64]. In stronger magnetic fields of up to 4T the spins in adjacent layers may be made parallel[64].

The ferromagnetic interaction between the cobalt ions in a layer may be characterised by an isotropic intralayer exchange interaction J_1, and the antiferromagnetic interaction between the layers by an isotropic exchange interaction, J_2 of opposite sign. Norath[65] discusses the factors determining the ratios of these two exchange interactions, while Lines[19]

estimates $J_1/J_2 = -11.6$ for cobalt-chloride.

For the calculation of the energies of the exchange split electronic states in cobalt-chloride the single ion molecular-field approximation was adopted. In this, an effective field represents the exchange interactions between the cobalt ions and the energy level scheme approximates that of a single cobalt ion in a magnetic field directed along the layers. The effective molecular field adopted is represented by the Hamiltonian:

$$\mathcal{H} = -2J_{eff}(S_x)_0 S_x \qquad (4.2)$$

where $(S_x)_0$ is the value of S_x for the groundstate of the cobalt ion and J_{eff} is the effective exchange interaction which includes both the intra- and interlayer interactions J_1 and J_2. The energies of the twelve exchange split levels of the $^4T_{1g}(^4F)$ term were obtained by diagonalising the 12 dimension matrices for this interaction. The basis states used were the eigenvectors of the full 120 dimension free-ion and crystal-field matrices of the $3d^7$ configuration appropriate to cobalt-chloride in its paramagnetic phase. The 144 matrix elements of the spin operator, S_x, obtained in this way are listed in Appendix III. The unperturbed cobalt paramagnetic ion energies are those calculated in Table 4-V.

For $2J_{eff} = +16$ cm^{-1} the energy levels given in Figure 4-10 were obtained and are in good agreement with experimentally observed transitions. However, the lowest lying magnon level is calculated to be 30 cm^{-1} whereas this level has been observed to occur at 19.2 cm^{-1} by Jacobs et al.[66]. This discrepancy can be attributed to the use of an exchange

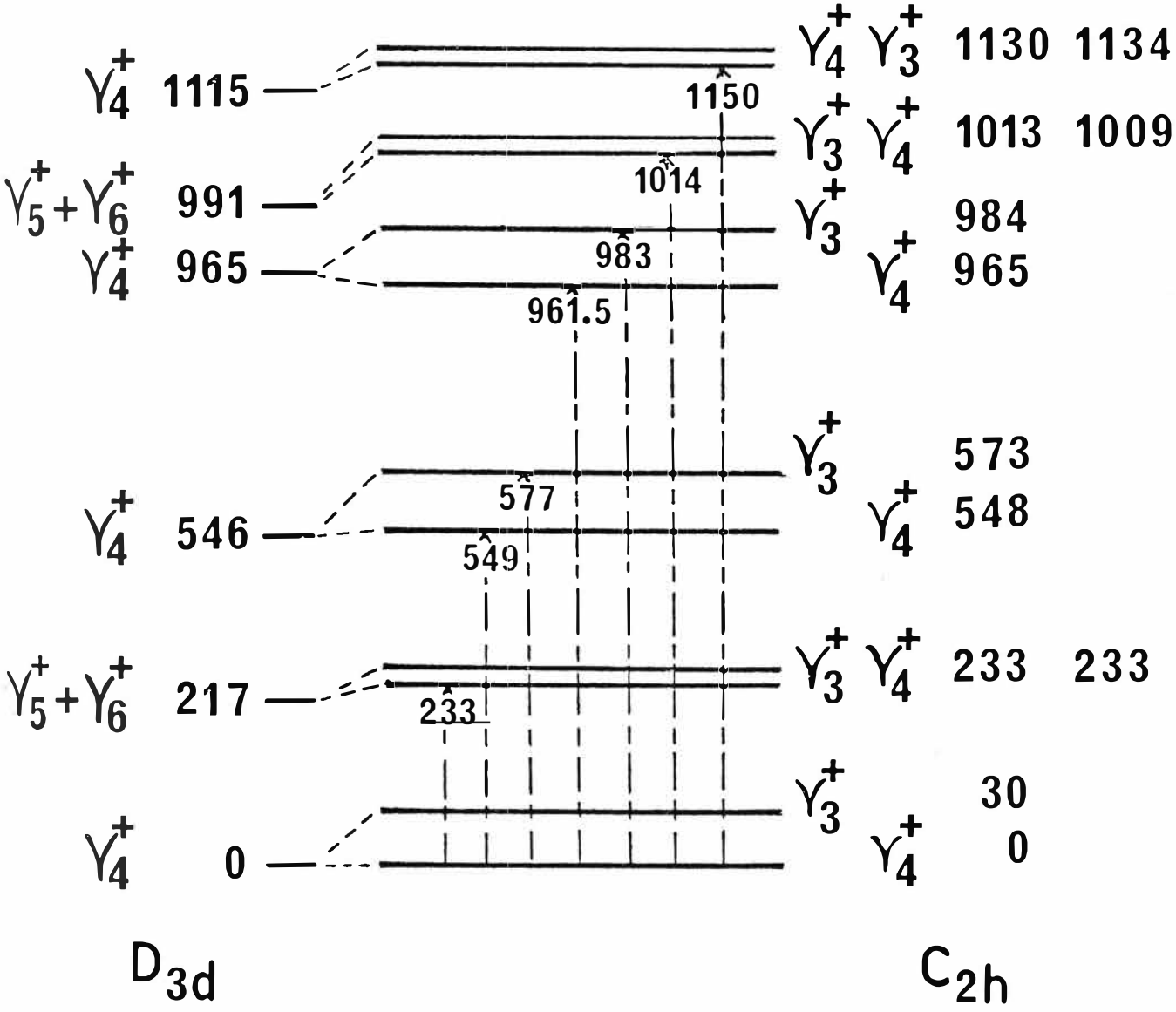

Figure 4-10: Calculated and observed energy levels within the $^4T_{1g}(^4F)$ term of a cobalt ion in a trigonal, and trigonal plus exchange field. Observed transitions are shown as vertical dotted lines.

interaction Hamiltonian appropriate for a S = ½ level for calculating the energy levels of a $^4T_1$ orbital triplet. Further, Loudon[67] has shown that the use of a model which neglects any correlations between the electronic spins of interacting ions is inappropriate for the lowest lying levels. The approximation is satisfactory for the upper electronic levels and can well account for the observed Raman lines using just one exchange parameter, J_{eff}. In a further study it is planned to follow the spin-wave theory as outlined by Buyers et al.[68]

C H A P T E R V

THE INFRARED ABSORPTION SPECTRA OF $CdCl_2(Co^{2+})$, $CdBr_2(Co^{2+})$, $MnCl_2(Co^{2+})$ AND $CoCl_2$

5.1 INTRODUCTION

The preceding chapter gives a description and analysis of the polarised electronic Raman scattering spectra of cobalt ions as substitutional impurities in cadmium-chloride, -bromide, manganese-chloride and of cobalt-chloride. In this chapter a study of the polarised infrared absorption spectra of the same crystals is presented. As has been described earlier, (Chapter 4.1) the infrared lines associated with low energy Co^{2+} electronic transitions will be relatively weak since they are parity forbidden as in all other d^n configuration spectra. The dominant features are the vibronic bands caused by admixture of odd parity vibrational modes into electronic states. These effects complicate the interpretation of the spectra.

A preliminary account of the infrared spectra of these cobalt doped lattices has been given by Christie and Lockwood[59] based on the work of Robson[20]. Robson's spectra were plagued by both impurity lines and the extreme weakness of the Co^{2+} electronic lines. Like the previous workers: Zuyagin et al.[69] and Newman and Chrenko[70], Robson also confused the superimposed features of the Co^{2+} electronic and vibronic spectra with the result that only the $(^{(2)}\Gamma_8^+, \Gamma_{5,6}^+)$ line was correctly identified. This line is a characteristic feature of the lattices measured, namely $CdCl_2(Co^{2+})$, $CdBr_2(Co^{2+})$

and $MnCl_2(Co^{2+})$. More recently Hsu and Stout[21] have reported the polarised infrared absorption spectra of cobalt-chloride and while the appropriate results discussed here are in agreement with theirs an additional assignment is given for some of the unassigned lines.

In this work a comprehensive survey of all spectral features in the axial and polarised infrared absorption spectra from 400 to 1500 cm^{-1} is presented for each crystal. The host crystals are transparent down to 400 cm^{-1} in the cases of the chlorides and to 250 cm^{-1} in the case of cadmium-bromide and the spectra observed comprise the electronic and vibronic transitions of the cobalt ion within the $^4T_{1g}(^4F)$ manifold. Specific lines are documented for each crystal in Section 5.3. The pure electronic transitions of single cobalt ions are discussed in Section 5.4 where the crystal field analysis developed in Chapters II and IV is used to calculate their relative intensities and polarisation. The predominant cobalt ion cluster spectra are also reported but are analysed, together with the corresponding Raman data, in Chapter VI using a model of exchange coupled pairs. The vibronic transitions observed are electric-dipole allowed and analysed in Section 5.5.2 to obtain the lattice phonon frequencies of the host lattices. A particular feature of the vibronic spectra is the occurrence of very sharp, low-frequency vibronic lines and these are discussed separately in Section 5.5.1.

5.2 GENERAL DESCRIPTION OF THE SPECTRA

The room temperature spectra of all crystals examined are characterised by a broad band centred at approximately 1160 cm^{-1} in the chlorides and 1100 cm^{-1} in the bromides. An

additional broad band near 650 cm^{-1} appears with weak intensity in thick samples of the heavily doped cobalt samples. The intensity of both bands increases with temperature indicating their vibronic nature.

At low temperatures a further broad band appears near 1260 cm^{-1} in the chlorides and 1170 cm^{-1} in the bromides, while sharp lines occur on the low frequency sides of all three broad bands (Figure 5-1).

The intensities of both bands and lines depend on the cobalt concentration and they are absent in both pure and nickel (Ni^{2+}) doped crystals of cadmium-chloride, -bromide and manganese-chloride. Some of the lines have intensities that increase linearly with the cobalt concentration, while others have intensities that increase more rapidly and appear as additional lines in the more heavily doped crystals.

Some of the lines of vibronic origin have an intensity markedly dependent on the crystal temperature and are absent from the lowest temperature spectra, as shown for example in Tables 5-Ia, Ib and Figure 5-2. These so called "hot-bands" originate from thermally populated levels above the ground-state.

The sharp lines can be assigned either as pure electronic, no-phonon transitions of the cobalt ion or as vibronics associated with the same electronic transitions. The pure electronic features can be identified by the coincidence of their frequencies to within ± 1 cm^{-1} of those Co^{2+} electronic transitions observed in the Raman spectra of the identical crystals. These no-phonon lines form parent lines for the vibronics which are located symmetrically about them with the

Figure 5-1: Axial infrared absorption spectrum of $CdCl_2$(Co):7.5wt% (1.32 mm) recorded at 15°K between 400 and 1500 cm^{-1}.

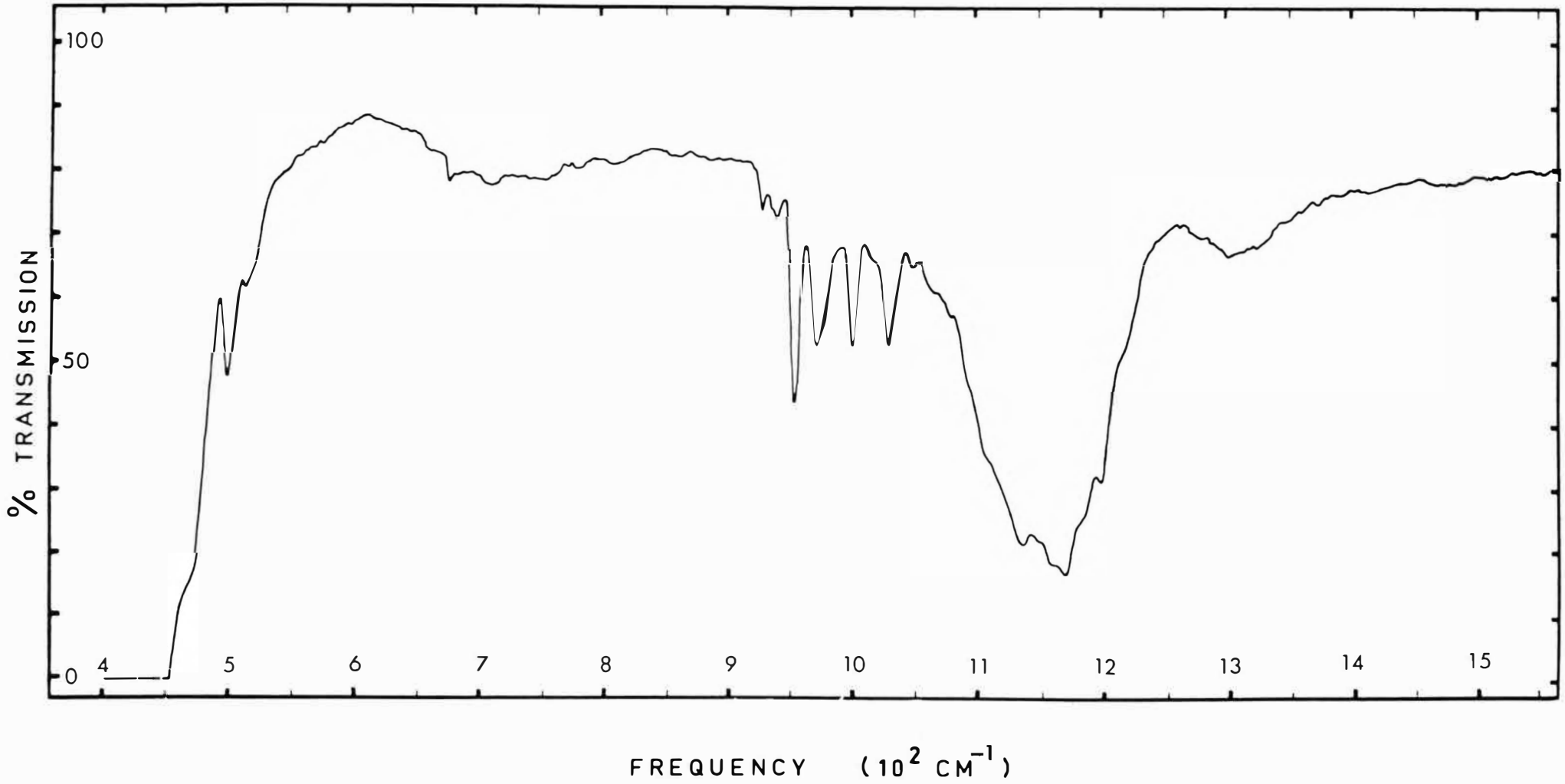

lower frequency line having a vanishing intensity at low temperature. The electronic lines due to single ions are principally identified by their linear increase in intensity with cobalt concentration. Their polarisation properties are consistent with magnetic-dipole allowed transitions for a single Co^{2+} ion in a site of D_{3d} symmetry. The remaining electronic lines are assigned to cobalt ion pairs or higher-order clusters by their dependence on the cobalt ion concentrations.

5.3 RESULTS

5.3.1 $CdCl_2(Co^{2+})$

Infrared spectra of cadmium-chloride crystals containing 0, 0.5, 1.0, 2.5, 5.0, 7.5, 10.0 and 100.0% by weight of cobalt-chloride were measured both at room and low temperatures. The cobalt concentration expressed as molar % is a factor 1.43 greater than the wt.% value. Figure 5-2 depicts the main spectral features for these crystals while the associated spectral data is listed in Tables 5-Ia and Ib.

The spectra of isolated cobalt ions is expected to be dominant in the most weakly doped crystals and, for the lowest concentration crystal measured here (viz. 0.5 wt.%) the occurrence of cobalt clusters is negligible. The 78°K spectra of this crystal showed several sharp lines at 500, 854, 883, 926, 954, 999 and 1028 cm^{-1}. At liquid helium temperatures the lines at 854 and 883 cm^{-1} vanished while the remaining lines shifted to slightly lower frequencies. The principal broad band has fine structure with peaks at 1100, 1128, 1154,

Figure 5-2: Axial infrared absorption spectra of $CdCl_2$(Co): 1.0, 2.5, 5.0, 7.5 and 10wt%.
Spectra recorded at 78 and 15°K are on the L.H.S. and R.H.S. respectively.

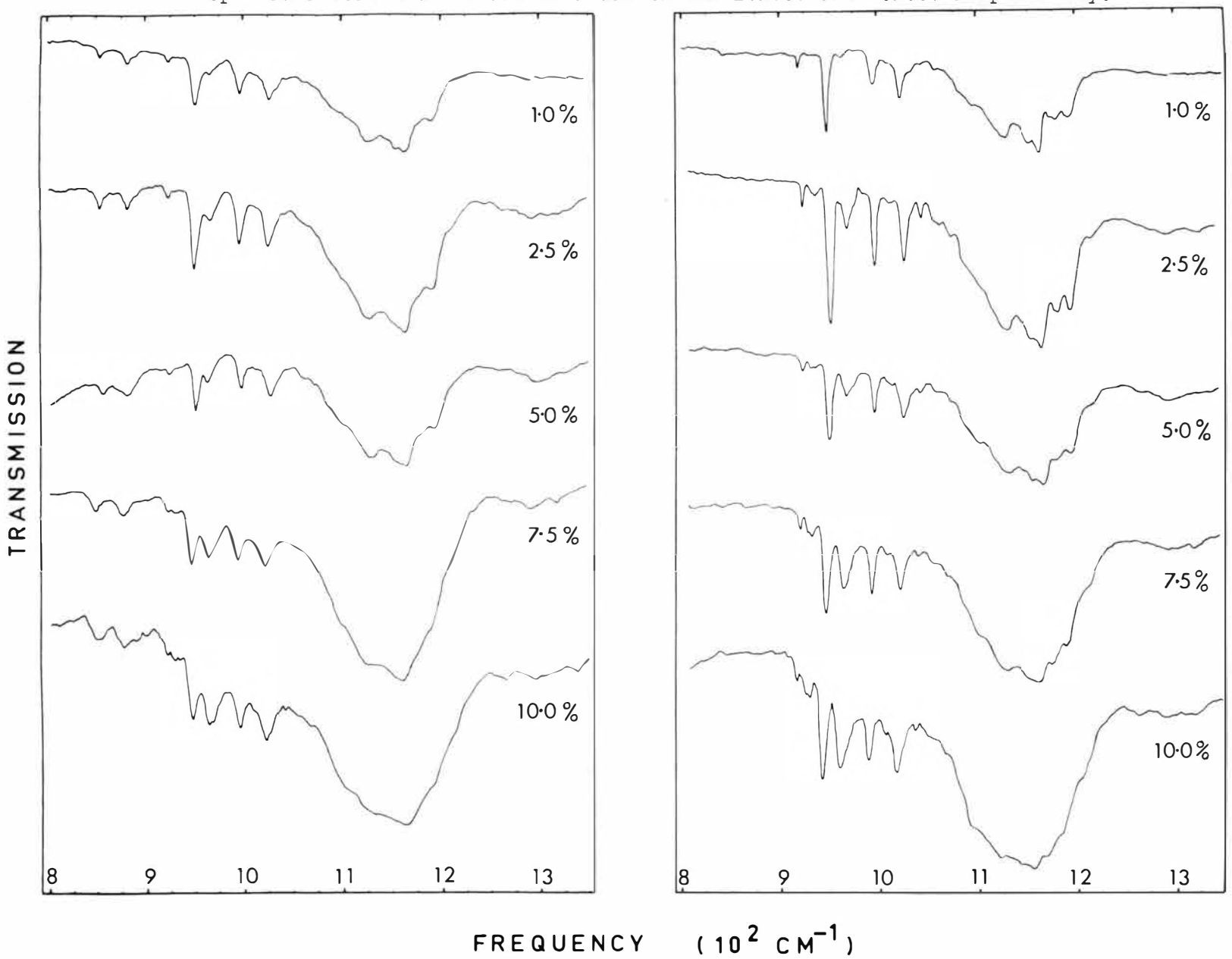

Table 5-Ia IR axial spectra of $CdCl_2(Co)$: 400 - 1500 cm^{-1} Temperature: 15°K

0.5%			1.0%			2.5%			5.0%			7.5%			10.0%		
Freq. (cm^{-1})	Width (cm^{-1})	Int.* (mm^{-1})	Freq. (cm^{-1})	Width (cm^{-1})	Int. (mm^{-1})	Freq. (cm^{-1})	Width (cm^{-1})	Int. (mm^{-1})	Freq. (cm^{-1})	Width (cm^{-1})	Int. (mm^{-1})	Freq. (cm^{-1})	Width (cm^{-1})	Int. (mm^{-1})	Freq. (cm^{-1})	Width (cm^{-1})	Int. (mm^{-1})
498.5±0.5	5	0,14	497.2±0.6	5	0.29	496.8±0.7	6	0.50	496.0±0.6	6		494.0±0.7	7	0.62	493.3±0.7	8	0.96
			516±2	4		515±1	7	0.07	513±1	8		510±1	9	0.37	508±1	11	0.87
												690±4]	~80		690±4]	~86	
922.3±0.4	2	0.01	921.8±0.4	2.5	0.02	920.5±0.4	3	0.0	920.2±0.5	4	0.07	918.0±0.5	4.5	0.10	916.2±0.6	5	0.15
									928±1]	8	0.09	926±1]	8	0.15	925±1	9	0.34
						933±1	4	0.02	934±1]			930±1]			928.8±0.7]		
951.1±0.3	3	0.17	950.2±0.4	3.5	0.21	949.1±0.3	5	0.53	948.5±0.5	6.5	0.74	944.8±0.5	7.5	0.99	942.9±0.6	8	1.56
			965±1	3		966±1]	7	0.15	965±1]	10	0.37	963.0±.5]	11	0.79	961±1]	13	1.57
						972±2]			971±2]			970±2]					
995.2±0.5	3	0.07	995.1±0.5	3.5	0.10	993.5±0.5	5	0.26	993.2±0.6	5.5	0.31	991.5±0.5	6	0.46	989.9±0.6	7	0.68
						1008±2			1007±1	5		1006±1	7		1005±1	8	
1025.0±0.5	4	0.08	1025.0±0.5	5	0.13	1023.2±5.6	6	0.27	1022.2±0.6	7	0.39	1020±0.7	8	0.61	1017.5±0.8	9	1.08
						1040±1	4		1039±1	45		1037±1	5		1035.5±0.5	5	
1060±2]			1060±2]			1060±2]			1060±2]			1055±2]					
						1070±2						1068±2					
1085±2			1085±2			1085±2			1085±2								
1100±1			1100±1			1100±1			1100±1			1100±1			1097±1		
1128±1	~ 85		1128±1	~ 90		1127±1	~105		1128±1	~110		1128±1	~120		1128±1	~125	
1154±1			1155±1			1154±1			1153±1			1151±1					
1164.5±0.5			1164.5±0.5			1164.8±0.7			1164±1			1161±1			1162±1		
1183±1			1183±1			1179±1			1177±1			1173±1			1171±1		
1194±1]			1195±1]			1193±1]			1191±1]			1189±1]			1188±1]		
			1265±2]	~ 40		1265±2]			1265±2]								
			1295±2]			1290±2	~ 50		1290±2	~ 55		1290±2	~ 60				
						1320±3]			1320±3]			1315±2]			1300±3]	~ 65	

* Int. = Width x Peak abosrbance for 1 mm thickness.

Table 5-Ib : IR Axial spectra of $CdCl_2(Co)$: 400-1500 cm^{-1} showing frequencies (cm^{-1}) and widths (cm^{-1}) of all observed lines. Temperature: 78°K.

0.5%		1.0%		2.5%		5.0%		7.5%		10.0%	
Freq.	Width	Freq.	Width	Freq.	Width	Freq.	Width	Freq.	Width	Freq.	Width
500±2	5	500±1	6	499±1	8			496±1	9	495±1	10
				516±2				514±2		511±2	12
						695±5] ~	65	690±5] ~	85	690±5] ~	90
854±1	5	854±1	6	853±1	7	852±1	9	850±1	10	849±1]	11
										856±2]	
883±1	7	883±1	8	881±1	9	880±1	10	879±1	13	877±1	16
										889±1	
								903±1		900±1	6
926±1		925±1	3	924±1	5	923±1	6	922±2	6	920±1	7
						930±1	5	930±2	10	929±1]	12
										933±1]	
954.0±0.5	6	953.2±0.5	7	952.0±0.5	8	949.5±0.5	8.5	948.0±0.5	9	946.2±0.7	9.5
		967±1	4	967±1	6	966±1	8	965±1	11	964±1	12
999.0±0.7	6	998.0±0.7	7	997.0±0.5	7	997.5±0.8	8	995.1	9	993.5±0.7	8
1028.0±0.8	9	1027.7±0.8	9	1025.8±0.7	10	1026±1	11	1023±1	13	1021±1	14
										1040±1	
1100±1]		1100±1]		1100±1]		1100±1]		1100±2]		1105±2]	
1130±1		1128±1		1130±1		1129±1		1130±2		1130±2	
1157±1	~ 80	1155±1	~ 90	1155±1	~ 110	1155±1	~ 110	1152±2	~ 120		~ 125
1167±1		1167±1		1164±1		1167±1		1162±1		1162±2	
1182±1				1180±1		1180±1		1180±1			
1196±1]		1195±1]		1195±1]		1195±1]		1192±2]		1187±2]	
		1265±2]		1265±2]				1263±2]		1265±2]	
		1293±1]	~ 40	1295±1]	~ 50	1297±2]	~ 55	1293±2]	~ 60	1295±2]	~ 64
				1320±1]		1322±2]		1320±2]		1340±2]	

Figure 5-3: Polarised infra-red absorption spectra of $CdCl_2$(Co):0.5wt% recorded at $78^{o}K$ (L.H.S.) and $15^{o}K$ (R.H.S.).

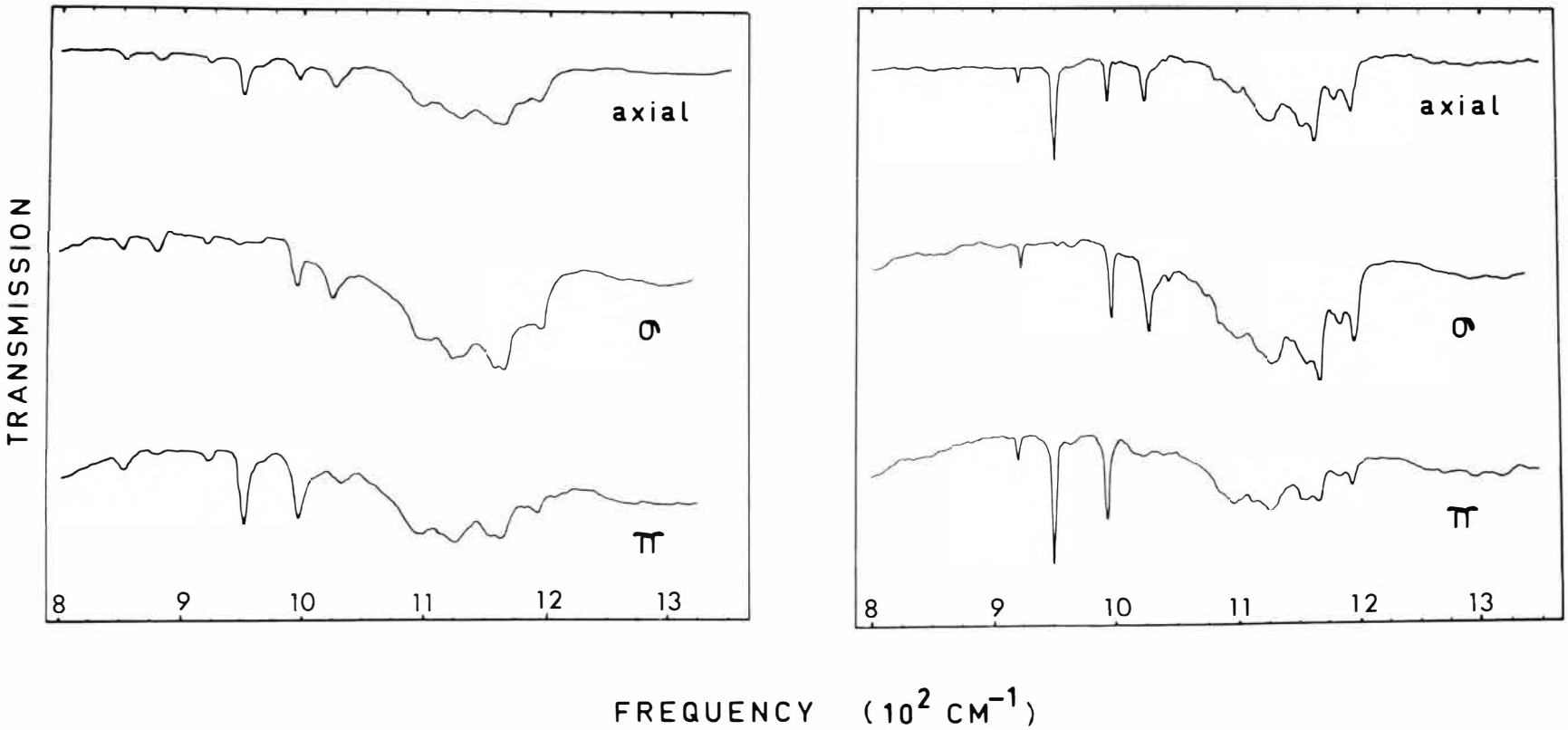

Figure 5-4: Polarised infra-red absorption spectra of $CdBr_2$(Co):5wt% (L.H.S.) and $CdCl_2$(Co):5wt% (R.H.S.). Both recorded at $15^{o}K$.

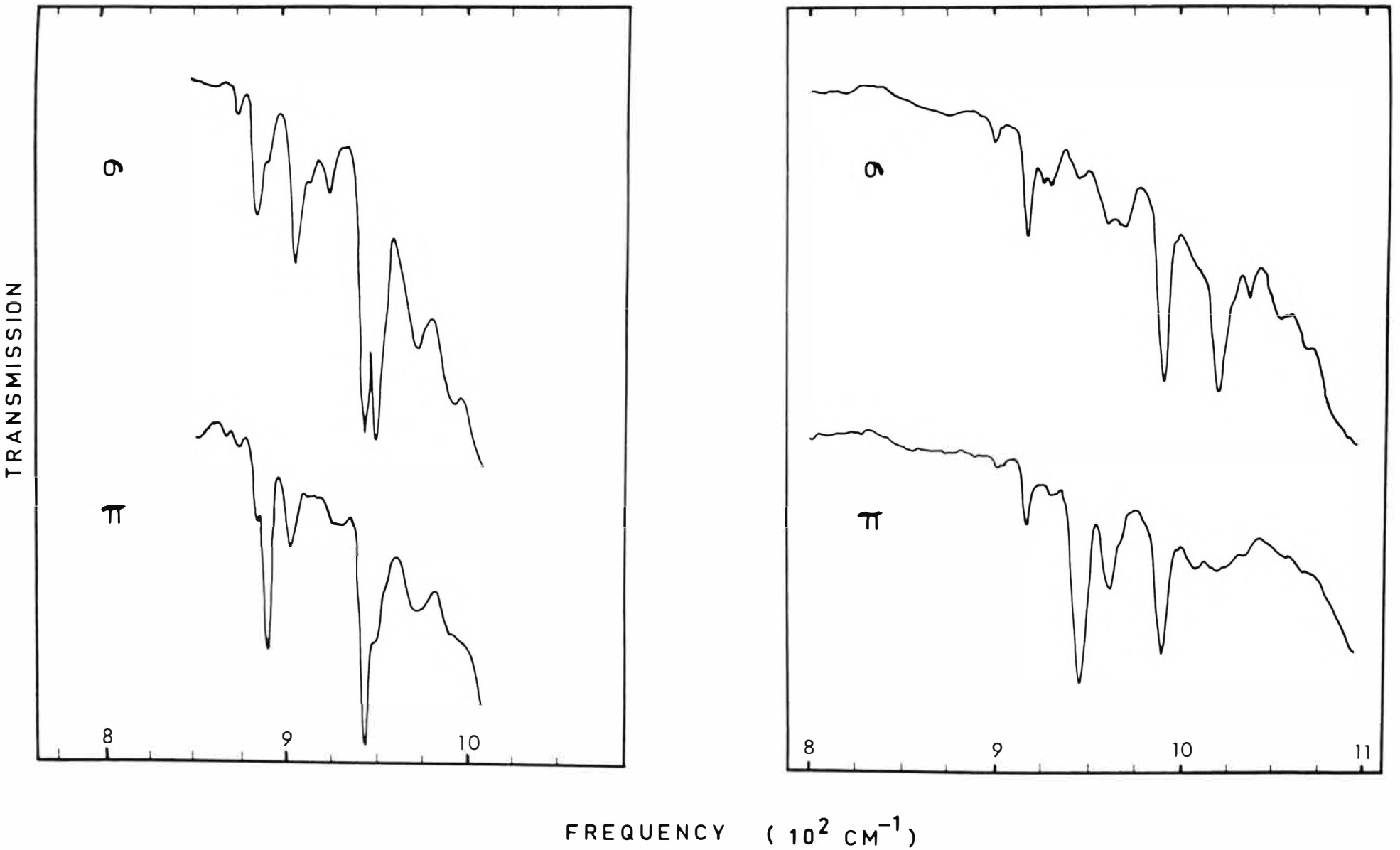

Table 5-II Polarised intensities of selected infrared absorptions in $CdCl_2$(Co) : 0.5%, 5% and $CdBr_2$(Co) : 1%, 5% at 15°K

$CdCl_2$(Co):0.5%			$CdCl_2$(Co):5%			$CdBr_2$(Co):1%			$CdBr_2$(Co):5%		
Freq. (cm^{-1})	Int.* (σ) (mm^{-1})	Int. (π) (mm^{-1})	Freq. (cm^{-1})	Int. (σ) (mm^{-1})	Int. (π) (mm^{-1})	Freq. (cm^{-1})	Int. (σ) (mm^{-1})	Int. (π) (mm^{-1})	Freq. (cm^{-1})	Int. (σ) (mm^{-1})	Int. (π) (mm^{-1})
922.3	0.019	0.013	920.2	0.065	0.048	887	0.002	0.001	886.6	0.048	0.029
			928	0.024							
			934	0.027	0.007						
951.1	0.006	0.111	948.5	0.006	0.616	893.1		0.065	892.6	0.009	0.088
			965	0.075	0.195				905		0.089
			971	0.090	0.016				910	0.02	
									915.5	0.018	
									928	0.066	0.005
995.2	0.064	0.064	993.2	0.357	0.349	947.0	0.043	0.049	946.5	0.214	0.205
1025.0	0.107	0.009	1022.2	0.413	0.042	953.2	0.053	0.004	952.4	0.250	0.022

* Int. = Width x Peak absorbance for 1 mm thickness.

1164.5, 1183 and 1193 cm^{-1} while the high frequency broad band has peaks at 1265 and 1295 cm^{-1}. The broad band at 690 cm^{-1} was barely visible in the thickest (6.6 mm) 0.5 wt.% crystal measured.

As the cobalt ion concentration is increased, all the cobalt absorptions increase in intensity and additional lines appear as shown in Table 5-Ia, Ib. The concentration dependence of these new lines indicates that these must be assigned to cobalt ion clusters.

Polarised spectra of the lines in the 900 cm^{-1} region were obtained for the crystals containing 0.5 wt.% (Figure 5-3), 5.0 wt.% (Figure 5-4) and 7.5 wt.% cobalt. Results are shown in Table 5-II. The measurement of the line at 498 cm^{-1} is rendered more difficult by the presence of the polarised lattice phonon absorption of the host crystals and the necessity to operate the Beckman IR12 in single beam mode when investigating strongly absorbing samples at low temperatures. Since only thin samples could be measured, because of the host crystal's absorption, 10.0 wt.% crystals were examined at liquid nitrogen temperatures. A polarisation ratio $Int(\sigma)/Int(\pi) = 5.4 \pm 0.4$ was found for this line which had a frequency of 495 cm^{-1}.

5.3.2 $\underline{CdBr_2(Co^{2+})}$

The infrared spectra of cadmium-bromide crystals containing 0, 1.0, 2.5, 5.0, 7.5 and 10.0% by weight of cobalt-bromide were measured both at room and low temperatures. The molar concentration percentages are a factor 1.24 larger.

The frequencies of all absorption lines and bands observed are listed in Table 5-IIIa, IIIb while Figure 5-5 gives the

Figure 5-5: Axial infra-red absorption spectra of $CdBr_2$(Co): 1.0, 2.5, 5.0, 7.5, and 10.0wt%. Spectra recorded at 78 and 15°K are on the L.H.S. and R.H.S. respectively.

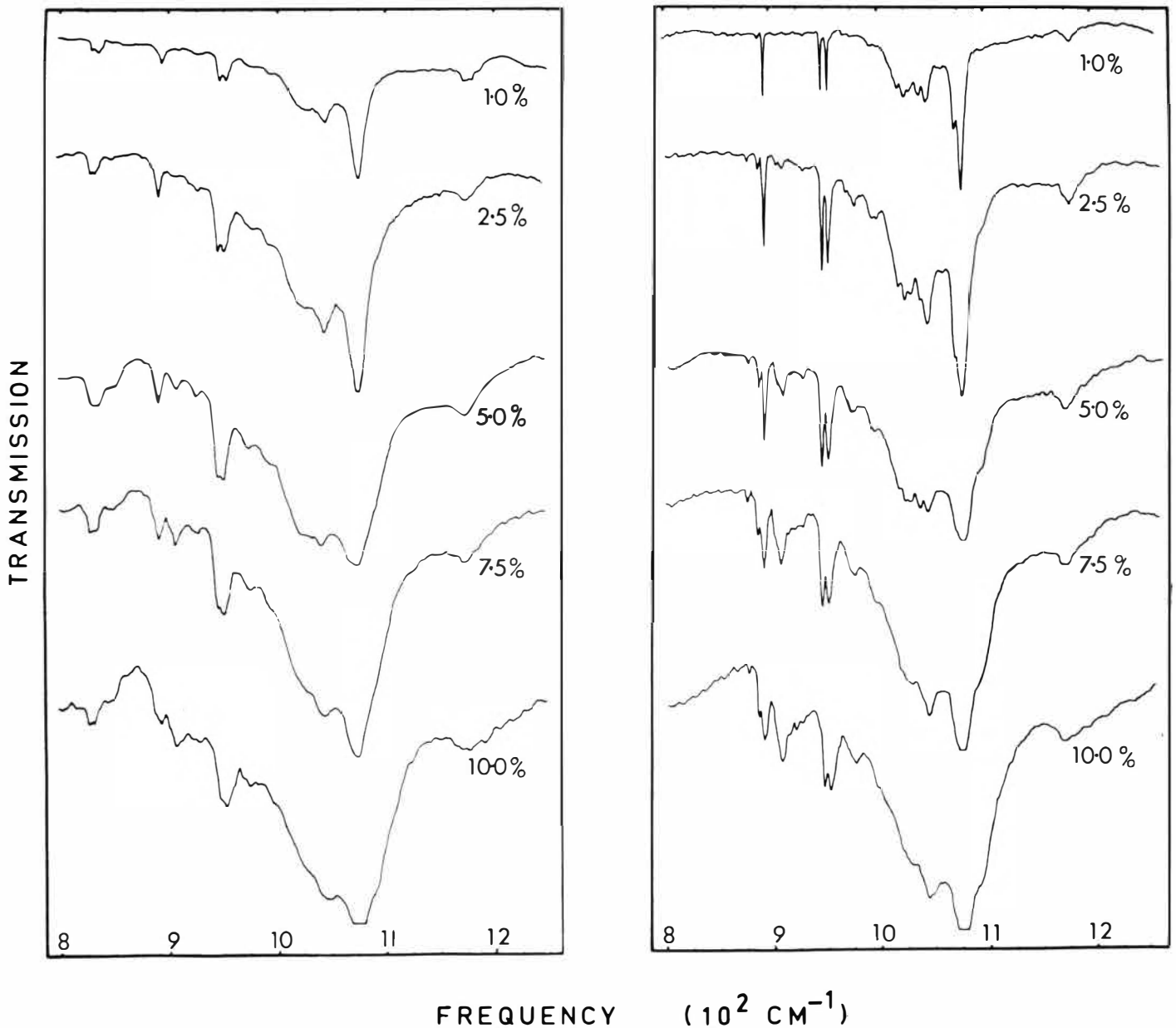

Table 5-IIIa IR Axial spectra of $CdBr_2$(Co): 400-1200 cm^{-1} Temperature: 15°K

1.0%			2.5%			5.0%			7.5%			10.0%		
Freq. (cm^{-1})	Width (cm^{-1})	Int.* (mm^{-1})	Freq. (cm^{-1})	Width (cm^{-1})	Int. (mm^{-1})	Freq. (cm^{-1})	Width (cm^{-1})	Int. (mm^{-1})	Freq. (cm^{-1})	Width (cm^{-1})	Int. (mm^{-1})	Freq. (cm^{-1})	Width (cm^{-1})	Int. (mm^{-1})
			877.7±0.7	2		876.5±0.5	2	0.01	876±1	3	0.03	867.0±0.7	3	0.05
887±1	1		887.2±0.4	2	0.02	886.6±0.4	2	0.06	886.2±0.6	3	0.16	885.5±0.8	4	0.20
893.1±0.3	1	0.06	892.6±0.3	2.5	0.16	892.6±0.3	2.5	0.16	891.3±0.4	4.5	0.48	890.6±0.5	6	0.66
			905.0±0.7	3	0.01	905±1	3	0.08	903±1	4	0.17	902±2	5	0.25
			910.0±0.8	4	0.04	910±1			907.3±0.6	5	0.35	907.0±0.7	7	0.70
						915.5±7	2	0.02	914.0±0.5	3	0.10	914±1	5	0.15
									920±1			920±1	6	
			928+1	4	0.01	928±1	4	0.01		6	0.14			0.28
									927±1			926±1	8	
947.0±0.3	1.5	0.05	947.0±0.3	2	0.21	946.5±0.3	3.5	0.42	946.2±0.3	5	0.72	945.8±0.3	6	0.96
953.2±0.3	1.5	0.05	952.6±0.3	4	0.36	952.4±0.3	5	0.52	951.5±0.5	6	0.81	951.2±0.5	8	1.30
			969±1	3		969±1	5							
978±1	2		978±1	3		976±1	5		976±1	7		975±1	9	
994±1	3		995±1	6		995±1	8		995±2			994±2		
1017.5±0.5	7		1018.0±0.5			1019±1			1020±1					
1023.0±0.5			1023.5±0.5			1023±1								
1029±1	~40		1028±1	~55		1030±1	~75		1030±1	~85		1028±1	~90	
1038.2±0.6			1037.5±0.7			1038±1								
1044.5±0.5			1043.8±0.5			1045±1			1045±1			1043±1		
1070.3±0.5	12		1070±1	14										
1076.5±0.4			1076.5±0.5			1075±1			1075±3			1075±3		
1177±2	10		1175±1	12		1174±1	14		1172±1	15		1173±1	18	

* Int.= Width x Peak absorbance for 1 mm thickness.

Table 5-IIIb IR Axial spectra of $CdBr_2$(Co) : 400-1200 cm^{-1} showing frequencies (cm^{-1}) and widths (cm^{-1}) of all observed lines. Temperature: 78°K.

1.0%		2.5%		5.0%		7.5%		10.0%	
Freq.	Width	Freq.	Width	Freq.	Width	Freq.	Width	Freq.	Width
832±1	4	832.5±0.6	4	832±1	5	830.5±0.7	5.5	829±1	6
837±1	6	837±1	6	837±1	6	835.5±0.7	7	834±1	6
		852±1	5	852±1	10	851±1	11	849±2	12
								878±1	3
896.5±0.5	4	896.8±0.5	5	896.2±0.5	6	894.5±0.5	7	894±1	9
		912±2	5	912±1	5	910.2±0.7	7	909±1	11
		932±2	3	931±1	5	931±1	7	929±2	10
950.5±0.6	4	950.5±0.6	5	950.4±0.7	6	949.5±0.8	7	949±1	8
956.5±0.6	6	956.2±0.7	7	956.0±0.7	7	955.2±0.8	9	955±1	11
		981±2	7	980±1	8	978±1	9	977±1	11
996±1	5	995±2	8	995±2	10	994±2	12		
1029±1	~ 35	1030±1	~ 35	1030±2	~ 80	1030±2	~ 85	1030±2	90
1048±1		1048±1		1047±1		1046±2		1050±1	
1079 ±1	15	1078±1	16	1078±1		1076±1		1076±2	
1178±2	~ 15	1178±2	16	1178±2	~ 18	1175±2	18	1176±2	20

Figure 5-6: Polarised infra-red absorption spectra of $CdBr_2$(Co):1.0wt% recorded at $78^{o}K$ (L.H.S.) and $15^{o}K$ (R.H.S.).

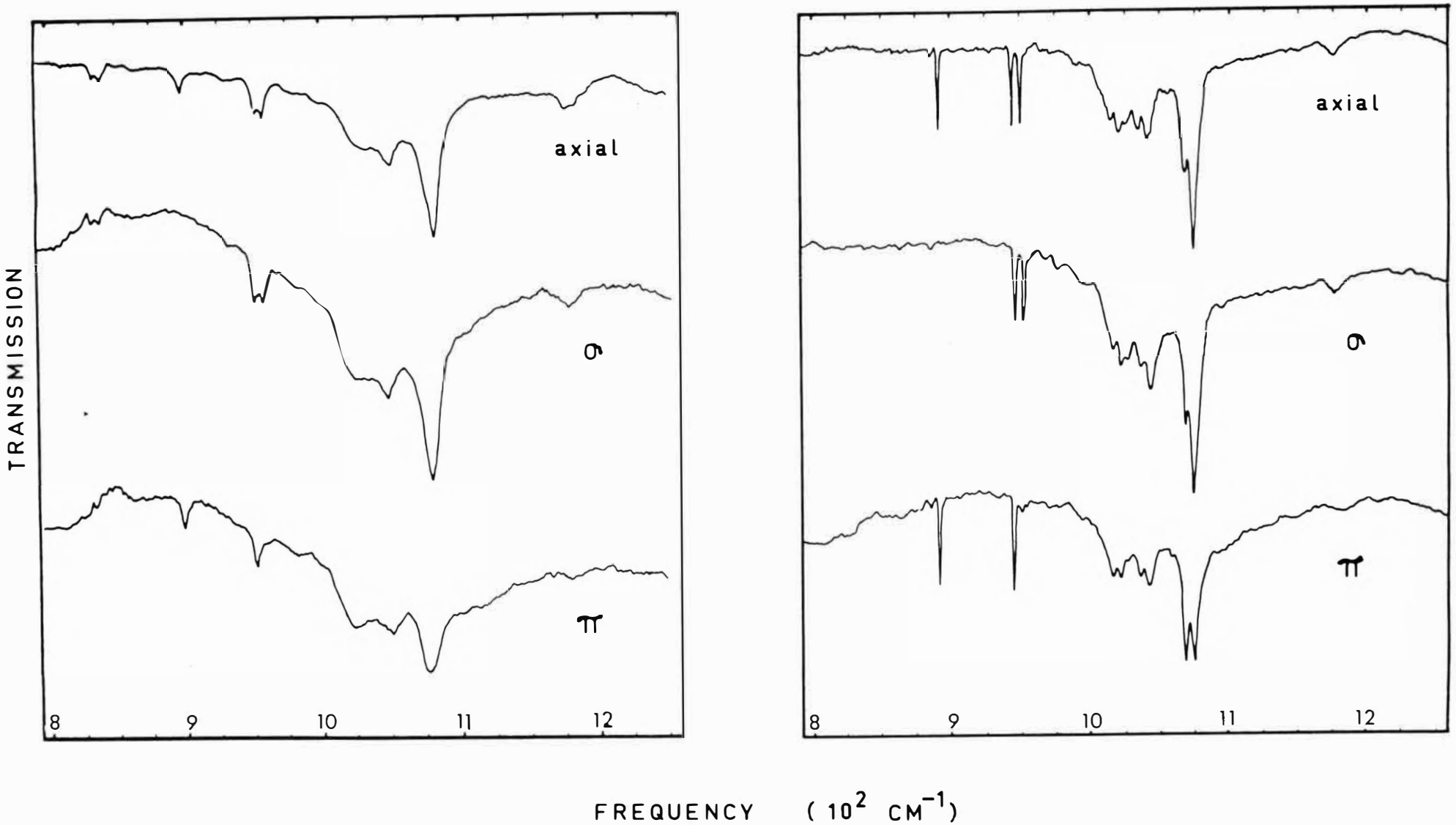

principal spectral features. The spectra differ from those of cadmium-chloride by having narrower lines and better resolved structure in the broad bands. In the 1.0 wt.% crystal, which gives the single cobalt ion spectra, lines were observed at 78°K with frequencies of 832, 837, 896.5 and 956.5 cm^{-1}. Of these lines, those at 832 and 837 cm^{-1} were absent from the 15°K spectra while the line at 896.5 cm^{-1} was found to be a closely split doublet with line components at 887 and 893.1 cm^{-1}.

Polarisation spectra were recorded for the 1.0 wt.% (Figure 5-6) and 5.0 wt.% (Figure 5-4) and the results are listed in Table 5-II. The results are qualitatively very similar to those observed for cadmium-chloride while the narrower lines allowed more precise data to be obtained.

5.3.3 $\underline{MnCl_2(Co^{2+})}$

Infrared spectra were observed for manganese-chloride containing 0, 1.0 and 5.0% by weight of cobalt-chloride. The spectral data is listed in Table 5-IV.

All the spectra are characterised by much broader lines than those observed in either cadmium-chloride or -bromide. The spectra were also complicated by the presence of sharp lines at 708, 1028 and 1055 cm^{-1} in crystals of the pure host and by additional lines at 681.5 and 733.0 cm^{-1} in the 5.0 wt.% doped crystals. All these lines are associated with oxide impurity in the crystals. Analogous lines can be obtained in cadmium-chloride and -bromide crystals which have been deliberately doped with cadmium-oxide (Chapter VIII).

In the 1.0 wt.% crystal, at 78°K, weak absorption lines appeared at 855, 890, 940, 975, 1025 and 1062 cm^{-1}. At 15°K

Table 5-IV IR Axial spectra of $MnCl_2(Co)$: 650 - 1350 cm^{-1} showing frequencies (cm^{-1}) and widths (cm^{-1}) of all observed lines.

Temperature : 78°K				Temperature : 15°K			
1.0% (3.62mm)		5.0% (1.99mm)		1.0% (3.62mm)		5% (1.99 mm)	
Freq.	Width	Freq.	Width	Freq.	Width	Freq.	Width
		681.5±0.5	7	682.0±0.5	2	681.4±0.5	5
708±1	7	708±1	12	707.8±0.4	4	708±1	10
		733.0±0.5	3			732.6±0.5	2.5
		752±2	10	750±1	9	752±1	8
757±1	10	755.5±0.5		756±1		755±0.5	
855±2		854±1	15				
890±2		887±2	20				
940±2	10	939±1	12	939±1	8	937±2	10
975±1	15	972±1	18	972±1	12	970±1	17
1026±2	12	1025±1	15	1023±1	9	1022±1	11
1062±2		1059±1	17	1058±1	12	1057±1	15
		1079±2		1080±1		1080±1	
1085±2							
		1122±2		1125±1		1121±1	
	~ 85	1147±2		1141±1		1140±2	~ 130
		1163±2	~ 135	1165±2	~ 80	1164±2	
1170±2				1175±2		1174±2	
1185±2		1186±2		1190±2		1190±2	
1260±2	~ 40			1261±2	~ 40		
1295±2		1300±2		1290±2		1300±2	

the lines at 855 and 890 cm^{-1} disappeared and the remaining lines shifted to slightly lower frequencies, with the pair of lines at 940 and 975 cm^{-1} becoming more clearly resolved. The principal broad band has peaks at 1080, 1125, 1141, 1165, 1175, 1190 and 1230 cm^{-1}. The high frequency broad band has peaks at 1261 and 1290 cm^{-1}.

5.3.4 $CoCl_2$

Axial spectra of cobalt-chloride crystals were obtained for the 400 to 1500 cm^{-1} infrared region at both room and low temperatures, and are given in Figure 5-7. Polarisation spectra were not measured. The spectral data is listed in Table 5-V. These frequencies may be compared with the Raman scattering results shown in Figures 4-7 and 4-8. As can be seen, the data agree to within ±2 cm^{-1} and there is no evidence for the uniform 7 cm^{-1} discrepancy reported by Hsu and Stout[21], which may have been due to different crystal temperatures for the infrared and Raman measurements and the use of different crystals in separate institutions.

The interpretation of the spectra is complicated by the onset of antiferromagnetic ordering below the Neel temperature of 24.7°K. At 78°K, lines due to cobalt occurred at 545, 905, 994 and 1055 cm^{-1} with bands at 875, 1220 and 1360 cm^{-1} in agreement with the values reported by Hsu and Stout[21]. At a temperature of approximately 30°K, the 905 cm^{-1} line was absent while the broad band at 993 cm^{-1} becomes asymmetrical with a shoulder at 962 cm^{-1}. On cooling to 15°K, this line shifted to 1012 cm^{-1} and has subsidiary peaks at 960 and 981 cm^{-1}. Peaks at 1058 and 1067 cm^{-1} also appeared on

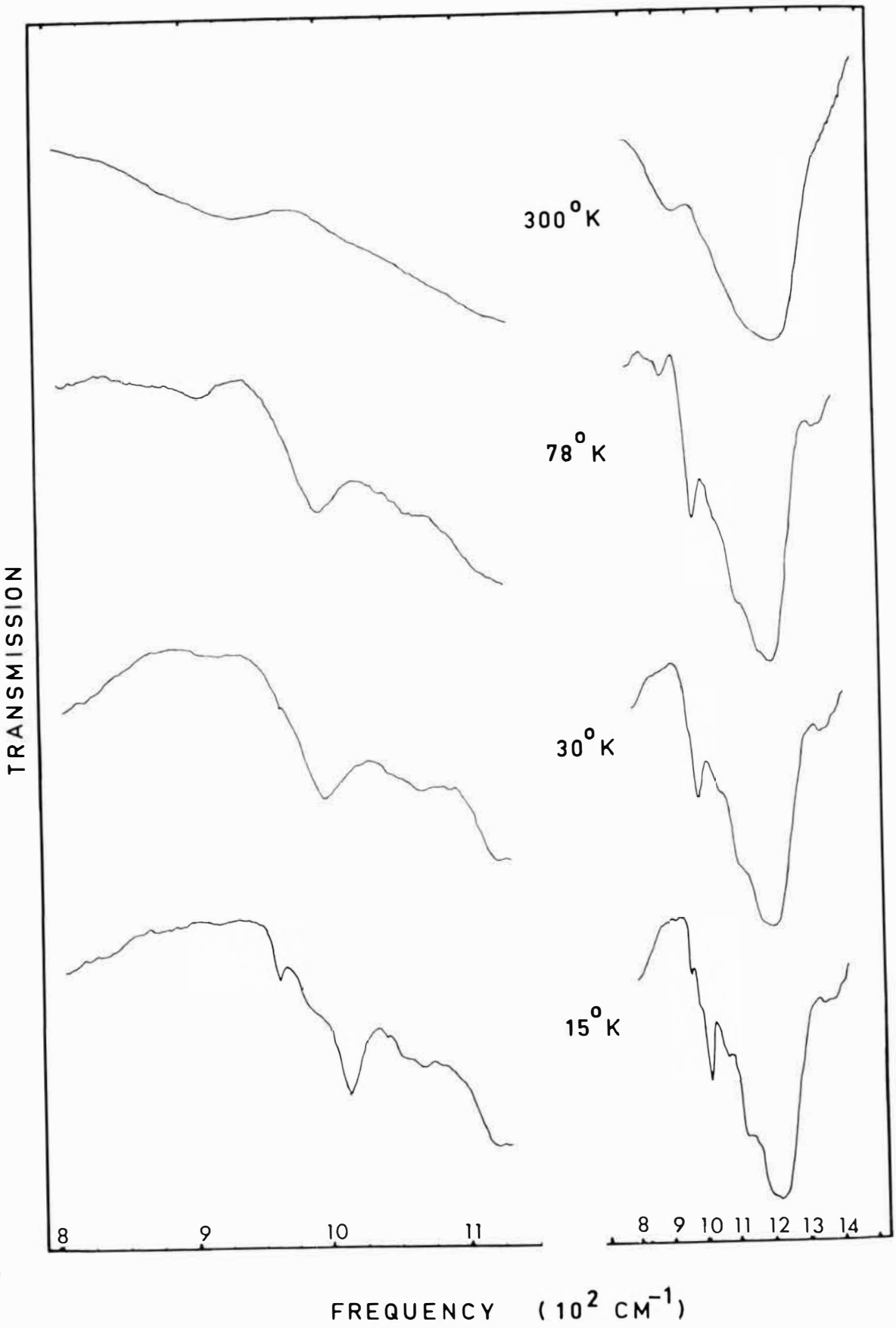

Figure 5-7: Axial infra-red absorption spectra of $CoCl_2$ recorded at 300, 78, 30, and 15°K between 800 and 1450 cm^{-1}.

Table 5-V IR Axial Spectrum of $CoCl_2$ (0.39mm) showing frequencies (cm^{-1}) and widths (cm^{-1}) of all observed lines.

400 - 600 cm^{-1}					
: 78°K		: 30°K		: 15°K	
Frequency	Width	Frequency	Width	Frequency	Width
455±2		456±1	2	456±1	2
		460±1		461±1	2
486±2	20	485±1	15	481±1	15
				490±1	
510±2	7	510±1		510±1	6
545±3	32	545±1	25	547±1	12
				575±2	
800 - 1500 cm^{-1}					
905±1	15				
		962±1		960.0±0.7	5
994±1	22	993±1	20	981±2	18
				1012±1	
1055±2		1055±2		1051±2	25
				1067±2	
1120±2	185	1120±2	180	1120±2	180
				1155±2	
1180±2		1180±2		1180±2	
1220±2		1220±2		1220±2	
1360±2		1360±3		1360±3	

the side of the principal broad band which has structure with peaks at 1120, 1155, 1180 and 1220 cm^{-1}. The high frequency band at 1360 cm^{-1} became more pronounced. The 547 cm^{-1} line had a weak shoulder at 575 cm^{-1}.

5.4 ANALYSIS OF SINGLE Co^{2+} ION ELECTRONIC SPECTRA

Of the five electronic transitions of single cobalt ions having energies between 0 and 1200 cm^{-1} which have all been identified by Raman scattering, three are observed by infrared absorption. The lowest energy transition was not observed because it lies in the region of intense restrahlen absorption of the host crystal; the highest was not observed because of its weak intensity (Table 5-VI) together with the masking by the principal broad absorption band of cobalt around 1170 cm^{-1}, in the chlorides.

The three electronic transitions observed have differing intensities and polarisations. In the axial spectra, where the infrared radiation is incident along the crystal c-axis, all three lines appear. In the polarisation spectra the two low frequency absorption lines appear in both polarisations with relative intensities given in Table 5-II while the highest frequency line only appears for the E vector of the infrared radiation parallel to the crystal c-axis (i.e. in π polarisation) and is absent in the spectra for which the same E vector is perpendicular to the crystal c-axis (i.e. σ polarisation). For all three lines, the axial and π polarisation spectra coincide and therefore the electronic transitions are magnetic-dipole allowed.

The electronic transitions observed are from a (Γ_6^+, γ_4^+) groundstate to excited states of either γ_4^+ or $\gamma_{5,6}^+$ symmetry (Chapter 2.2). The selection rules governing the occurrence of infrared active magnetic-dipole transitions can be derived from the symmetry properties of the components of the magnetic-dipole transition operator $M_i = \frac{1}{2M}(L_i + 2S_i)$ where L_i and S_i are the components of orbital and spin angular momenta respectively. These transform as the γ_2^+ and γ_3^+ irreducible representations of the D_{3d} double group and, from the product representations:

$$\gamma_4^+ \times \gamma_2^+ = \gamma_4^+ \tag{5.1}$$

$$\gamma_4^+ \times \gamma_3^+ = \gamma_4^+ + (\gamma_5^+ + \gamma_6^+)$$

it follows that only γ_4^+ electronic upper states can be observed for σ polarised spectra. The highest frequency line is, therefore, assigned to a $(^{(2)}\Gamma_8^+, \gamma_{5,6}^+)$ upper state and the other two, for decreasing energy, are assigned to $(^{(2)}\Gamma_8^+, \gamma_4^+)$ and $(^{(1)}\Gamma_8^+, \gamma_4^+)$ electronic levels.

The crystal-field calculation, described in Chapter II, can be used to calculate the intensities of these electronic levels as follows:

The oscillator strength, f, of a magnetic-dipole transition between two states $|g\rangle$ and $|e\rangle$ is given by[71]

$$f = \frac{4\pi m\nu}{h} |\langle g|M_i|e\rangle|^2 \tag{5.2}$$

where the M_i are the matrix elements of the magnetic-dipole operator:

$$M_i = \frac{1}{3}\left(\frac{1}{2mc}\right)(L_i+2S_i) \tag{5.3}$$

where the L_i and S_i are the components of the orbital and spin angular momenta respectively, m is the electronic mass, and ν is the frequency of the transition. Numerically[21]

$$f = 1.21 \times 10^{-10}\, n\nu\,|\langle g|L_i+2S_i|m\rangle|^2 \tag{5.4}$$

where n is the refractive index of the crystal at frequency ν. The matrix elements of (L_z+2S_z) and (L_x+2S_x) may be obtained by evaluating these operators between the six lowest Kramers degenerate states. These states are characterised by the eigenvectors of the twelve lowest levels of the full 120 dimension free-ion and crystal-field matrices of the $3d^3$ configuration appropriate for the crystal being examined. The calculated oscillator strengths are listed in Table 5-VI.

The oscillator strengths were determined experimentally from the peak absorbance and half-widths of each infrared absorption line. Dexter[72] gives the oscillator strength of a transition as:

$$f = \frac{1}{N}\frac{nmc}{2\pi^2 e^2 \hbar}\left(\frac{\varepsilon_0}{\varepsilon_{eff}}\right)^2 \int \mu_{ab}(E)\,\partial E \tag{5.5}$$

$$= \frac{K}{N}\left(\frac{n}{n^2+2}\right)^2 \mu_{ab}(max)V_{ab} \tag{5.6}$$

where the factor K depends on the particular line profile and has values 1.29×10^{17} and 0.87×10^{17} cm^{-3} for Lorentzian and Gaussian lines respectively. N is the number of absorbing

Table 5-VI Calculated and experimental oscillator strengths for assigned transitions in $CdCl_2$(Co):0.5% and $CdBr_2$(Co) : 1% at 15°K in units of (10^{-10}).

Assignment	$CdCl_2$(Co):0.5%				$CdBr_2$(Co):1%			
	Oscillator – Strength (σ)		Oscillator–Strength (π)		Oscillator – Strength(σ)		Oscillator – Strength(π)	
	Exptl.	Calc.	Exptl.	Calc	Exptl.	Calc.	Exptl.	Calc.
$\gamma_4^+(\Gamma_6^+)$								
$\gamma_5^+ + \gamma_6^+(^{(1)}\Gamma_8^+)$		0		2868		0		3396
$\gamma_4^+(^{(1)}\Gamma_8^+)$	1103[a]	5656	206[a]	958.3		5285		1041
$\gamma_4^+(^{(2)}\Gamma_8^+)$	22.4	73.2	15.6	55.7	10.0	10.0	7.0	3.37
$\gamma_5^+ + \gamma_6^+(^{(2)}\Gamma_8^+)$	0	0	850	936.2	0	0	262	232.6
$\gamma_4^+(\Gamma_7^+)$		46.7		31.1		16.9		6.53

a. $CdCl_2$(Co) : 10% at 78°K

ions per cm^3, n is the refractive index of the crystal, $\mu_{ab}(max)$ is the peak absorbance of the line in cm^{-1}, and V_{ab} is the width of the line at half-maximum absorbance in electronvolts.

The absorption data for cadmium-chloride and -bromide crystals containing 0.5 wt.% and 1.0 wt.% of cobalt respectively were taken as representative for the oscillator strength calculations and were supplemented by data for the 5.0 wt.% crystal, where necessary. The refractive index of cadmium-chloride in the visible region of the spectrum is 1.68[73], while its value in the infrared has not been measured. The value of n was estimated from the mean transmittance $\bar{T}$ of the crystal using:

$$\bar{T} = \frac{2n}{n^2+1} \qquad (5.7)$$

for the transmittance of a non absorbing material. The transmittance measured for the crystals was 0.78 ± 0.02 and 0.80 ± 0.02 at 1500 and 900 cm^{-1} respectively and was independent of the crystal thickness. An allowance had to be made for the scattering of the radiation by the imperfect optical faces of the cleaved crystal and with this set at 5%, the apparent refractive index was calculated to be 1.84. This may be compared with the results of Hsu and Stout[21] for cobalt-chloride who obtained a value for n of 1.87 from the measured transmittances of 0.79 ± 0.01 and 0.80 ± 0.01 at 1550 and 915 cm^{-1} respectively.

The number, N, of absorbing cobalt ions per cm^3 was calculated from the crystal's molar doping and its mean density. The accuracy of doping of the crystal was checked by

measuring the peak absorbance of the $^4T_{1g}(^4P)$ visible band for a solution containing a known weight of the doped crystal and comparing this with that for a solution of cobalt-chloride. For a 5 wt.% crystal this spectrophotometric comparison indicated a cobalt concentration of (4.9 ± 0.1) wt.% so the molar doping of the crystals was assumed accurate.

With the assumption of Gaussian line shapes, the experimental oscillator strengths are listed in Table 5-VI, together with the corresponding calculated values. These results show substantial agreement and give good quantitative confirmation of the assignment of the lines observed as magnetic dipole allowed transitions. They also show that the non-observance of the highest electronic transition ($\Gamma_7^+\gamma_4^+$) is consistent with its weak intensity.

5.5 ANALYSIS OF THE Co^{2+} ION VIBRONIC SPECTRA

The vibronic bands comprise both sharp lines and broad bands. Neither of these are observed in the Raman spectra of the same crystals.

5.5.1 Sharp Lines

The sharp lines were assigned as vibronic in origin because they were observed as pairs associated with a given electronic level and located symmetrically about it. Their frequencies are listed in Table 5-VII, together with those of their electronic parent levels. The lines are nearly as narrow as their parent electronic levels and the vibronic frequencies are well defined yielding definite vibronic frequencies for each crystal host.

Table 5-VII Frequencies (cm^{-1}) of sharp acoustic phonons observed in $CoCl_2$ and crystals of $CdCl_2$, $CdBr_2$, $MnCl_2$ containing Co^{2+} ions.

Temp. (^oK)	$CdCl_2$(Co):1%			$CdBr_2$(Co):1.0%			$MnCl_2$(Co):1.0%			$CoCl_2$		
	Electronic Parent	Vibronic	Vibronic Interval	Electronic Parent	Vibronic	Vibronic Interval	Electronic Parent	Vibronic	Vibronic Interval	Electronic Parent	Vibronic	Vibronic Interval
78	925±1	854±1	-71±2	—	832±1		940±2	855±2	-85±4	963±4 (a)		
		998.0±0.7	+73±1.7		950.5±0.6			1025±2	+85±4		1055±2	+92±6
	953.2±0.5	883±1	-70±1.5	896.5±0.5	837±1	-59.5±1.5	975±1	890±2	-85±3	994±1	905±1	-89±2
		1027.7±0.8	+74.5±1.3		956.5±0.6	+59.7±1.1		1062±2	+87±3		- (b)	
15	921.8±0.4			887±1			939±1			960.0±0.7		
		995.1±0.5	+73.3±0.9		947.0±0.3	+60±1.3		1023±1	+84±2		1051±2	+91±2.7
	950.2±0.4			893.1±0.3			972±1			981±2		
		1025.0±0.5	+74.8±0.9		953.2±0.3	+59.9±0.6		1058±1	+86±2		1067±2	+86±4
										1012±1	- (b)	

a. Raman data (Table 4-IV) not observed in infrared.

b. Masked by lattice phonon sideband.

The intensity of the lines is temperature dependent. The intensity of the summation lines is proportional to (1+n) while that of the difference lines is proportional to n[74] where:

$$n = \frac{1}{\exp\left(\frac{\hbar w}{kT}\right) - 1} \qquad (5.8)$$

The difference lines, therefore, disappear at low temperature as shown by their absence from the liquid helium spectra of all crystals. From the relative intensities of the summation and difference lines the crystal temperature could be estimated. (The temperature of the 30°K spectra in Figure 5-7 was found in this way.)

The polarisation spectra show that the axial and σ-polarised spectra coincide indicating that the vibronic lines are, therefore, electric-dipole allowed. The intensity of the vibronics follow that of their electronic parents but in the opposite polarisation due to their electric- rather than magnetic-dipole character. In particular, the vibronics associated with the $(^{(2)}\Gamma_8^+, \Gamma_{5,6}^+)$ electronic appear strongly in the σ polarised spectra, while their electronic parent appears strongly in the π polarised spectra (Figure 5-4).

Analogous sharp vibronic lines have been observed in cadmium-chloride and -bromide crystals containing divalent iron. Hence, the vibronic intervals appear to be characteristic of the crystal host rather than the particular transition ion present.

The case of cobalt-chloride is now discussed in more detail because of its relevance to the assignment of this crystal's spectra by Hsu and Stout[21]. The sharp vibronic

lines observed at 905 and 1055 cm^{-1} (at $78^{o}K$. Table 5-V) are much broader than those observed in other crystals and correspond to the unidentified (vibronic) lines at 900 and 1050 cm^{-1} observed by Hsu and Stout. By comparison with the data for the other isomorphic crystals, they are assigned as difference and summation vibronic lines associated with the unresolved pair of electronic lines at 994 cm^{-1}. At $30^{o}K$, the former becomes barely visible while the electronic parent line becomes resolved into two components at 962 and 993 cm^{-1}. At $15^{o}K$, the crystal is antiferromagnetically ordered with summation lines at 1051 and 1067 cm^{-1} associated with the 960 and 981 cm^{-1} parent electronic lines. The expected summation line associated with the 1012 cm^{-1} line is masked by the broad vibronic band centred at 1220 cm^{-1}.

These summation lines yield a vibrational interval of 90 cm^{-1} for cobalt-chloride, in comparison with 73 cm^{-1} for $CdCl_2(Co^{2+})$, 60 cm^{-1} for $CdBr_2(Co^{2+})$ and 85 cm^{-1} for $MnCl_2(Co^{2+})$. The low frequency vibronic interval thus obtained is assigned to a sharp peak in the phonon density of states of the host crystals. It does not correspond to any of the well established $\vec{k} = 0$ phonons listed in Table 5-VIII, while its low frequency requires its assignment to an acoustic branch of the phonon dispersion curves, necessarily away from $\vec{k} = 0$. This assignment is confirmed by the absence of any infrared absorption at, or near 73 cm^{-1} in the far infrared spectra of cadmium-chloride crystals. No specific assignment of this vibrational interval to a particular peak in the acoustic phonon density of states can be made until the phonon dispersion curves for the cadmium-chloride lattice are determined.

It is expected that these sharp vibronic lines should also appear in the optical spectra of these crystals. In particular, it is suggested that the line at 18887 cm^{-1} in the $^2T_2(^2P)$ term of cadmium-chloride crystals containing cobalt which was assigned by Mooney et al.[75] as a γ_4^+ symmetry electronic line could be vibronic in origin and associated with the γ_4^+ symmetry line at 18820 cm^{-1}. This is supported by the appearance of the variable temperature spectra also reported by Mooney et al. Our alternative assignment could be verified by a Zeeman or M.C.D. investigation of these particular lines.

5.5.2 Broad Bands

Broad vibronic bands associated with the electronic lines are also observed and their intensity varies with the parent electronic level. In particular, the combined absorption of the vibronic bands associated with the $(^{(2)}\Gamma_8^+, \gamma_4^+)$ and $(^{(2)}\Gamma_8^+, \gamma_{5,6}^+)$ levels is stronger by a factor of twenty over the bands associated with the $(^{(1)}\Gamma_8^+, \gamma_4^+)$ and (Γ_7^+, γ_4^+) levels. These bands are all electric-dipole as shown by the similarity of their axial and σ-polarised spectra. Their polarisation depends on that for the parent electronic level and, as for the sharp vibronic lines, the bands associated with the $(^{(2)}\Gamma_8^+, \gamma_{5,6}^+)$ level are principally σ polarised.

The structure of the vibronic bands was analysed to give frequencies of peaks in the density of states for the host crystals. These are listed in Table 5-VIII. Some phonon frequencies correspond with those of the infrared and Raman lattice phonons while some must be associated with high

Table 5-VIII: Analysis of Vibronic Bands in $CdCl_2$(Co):1% and $CdBr_2$(Co):1% to give frequencies (cm^{-1}) of peaks in the phonon density of states at 15°K.

$CdCl_2$(Co):1%			$CdBr_2$(Co):1%		
Electronic Parent	Vibronic	Vibronic Interval	Electronic Parent	Vibronic	Vibronic Interval
921.8±0.4	1100±1	178.2±1.4	887±1	1017.5±0.5	130.5±1.5
	1128±1	206.2±1.4		1023.0±0.5	136±1.5
	1155±1	233.2±1.4		1038.2±0.6	151.2±1.6
	1164.5±0.5	242.7±0.9		1070.3±0.5	183.3±1.5
950.2±0.4	1128±1	177.8±1.4	893.1±0.3	1023.0±0.5	129.9±0.8
	1155±1	204.8±1.4		1029±1	135.9±1.3
	1183±1	232.8±1.4		1044.5±0.5	151.4±0.8
	1195±1	244.8±1.4		1076.5±0.4	183.4±0.7
1088±3 [a]	1265±2	177±5	995±1 [a]	1177±2	182±3
	1295±2	207±5			
	1320±3 [b]	232±6			
K=0 Phonons [c]			K=0 Phonons [c]		
A_{1g}	E_g	A_{2u} E_u	A_{1g}	E_g	A_{2u} E_u
233±1	131±1	164±2 210±2	148±1	77±1	102±2 161±2

a. Raman data (Table 4-IV)

b. Weak, observed in 2.5% and more heavily doped samples

c. D.J. Lockwood [40]

symmetry points in the Brillouin zone, necessarily away from $\vec{k} = 0$.

In the case of the strongest vibronic band centred near 1170 cm^{-1} in the chlorides there are two parent electronic levels and hence all band peaks due to a given feature in the phonon density of states occur in pairs with a separation matching that of the $(^{(2)}\Gamma_8^+, \gamma_4^+)$ and $(^{(2)}\Gamma_8^+, \gamma_{5,6}^+)$ levels. These pairs of peaks show differing polarisations consistent with the different symmetries of their parents and this served to resolve ambiguities in their assignments. (Figures 5-3 and 5-6). The other broad bands are much weaker and show little structure. The peaks observed are consistent with those obtained for the strongest vibronic band. Also, the peaks in the highest frequency vibronic band allowed the position of the electronic (Γ_7^+, γ_4^+) level to be inferred which confirmed the Raman results.

C H A P T E R V I

THE SPECTRA OF EXCHANGE-COUPLED COBALT ION-PAIRS IN $CdBr_2$ AND $CdCl_2$

6.1 INTRODUCTION

Both the Raman and infrared spectra of crystals containing a low concentration of cobalt arise from single, or isolated cobalt ions. As the cobalt concentration is increased, these lines broaden and shift to lower frequencies (Tables 4-III, 5-Ia and -Ib, 5-IIIa and -IIIb). New lines also appear which may be associated with cobalt ion clusters and have intensities which become comparable with that of the single ion spectral features at a cobalt concentration of approximately 10.0 wt.% (Figure 6-1). The intensity of the lines due to cobalt ion pairs have a quadratic dependence on the cobalt concentration while that due to more complex clusters has a more rapid dependence. From these concentration dependences, then, the various lines due to single cobalt ions, cobalt ion pairs and clusters can be resolved.

In order to obtain the precise data with which to attempt a quantitative analysis of the spectra of cobalt ion pairs the infrared spectra of $CdCl_2(Co^{2+})$:5.0 wt.% and $CdBr_2(Co^{2+})$:5.0 wt.% have been re-recorded using the new dewar, described in Chapter III. These specific hosts were chosen because their cobalt electronic features are the most clearly resolved of all the crystals examined while the particular cobalt concentration was chosen to give optimum intensities and line-widths for the cobalt ion pair lines.

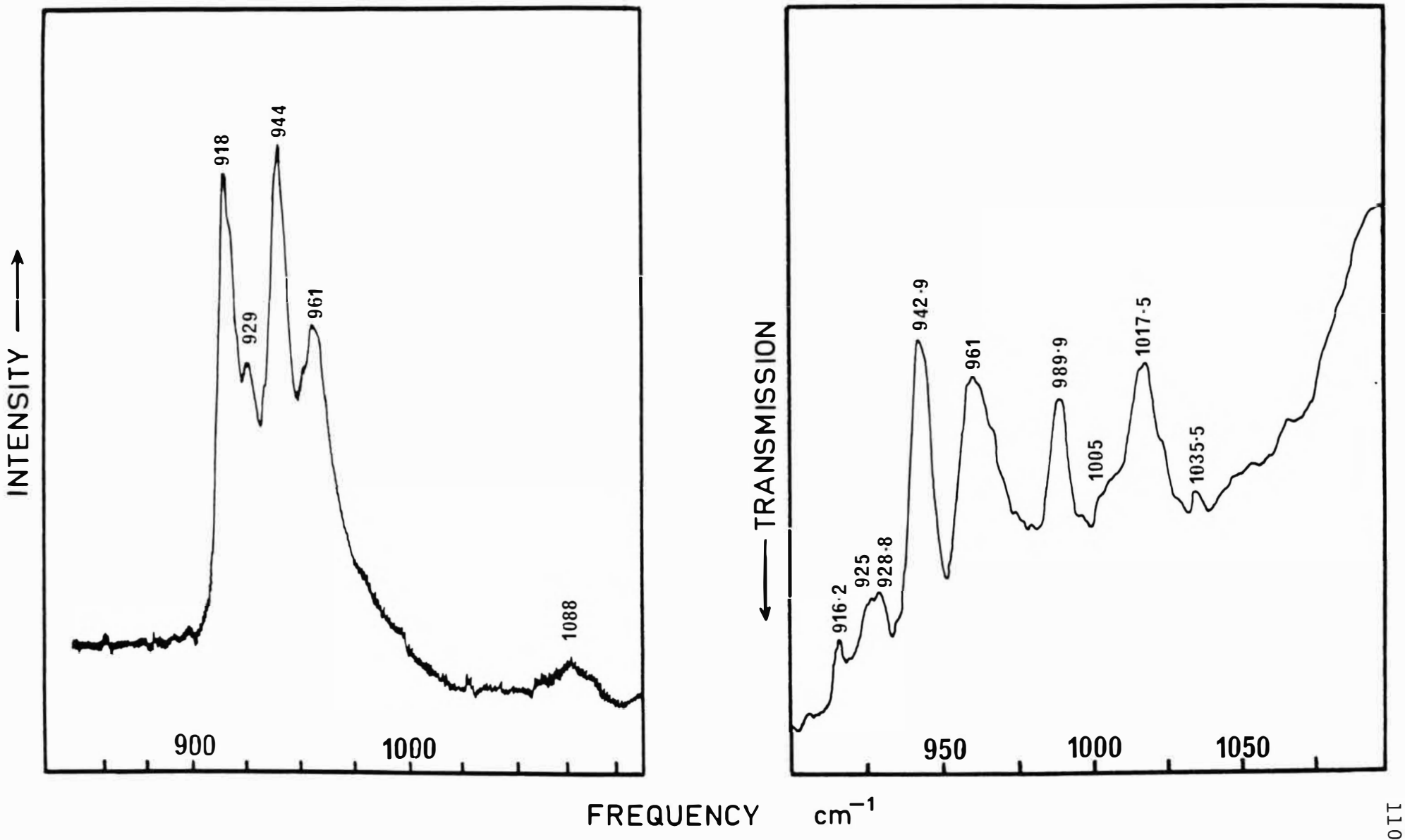

Figure 6-1: Raman and infra-red axial spectra of $CdCl_2$(Co):10wt% recorded at 15°K in the region 850-1150 cm^{-1}.

Specific results for each crystal are listed separately in Section 6.6. In order to interpret the spectra obtained, the relative probability of occurrence for single, pair and triple-clusters of cobalt ions in these crystals is evaluated in Section 6.2. As a background, a review of the current formalism of exchange interactions between magnetic ions is given in Section 6.3. The real spin exchange model used to analyse the spectra obtained in this work is outlined in Sections 6.4 and 6.5. A comparison of this model with the more conventional Spin Hamiltonian treatment is presented in Section 6.7. Finally, an alternative interpretation of Bailey et al.'s[79] spectra of $CdBr_2$ crystals containing cobalt is discussed in Section 6.8.

6.2 COBALT CONCENTRATION THEORY

In the crystals examined, the cobalt ions substitute for the cations, and are surrounded by a nearest neighbour distorted octahedron of anions. All the cobalt ions experience similar next-nearest neighbour environments. The nearest neighbour cations for each cobalt ion can differ, however, depending on the cobalt concentration and the different possible sets of nearest neighbour cations cause changes in the position of the cobalt ion energy levels.

Within each cation layer, each ion has six nearest neighbours; interlayer effects can be ignored, as each cation layer is separated by two layers of anions (Figure 2-1). The simplest of the cluster sites that can be formed therefore, arise from cobalt ions having a different number of nearest

neighbour cobalt ions. Tables for the relative percentage probability of these have been published by Mooney et al.[75] who compare the results obtained from Trutia and Voda's[80] and Behringer's[81] formulae. These values are reproduced here in Table 6-I for comparison with the results calculated below.

In general we assume a similar, random distribution of cobalt ions in each and every layer so that there is no segregation of cobalt ions in any one sector of the crystal. Then, if N is the total number of ions in the lattice, c is the mole-fraction of cobalt, and (1-c) the mole-fraction of cadmium ions we may derive the probability of occurrence for each cluster configuration as follows (refer Figure 6-2).

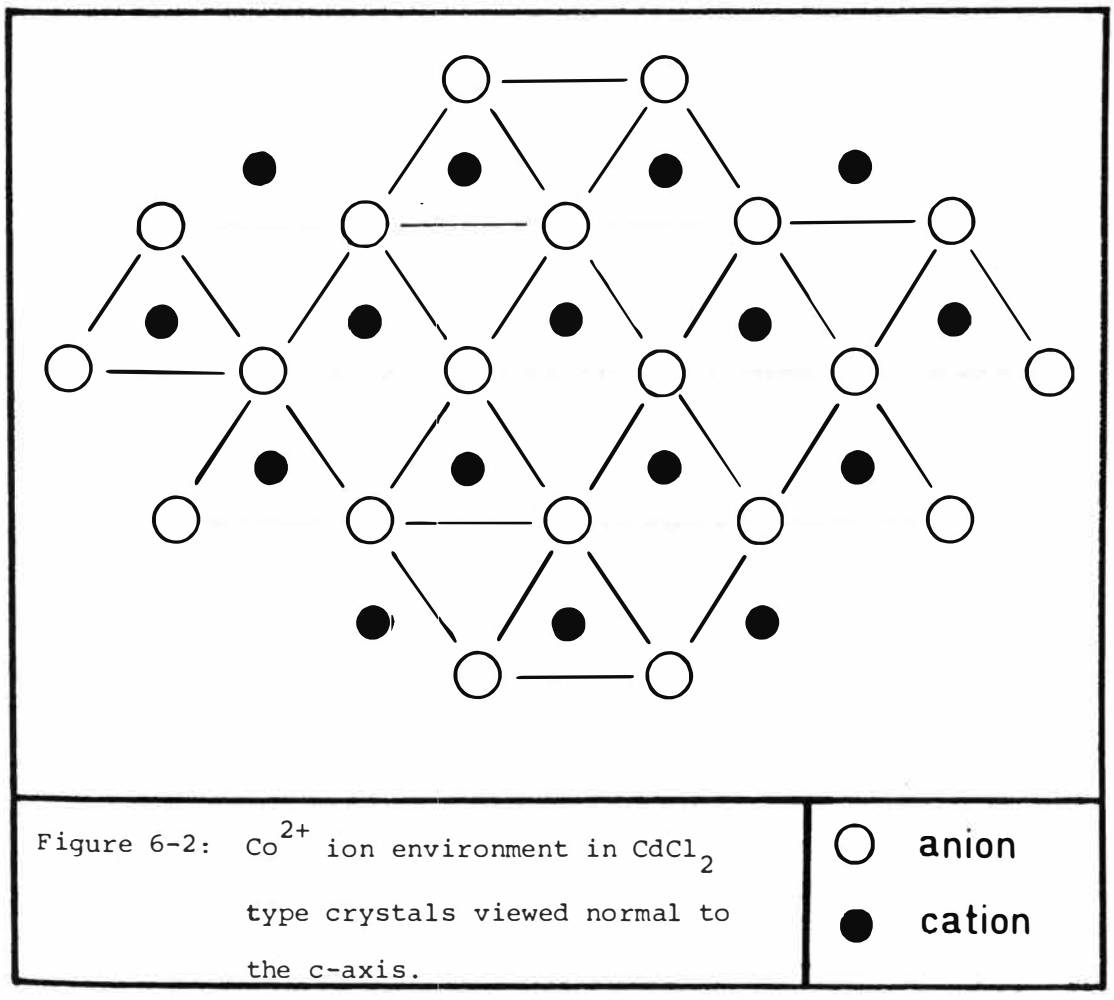

Figure 6-2: Co^{2+} ion environment in $CdCl_2$ type crystals viewed normal to the c-axis.

Mole % $[Co^{2+}]$	TRUTIA AND VODA[80]			BEHRINGER[81]			THIS WORK					
	Singles	Pairs	Triples	Singles	Pairs	Triples	Singles	Pairs	Triples T_1	Triples T_2	Triples T_3	Triples T
1	94.2	5.7	0.14	94.2	5.4	0.39	94.1	5.5	0.11	0.22	0.11	0.44
3	83.3	15.5	1.2	82.3	13.9	2.3	83.3	14.1	0.82	1.59	0.80	3.4
11.8	47.1	37.8	12.6	47.1	20.2	12.0	47.1	25.9	5.40	9.52	4.76	19.7
20	26.2	39.3	24.6	21.8	10.6	7.9	26.2	20.1	6.44	10.31	5.15	21.9
76	0.0	0.3	2.9	0.0	0.0	0.0	0.2	0.0	0.002	0.004	0.002	0.008

TABLE 6-I. Relative percentage probabilities for the occurrence of single, pair and triple cobalt ion centres.

For the probability of single cobalt ions with concentration c; if we fix any cobalt ion site, all six of its nearest neighbours must be cadmium ions to ensure the formation of an isolated cobalt ion site. Hence, the number of single centres is given by $Nc(1-c)^6$.

For the number of cobalt ion pairs, we fix any cobalt ion and note that any of its six neighbours may serve to form the other ion of the pair. By ensuring that all the nearest neighbour ions to both members of the pair are cadmium ions there is no possibility of a triple cluster and so the number of pair centres is given by $6Nc^2(1-c)^8$.

To evaluate the number of triple cobalt ion clusters we must consider the three possible arrangements of the cobalt ions themselves, which are labelled as T_1, T_2 and T_3:

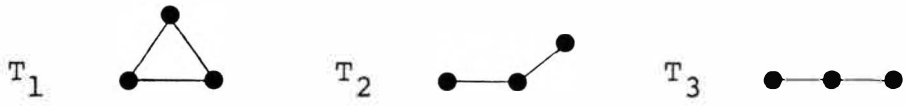

and occur with slightly varying frequency. To evaluate their number we fix any pair and note there are only two lattice sites for which a third cobalt ion will complete the triangle. Where the nearest neighbours of the triangle are all cadmium ions the number of T_1 triples is:

$$Nc(6c)(2c)(1-c)^9 = 12Nc^3(1-c)^9 \qquad (T_1)$$

Similarly the number of T_2 and T_3 triples is respectively:

$$Nc(6c)(4c)(1-c)^{10} = 24Nc^3(1-c)^{10} \qquad (T_2)$$

and $$Nc(6c)(2c)(1-c)^{10} = 12Nc^3(1-c)^{10} \qquad (T_3)$$

The total number of triples is given in Table 6-I as T where $T = T_1 + T_2 + T_3$.

The formulae of Trutia and Voda[80] were obtained by considering an isolated hexagon of cobalt and cadmium ions with no regard to the nearest neighbours outside this hexagon. Hence, many of our triple configurations will be classified as pairs by them. Their formulae for the number of singles, pairs and triple centres have been deduced from their tables as: $Nc(1-c)^6$, $6Nc^2(1-c)^5$ and $15Nc^3(1-c)^4$ respectively and differ from ours. Behringer's[81] formulae are only appropriate for a face-centred cubic lattice.

From these numbers for each individual arrangement, the probability of their occurrence may be simply obtained by dividing each expression by the total number (Nc) of sites available.

6.3 THEORETICAL REVIEW

In a weakly-coupled cobalt ion pair each electronic transition can be considered as that of a single cobalt ion, shifted in frequency due to the neighbouring cobalt ion(s) and split by the exchange interaction between them. To interpret such spectra it is necessary to apply the current exchange interaction formalism to the interactions between the magnetic ions involved. This is briefly reviewed below.

The interaction between a pair of magnetic ions can arise in several ways. Four classes of interactions are usually important and these are the (i) magnetic-dipole (ii) electric-multipole (iii) virtual phonon and (iv) exchange interactions.

The electrostatic interaction between a pair of electrons may be written as:

$$\langle\psi_a'(1)\psi_b'(2)|\frac{e^2}{r_{12}}|\psi_a(1)\psi_b(2)\rangle - \langle\psi_a'(1)\psi_b'(2)|\frac{e^2}{r_{12}}|\psi_a(2)\psi_b(1)\rangle \tag{6.1}$$

where the electrons (1) and (2) have their wavefunctions centred on (a) and (b). The first, and classical term is the direct or Coulomb interaction and gives rise to the electric-multipole interaction listed (ii) above. The second, known as the exchange term arises from the indistinguishability of the electrons and the overall antisymmetry requirements of the quantum mechanical description of the wavefunction for the system.

Heisenberg[82] and Dirac[83] have shown that this exchange interaction gives rise to an effective "spin-coupling" between the electrons. For the particular case of two orbitally non-degenerate s electrons the interaction may be characterised by the Hamiltonian:

$$\mathcal{H}_{ex} = \mathcal{J}(\tfrac{1}{2} + 2\mathbf{s}_1\cdot\mathbf{s}_2) \tag{6.2}$$

Van Vleck[84] extended these ideas to explain the properties of magnetic ions in solids. He showed that for the simple case of two s state electrons a similar Hamiltonian to (6.2) could be used, but with the total ionic spin $\mathbf{S}_i$ replacing the individual electronic spin $\mathbf{s}_i$. This Hamiltonian could be applied to the case of an ion whose orbital angular momentum was completely quenched. In this way the ferromagnetic or

antiferromagnetic properties of the solid could be understood in terms of a "spin-only" exchange interaction where the electron spins were coupled parallel or antiparallel. If there is no particular direction of spin alignment with respect to the crystal axes such exchange is termed "isotropic" and the crystal's magnetic susceptibility will be independent of field-direction. Conversely, when there is a preferred direction, the exchange is "anisotropic" while for "asymmetric" exchange the spins tend to align perpendicular to each other.

Because of the early successes of this model there has been a tendency to assume the universal validity of the Heisenberg-Dirac Hamiltonian, even for ions with non-zero angular momentum. More recently, many authors (in particular: Van Vleck[85] (1962), Levy[86,87] (1964,1969), Elliott and Thorpe[88] (1968) and Wolf[89] (1971)) have shown that such an assumption is not generally valid and have consequently resorted to a more general formalism to describe the interaction. Essentially, they point out that the mutual electrostatic energy of the two ions depends on the relative alignment of their orbital angular momentum vectors as well as that of their spins.

The Hamiltonian in (6.2) may be generalised to describe ions with orbital degeneracy. In a simple extension of the Heisenburg-Dirac Hamiltonian the exchange parameter $\mathcal{J}$ is no longer considered to be a constant but is instead assumed to be a function of the components of the orbital angular momentum of the ions involved in the interaction. The exchange Hamiltonian between a pair of ions (a) and (b) may

then be written as:

$$\mathcal{H}_{ex} = \sum_{m_a,m_b,m_a',m_b'} \mathcal{J}(m_a m_b; m_a' m_b')(\tfrac{1}{2} + 2S_a \cdot S_b) \qquad (6.3)$$

where the m_a, m_b, m_a' and m_b' refer to the components of the orbital angular momentum for each ion. A more fundamental approach which can be shown to lead to (6.3) above, involves a multipolar expansion of the two-centre exchange interaction in terms of operators which operate on the orbital states of the ions. The spin part of the interaction is assumed to carry through the calculation in its original form. The matrix elements of the orbital operators are found to be the generalised $\mathcal{J}(m_a m_b m_a' m_b')$ in (6.3). The form of the operators and the number of independent parameters is limited by time reversal, hermiticity, and spatial symmetry considerations.

Levy[87] has published a detailed derivation of such an exchange Hamiltonian. His approach, although explicitly intended for direct exchange between ions, is equally valid for a superexchange interaction where the exchange interaction between magnetic ions is transmitted via an adjacent diamagnetic ligand. Because Levy's work is extremely complex and goes beyond the scope of this work only his principal results are quoted here. The exchange Hamiltonian is written in the form:

$$\mathcal{H}_{ex} = \sum_{\substack{k_1 k_2 \\ \Lambda m}} \Gamma_m^{(\Lambda)}(k_1 k_2) \left[T^{(k_1)}(1) \times T^{(k_2)}(2) \right]_m^{(\Lambda)} (\tfrac{1}{2} + 2S_1 \cdot S_2) \qquad (6.4)$$

The $\Gamma_m^{(\Lambda)}(k_1 k_2)$ are constants whose magnitude depends on the nature of the interaction. They are calculable in principle,

for specific cases if the radial dependence of the wave-functions for the magnetic ions and ligands is known. However, they are usually treated as empirical parameters. The operator product is written in component form as:

$$\left[T^{(k_1)}(1) \times T^{(k_2)}(2)\right]^{(\Lambda)}_{m} = \sum_{q_1 q_2} (-1)^{k_2-k_1-m} [\Lambda] \begin{pmatrix} k_1 & k_2 & \Lambda \\ q_1 & q_2 & -m \end{pmatrix} \cdot T^{(k_1)}_{q_1}(1)\, T^{(k_2)}_{q_2}(2). \qquad (6.5)$$

The operators $T^{(k)}_{q}$ act on the orbital angular momenta of the ions and thus the range of values taken by the rank k depends on the initial and final angular momenta of the ion involved $|\ell-\ell'| \leq k \leq \ell+\ell'$. The rank Λ of the coupled product is restricted to $|k_1-k_2| \leq \Lambda \leq k_1+k_2$. The particular values of Λ taken determine the nature of the interaction. For example, when Λ is zero, $k_1 = k_2$ and the interaction is isotropic while for non-zero Λ the interaction is anisotropic. Further restrictions may be imposed on the allowed values of Λ by consideration of the time reversal and hermiticity properties of the Hamiltonian together with the symmetry of the ion pair.

The effects of spin-orbit coupling can be accounted for by coupling the spin and orbital operators in (6.4) to produce effective operators $\hat{J}$ which act on the total angular momentum j of each ion. This leads to the Levy and Copland[90] Hamiltonian:

$$\mathcal{H}_{ex} = -\sum_{\Lambda m}\left\{\tfrac{1}{2}\Gamma_m^{(\Lambda)}(k_1k_2)\left[T^{(k_1)}(1)\times T^{(k_2)}(2)\right]_m^{(\Delta)}\right.$$

$$\left. + 2\sum_{r_1r_2}\Gamma_m^{(\Delta)}(r_1r_2)\left[\hat{J}^{(r_1)}(1)\times\hat{J}^{(r_2)}(2)\right]_m^{(\Lambda)}\right\} \qquad (6.6)$$

where $$\hat{J}^{(r)} = \left[T^{(k)}\times S^{(1)}\right]^{(r)} \qquad |k-1| \leqslant r \leqslant k+1 \qquad (6.7)$$

and $$\Gamma_m^{(\Lambda)}(r_1r_2) = (-1)^{k_1+r_2+\Lambda+1}([r_1][r_2])^{\frac{1}{2}}\begin{Bmatrix} k_1 & k_2 & \Lambda \\ 2 & 1 & 1 \end{Bmatrix}\Gamma_m^{(\Lambda)}(k_1k_2) \qquad (6.8)$$

The expression (6.6) has two parts. The first is a purely orbital term and arises because the factor ½ has been retained in the spin permutation operator. For the simple case of electrons with no orbital angular momentum this factor is frequently omitted since it merely shifts the centre of gravity of all levels equally and hence has no experimental significance. In general, however, this term produces an effective scalar contribution $j_1\cdot j_2$ to the exchange, in addition to that introduced through the usual spin dependent term. In this way the constant terms arising will be different for each j manifold and produce shifts in the relative positions of their centres of gravity causing apparent deviations from the Landé interval rule for exchange coupled ions. This point has been discussed in more detail by Levy and Copland[90,91].

The Levy and Copland Hamiltonian (6.4) is much too general for describing most experimentally observed situations. Even though symmetry requirements restrict the number of parameters, the number required to specify the exchange between

a pair of identical ions with axial symmetry is still very large. For this highest symmetry case the number of parameters required for s-electrons is 1, for p-electrons is 7, for d-electrons is 22, and for f-electrons is 50. Consequently, most experimental work to date has attempted to find realistic values for the single isotropic exchange constant $\mathcal{J}$, corresponding to $\Gamma_0^{(0)}(00)$ in Levy's notation. However, since systems with strong anisotropic exchange are more likely to lead to an understanding of the mechanisms of exchange interactions, efforts have been made to find values for the more dominant anisotropic exchange constants by choosing experimental systems requiring a minimum number of empirical parameters.

We will now consider two possible approaches for applying the above exchange interaction to the problem of exchange coupled cobalt ion pairs. These are the Real Spin Exchange and the Spin Hamiltonian Models which will be discussed in Sections 6.4 and 6.7 respectively.

6.4 REAL SPIN EXCHANGE MODEL

The number and frequencies of electronic lines due to cobalt ion pairs may be interpreted on the basis of adjacent single cobalt ions coupled by a Heisenburg exchange interaction. The total Hamiltonian for the pair is:

$$\mathcal{H} = \mathcal{H}_0(1) + \mathcal{H}_0(2) + \mathcal{H}_{12} \tag{6.9}$$

where $\mathcal{H}_0(1)$ and $\mathcal{H}_0(2)$ are the Hamiltonians of the two non-interacting single ions, given in Eqn (1.2). $\mathcal{H}_{12}$ is the exchange Hamiltonian between them and has the form:

$$\mathcal{H}_{12} = -J(\tfrac{1}{2} + 2S_1 \cdot S_2) \qquad (6.10)$$

where J is the isotropic exchange constant and S_1 and S_2 are the total real spins of the two ions. The states of the pair system are taken as product states $|\psi_1\rangle \cdot |\psi_2\rangle$ of the two single ions (1) and (2). Since all the observed transitions have frequencies less than 1100 cm^{-1} these pair states are formed by considering only those single ion eigenstates from among the six Kramers degenerate levels of the $^4T_{1g}(^4F)$ manifold. These are labelled $|i\rangle$, i = 0,11 as shown in Table 6-II.

TABLE 6-II

Labelling for the states of the $^4T_{1g}(^4F)$ manifold used in the real spin exchange model for Co^{2+} ion pairs

$\Gamma_7^+, \gamma_4^+ \pm \frac{1}{2}$	$\|11\rangle$
	$\|10\rangle$
$^{(2)}\Gamma_8^+, \gamma_{5,6}^+ \pm \frac{3}{2}$	$\|9\rangle$
	$\|8\rangle$
$^{(2)}\Gamma_8^+, \gamma_4^+ \pm \frac{1}{2}$	$\|7\rangle$
	$\|6\rangle$
$^{(1)}\Gamma_8^+, \gamma_4^+ \pm \frac{1}{2}$	$\|5\rangle$
	$\|4\rangle$
$^{(1)}\Gamma_8^+, \gamma_{5,6}^+ \pm \frac{3}{2}$	$\|3\rangle$
	$\|2\rangle$
$\Gamma_6^+, \gamma_4^+ \pm \frac{1}{2}$	$\|1\rangle$
	$\|0\rangle$

This gives 144 possible pair states $|ij\rangle$ i,j = 0,11. In principle, either ion may be excited but the resulting degeneracy will be lifted by off-diagonal transfer energy integrals which transfer the excitation from one ion to the other. The resulting states will be symmetric or anti-symmetric with respect to the permutation of the two ions. The number of magnetic-dipole (or electric-dipole) allowed transitions observed will not be increased by these transfer energy terms because the appropriate operator will only link symmetric with symmetric (antisymmetric) states respectively.

The energy transfer induced splittings are much smaller than the diagonal exchange splitting of a given product state. Consider the two states $|ab\rangle$ and $|ba\rangle$ which are appropriate for a cobalt ion pair with one ion in an excited state, denoted by a, and the other in the groundstate, denoted by b. The exchange interaction matrix between these states is:

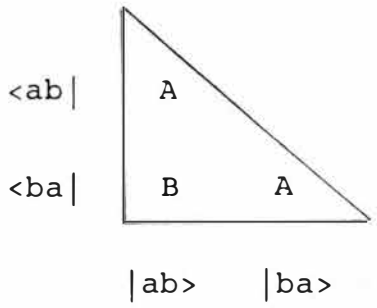

where A is the exchange splitting of each product state and B is the transfer excitation splitting.

This matrix has eigenvalues A±B with eigenvectors $\frac{1}{\sqrt{2}}\left[|ab\rangle \mp |ba\rangle\right]$. The values of A and B for the pair states $|91\rangle$ and $|19\rangle$ formed from the $|9\rangle$ and $|1\rangle$ levels of the $^4T_{1g}(^4F)$ manifold are A = 0.720J and B = 0.014J for the case of $CdCl_2(Co^{2+})$:5.0 wt.% crystals. Here, A = 50B so that the transfer energy splitting can be neglected to very good

approximation between product states |ab> and |ba>. Similar results are obtained for interactions between unlike states |ab> and |cd>, such as |91> and |45>. Hence, we may, with very little error, restrict our exchange splitting calculation to considering only those pair states in which the first ion is excited. Consequently, the basis set has been truncated to include only those 24 states in which ion (1) is excited and ion (2) remains in its groundstate. The resulting pair states are thus labelled |ij> with i = 0,11 and j = 0,1.

We need the matrix elements of the operator $(S_{1x}S_{2x} + S_{1y}S_{2y} + S_{1z}S_{2z})$ between these pair states. The matrix elements of $S_{1x}S_{2x}$ between each product state are obtained by considering the product of the matrix elements of S_{1x} and S_{2x}; each evaluated between the appropriate single ion states using their 120-dimension eigenvectors obtained in the single ion crystal-field analysis and the 120 x 120 dimension S_x matrix. The matrix elements of $S_{1y}S_{2y}$ are of the same magnitudes as those of $S_{1x}S_{2x}$ and so matrix elements of $S_{1x}S_{2x} + S_{1y}S_{2y}$ are either equal to twice those of $S_{1x}S_{2x}$ or zero (Appendix IV). The matrix elements of $S_{1z}S_{2z}$ are evaluated in a similar way to those of $S_{1x}S_{2x}$ and all matrix elements are listed in Appendices IV and V.

The total Hamiltonian used,

$$\mathcal{H} = \mathcal{H}_0 - J(\tfrac{1}{2} + 2[S_{1x}S_{2x} + S_{1y}S_{2y} + S_{1z}S_{2z}]) \qquad (6.11)$$

is diagonalised to give the exchange coupled ion energy level scheme.

To allow for the different orbital character of the parent single ion levels of the cobalt ion within the $^4T_{1g}(^4F)$ term, different values of J are used for the ground level product states, $|ij\rangle$ i,j = 0,1, and the optically observed excited states, $|ij\rangle$ i = 9,8,7,6 and j = 0,1. The Hamiltonian $\mathcal{H}_0$ relates to the position of the single ion levels for the particular cobalt doped crystal used and those obtained from a fitting of the spectra of cadmium-chloride (-bromide) crystals containing 5.0% by weight of cobalt were adopted. This takes account of the effects of the change in crystal dimensions on the single ion levels with the variation of cobalt concentration. However, these single ion levels will be further shifted by the lowering in symmetry of the local crystal-field caused by the presence of the neighbouring cobalt ion of the pair. This shift, can in principle, be estimated by examining the spectra of cadmium-chloride crystals containing 1.0 wt.% of cobalt and 4.0 wt.% of a non-magnetic ion with the same ionic radius as cobalt, such as zinc. The shift is the difference in position of the absorption lines due to cobalt-other ion pairs when compared to those of single cobalt ions. The spectra examined showed no distinct pair features but the asymmetric broadened cobalt single ion line-shapes gave an upper limit for the shifts of the levels of interest as +5 cm^{-1} for the $^{(2)}\Gamma_8^+,\gamma_{5,6}^+$ level and -3 cm^{-1} for the $^{(2)}\Gamma_8^+,\gamma_4^+$ level.

6.5 ZEEMAN SPLITTING OF THE PAIR STATES

Because of the symmetry of the exchange Hamiltonian (6.11) used, the magnetic properties of the ion pairs will be isotropic in the chlorine (bromine) plane, normal to the crystal c-axis. Hence, the splittings of the states in our model will not depend on the orientation of an in-plane external magnetic field with respect to the internuclear axes of the pairs. Accordingly, external magnetic fields, parallel and perpendicular to the c-axis may be characterised as H_z and H_x respectively. The Hamiltonian describing the splitting of pair levels for a magnetic field H orientated at θ degrees to the c-axis is given as:

$$\mathcal{H} = \mathcal{H}_0 - J(\tfrac{1}{2} + 2S_1 \cdot S_2) + \beta H_z[(kL_{1z} + 2S_{1z}) + (kL_{2z} + 2S_{2z})]$$
$$+ \beta H_x[(kL_{1x} + 2S_{1x}) + (kL_{2x} + 2S_{2x})] \qquad (6.12)$$

where $H_z = H \cos\theta$ and $H_x = H \sin\theta$, β is the Bohr magneton, and the other factors are defined in Chapter II. The required matrices of L_x, S_x, L_z and S_z are generated in an identical manner to those for the exchange interaction $\mathcal{H}_{12}$ and then the summed matrix elements are diagonalised within the same pair-states for specific field-strengths and -orientations.

6.6 RESULTS

Polarised infrared absorption spectra were recorded for temperatures of 78, 30, 15 and 5°K in the region 800-1050 cm^{-1}. The results for each crystal are listed below.

6.6.1 $\underline{CdCl_2(Co^{2+}):5.0\ wt.\%}$

The main spectral features observed are depicted in Figure 6-3.

The 30°K σ-polarisation spectra show electronic lines at 903, 920.5, 930, 934, 948.5 (v. weak), 965 and 972 cm^{-1}. Corresponding lines in the π-polarisation spectra were recorded at frequencies of 903, 920.5, 934, 948.5 and 965 cm^{-1}. The appearance of the line at 948.5 cm^{-1} as a weak remnant in the σ-polarisation spectra is caused by possible slight mis-orientation of the crystal or possible depolarisation due to the optically active nature of the crystal itself. On cooling to 15°K, all lines show small shifts to lower frequencies and are also more clearly resolved. For the lowest crystal temperature of 5°K, additional "pair-lines" can be discerned at 926 and 937 cm^{-1} in the σ-polarisation spectra. The other prominent pair features have frequencies of 932.0, 964.0 and 971.0 cm^{-1}. The lines at 903 and 930 cm^{-1} have a common interval of 34 cm^{-1} from the lines at 937 and 964.0 and though readily visible at 30°K, are absent from all spectra recorded at 5°K.

In the vibronic spectra the lines at 993, 1006, 1023, 1033 and 1041 cm^{-1} all share a common vibronic interval of 73 cm^{-1} from their electronic parents at 920.2, 932, 948.3, 964.0 and 971 cm^{-1} while traces of the difference bands at 852, 863, 882 and 892 cm^{-1} are visible in the 30°K spectra.

As can be seen, the absorptions due to cobalt ion pairs fall into two distinct groups, each being associated with one of the single cobalt ion electronic transitions. The lines at 964.0 and 971 cm^{-1} come from the shifted and exchange split

Figure 6-3: Polarised infra-red spectra of $CdCl_2$(Co):5.0wt% recorded at 30,15 and 5°K between 875 and 1075 cm^{-1}. π and σ polarised spectra appear on the LHS and RHS respectively.

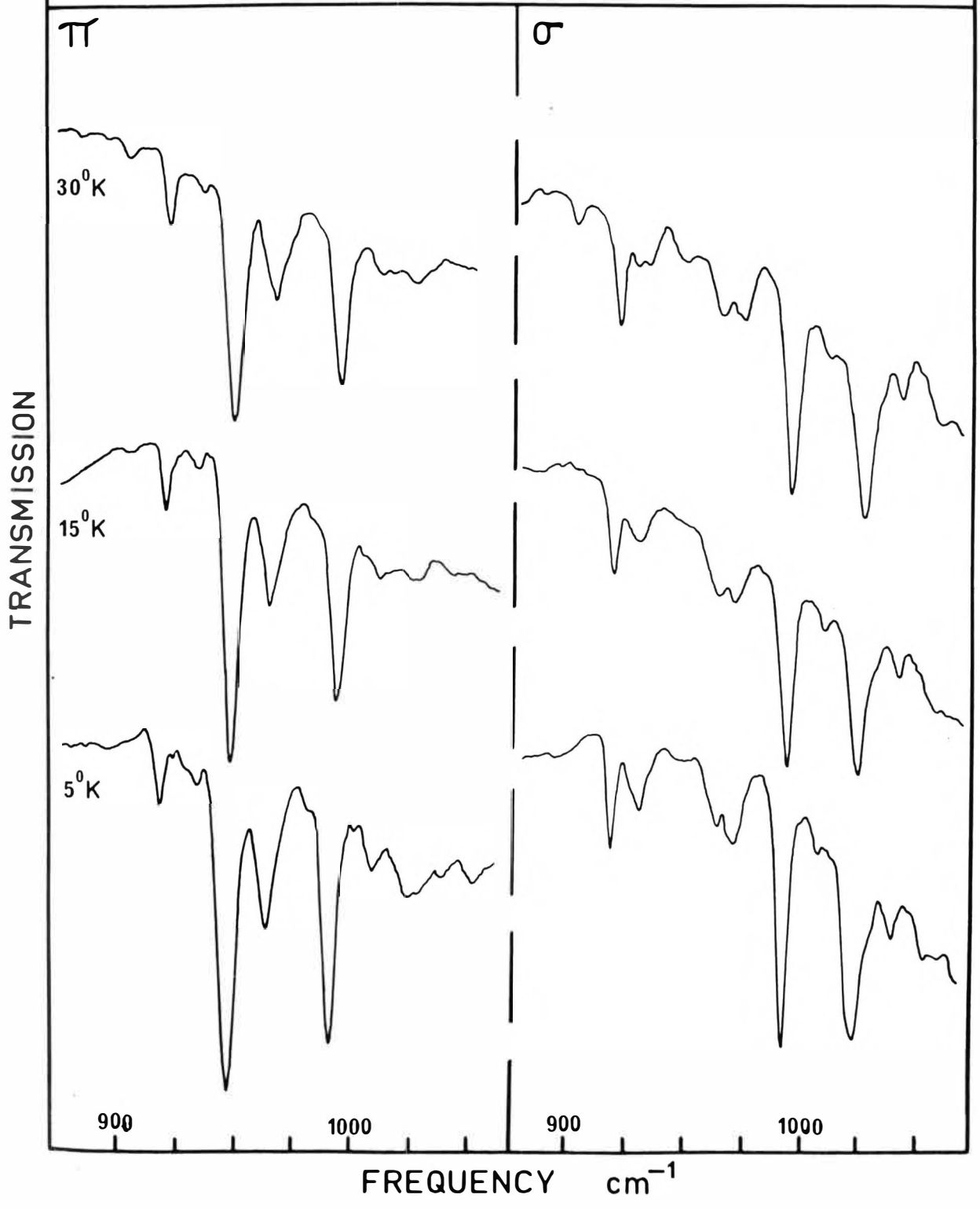

$|\Gamma_6^+\gamma_4^+> \rightarrow |^{(2)}\Gamma_8^+,\gamma_{5,6}^+>$ transitions of each ion. Although the 7 cm^{-1} splitting between these lines is small it can be resolved by the different polarisation of the two components. Both the levels are higher in energy than the parent single ion level at 948.3 cm^{-1} since they are shifted upwards by an amount determined by the splitting of the $|\Gamma_6^+\gamma_4^+>$ level and are also repelled by the adjacent levels of slightly lower energy.

Similarly, the lines at 926, 932 and 937 cm^{-1} are associated with the single ion transition $|\Gamma_6^+\gamma_4^+> \rightarrow |^{(2)}\Gamma_8^+,\gamma_4^+>$ at 920.2 cm^{-1}. For these, the degree of splitting is much larger than for the upper levels and is approximately symmetric about the central line at 932 cm^{-1}. The line at 926 cm^{-1} is not very distinct and could be confused with the envelope of the single ion level at 920.2 cm^{-1}. However, an analogous and distinct line has been observed at 926 cm^{-1} in crystals containing 1.0 wt.% of cobalt and 4.0 wt.% of manganese. The resulting energy scheme for both the ground and these upper levels is given in Figure 6-5.

Analysis of the hot band spectra shows that the lines at 903 and 930 cm^{-1} are due to transitions from a thermally populated electronic level at 34 cm^{-1} which is assigned to be the uppermost component of the exchange split ground state of the pair system (Figure 6-5). In an attempt to see this transition directly the axial far infrared spectra of $CdCl_2(Co^{2+})$:0,2.5,5.0 and 10.0 wt.% crystals were studied in detail by Dr John Campbell of this department, while at Cornell. These spectra showed no trace of the line at 34 cm^{-1} but did reveal a strong line at 8.55 cm^{-1} which was not present

Figure 6-4: Far infra-red spectrum of $CdCl_2$(Co): 10.0wt% showing the position and magnetic field dependence of the cobalt pair line at 8.55 cm^{-1}. Spectra were recorded at 1.2°K for magnetic fields of 0-60 kG aligned at approximately 45° to c-axis by Dr J.A. Campbell of this department, while at Cornell University.

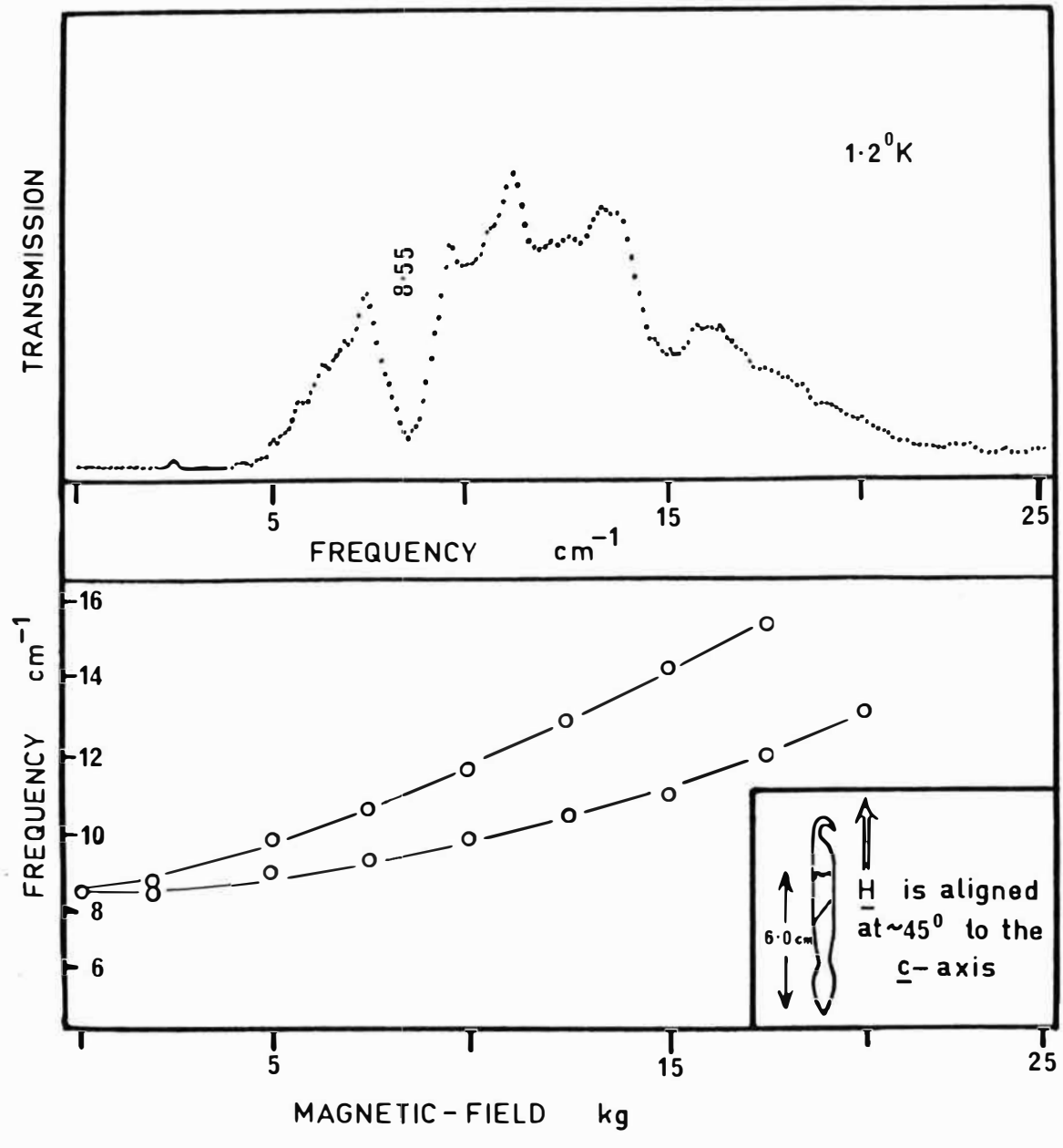

in spectra of either the pure lattice or lightly doped crystals. Further, in the presence of a magnetic field this line split with a g-factor equal to twice that of the single ion Kramers groundstate (Figure 6-4). Hence, the line was assigned to be the doublet of the exchange split groundstate. The search for these two lines, at 34 and 8.55 cm^{-1}, required crystals of differing thicknesses. Although crystals typically 6.0 cm thick could be used for energies below 20 cm^{-1}, above this the intense restrahlen absorption necessarily limited crystal thicknesses to less than 5.0 mm. Therefore, it is possible that the 34 cm^{-1} line is too weak to be observed for crystal specimens which are so thin.

This experimental data was then fitted, within the assumptions of the model outlined in Section 6.4, using a separate isotropic exchange parameter J for the excited and ground pair levels and allowing for the pair induced shift in the parent single ion levels. The resulting calculated energy level scheme is shown in Figure 6-5. The values of the isotropic exchange parameters which best reproduced the experimental splittings are listed below. For the groundstate, $J = 5.0 \pm 0.1$ cm^{-1} while for the excited states J has a magnitude of 2.6 ± 0.3 cm^{-1} together with single ion level shifts of +4.0 cm^{-1} for the $(^{(2)}\Gamma_8^+, \gamma_{5,6}^+)$ level and -2.0 cm^{-1} for the neighbouring $(^{(2)}\Gamma_8^+, \gamma_4^+)$ level. The sign of the exchange parameter for the groundstate indicates that the exchange interaction between these states is ferromagnetic which is consistent with the in-plane, nearest neighbour, ferromagnetic exchange interactions that exist for $CoCl_2$ and $CoBr_2$. The sign of the exchange parameter for the excited

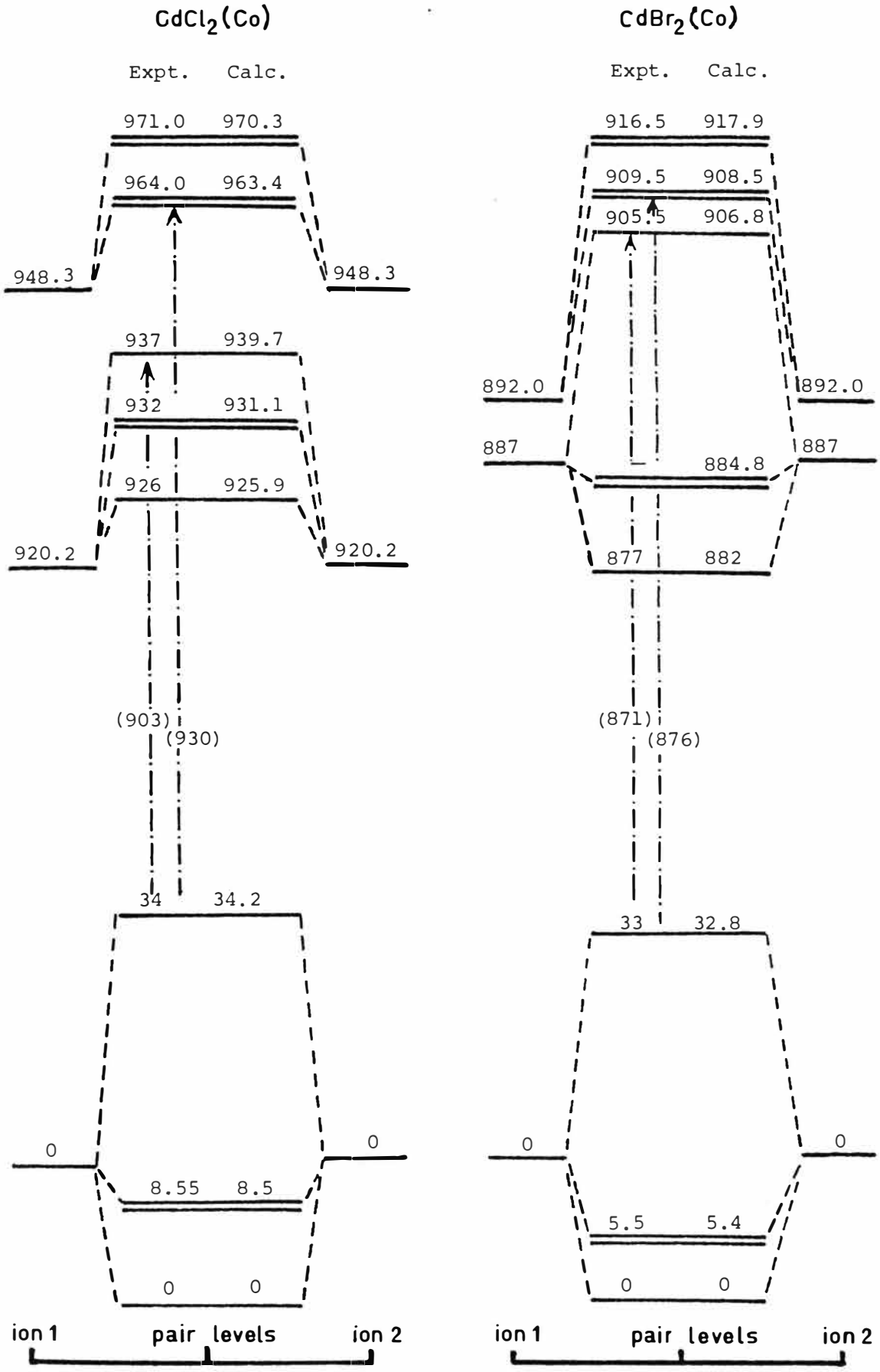

Figure 6-5: Calculated and observed energy levels for an exchange coupled Co^{2+} ion pair in $CdCl_2$ and $CdBr_2$ crystals.

Figure 6-6: Predicted Zeeman splittings of observed pair lines for fields parallel and perpendicular to the c-axis.

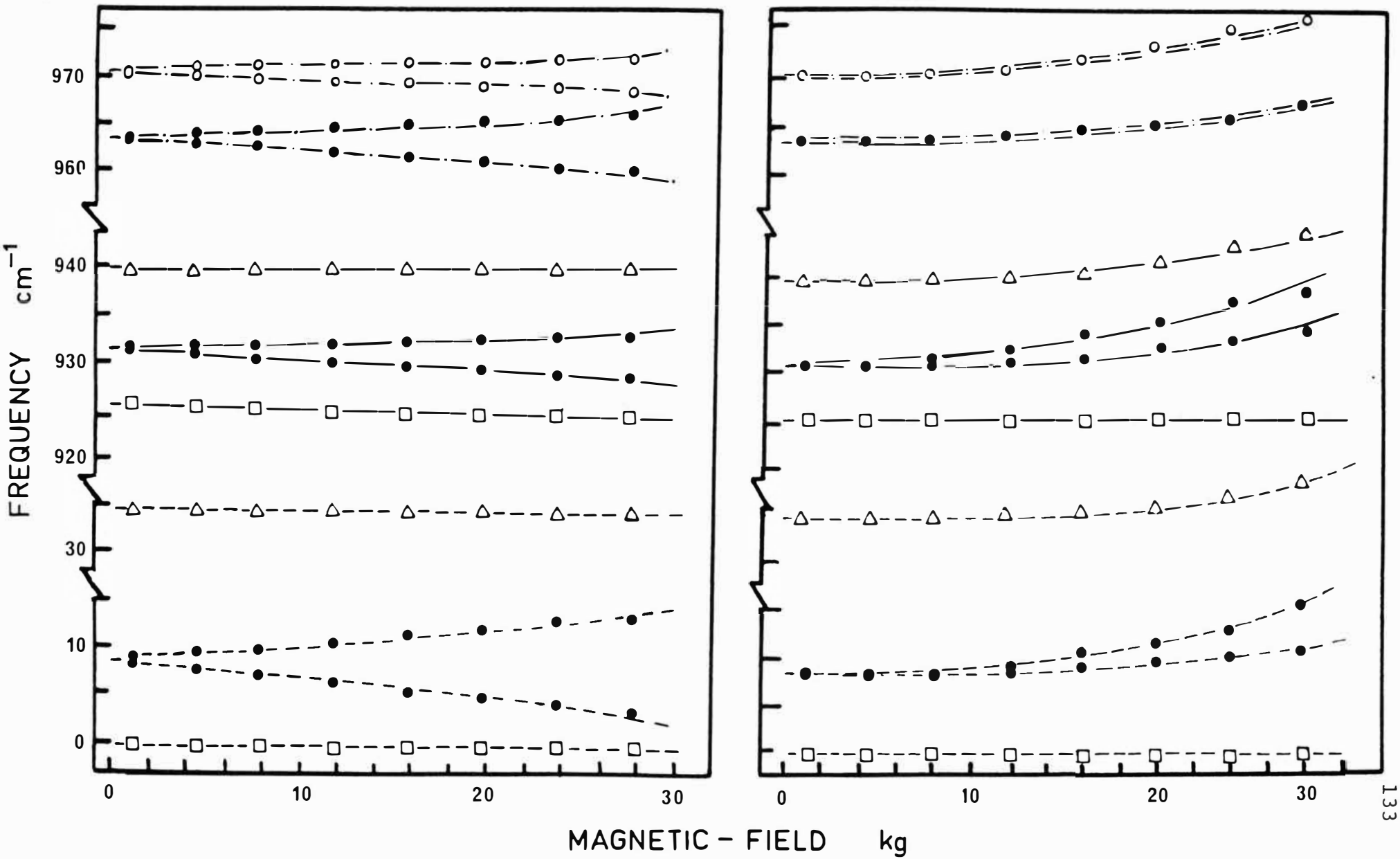

states can not be determined without knowledge of their magnetic-field dependence.

The predicted Zeeman splittings of all observed lines is plotted in Figure 6-6 for fields parallel and perpendicular to the crystal c-axis.

6.6.2 $CdBr_2(Co^{2+})$:5.0 wt.% .

The main features observed are shown in Figure 6-7. As noted earlier, all absorption lines are narrower and slightly weaker than for the corresponding $CdCl_2(Co^{2+})$ spectra and appear to be more complex with some superimposed lines.

At 30°K, electronic lines with σ-polarisation were measured with frequencies of 877, 888, 893 (v.weak), 909, 917 (barely resolved) and 928 cm^{-1} while for π-polarisation spectra corresponding lines were noted at frequencies of 871, 876, 888, 893, 905.5 and 929 cm^{-1}. Of these, the single ion lines at 887 and 893 cm^{-1} are the analogues of the lines at 920.2 and 948.3 cm^{-1} in the chlorides and have symmetries of $|^{(2)}\Gamma_8^+,\gamma_4^+>$ and $|^{(2)}\Gamma_8^+,\gamma_{5,6}^+>$ respectively. With the exception of the line at 928 cm^{-1}, the others are assigned to levels associated with cobalt ion pairs. Because the intensity of the 928 cm^{-1} line has a higher than quadratic dependence with cobalt concentration it is associated with a higher order cobalt ion cluster (Figure 6-8).

At 15°K, the weak line at 871 cm^{-1} is absent while the line at 877 cm^{-1} sharpens markedly, especially for σ-polarisation spectra and effectively masks the behaviour of the line at 876 cm^{-1} for this polarisation. A common interval of 33 cm^{-1} can be deduced for the separation of the lines at 905.5 and 871 cm^{-1} together with the pair at 909.5 and 876 cm^{-1}

Figure 6-7: Polarised infra-red spectra of $CdBr_2$(Co):5.0wt% recorded at 78, 30, 15 and 5°K between 800 and 1000 cm^{-1}. π and σ polarised spectra appear on the LHS and RHS respectively.

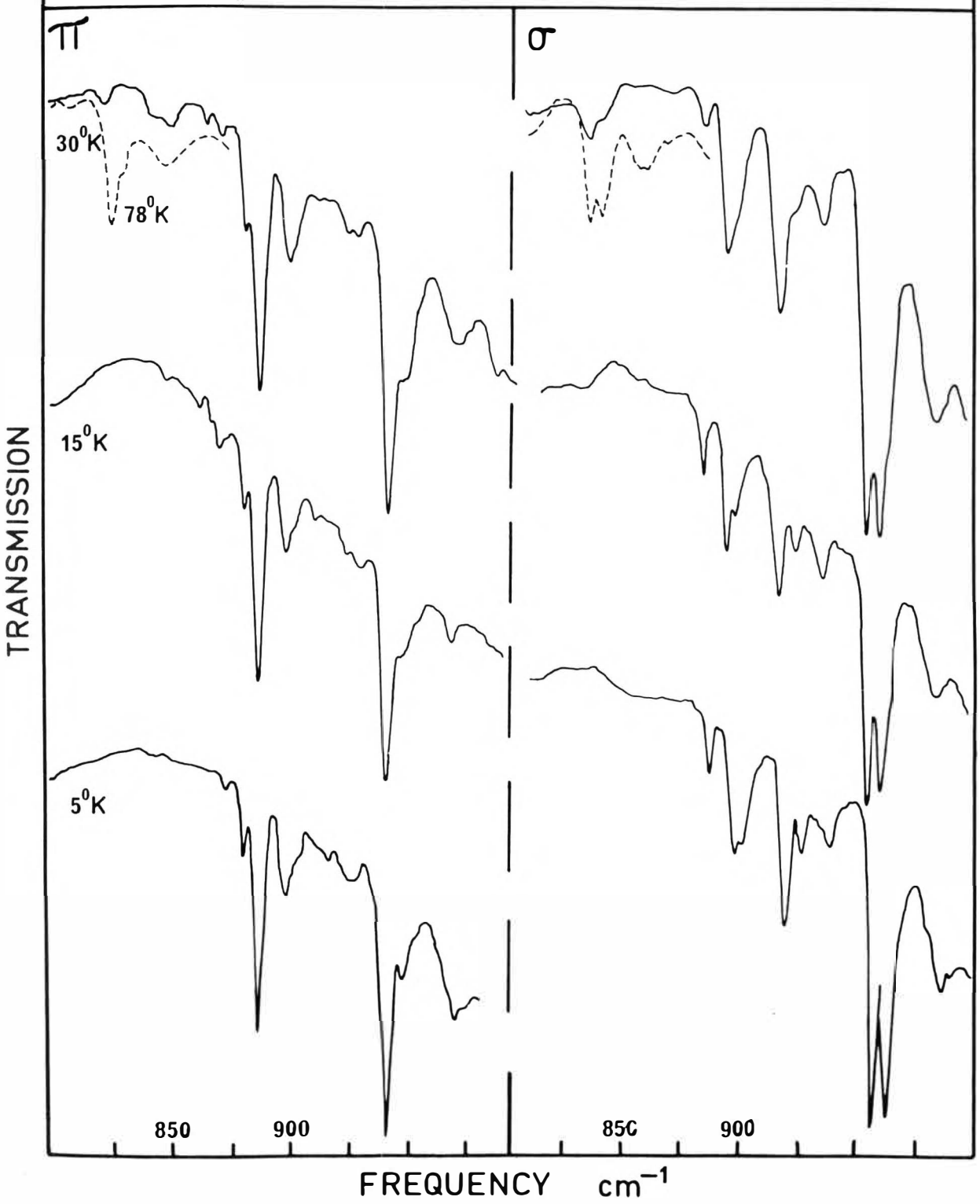

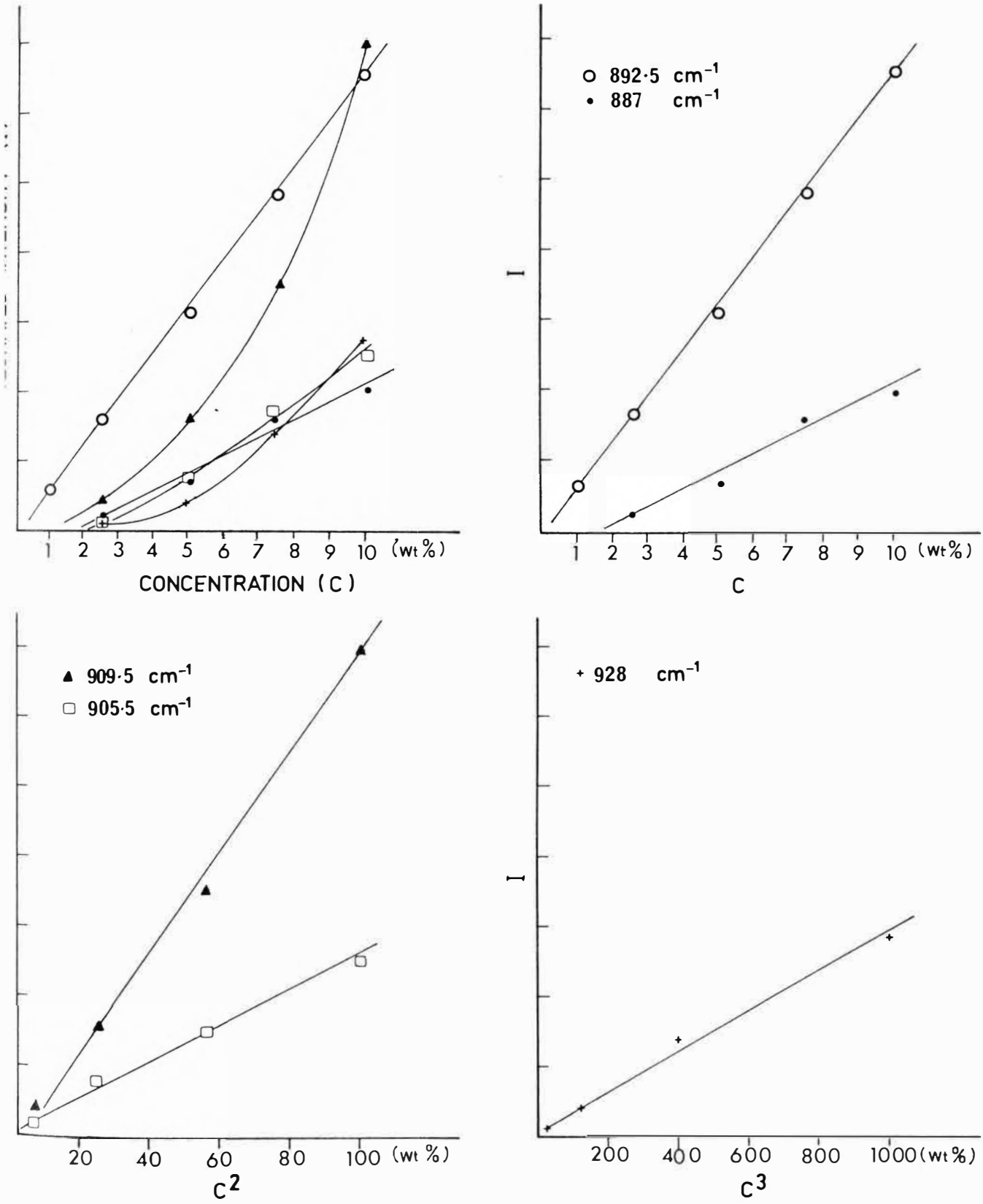

Figure 6-8: Cobalt concentration dependence of the electronic lines in the infra-red spectra of $CdBr_2$(Co) crystals.

in analogy with the corresponding line-pairs at 937 and 903 cm^{-1} and at 930 and 964.0 cm^{-1} in the chloride. For the lowest temperature of $5^{o}K$ the previous asymmetry of the line at 887 cm^{-1} in σ-polarisation is resolved to give a small shoulder at ~891 cm^{-1} which is a polarisation remnant, while the line at 928 cm^{-1} also shows a small shoulder, but on its low frequency side.

The lines at 936, 946.6, 952.7, 970 and ~976 cm^{-1} all have a common vibronic interval of 60 cm^{-1} from the no-phonon lines at 877, 887, 892.0, 909.5 and 916.5 cm^{-1}. The observation of the last two vibronics is hampered by the proximity of the broad vibronic band centred at 1090 cm^{-1}. The corresponding vibronic difference lines may be just discerned in the $30^{o}K$ spectra as two bands: one with components at 828 and 832 cm^{-1} and the other with peaks at 846, 851 (v. weak) and 856 cm^{-1}.

Unlike the pair spectra of $CdCl_2(Co^{2+})$, it is not immediately obvious which pair absorptions in the bromide are to be associated with which of the two single ion levels at 887 and 892.0 cm^{-1}. A possible splitting pattern was obtained by decreasing the separation of the single ion levels at 920.2 and 948.3 cm^{-1} in the chloride from 28 cm^{-1} to the separation of the bromide (5.0 cm^{-1}) and monitoring the change in the energy levels. As can be seen in Figure 6-9, a cross-over of levels occurs for a separation of 4 cm^{-1} but above this the pattern remains distinct. This procedure assumes that the same value of J is appropriate for both the chloride and bromide which is not fully justified in regard to the following. The observation of the level at 877 cm^{-1}, below its single-ion parent, requires that the exchange interaction

Figure 6-9: Predicted energy level scheme for the upper exchange split states of $CdBr_2(Co)$.

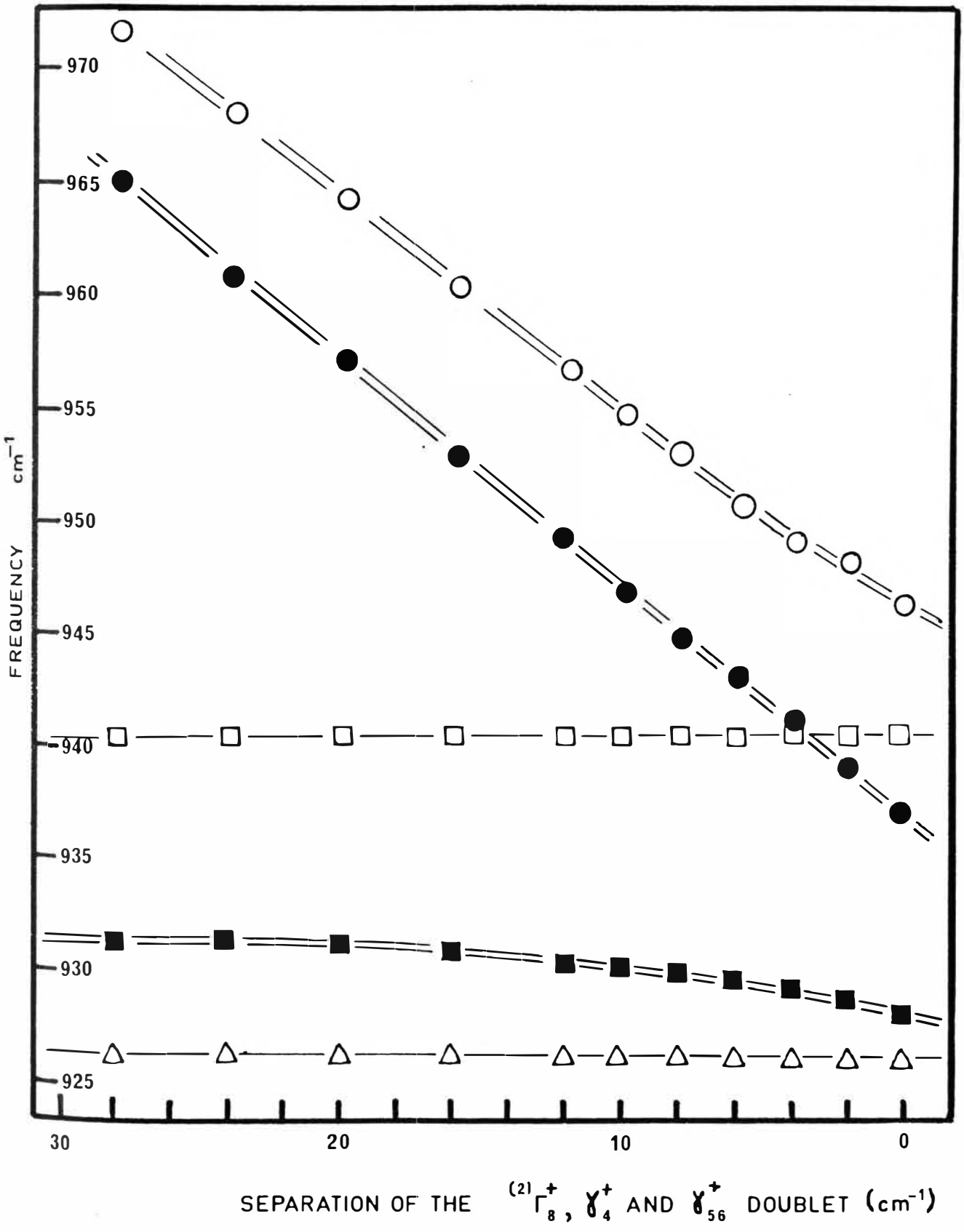

is much larger for the bromide than the chloride for these excited levels. This would certainly modify the splitting pattern predicted above.

With the splitting pattern to be expected approximately established the chloride and bromide spectra can now be usefully compared. The common polarisation properties of some of the lines in both spectra suggest their possible assignments. For $CdCl_2(Co^{2+})$ the line at 971 cm^{-1} is only visible for σ-polarisation and has comparable intensity with its neighbour at 964.0 cm^{-1} which in turn dominates completely in the π-polarisation spectra. The analogous lines in the $CdBr_2(Co^{2+})$ spectra are those at 916.5 and 909.5 cm^{-1} respectively and are therefore assigned to the shifted and exchange split single ion $|\Gamma_6^+\gamma_4^+> \rightarrow |^{(2)}\Gamma_8^+\gamma_{5,6}^+>$ transition of the cobalt ion pair. Similarly the analogues of the lines at 937 and 926 cm^{-1} have energies of 905.5 and 877 cm^{-1} in the bromide with the 877 cm^{-1} line completely resolved and below its single ion parent. However, there is no resolvable feature which corresponds to the line at 932 cm^{-1} and it is therefore assumed any such absorption is buried within the asymmetric envelope of the single ion level at 887 cm^{-1}.

Analysis of the hot band spectra is complicated by the closer proximity of the difference vibronic bands for this crystal. (Figure 6-7). However, the lines at 871 and 876 cm^{-1} are assigned to be electronic transitions from the uppermost component at 33 cm^{-1} of the exchange split groundstate. As yet no far infrared spectra of $CdBr_2(Co^{2+})$ have been recorded. The existing data was fitted, as for the chloride, and the resulting energy level scheme is shown in Figure 6-5.

The values of the isotropic exchange parameters which gave the closest agreement with observed levels are given below. For the groundstate J = +5.2±0.1 cm^{-1} which corresponds to ferromagnetic exchange. The excited states could only be fitted with J's of equal magnitude, but of opposite sign with $J(^{(2)}\Gamma_8^+, \Upsilon_4^+)$ = -5.3±0.3 cm^{-1} and $J(^{(2)}\Gamma_8^+, \Upsilon_{5,6}^+)$ = +5.3±0.3 cm^{-1} with single ion level shifts of +0.5 and -3.0 cm^{-1} for the $(^{(2)}\Gamma_8^+, \Upsilon_{5,6}^+)$ and $(^{(2)}\Gamma_8^+, \Upsilon_4^+)$ levels respectively.

The model predicts a lowest lying doubly degenerate level at 5.4 cm^{-1} which corresponds to the line already observed at 8.55 cm^{-1} in $CdCl_2(Co^{2+})$. Such a level has been previously reported by Bailey et al.[79] from consideration of the hot band spectra associated with transitions to the $^2T_{1g}(^2H)$ levels in the optical region of the spectrum. Discussion of these results in relation to the theoretical results predicted here is left to Section 6.8.

6.6.3 Summary

As can be seen, the real spin exchange model is successful in reproducing the observed energy level splitting pattern for $CdCl_2(Co^{2+})$ and $CdBr_2(Co^{2+})$ using a minimum number of parameters. For $CdCl_2(Co^{2+})$, the hot level at 34 cm^{-1} was fitted exactly using the ground isotropic exchange parameter J which also fixed the position of the 8.5 cm^{-1} level, independent of the experiments at Cornell (Section 6.6.1). Similarly, the level predicted at 5.4 cm^{-1} for $CdBr_2(Co^{2+})$ has been observed at 5.5 cm^{-1} [79]. The fitting of the excited levels is also very good. In particular, for the chloride where the splittings are more distinct the agreement between

calculated and observed levels is excellent. Because the polarisation and splitting of the lines in the bromide are not so clear the fitting for this crystal is not as precise. The assignment of levels for both crystals may be checked by their magnetic-field dependence which should be consistent with that predicted using the Hamiltonian described in Section 6.5. The main advantage of using such a model is that it is purely isotropic and there is no need to introduce any additional anisotropic exchange parameters to reproduce the spectrum, unlike the more usual Spin Hamiltonian approach used by Bailey et al.[79] and discussed in the next section.

6.7 SPIN HAMILTONIAN MODEL

The theory of the Spin Hamiltonian, when applied to the problem of exchange coupled ions has been well established[92]. The levels of each single ion are characterised by an effective, or pseudo spin and the interaction between them by the general anisotropic exchange Hamiltonian:

$$\mathcal{H}_{12} = -2\mathcal{J}(S_1 \cdot S_2) + D(3S_{1z}S_{2z} - S_1 \cdot S_2) + E(S_{1x}S_{2x} - S_{1y}S_{2y}) \qquad (6.13)$$

When the interaction is anisotropic but axially symmetric, E is zero while for any isotropic exchange interaction both D and E are zero.

For an ion pair the basis states are taken as the product states of the single ion wavefunctions which are expressed in terms of the z-component of the effective spin. Hence, the general product state has the form $|m_s(1)m_s(2)>$ for the two ions (1) and (2).

For the case of two cobalt ions in their groundstates each ion has an effective spin of $+\frac{1}{2}$, which is appropriate for an isolated Kramers degenerate level, and there are four basis states $|\pm\frac{1}{2}\ \pm\frac{1}{2}\rangle$ for the pair. The exchange interaction between the ions is given by:

$$\mathcal{H}_{12} = -2J(S_1 \cdot S_2) \tag{6.14}$$

$$= -2J_{\parallel} S_{1z} S_{2z} - J_{\perp}(S_{1+}S_{2-} + S_{1-}S_{2+}) \tag{6.15}$$

where $J_{\parallel}$ and $J_{\perp}$ may differ for anisotropic exchange interactions. The 4×4 energy matrix is given in Table 6-III together with the resulting eigenvalues and eigenvectors. For the case of isotropic exchange, $J_{\parallel} = J_{\perp}$ and there are three levels at $-J_{\parallel}/2$ with one level at $3J_{\parallel}/2$ corresponding to total spins of S = 1 and S = 0 for the pair. Other splitting patterns are possible when $J_{\parallel} \neq J_{\perp}$ as shown below:

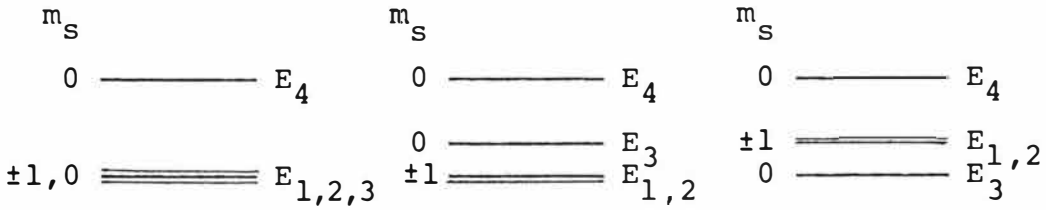

(i) isotropic, $J_{\parallel} = J_{\perp}$ (ii) anisotropic, $J_{\parallel} > J_{\perp}$ (iii) anisotropic $J_{\parallel} < J_{\perp}$.

When one of the cobalt ions is in an excited state the pair states have the form $|m_s(1)\ \pm\frac{1}{2}\rangle$. Observed transitions are to the excited states arising from the $^{(2)}\Gamma_8^+$ quartet single ion parent which are described by an effective spin S = 3/2. The γ_4^+ and $\gamma_{5,6}^+$ components correspond to states with m_s values of ± 1/2 and ± 3/2 respectively. The matrices of the exchange

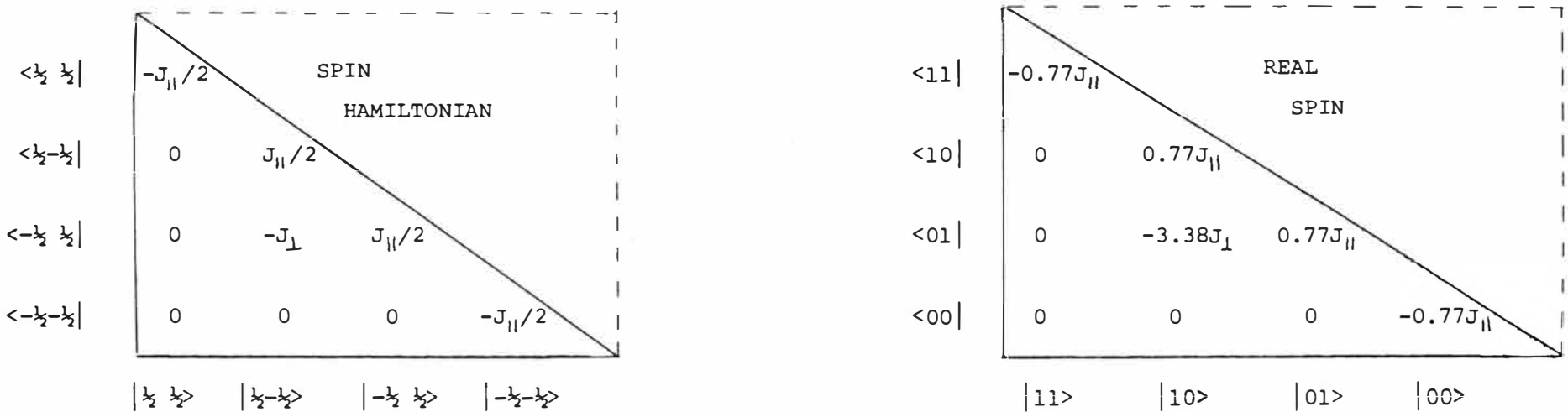

$(S=0, M_S=0)\, E_4,\ 3J_{\parallel}/2$ ——— $\frac{1}{\sqrt{2}}\{-|\tfrac{1}{2}\text{-}\tfrac{1}{2}\rangle + |\text{-}\tfrac{1}{2}\ \tfrac{1}{2}\rangle\}$

$\left(S=1, M_S=\begin{matrix}1\\0\\-1\end{matrix}\right)\begin{matrix}E_2\\E_3\\E_1\end{matrix}$ $-J_{\parallel}/2$ ═══ $\frac{1}{\sqrt{2}}\{\begin{matrix}|\text{-}\frac{1}{2}\text{-}\frac{1}{2}\rangle\\ |\ \frac{1}{2}\text{-}\frac{1}{2}\rangle\\ |\ \frac{1}{2}\ \frac{1}{2}\rangle\end{matrix} + |\text{-}\tfrac{1}{2}\ \tfrac{1}{2}\rangle\}$

$E_4, 4.15J_{\parallel}$ ——— $\frac{1}{\sqrt{2}}\{-|10\rangle+|01\rangle\}$

$\begin{matrix}E_2\\ 1\end{matrix}, -0.77J_{\parallel}$ ═══ $\begin{matrix}|00\rangle\\ |11\rangle\end{matrix}$

$E_3, -2.61J_{\parallel}$ ——— $\frac{1}{\sqrt{2}}\{|10\rangle+|01\rangle\}$

TABLE 6-III. Comparison of the spin Hamiltonian and real spin exchange models. The matrix elements, eigenvalues and eigenvectors are evaluated using eqn (6.14) with $J_{\parallel} = J_{\perp}$ (cm^{-1}).

interaction among these states have been given by Bailey et al.[79]. For an anisotropic exchange interaction with $J_{\parallel} \neq J_{\perp}$ the energy level scheme obtained is the same as that obtained using the purely isotropic real spin exchange model (Figure 6-5). It is also necessary to use an anisotropic exchange spin Hamiltonian to fit the available data for the lowest lying pair levels in $CdCl_2(Co^{2+})$. In particular, the levels at 34 and 8.55 cm^{-1} can be reproduced using the parameters, $J_{\parallel} = 8.5$ and $J_{\perp} = 17.0$ cm^{-1}.

This difference between the two models may be demonstrated by comparing the matrix elements of the exchange interaction (6.14) between the four lowest pair states. The matrices are given in Table 6-III. When $J_{\parallel} = J_{\perp}$ the spin Hamiltonian reproduces the singlet and triplet pattern as outlined above since the off-diagonal induced splitting is exactly twice the magnitude of the diagonal matrix elements. For the real spin exchange model the diagonal and off-diagonal matrix elements are unrelated and instead a degenerate doublet at $-0.77J_{\parallel}$ is obtained together with two singlets with energies $0.77J_{\parallel} \pm 3.38J_{\parallel}$. Thus, a similar pattern may only be reproduced if an anisotropic spin Hamiltonian is used with $J_{\parallel} < J_{\perp}$.

The spin Hamiltonian formalism has been applied with some success to the spectra of cobalt in cadmium-bromide crystals by Bailey et al.[79]. Their analysis of the results obtained and its relevance to this work will now be discussed.

6.8 THE RESULTS OF BAILEY ET AL. FOR $CdBr_2(Co^{2+})$ CRYSTALS

Bailey et al.[79] have reported the polarised absorption spectra of crystals doped with varying concentrations of cobalt in the region near 17700 cm^{-1}. The Zeeman and Magnetic Circular Dichroism (M.C.D.) spectra of the lines, for magnetic-fields applied parallel and perpendicular to the crystal c-axis, were also recorded. Two sharp zero phonon lines were identified as being due to isolated cobalt ions and assigned to be the $\pm\frac{1}{2}$ and $\pm\frac{3}{2}$ components of the U_g (Γ_8^+ in our notation) $^2T_{1g}(^2H)$ term. Two additional sharp lines were observed in the more concentrated crystals and were attributed to ferromagnetically coupled, in-plane cobalt ion pairs. One of the pair lines, at ~17714 cm^{-1} (their line 4), had a marked temperature dependence indicating an exchange splitting of 5.5 cm^{-1} among the lowest lying states of the pair. Since the groundstate of the single ion is characterised by an effective spin of +½ the lowest energy levels are as outlined in the previous section. The predicted splitting of 5.5 cm^{-1} is small in comparison with the isotropic exchange parameters for cobalt compounds which are between 14[19] and 20[93] cm^{-1} for $CoCl_2$ and approximately 10 cm^{-1} for $MgF_2(Co^{2+})$[94]. On this basis, Bailey et al. assigned the 5.5 cm^{-1} to be the anisotropic exchange splitting of the S = 1, M_S = ±1 and M_S = 0 levels (Table 6-III). The order of levels was determined from the temperature dependence of the M.C.D. spectra which predicted the S = 1, M_S = ±1 level to be the groundstate with the S = 1, M_S = 0 level 5.5 cm^{-1} above it. The position of the uppermost ground level was left undetermined.

With these assignments Bailey et al. have interpreted the Zeeman and exchange splittings of the excited levels of the U_g $^2T_{1g}(^2H)$ term. Several empirical spin Hamiltonians are introduced, with varying success, to assign these levels and their Zeeman splittings for specific choices of parameters. However, the number of parameters (5) used in relation to the available data is large.

For the groundstate, the assignment of the S = 1, $M_S = \pm 1$ doublet as lowest in energy is in conflict with our results. Our justification for fixing the doublet above the S = 1, $M_S = 0$ level is based on the far infrared spectra of $CdCl_2(Co^{2+})$ crystals. The results show a level at 8.55 cm^{-1} which is definitely degenerate since it has a clearly defined Zeeman splitting pattern for magnetic fields parallel to the c-axis and has a g-factor twice that of the single ion. Also, at 1.2°K there is no evidence of thermal depopulation of the lower component as the field is increased to a maximum of 60 kG. This data has been fitted using a real spin exchange model and for similar parameters the energy matrices appropriate to $CdBr_2(Co^{2+})$ gave a corresponding level at 5.4 cm^{-1}. An inversion of levels is not possible without using an anisotropic exchange interaction and is unlikely for a crystal which is isomorphic to $CdCl_2(Co^{2+})$.

Bailey et al. support their assignments by citing the temperature dependence of the M.C.D. spectra. However, the evidence is not conclusive since the spectra may equally support the assignment of the S = 1, $M_S = \pm 1$ doublet to be 5.5 cm^{-1} above the groundstate. This is because at the magnetic-field strength used, the splitting of the 5.5 cm^{-1}

level is sufficiently large to cause a cross-over of levels which is equally likely to give rise to the observed M.C.D. spectra. In particular, for a field of 47 kG and a ground-state single ion $g_{\parallel}$ value of 3.74 (Table 4-VI) the 5.5 cm^{-1} ($S = 1$, $M_S = \pm 1$) doublet splits to give two new components at 5.5 ± 8.2 cm^{-1}. At 15°K, the population ratio for the upper versus lower component is 0.28, which is very close to the degree of asymmetry in the given M.C.D. spectra. At 4.5°K, this ratio is 0.01 which implies there should be no transitions from the upper component. The lower one will, however, become more populated upon crossing the ($S = 1$, $M_S = 0$) ground level and thereby exhibit strong M.C.D. signals. No M.C.D. signal will be observed from the $S = 1$, $M_S = 0$ groundstate. This behaviour could equally well explain Bailey et al.'s spectra.

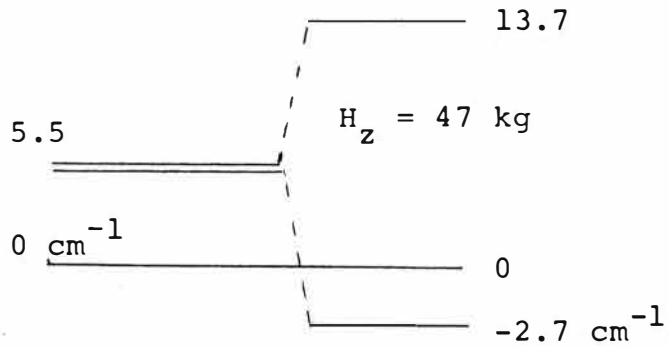

Further, Bailey and co-workers note that "hot band F moves to the red at $H_{\perp}$ = 45 kG so that the groundstate level from which it originates has moved up by 4-5 cm^{-1}". They maintain that this could only occur if the level concerned was the $S = 1$, $M_S = 0$ component of the groundstate. If instead this level is replaced by the $S = 1$, $M_S = \pm 1$ doublet, as in our assignment, it will exhibit a second-order splitting in the field and move upwards while the lowest $S = 1$, $M_S = 0$ level will be depressed in energy. Hence, the behaviour of the band F is not critically dependent on which of the two levels is assigned to be 5.5 cm^{-1} above the groundstate for

the pair.

In the light of our reservations as to Bailey et al.'s assignment of the order of the ground exchange split levels and the revised single ion $g_{\parallel}$ and $g_{\perp}$ values for $CdBr_2(Co^{2+})$ it would be useful to reinterpret their data. It is expected that an equally satisfactory fitting would be obtained. To resolve the assignment of the lowest levels it would be desirable to observe the 5.5 cm^{-1} level directly as a feature of the far-infrared spectrum of $CdBr_2$ doped with a high concentration of cobalt. It would also be preferable to use the real spin exchange model in any reinterpretation of the optical spectra. However, in our crystal-field calculation there are several Γ_8^+ quartet levels in the 18,000 cm^{-1} region which are possible candidates for the levels identified as belonging to the $^2T_{1g}(^2H)$ term by Bailey et al. No reliable crystal-field splitting of any of these Γ_8^+ quartets can be obtained for the same set of parameters used for the calculation of the levels of the $^4T_{1g}(^4F)$ cubic-field ground term. In particular, splittings of 56, 74, 28, 46 and 51 cm^{-1} are obtained. These may be compared with the 6 cm^{-1} splitting reported by Bailey et al. The position of the centre of gravity of a particular term is determined by the particular choice of parameters Δ, B and C. Since the splitting of the $^4T_{1g}(^4F)$ multiplet is virtually independent of all of these parameters, a re-fitting of the optical absorption spectra of the crystals could yield a set which would accurately match the position of the particular doublet required without altering the energies of the $^4T_{1g}(^4F)$ levels. With this term fitted exactly, one would have realistic wavefunctions with

which to interpret the spectra. A preliminary study shows that the values of the trigonal crystal-field parameters v and v' still have to be either reduced or their ratio altered to reduce the splitting of the Γ_8^+ level to that observed. Since the values of v and v' fit the $^4T_{1g}(^4F)$ splittings very successfully it would be difficult to justify any large change in v and v' without invoking a Jahn-Teller reduction in the crystal-field parameters, i.e. the so-called Ham effect. With this present the g values will also be reduced and approach their spin only values. Experimentally, such effects will not be very large since the orbital contribution to the g values through the Zeeman operator (kL+2S) is only ~20% of the total. In this case, it would not be appropriate to use the pure crystal-field wavefunctions obtained using reduced v and v' parameters except for a preliminary, first-calculation. Clearly, further work is needed before one could usefully attempt a re-interpretation of Bailey's work using a real spin exchange model.

C H A P T E R V I I

OVERALL SUMMARY AND CONCLUSIONS

The Raman spectra of single Co^{2+} ions in the four isomorphic crystals of $CdCl_2(Co^{2+})$, $CdBr_2(Co^{2+})$, $MnCl_2(Co^{2+})$ and $CoCl_2$ have been quantitatively analysed and are now well understood. All five electronic transitions from the lowest to the upper spin-orbit and trigonal crystal-field split levels of the $^4T_{1g}(^4F)$ cubic-field ground term have been identified for each crystal. The assignment of the single ion electronic lines from their cobalt concentration dependence has been confirmed by their polarisation properties.

Polarised, infrared absorption spectra of the same crystals provide both confirmation of the Raman results and information concerning the lattice modes of the host and the nature of the interaction between exchange coupled cobalt ion pairs. In particular, the oscillator strengths of the three single ion electronic transitions observed are in quantitative agreement with those calculated using crystal-field theory. Of the vibronics observed, the very sharp, low-frequency peaks are associated with acoustic modes and are a new feature of these lattices while other absorptions in the infrared spectra of $CdCl_2(Co^{2+})$ and $CdBr_2(Co^{2+})$ have been assigned as the isotropic exchange split levels of cobalt ion pairs.

In contrast with previous attempts to fit the single ion electronic transitions for these crystals, excellent agreement with experimental results has been achieved using a crystal-field model involving all states of the $3d^7$ configuration. There is always a danger that the empirical parameters used in

such a model may mask its deficiencies or merely express the results of specific experimental measurements. However, the parameters used successfully explain the g-values of the groundstate level. Further, the crystal-field eigenvectors obtained seem to be good wavefunctions for characterising the single ion electronic states and give successful descriptions of the spectra of antiferromagnetic $CoCl_2$ and exchange-coupled cobalt ion pairs in $CdCl_2$ and $CdBr_2$.

Several avenues exist for further work to be undertaken. Firstly, infrared- and Raman-Zeeman experiments would provide data for comparison with the g-values predicted for the low-lying single ion electronic levels. The infrared measurements should also be extended to a study of the Zeeman splitting of the sharp vibronic lines to verify their vibronic nature. It seems likely that the most rewarding results will come from a careful study of the magnetic-field dependence of those absorption lines assigned to cobalt ion pairs. Such a study would confirm the assignments made in this work. Secondly, in cooperation with Lucas Heights in Sydney, Australia, neutron-diffraction experiments could be performed on $MnCl_2$ to measure the lattice phonon spectra and identify the sharp acoustic phonon peak observed in the vibronic spectrum.

CHAPTER VIII

THE POLARISED INFRARED ABSORPTION SPECTRA OF AN OXYGEN-INDUCED SITE IN $CdCl_2$-TYPE CRYSTALS

8.1 INTRODUCTION

In this chapter, the polarised infrared spectra of an oxygen induced impurity in $CdCl_2$-type crystals is discussed. While a reasonably complete description of the spectra can be given, it is not possible using this alone to identify the ionic arrangement of the molecular cluster causing the spectrum and further work is needed. The present stage of this research, which is an aside from the main body of work, will be given here together with suggestions for further work that could aid its completion.

The infrared spectrum of pure $CdCl_2$-type crystals has been studied by Lockwood[43] and many others[42,76,77]. The infrared active first-order lattice modes of $CdCl_2$ have frequencies of 164±2 cm^{-1} (A_{2u}) and 210±2 cm^{-1} (E_u). The crystals are hygroscopic and samples exposed to atmospheric water vapour often show additional sharp absorption lines in the region of interest due to the vibrational modes of water molecules adsorbed on the crystal surface. These principally comprise the stretching and bending modes of liquid water at 3400 and 1600 cm^{-1}. Other lines also appear. Identification of these modes has been confirmed by the study of the same crystals exposed to heavy-water D_2O[42].

The crystals grown without removal of oxide impurities by treatment with HCl (or HBr) gas often show a sharp, strong

absorption line with a frequency of 700 cm^{-1} in $CdCl_2$, 695 cm^{-1} in $CdBr_2$, 708 cm^{-1} in $MnCl_2$, 735 cm^{-1} in $CoCl_2$ and 738 cm^{-1} in $MgCl_2$. Both Upsall[76] and Driver[77] have shown that this line may be enhanced by addition of 0.1 to 1.0 wt.% of oxide to the crystal starting materials before growth, by heating the crystal in the presence of oxygen, or by heating the crystal after growth in oxygen. These lines are absent from pure crystals but could also be weakly produced in crystals grown with CdS or ZnS. Other absorption lines were also observed, as shown in Table 8-I.

TABLE 8-I

Spectral data† for the crystals studied by Upsall[76] and Driver[77]

$CdBr_2$(CdO)	$CdCl_2$(CdO)	$MnCl_2$(MnO)	$MgCl_2$(MgO)
267.5 ± 0.5			
282.5 ± 0.5			
290.5 ± 0.5			
656.5 ± 0.5	658 ± 1	644 ± 1	
696.5 ± 0.3	700.5 ± 1.0	708.3 ± 0.3	738 ± 1
738.5 ± 0.5	744 ± 1	735 ± 3	
938.5 ± 0.5	1012 ± 1		
996 ± 1			

† all measurements are in wavenumbers (cm^{-1})

The motivation for this present investigation was:

(i) to establish the polarisation of the known, oxygen-induced lines and search for any associated absorption lines.

(ii) to study the spectra of crystals doped with O^{18} oxide in order to establish the number and identity of atoms involved in the site. For an efficient incorporation of oxygen-18 into the crystal the isotope was added in the form of a solid oxide. This was commercially available only as NiO^{18} (75% enrichment) from Miles-Servac using Israeli sources. The isotope studies using NiO^{18} necessitated a detailed preliminary investigation of $CdCl_2$ and $CdBr_2$ doped with NiO^{16}.

(iii) to propose a model to explain the lines observed up to this date.

8.2 THE CRYSTALS

The undoped crystals, purified by bubbling HCl (or HBr) gas through the melt prior to growth, were grown in an identical manner to that used for the cobalt-doped hosts (Chapter 3.1). The pure hosts, prepared in this way, were completely free of any oxide absorption in contrast with the absorption lines obtained with Upsall[76] and Driver's[77] nominally pure crystals. Addition of cadmium-oxide gave clear, pale yellow crystals of $CdCl_2$(CdO) and $CdBr_2$(CdO) whose structural quality deteriorated with progressively heavier oxide concentration. Crystals containing more than 1 wt.% of oxide were poly-crystalline and unsuitable for spectral measurements. Addition of nickel-oxide resulted in pale orange $CdCl_2$(NiO) and pink $CdBr_2$(NiO) crystals due to the absorption bands of the nickel ion (Ni^{2+}) in the visible region of the spectrum. The crystals grown with the enriched isotope

NiO^{18} were generally paler than those grown with the same concentration of NiO^{16}, showing that the NiO^{18} dopant was rejected to some degree. The difference in behaviour is attributed to the use of black NiO^{18} which is non-stoichiometric while the NiO^{16} used was the green variety.

Samples for axial and polarised spectra were prepared in an identical manner to the cobalt doped crystals and the spectra were recorded using the Hofman conduction-type dewar described in Chapter 3.3.

8.3 RESULTS

The results of the investigation of $CdCl_2$ and $CdBr_2$ containing CdO and NiO are given in Tables 8-II and 8-III while the corresponding lines for $MnCl_2$(MnO) and $MgCl_2$(MgO) are listed in Table 8-IV for comparison.

8.3.1 $CdCl_2$(CdO) and $CdCl_2$(NiO)

In the liquid nitrogen, axial absorption spectra of $CdCl_2$(CdO):0.5 wt.% sharp lines may be seen at 658.0, 700.0, 708, 741.5, 1010.8 and 1020.0 cm^{-1}. Of these, the line at 708 cm^{-1} was absent from the spectra of $CdCl_2$(CdO):0.1 wt.% crystals where the line at 700.0 cm^{-1} is quite symmetric. The pair of asymmetric lines at 658.0 and 741.5 cm^{-1} are arranged symmetrically about the line at 700.0 cm^{-1}. At 15°K, the line at 658.0 cm^{-1} disappeared while the other at 741.5 cm^{-1} was clearly resolved into two components at 738 and 742.8 cm^{-1}. The line at 700.0 cm^{-1} was very intense and crystals were completely absorbing at this frequency, even for crystal-thicknesses as small as one millimetre.

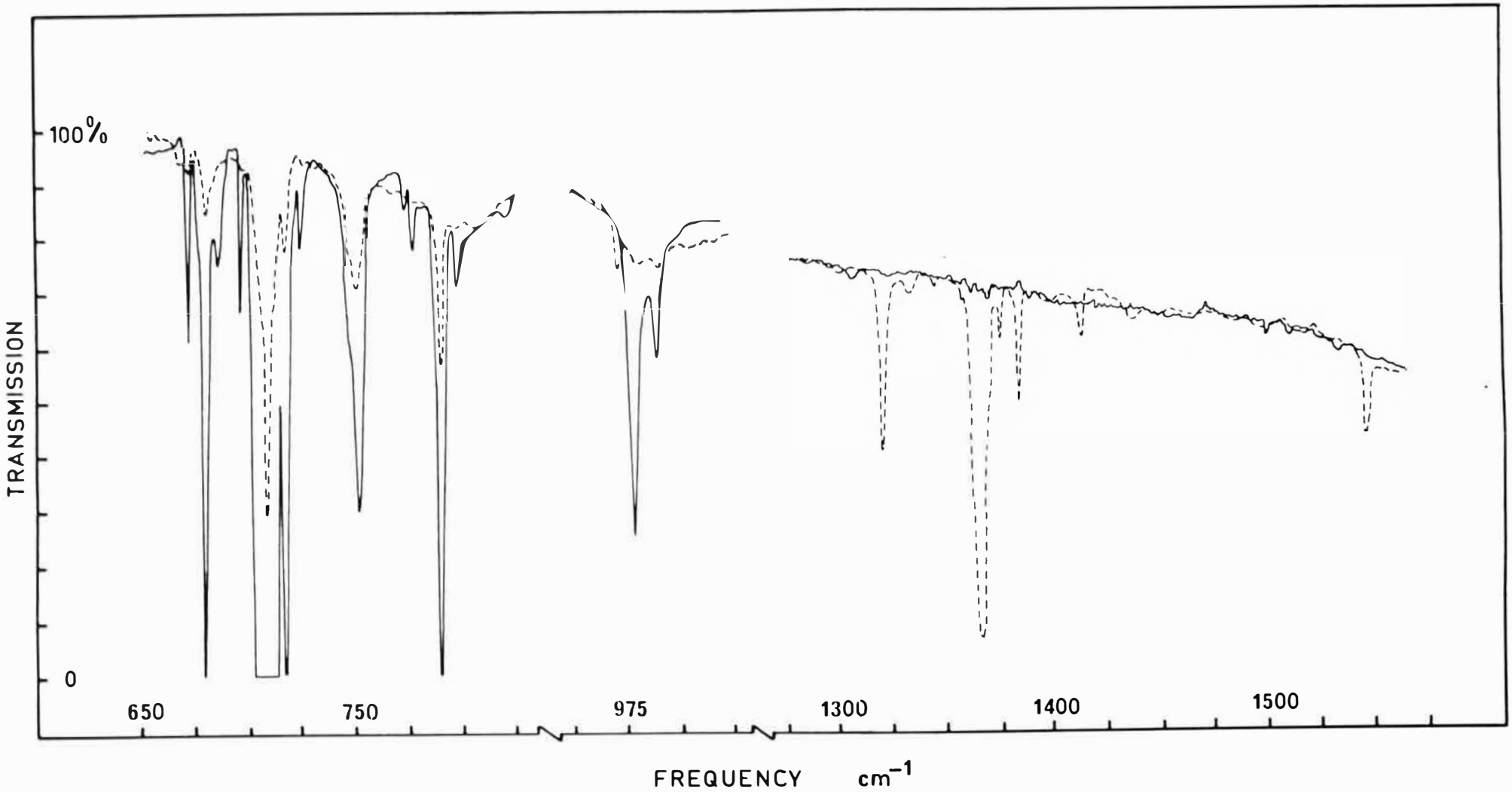

Figure 8-1: Polarised infrared absorption spectra of $CdCl_2(NiO^{16})$:0.5wt% recorded at 15^{o}K. σ and π polarised spectra are shown as solid and dotted lines respectively.

TABLE 8-II

Polarised infrared absorption spectra of $CdCl_2(CdO^{16})$ and $CdCl_2(NiO^{16})$:0.5 wt.%†

15°K				78°K			
Frequency	Pol.	Width	Rel.Int.	Frequency	Pol.	Width	Rel. Int.
				658.0±0.5	σ	8	6
*662.5±0.2	σ	1.5					
*670.0±0.2	σ	2.5	5	*669.7±0.5	σ	2.5	5
*676.5±0.3	σ	2.0					
687.5±0.2	σ	1.5					
695±1							
699.5±0.3	σ	11	100	700.0±0.5	σ	13	100
703±1	σ						
708.3±0.2	σ	2.0		708.0±0.5	σ	2	
715.2±0.2	σ	1.5					
738±1	σ						
742.8±0.2	σ	5.0	9	741.5±0.5	σ	8	9
*754.0±0.3	σ	1.0					
*768.2±0.3	σ	1.5	5				
*780.8±0.2	σ	3.0		*781.0±0.5	σ	4	5
*788.0±0.3	σ	1.5					
*1003.0±0.5	σ	2.5					
1010.5±0.2	σ	4.5	6	1010.8±0.5	σ	5	5
1020.2±0.3	σ	2.0	1	1020.0±0.5	σ	3	1
*1325.5±0.2	π	2.5	1	*1325.0±0.5	π	3	1
1371.0±0.5	π	6.5	10	1356.0±0.3	π	8	5
*1379.5±0.1	π	1.0		1377.0±0.5	π	13	15
*1388.8±0.3	π	1.0	0.5				
*1428.5±0.5	π	2	0.3				
*1552.0±0.3	π	3.5	0.5	*1553.5±0.5	π	5	0.5

† all measurements are in wavenumbers (cm^{-1})

* lines only appearing in $CdCl_2(NiO)$ crystals

The polarised spectra showed that all these lines were σ-polarised and almost absent in π-polarised spectra. The small absorption observed for this polarisation was believed to be due to slight mis-orientation of the crystals, some non-parallelism of the infrared beam incident on the sample, and the imperfect polarisation of the silver-chloride polariser itself. The π-polarised spectra showed new lines in the 1370 cm^{-1} region whose intensity correlated with that of the lines observed in the σ-polarised spectra. At 78°K, these new lines had frequencies of 1356.0 and 1377.0 cm^{-1}. On cooling to 15°K, the former vanished completely leaving one purely symmetric line at 1371 cm^{-1} (Figure 8-3).

When NiO^{16} was used as the oxide dopant instead of CdO^{16}, the lines observed above reappeared together with additional lines at 662.5, 670.0, 676.5, 687.5, 715.2, 754.0, 768.2, 780.8, 788, 1003, 1325.5, 1379.5, 1388.8 and 1552.0 cm^{-1}. The polarised spectra of $CdCl_2(NiO^{16})$:0.5 wt.% is shown in Figure 8-1. Examination of the spectra of $CdCl_2(NiO^{18})$:0.5 and 0.1 wt.% revealed no additional lines from those observed for crystals doped with NiO^{16} and only very small differences in line positions for the analogous absorptions in the two crystals. In particular, the line at 699.5±0.3 cm^{-1} in the NiO^{16} crystal (15°K) is reproduced at 699.1±0.2 cm^{-1} in the NiO^{18} crystal, which is within the experimental uncertainty of the spectrophotometer. Thus, there was no evidence of isotope shifts of any of the lines due to the presence of the oxygen-18 isotope. If O^{18} was actually present one must conclude that the lines do not directly involve the oxygen ions. It is quite likely that the O^{18} is not present for the following reasons:

(i) The chemical supplied as NiO^{18} may in fact contain O^{16}. It was not possible to check this using existing mass-spectrometry facilities;

and (ii) during growth the O^{18} isotope could exchange with O^{16} in the quartz ampoule and be greatly reduced.

8.3.2 $CdBr_2(CdO)$ and $CdBr_2(NiO)$

The spectra observed for these crystals is very similar to that observed for $CdCl_2$ in Section 8.3.1. The axial spectrum of $CdBr_2(CdO)$:0.1 wt.% is given in Figure 8-2 while the spectral data for $CdBr_2(CdO)$:0.5 wt.% is given in Table 8-III.

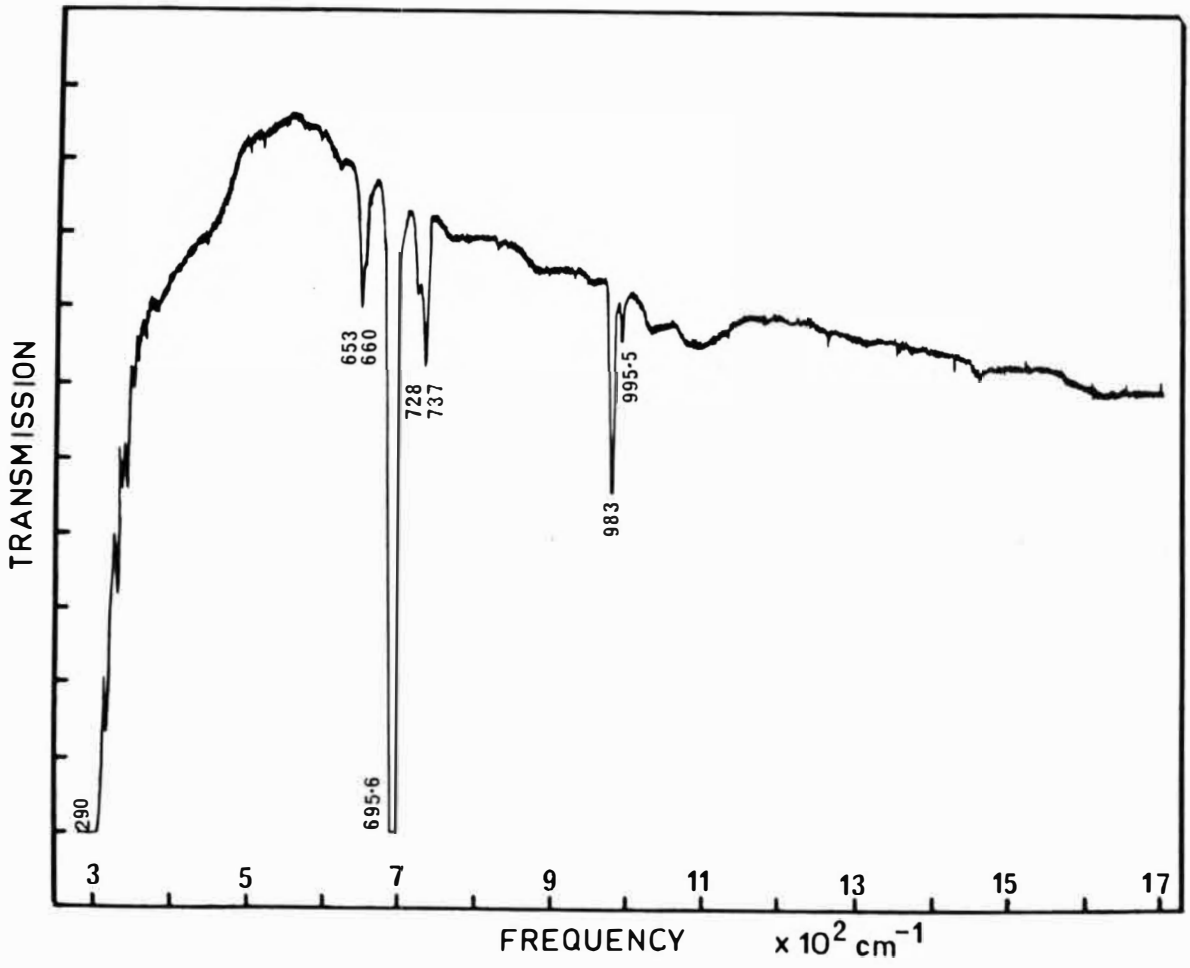

Figure 8-2: Infra-red axial absorption spectrum of $CdBr_2(CdO)$ 0.1wt% recorded at $78^{\circ}K$.

TABLE 8-III

Polarised infrared absorption spectra of $CdBr_2$(CdO):0.5 wt.%†

15°K				78°K			
Frequency	Pol.	Width	Rel.Int.	Frequency	Pol.	Width	Rel.Int.
				280±1			
				290±1			
-				653±1	σ	15	5
-				660±1	σ		5
695.6±0.5	σ	9	100	695.5±0.5	σ	9.5	100
726±1	σ	7	9	728±1	σ	8	9
738±1	σ			737±1	σ		
983.0±0.2	σ	2.5	2	983.0±0.5	σ	4.0	2
995.5±0.2	σ	2.0	0.4	995.5±0.5	σ	2.5	0.4
1361.3±0.2	π	5.0	10	1350±1	π	10	4
				1367.0±0.5	π	13	16

† all measurements in wavenumbers (cm^{-1}).

The majority of lines are σ-polarised while the π-polarised spectrum, recorded at 78°K, showed new lines at 1350 and 1367.0 cm^{-1} which have a similar temperature dependence to those analogous lines observed in $CdCl_2$ crystals (Figure 8-3).

Since $CdBr_2$(CdO) is transparent down to 250 cm^{-1} (400 cm^{-1} in $CdCl_2$) Upsall[76] and Driver[77] were able to report additional lines at 267.5, 282.5 and 290.5 cm^{-1} for this crystal (Table 8-I). However, these lines are easily confused with the absorption lines of atmospheric water vapour in this region, so their results are difficult to confirm using the Beckman Spectrophotometer. Recently however, M.Quin[95]

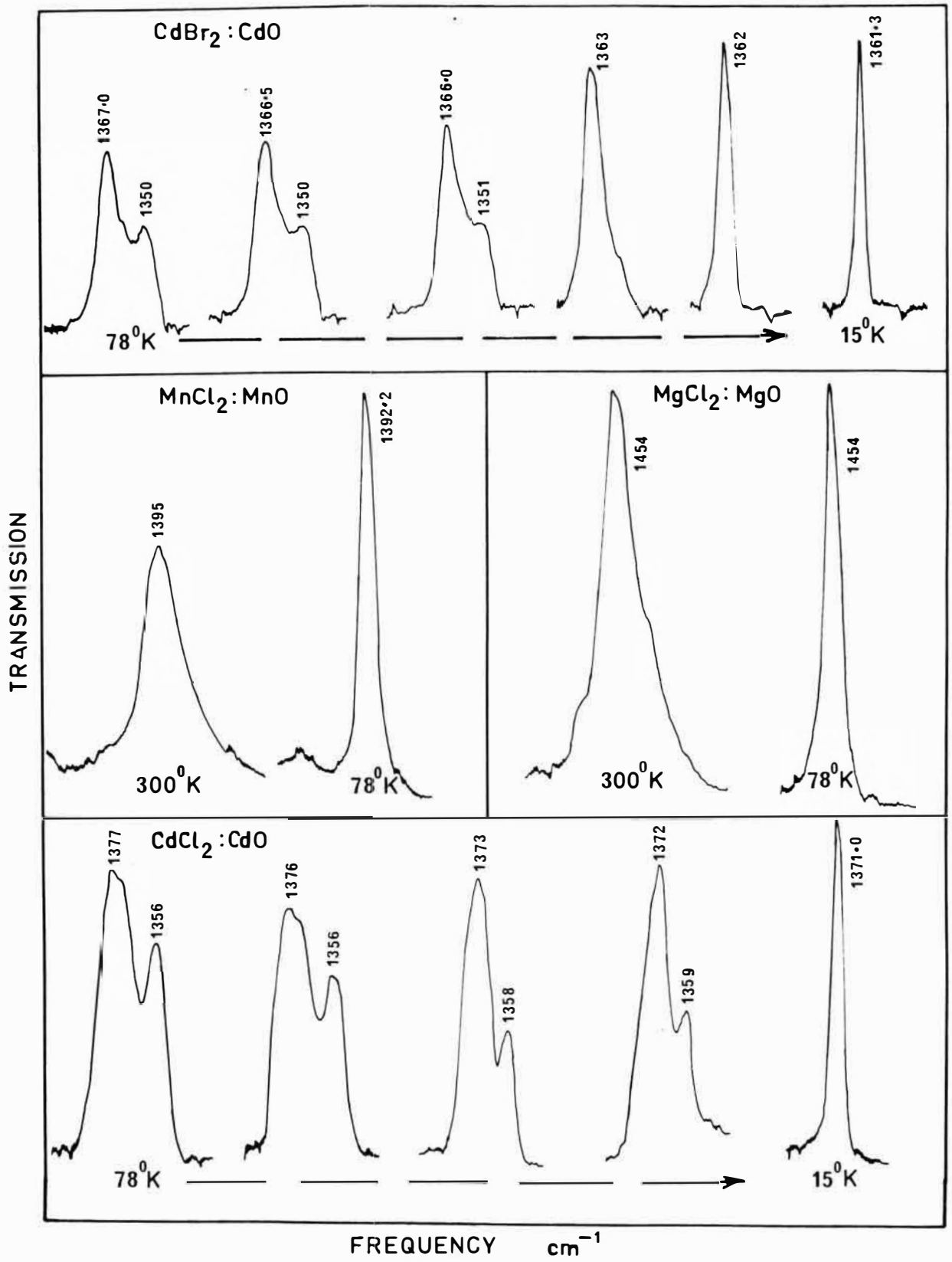

Figure 8-3: Temperature dependence of the second-harmonic infra-red absorption line near 1400 cm^{-1} in $CdBr_2$(CdO), $MnCl_2$(MnO), $MgCl_2$(MgO) and $CdCl_2$(CdO).

and K.M. Lee[96] of this department have detected absorption lines at 290 and 300 cm^{-1} for $CdBr_2(CdO)$ crystals using an evacuated, Grubb Parsons IS3 far-infrared interferometer.

TABLE 8-IV

Infrared absorption spectra of $MnCl_2(MnO)$ and $MgCl_2(MgO)$†

78°K			78°K		
Frequency	Pol.	Width	Frequency	Pol.	Width
668±1	σ	2			
674±1	σ	3			
708±1	σ	11	738±1	σ	10
745.5±1.0	σ	5			
1028.5±1.0	σ	5			
1055.0±1.0	σ	5			
1392.0±0.5	π	7	1454.0±0.5	π	8

† all measurements in wavenumbers (cm^{-1})

8.4 ANALYSIS OF RESULTS TO DATE

The earlier work of Upsall[76] and Driver[77] established that the line at 700 cm^{-1} in $CdCl_2(CdO)$ crystals correlated with the concentration of oxide impurity and this result has been confirmed. The polarisation results place some restriction on the possible site symmetries for any atomic arrangements causing the vibrations. The negative results for crystals doped with O^{18} enriched oxide neither confirm or disprove the presence of oxygen at the impurity site as it is

doubtful whether or not the O^{18} isotope was successfully incorporated into the crystal.

Strong absorptions, analogous to the line at 700 cm^{-1} in $CdCl_2(CdO)$, also appear in $CdBr_2(CdO)$, $MnCl_2(MnO)$, $CoCl_2(CoO)$ and $MgCl_2(MgO)$ crystals with frequencies of 695.6, 708, 735 and 738 cm^{-1}. Because there is very little variation in these line-positions with differing cation or anion this particular vibrational mode cannot involve either of these ions to any great extent. The line is purely σ-polarised, being only excited by an E-vector incident along a direction perpendicular to the crystal c-axis and hence represents a vibration in either the cation or anion plane (Figure 2-1). The line is two-fold degenerate since addition of a small fraction of transition metal ions (ex. Co, Ni, Fe, Zn) to the crystals gives rise to a satellite line on either side of the fundamental. These result from a lowering of the site symmetry of the vibrational species by the presence of a different adjacent cation. For these reasons, the 700 cm^{-1} line in $CdCl_2(CdO)$ and its analogues are assigned as doubly degenerate vibrational modes within the cation or anion planes.

The line at 1371.0 cm^{-1} is almost twice the frequency of the line at 700.0 cm^{-1} and is approximately 10 times weaker. It is assigned as the second-harmonic of the 700.0 cm^{-1} fundamental and has an anharmonic shift of -29 cm^{-1}. Because the line is purely π-polarised there is automatically a group theoretical restriction on the possible symmetry of the vibrational mode at 700.0 cm^{-1}. Second-harmonics of the side line at 708 cm^{-1} and the nickel-induced satellite lines also occur. Their frequencies, together with their anharmonic shifts, are listed in Table 8-V.

For any vibrational species one would also expect an associated infrared active fundamental vibration aligned along the crystal c-axis. No such lines were found in any of the spectra of the chloride crystals although their energies were indicated by the presence of weak, σ-polarised lines at 1010.5 and 1020.0 cm^{-1} which always correlated with the 700 cm^{-1} line. From their intensities these two lines can be assigned as intercombination modes and, neglecting any anharmonic shifts, would require vibrational fundamentals at 310.5 and 320.2 cm^{-1}. Because of the intense restrahlen absorption of the host crystals these cannot be observed.

For $CdBr_2$(CdO) the analogous intercombination lines occur at 983.0 and 995.5 cm^{-1} which suggests there are two low-lying fundamentals at 287.4 and 300.5 cm^{-1}. These have been subsequently observed by Quin[95] and Lee[96] at 290 and 300 cm^{-1} for σ and π polarisation respectively, thereby confirming the assignment of the lines at 983.0 and 995.5 cm^{-1}. The anharmonic shifts are 2.6 and 0.1 cm^{-1} respectively and are listed together with the data for the other modes in Table 8-V.

Similar behaviour has been observed for CdI_2(CdO) crystals[97] in which the intercombination line and the two fundamentals have frequencies of 944, 686 and 260 cm^{-1} respectively.

So far then, we have identified three fundamentals: 695(σ), 290(σ), and 300(π) cm^{-1} and their associated combination modes. Additional intercombination modes have been observed for $CdCl_2$(CdO) and $CdBr_2$(CdO) crystals. In the bromide there are two barely resolved pairs of lines at 653,

TABLE 8-V

Anharmonic shifts of combination modes observed in oxide doped $CdCl_2$-type Crystals†

Fundamental ν_1	×	Fundamental ν_2	=	Combination $\nu_1+\nu_2$	Shift
		$CdCl_2(NiO^{16})$:0.5 wt.%			
699.5±0.3	×	(310.5)	=	1010.5±0.2	
699.5±0.3	×	(320.2)	=	1020.2±0.3	
699.5±0.3	×	699.5±0.3	=	1371.0±0.5	- 28.0±1.1
670.0±0.2	×	670.0±0.2	=	1325.5±0.2	- 14.6±0.6
670.0±0.2	×	780.8±0.2	=	1428.5±0.5	- 22.3±0.9
780.3±0.2	×	708.3±0.2	=	1379.5±0.1	- 37.1±0.5
708.3±0.2	×	699.5±0.3	=	1388.8±0.3	- 19.0±0.8
780.8±0.2	×	780.8±0.2	=	1552.0±0.3	- 9.6±0.7
		$CdBr_2$(CdO):0.5 wt.%			
695.6±0.5	×	290±1	=	983.0±0.2	- 2.6±1.7
695.6±0.5	×	300±1	=	995.5±0.2	- 0.1±1.7
695.6±0.5	×	695.6±0.5	=	1361.3±0.2	- 29.9±1.2
		$MnCl_2$(MnO):0.1 wt.%			
708±1	×	(320.5)	=	1028.5±1.0	
708±1	×	(347.0)	=	1055.0±1.0	
708±1	×	708±1	=	1392.0±0.5	- 24.0±2.5
		$MgCl_2$(MgO):0.1 wt.%			
738±1	×	738±1	=	1454.0±0.5	- 22.0±2.5

† all measurements in wavenumbers (cm^{-1})

660 cm^{-1} and at 728, 737 cm^{-1} arranged symmetrically about the fundamental at 695.6 cm^{-1}. Similar lines at 657.5, 662 cm^{-1} and 738, 742.8 cm^{-1} occur in the chloride. The lower frequency pair in each case are much weaker at liquid helium temperature indicating the presence of low-lying energy levels at frequencies of 42 and 34 cm^{-1} in the bromide and at 42.5 and 39 cm^{-1} in the chloride. These modes need not be infrared active and have not been observed by infrared absorption as yet.

The well defined polarisation behaviour does suggest some group theoretical restrictions on the site symmetry and precise selection rules for the vibrations. In order to establish the particular site symmetry in this case, a point group was sought which satisfied the observed behaviour. To reiterate briefly, there are at least three infrared active fundamentals which are for $CdBr_2(CdO)$ as follows: one doubly degenerate, σ-polarised vibration at 695.6 cm^{-1}, a σ-polarised vibration at 290 cm^{-1}, and a π-polarised vibration at 300 cm^{-1}. The σ-polarised lines transform as the Γ_{xy} representation of the particular symmetry group chosen while the π-polarised lines transform as the Γ_z representation and together they must satisfy the following group theoretical relations:

(i) $\Gamma_{xy}(695.6\ cm^{-1}) \times \Gamma_{xy}(695.6\ cm^{-1}) \supset \Gamma_z\ (1361\ cm^{-1})$

(ii) $\Gamma_{xy}(695.6\ cm^{-1}) \times \Gamma_z\ (300\ cm^{-1}) \supset \Gamma_{xy}(995.5\ cm^{-1})$

(iii) $\Gamma_{xy}(695.6\ cm^{-1}) \times \Gamma_{xy}(290\ cm^{-1}) \supset \Gamma_{xy}(983.0\ cm^{-1})$

If one assumes the oxygen impurity is monatomic and replaces the chlorine anion the site symmetry would be C_{3v}. However, this model does not agree with the above experimental criterion. If the cations are considered to exert very little influence at the impurity site, which is reasonable bearing in mind the small variation in Γ_{xy}(695.6 cm^{-1}) fundamental frequency with change of cation or anion, then the site can be regarded as being principally of C_{6v} symmetry. For only a small C_{3v} component the polarisation rules largely follow those of the C_{6v} site group. However, the third relation is unsatisfied. Further, no single point group can satisfy all three relations and hence the impurity species cannot be monatomic.

On closer examination, the number of fundamentals would suggest that the species is at least diatomic. A two atom species has three infrared active vibrational and rotational modes together with three translational modes which are usually infrared inactive. Also, there will be one non-degenerate, totally symmetric vibrational mode within the complex which will have a relatively high frequency. Using this model one could assign the line at 290 cm^{-1} as a doubly degenerate Γ_{xy} vibration of the two atoms against the bromine cage while the line at 300 cm^{-1} to be due to a similar vibration in the z direction. Similarly one of the two lowest lying lines at 34 and 42 cm^{-1} or higher will be a degenerate rotation, or rocking, of the complex and the other, a similar mode in the z direction. Further, the two frequencies of vibration (and rotation) 290 and 300 cm^{-1} (34 and 42 cm^{-1}) are very similar for the xy and z directions which is consistent

with the assumption that the cations exert little influence at the impurity site. This model would require that the line near 700 cm^{-1} is non-degenerate and necessarily of Γ_1 symmetry. However, these criterion are in conflict with experiment since the line near 700 cm^{-1} is known to be degenerate and the polarisations of it and of its second harmonic at 1361.3 cm^{-1} are different.

There is the possibility that there are three atoms at the impurity site, having an infrared active internal vibration with additional vibrations and rotations of the complex as a whole. However, it is difficult to envisage such a species. It is also possible that the site, though oxygen induced, does not actively involve oxygen and obviously there is a need for more work to be done before any definite predictions can be made as to the number and nature of the atoms in the vibrational species.

A knowledge of the impurity centre will also be necessary before a satisfactory explanation of the temperature dependence of the second-harmonic of the fundamental near 700 cm^{-1} can be made (Figure 8-3). The temperature dependence correlates with the lattice frequencies of the host since for liquid-nitrogen temperatures the second-harmonic is double for cadmium-halide lattices but single, though slightly asymmetric, for manganese-chloride, cobalt-chloride, and magnesium-chloride. At helium temperatures the second harmonic of the first two crystals is perfectly symmetric and single, whereas this same behaviour is observed for the latter crystals at liquid nitrogen temperature. No similar temperature dependence is observed for the first harmonic. At present, the explanation

of this behaviour is pure speculation. One possibility is that the excitation is able to tunnel between two inequivalent impurity sites at warmer temperatures but cannot surmount the potential barrier between them at liquid helium temperatures and is frozen in one state.

8.5 CONCLUSIONS AND FURTHER WORK

No definite explanation of the behaviour observed can be made as yet. Although the excitations are due to a reasonably high symmetry, oxygen induced site the nature of the excitations is uncertain.

The main emphasis of future work should be a further attempt to grow crystals with oxygen-18 isotope since this alone can establish the number and identity of the atoms within the vibrational species. To overcome the possibility of exchange of the isotope with the quartz ampoule walls the crystals could be grown in an ampoule with a platinum inner lining. A search for the lowest frequency lines in the far infrared would establish whether they are oxide induced while also fixing their line position and oscillator-strengths. Similarly, a search for the third harmonics of the line near 700 cm^{-1} in all crystals would provide further clues as to the symmetry of the site and the degree of anharmonicity in the excitations. E.P.R. studies of the crystals may establish whether the impurity is paramagnetic while luminescence experiments have proved useful in determining the behaviour of alkali-halides with O_2^- impurities[98] and could be performed using cadmium-halide crystals.

Initially, the investigation outlined in this chapter was intended merely as a small aside from the main research interest and was designed to eliminate the early confusion of the cobalt electronic spectra with the impurity induced absorptions of the host lattice. However, as can be seen many intriguing features have arisen which require future investigation in their own right to explain their behaviour.

REFERENCES

1. A. Abragaham and M.H.L. Pryce: Proc. Roy. Soc.(Lond.) A206, 173 (1951).
2. J. Ferguson, D.L. Wood and K. Knox: J. Chem. Phys. 39, 881 (1963).
3. T. Nasu: Phys. Stat. Solidi, (b) 66, 561 (1974).
4. H.A. Bethe: Ann. Physik [5] 3, 133 (1929).
5. J.H. Van Vleck: Phys. Rev. 41, 208 (1932).
6. J.H. Van Vleck: J. Chem. Phys. 3, 803, 807 (1935).
7. J.H. Van Vleck: J. Chem. Phys. 8, 787 (1940).
8. R. Finkelstein and J.H. Van Vleck: J. Chem. Phys., 8, 790 (1940).
9. R.S. Mulliken: Phys. Rev. 40, 55 (1932).
10. J.S. Griffith: The Theory of Transition Metal Ions (Cambridge University Press, Cambridge, 1961).
11. Y. Tanabe and S. Sugano: J. Phys. Soc. Japan 9, 753 (1954).
12. Y. Tanabe and S. Sugano: J. Phys. Soc. Japan 9, 766 (1954).
13. Y. Tanabe and S. Sugano: J. Phys. Soc. Japan 11, 864 (1956).
14. L.E. Orgel: J. Chem. Phys. 23, 1004 (1955).
15. L.E. Orgel: J. Chem. Phys. 23, 1819 (1955).
16. L.E. Orgel: J. Chem. Phys. 23, 1824 (1955).
17. E.U. Condon and G.H. Shortley: The Theory of Atomic Spectra (Cambridge University Press, Cambridge, 1951).
18. S. Sugano and R.G. Shulman: Phys. Rev. 130, 517 (1963).
19. M.E. Lines: Phys. Rev. 131, 546 (1963).

20. A.B. Robson: M.Sc. Thesis, University of Canterbury (1969).

21. E.C. Hsu and J.W. Stout: J. Chem. Phys. 59, 502 (1973).

22. K. Ono, A. Ito and T. Fumita: J. Phys. Soc. Japan 19, 2119 (1964).

23. R.W.G. Wyckoff: Crystal Structures, Vol. 1, p.270 (Interscience, New York, 1964).

24. B. Bleaney and K.W.H. Stevens: Rept. Progr. Phys. 16, 107 (1953).

25. W.A. Runciman and K.A. Schroeder: Proc. Roy. Soc. (Lond.) A265, 489 (1962).

26. K. Morigaki: J. Phys. Soc. Japan 16, 1639 (1961).

27. J.W. Orton: Rept. Prog. Phys. 22, 204 (1959).

28. A. Edgar: (private communication).

29. A. Edgar: (private communication).

30. S. Sugano, Y. Tanabe and H. Kamimura: Multiplets of Transition-Metal Ions in Crystals (Academic Press, 1970).

31. Reference 10, p.245.

32. C.J. Ballhausen: Introduction to Ligand Field Theory (McGraw-Hill, 1962), p.105.

33. M.H.L. Pryce and W.A. Runciman: Discuss. Faraday Soc. 26, 34 (1958).

34. Reference 30, p.286.

35. Y. Tanabe and H. Kamimura: J. Phys. Soc. Japan 13, 394 (1956).

36. S. Sugano and M. Peter: Phys. Rev. 122, 381 (1961).

37. K.A. Schroeder: Ph.D. thesis, University of Canterbury (1963).

38. K. Zdansky: (private communication).

39. R.M. Macfarlane: Phys. Rev. B 1, 989 (1970).

40. D.J. Lockwood: J. Opt. Soc. Am. 63, 374 (1973).

41. J.H. Christie and D.J. Lockwood: in Light Scattering in Solids, edited by M. Balkanski (Flammarion, Paris, 1971) p.145.

42. I.W. Johnstone: Physics Honours III Project, University of Canterbury, 1972.

43. D.J. Lockwood: Ph.D. thesis, University of Canterbury, 19.

44. J.H. Christie: Ph.D. thesis, University of Canterbury, 1974.

45. R. Borrell: (private communication).

46. A.C. Rose: Low Temperature Laboratory Techniques (England University Press, 1973).

47. R.J. Elliot and R. Loudon: Phys. Letters 3, 189 (1963).

48. A. Kiel, T. Damen, S.P.S. Porto, S. Singh and F. Varsanyi: Phys. Rev. 178, 1518 (1969).

49. J.A. Koningstein and O. Sonnich Mortensen: J. Chem. Phys. 46, 2811 (1967). Phys. Rev. Lett. 18, 831 (1967).

50. J.A. Koningstein, J. Opt. Soc. Am. 56, 1405 (1966).

51. A. Azima, P. Brunberg, J. Hoff, J.A. Koningstein and J. Preudhomme: J. Chem. Phys. 56, 354 (1972).

52. J.A. Koningstein: J. Chem. Phys. 51, 1163 (1969).

53. P.A. Fleury, S.P.S. Porto, L.E. Cheesman and H.J. Guggenheim: Phys. Rev. Lett. 17, 84 (1966).

54. P.A. Fleury: in Light Scattering Spectra of Solids, ed. G.B. Wright (Springer-Verlag, New York, 1969), p.185.

55. R.M. Macfarlane: Phys. Rev. Lett. 25, 1454 (1970).

56. R.M. Macfarlane and H. Morawitz: in Proceedings of the Second International Conference of Light Scattering in Solids, ed. M. Balkanski (Flammarion, Paris, 1971), p.133.

57. S. Nakashima, H. Yoshida, T. Fukumoto, A. Mitsuishi: J. Phys. Soc. Japan 31, 1847 (1971).

58. J.H. Christie and D.J. Lockwood: Chem. Phys. Lett. 8, 120 (1971).

59. J.H. Christie and D.J. Lockwood: Chem. Phys. Lett. 9, 559 (1971).

60. M.H. Kuok: (private communication).

61. J.H. Christie, I.W. Johnstone, G.D. Jones and K. Zdansky: Phys. Rev. B 1 (1975) - Appendix VI.

62. R.M. Macfarlane: J. Chem. Phys. 39, 3118 (1963).

63. J. Kanamori: Prog. Theor. Phys. Japan 20, 890 (1958).

64. M.K. Wilkinson, J.W. Cable, E.D. Wollan and W.C. Koehler: Phys. Rev. 113, 497 (1959).

65. A. Narath: Phys. Rev. 136, A766 (1964).

66. I.S. Jacobs, S. Roberts and S.D. Silverstein: J. Appl. Phys. 39, 816 (1968).

67. R. Loudon: Adv. in Phys. 17, 243 (1968).

68. W.J.L. Buyers, T.M. Holden, E.C. Svensson, R.A. Cowley and M.T. Hutchings: J. Phys. C.: Solid St. Phys. 4, 2139 (1971).

69. A.I. Zvyagin, V.V. Eremenko and I.V. Skorobogatova: Ukrayin. Fiz. Zh. 11, 520 (1966). (English translation available Physics Dept, University of Canterbury).

70. R. Newman and R.M. Chrenko: Phys. Rev. 115, 1147 (1959).

71. Reference 10, p.57.

72. D.L. Dexter: in Solid State Physics (Academic Press, New York and London, 1958) p.370.

73. Index to the Xray Diffraction File (Am. Soc. for Testing and Materials - Philadelphia, 1945).

74. S.J. Fray, F.A. Johnson and R.H. Jones: Proc. Phys. Soc., 76, 939 (1960).

75. A. Mooney, R.H. Nuttall and W.E. Smith: J. Phys. C 7, 807 (1974).

76. I. Upsall: Physics Honours III project, University of Canterbury.

77. O.G. Driver: Physics Honours III project, University of Canterbury.

78. D.J Newman: Adv. in Phys. 20, 197 (1970).

79. A. Bailey, D.J. Robbins and P. Day: Mol. Phys. 28, 1519 (1974).

80. A.T.H. Trutia and M. Voda: Rev. Fiz. Chim (Romania) A 7, 301 (1970).

81. R.E. Behringer: J. Chem. Phys. 29, 537 (1958).

82. W. Heisenburg: Z. Phys. 38, 411 (1926).

83. P.A.M. Dirac: Proc. Roy. Soc. A123, 714 (1929).

84. J.H. Van Vleck: Phys. Rev. 52, 1178 (1937).

85. J.H. Van Vleck: Rev. Math. Fis. Teór. Univ. Nath. Tucúman, 14, 189 (1962) - unobtainable.

86. P.M. Levy: Phys. Rev. 135, A155 (1964).

87. P.M. Levy: Phys. Rev. 177, 509 (1969).

88. R.J. Elliot and M.F. Thorpe: J. Appl. Phys. 39, 802 (1968).

89. W.P. Wolf: J. Physique 32, suppl. C1, 24 (1971).

90. P.M. Levy and G.M. Copland: Phys. Rev. 180, 439 (1969).

91. G.M. Copland and P.M. Levy: Phys. Rev. B1, 3043 (1970).

92. J. Owen and E.A. Harris: in Electron Paramagnetic Resonance, edited by S. Geschwind (Plenum Press, New York, 1972) p.427.

93. M.T. Hutchings: J. Chem. Phys. 6, 3143 (1973).

94. E. Belorsky, S.C. Ng, T.G. Philips: Phys. Lett. A27, 489 (1968).

95. M. Quin: Physics Honours III Project, University of Canterbury, 1975.

96. K.M. Lee: (private communication).

97. M.H. Kuok: (private communication).

98. M. Ikezawa and J. Rolfe: J. Chem. Phys. 58, 2024 (1973).

APPENDIX I

Matrix Elements of the Trigonal Crystal-Field Between States of the $3d^3(3d^7)$ Configuration

The trigonal crystal-field operator has non-zero matrix elements only between states of the same symmetry. There are thus two matrices for the states of γ_4^+ and $\gamma_{5,6}^+$ symmetry which are of dimension 78 and 42 respectively. The γ_4^+ matrix separates further into two identical submatrices of dimension 39 corresponding to each of its two components $\gamma_4^+(+\frac{1}{2})$ and $\gamma_4^+(-\frac{1}{2})$. The states of the $3d^3(3d^7)$ configuration are also characterised by their $t_{2g}^m e_g^n$ configuration which determines what parameters are to be associated with the matrix elements.

Figure AI-1 shows the structure of the matrices. Matrix elements between the same $t_{2g}^m e_g^n$ configurations are to be multiplied by $\frac{1}{\sqrt{3}}$ v (Blocks I, V, VII, and X of Figure AI-1), while those differing in one t_{2g} and one e_g electron are to be multiplied by $\frac{1}{\sqrt{3}}$ v' (Blocks II, VI and IX). Those differing by more than one e_g electron are identically zero (Blocks III, IV, VII). These relations follow from the one-electron nature of the trigonal crystal-field operator. The matrix elements are presented in block form; those for the γ_4^+ matrices in Figures AI-2a,-2b,-2c,-2d and -2e while those for the $\gamma_{5,6}^+$ matrices are in Figures AI-3a,-3b,3-c,-3d and -3e.

The reduced matrix elements for any general operator with cubic T_2 symmetry are listed in Figure AI-4.

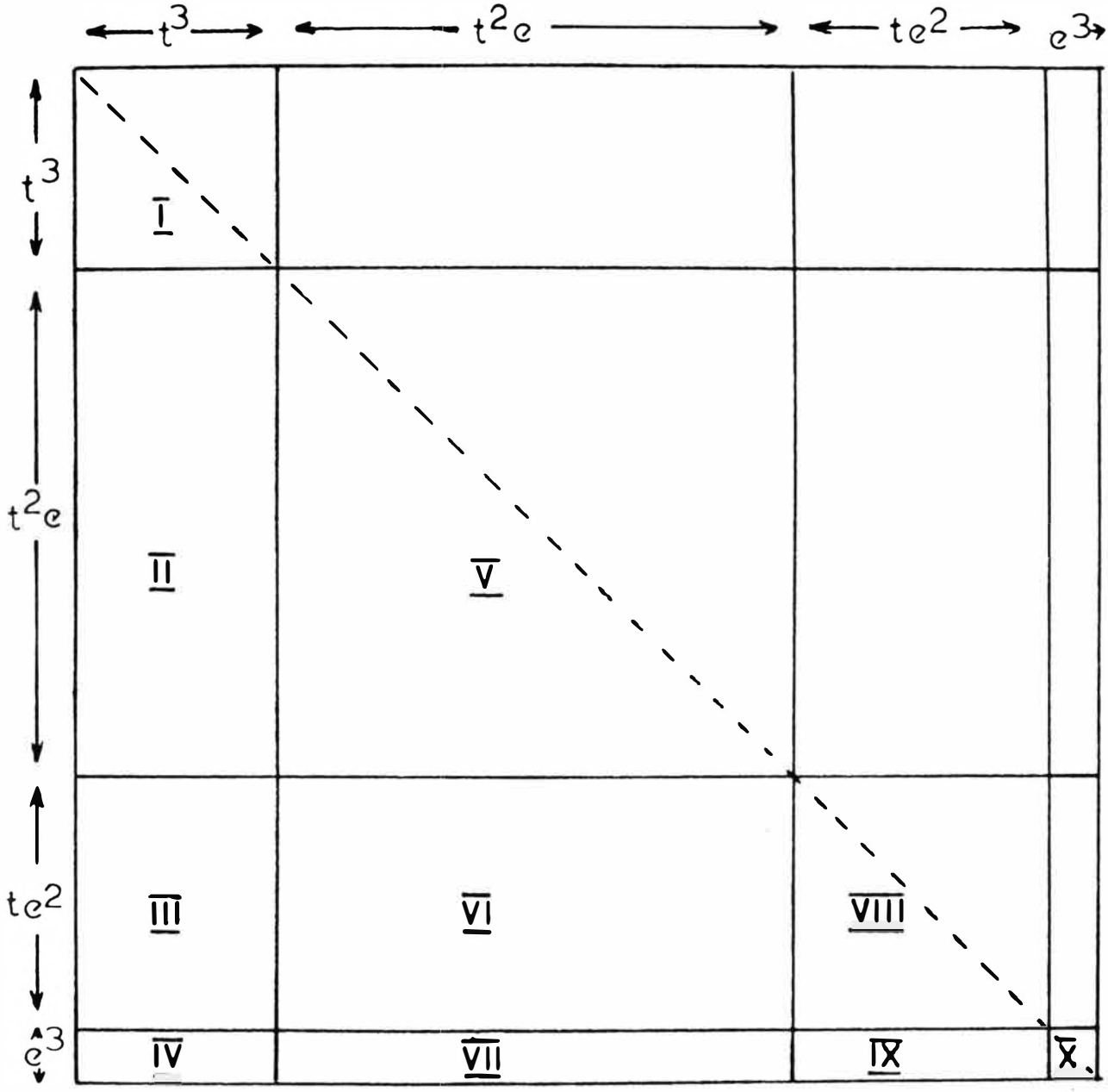

Figure AI-1

Figure AI-2a

t^3 →

I		$^4A_2$	^2E	$^2T_1$		$^2T_2$	
		Γ_8	Γ_8	Γ_6	Γ_8	Γ_7	Γ_8
$^4A_2$	Γ_8	∘					
^2E	Γ_8	∘	∘				
$^2T_1$	Γ_6	•	∘	∘			
	Γ_8	∘	•	∘	∘		
$^2T_2$	Γ_7	∘	$\frac{-\sqrt{2}}{\sqrt{3}}$	$\frac{-\sqrt{2}}{3}$	$\frac{-1}{3}$	∘	
	Γ_8	∘	$\frac{-1}{\sqrt{3}}$	$\frac{-1}{3}$	$\frac{-1}{3\sqrt{2}}$	∘	∘

t^2e ↕

Figure AI-2b

t^3 →

II		$^4A_2$	^2E	$^2T_1$		$^2T_2$	
		Γ_8	Γ_8	Γ_6	Γ_8	Γ_7	Γ_8
$(^3T_1)\,^4T_1$	Γ_6	$\frac{1}{\sqrt{3}}$	∘	∘	•	•	•
	Γ_7	$\frac{-1}{\sqrt{3}}$	•	•	•	∘	∘
	Γ_8	$\frac{1}{\sqrt{15}}$	∘	∘	∘	∘	∘
	Γ_8'	$\frac{-2}{\sqrt{15}}$	∘	∘	∘	∘	∘
$(^3T_1)\,^4T_2$	Γ_6	∘	∘	∘	∘	∘	∘
	Γ_7	∘	∘	∘	∘	∘	∘
	Γ_8	∘	∘	∘	∘	∘	∘
	Γ_8'	∘	∘	∘	∘		•
$(^1E)\,^2A_1$	Γ_6	∘	∘	∘	∘	$\frac{-1}{3\sqrt{2}}$	$\frac{1}{3}$
$(^1E)\,^2A_2$	Γ_7	∘	∘	$\frac{-1}{\sqrt{6}}$	$\frac{1}{\sqrt{3}}$	∘	∘
$(^1A_1)\,^2E$	Γ_8	∘	∘	∘	∘	$\frac{-\sqrt{2}}{3}$	$\frac{-1}{3}$
$(^1E)\,^2E$	Γ_8	∘	∘	$\frac{-1}{\sqrt{6}}$	$\frac{-1}{2\sqrt{3}}$	$\frac{-1}{3\sqrt{2}}$	$\frac{-1}{6}$
$(^3T_1)\,^2T_1$	Γ_6	•	$\frac{-1}{\sqrt{3}}$	∘	$\frac{1}{2\sqrt{2}}$	$\frac{-1}{2\sqrt{3}}$	$\frac{-1}{2\sqrt{6}}$
	Γ_8	∘	$\frac{-1}{\sqrt{6}}$	$\frac{1}{2\sqrt{2}}$	$\frac{-1}{4}$	$\frac{-1}{2\sqrt{6}}$	$\frac{-1}{4\sqrt{3}}$
$(^1T_2)\,^2T_1$	Γ_6	•	∘	∘	$\frac{-1}{2\sqrt{2}}$	$\frac{1}{2\sqrt{3}}$	$\frac{1}{2\sqrt{6}}$
	Γ_8	•	∘	$\frac{-1}{2\sqrt{2}}$	$\frac{1}{4}$	$\frac{1}{2\sqrt{6}}$	$\frac{1}{4\sqrt{3}}$
$(^3T_1)\,^2T_2$	Γ_7	•	•	$\frac{-1}{2}$	$\frac{-1}{2\sqrt{2}}$	•	$\frac{-\sqrt{3}}{2\sqrt{2}}$
	Γ_8	∘	•	$\frac{-1}{2\sqrt{2}}$	$\frac{-1}{4}$	$\frac{\sqrt{3}}{2\sqrt{2}}$	$\frac{\sqrt{3}}{4}$
$(^1T_2, ^2T_2)$	Γ_7	•	$\frac{-1}{\sqrt{3}}$	$\frac{-1}{6}$	$\frac{-1}{6\sqrt{2}}$	•	$\frac{-1}{2\sqrt{6}}$
	Γ_8	•	$\frac{-1}{\sqrt{6}}$	$\frac{-1}{6\sqrt{2}}$	$\frac{-1}{12}$	$\frac{-1}{2\sqrt{6}}$	$\frac{1}{4\sqrt{3}}$

t^2e →

$\overline{V}$		$(^3T_1)\ ^4T_1$				$(^3T_1)\ ^4T_2$				$(^1E)\ ^2A_1$	$(^1E)\ ^2A_2$	$(^1A_1)\ ^2E$	$(^1E)\ ^2E$	$(^3T_1)\ ^2T_1$		$(^1T_2)\ ^2T_1$		$(^3T_1)\ ^2T_2$		$(^1T_2)\ ^2T_2$	
		Γ_6	Γ_7	Γ_8	Γ_8'	Γ_6	Γ_7	Γ_8	Γ_8'	Γ_6	Γ_7	Γ_8	Γ_8	Γ_6	Γ_8	Γ_6	Γ_8	Γ_7	Γ_8	Γ_7	Γ_8
$(^3T_1)\ ^4T_1$	Γ_6	•																			
	Γ_7	$\frac{-1}{2\sqrt{6}}$	•																		
	Γ_8	$\frac{1}{2\sqrt{30}}$	$\frac{-1}{2\sqrt{30}}$	$\frac{-\sqrt{2}}{5\sqrt{3}}$																	
	Γ_8'	$\frac{-1}{\sqrt{30}}$	$\frac{1}{\sqrt{30}}$	$\frac{-1}{5\sqrt{6}}$	$\frac{-1}{10\sqrt{6}}$																
$(^3T_1)\ ^4T_2$	Γ_6	•	$\frac{-1}{2\sqrt{6}}$	$\frac{\sqrt{3}}{2\sqrt{10}}$	$\frac{\sqrt{2}}{\sqrt{15}}$	•															
	Γ_7	$\frac{1}{2\sqrt{6}}$	•	$\frac{-\sqrt{5}}{2\sqrt{6}}$	•	$\frac{1}{2\sqrt{6}}$	•														
	Γ_8	$\frac{-\sqrt{5}}{2\sqrt{6}}$	$\frac{-\sqrt{3}}{2\sqrt{10}}$	$\frac{-1}{5\sqrt{6}}$	$\frac{-\sqrt{3}}{5\sqrt{2}}$	$\frac{1}{2\sqrt{30}}$	$\frac{1}{2\sqrt{30}}$	$\frac{-\sqrt{2}}{5\sqrt{3}}$													
	Γ_8'	•	$\frac{-\sqrt{2}}{\sqrt{15}}$	$\frac{-\sqrt{3}}{5\sqrt{2}}$	$\frac{7}{10\sqrt{6}}$	$\frac{-1}{\sqrt{30}}$	$\frac{-1}{\sqrt{30}}$	$\frac{-1}{5\sqrt{6}}$	$\frac{-1}{10\sqrt{6}}$												
$(^1E)\ ^2A_1$	Γ_6	•	•	•	•	•	•	•	•	•											
$(^1E)\ ^2A_2$	Γ_7	•	•	•	•	•	•	•	•	•	•										
$(^1A_1)\ ^2E$	Γ_8	•	•	•	•	•	•	•	•	•	•	•									
$(^1E)\ ^2E$	Γ_8	•	•	•	•	•	•	•	•	•	•	•	•								
$(^3T_1)\ ^2T_1$	Γ_6	•	•	•	•	•	•	•	•	•	•	•	•	•							
	Γ_8	•	•	•	•	•	•	•	•	•	•	•	•	$\frac{-1}{2\sqrt{3}}$	$\frac{1}{2\sqrt{6}}$						
$(^1T_2)\ ^2T_1$	Γ_6	•	•	•	•	•	•	•	•	•	$\frac{-1}{3}$	$\frac{-2}{3}$	$\frac{1}{3}$	•	•	•					
	Γ_8	•	•	•	•	•	•	•	•	•	$\frac{\sqrt{2}}{3}$	$\frac{-\sqrt{2}}{3}$	$\frac{1}{3\sqrt{2}}$	•	•	$\frac{1}{2\sqrt{3}}$	$\frac{-1}{2\sqrt{6}}$				
$(^3T_1)\ ^2T_2$	Γ_7	•	•	•	•	•	•	•	•	•	•	•	•	$\frac{-1}{\sqrt{6}}$	$\frac{-1}{2\sqrt{3}}$	•	•	•			
	Γ_8	•	•	•	•	•	•	•	•	•	•	•	•	$\frac{-1}{2\sqrt{3}}$	$\frac{-1}{2\sqrt{6}}$	•	•	$\frac{-1}{2\sqrt{3}}$	$\frac{1}{2\sqrt{6}}$		
$(^1T_2)\ ^2T_2$	Γ_7	•	•	•	•	•	•	•	•	$\frac{-1}{3}$	•	$\frac{-2}{3}$	$\frac{-1}{3}$	•	•	$\frac{1}{\sqrt{6}}$	$\frac{1}{2\sqrt{3}}$	•	•	•	
	Γ_8	•	•	•	•	•	•	•	•	$\frac{\sqrt{2}}{3}$	•	$\frac{-\sqrt{2}}{3}$	$\frac{-1}{3\sqrt{2}}$	•	•	$\frac{1}{2\sqrt{3}}$	$\frac{1}{2\sqrt{6}}$	•	•	$\frac{1}{2\sqrt{3}}$	$\frac{-1}{2\sqrt{6}}$

↓ t^2e

Figure AI-2c

t^2e →

te^2 ↓

VI		$(^3T_1)\ ^4T_1$				$(^3T_1)\ ^4T_2$				$(^1E)\ ^2A_1$	$(^1E)\ ^2A_2$	$(^1A_1)\ ^2E$	$(^1E)\ ^2E$	$(^3T_1)\ ^2T_1$		$(^1T_2)\ ^2T_1$		$(^3T_1)\ ^2T_2$		$(^1T_2)\ ^2T_2$	
		Γ_6	Γ_7	Γ_8	Γ_8'	Γ_6	Γ_7	Γ_8	Γ_8'	Γ_6	Γ_7	Γ_8	Γ_8	Γ_6	Γ_8	Γ_6	Γ_8	Γ_7	Γ_8	Γ_7	Γ_8
$(^3A_2)\ ^4T_1$	Γ_6	·	$\frac{1}{2}$	$\frac{-1}{2\sqrt{5}}$	$\frac{1}{\sqrt{5}}$	·	$\frac{-1}{6}$	$\frac{\sqrt{5}}{6}$	·	·	·	·	·	·	·	·	·	·	·	·	·
	Γ_7	$\frac{1}{2}$	·	$\frac{1}{2\sqrt{5}}$	$\frac{-1}{\sqrt{5}}$	$\frac{1}{6}$	·	$\frac{1}{2\sqrt{5}}$	$\frac{2}{3\sqrt{5}}$	·	·	·	·	·	·	·	·	·	·	·	·
	Γ_8	$\frac{-1}{2\sqrt{5}}$	$\frac{1}{2\sqrt{5}}$	$\frac{2}{5}$	$\frac{1}{5}$	$\frac{-1}{2\sqrt{5}}$	$\frac{\sqrt{5}}{6}$	$\frac{1}{15}$	$\frac{1}{5}$	·	·	·	·	·	·	·	·	·	·	·	·
	Γ_8'	$\frac{1}{\sqrt{5}}$	$\frac{-1}{\sqrt{5}}$	$\frac{1}{5}$	$\frac{1}{10}$	$\frac{-2}{3\sqrt{5}}$		$\frac{1}{5}$	$\frac{-7}{30}$	·	·	·	·	·	·	·	·	·	·	·	·
$(^3A_2)\ ^2T_1$	Γ_6	·	·	·	·	·	·	·	·	·	$\frac{-1}{\sqrt{6}}$	$\frac{1}{\sqrt{6}}$	$\frac{1}{\sqrt{6}}$	·	$\frac{1}{2\sqrt{2}}$	·	$\frac{-1}{2\sqrt{2}}$	$\frac{1}{6}$	$\frac{1}{6\sqrt{2}}$	$\frac{1}{2}$	$\frac{1}{2\sqrt{2}}$
	Γ_8	·	·	·	·	·	·	·	·	·	$\frac{1}{\sqrt{3}}$	$\frac{1}{2\sqrt{3}}$	$\frac{1}{2\sqrt{3}}$	$\frac{1}{2\sqrt{2}}$	$\frac{-1}{4}$	$\frac{-1}{2\sqrt{2}}$	$\frac{1}{4}$	$\frac{1}{6\sqrt{2}}$	$\frac{1}{12}$	$\frac{1}{2\sqrt{2}}$	$\frac{1}{4}$
$(^1E)\ ^2T_1$	Γ_6	·	·	·	·	·	·	·	·	·	$\frac{-1}{3\sqrt{2}}$	$\frac{1}{3\sqrt{2}}$	$\frac{1}{3\sqrt{2}}$	·	·	·	$\frac{1}{\sqrt{6}}$	$\frac{1}{\sqrt{3}}$	$\frac{1}{\sqrt{6}}$	·	·
	Γ_8	·	·	·	·	·	·	·	·	·	$\frac{1}{3}$	$\frac{1}{6}$	$\frac{1}{6}$	·	·	$\frac{1}{\sqrt{6}}$	$\frac{-1}{2\sqrt{3}}$	$\frac{1}{\sqrt{6}}$	$\frac{1}{2\sqrt{3}}$	·	·
$(^1A_1)\ ^2T_2$	Γ_7	·	·	·	·	·	·	·	·	$\frac{-1}{3\sqrt{2}}$	·	$\frac{1}{3\sqrt{2}}$	$\frac{-1}{3\sqrt{2}}$	$\frac{-1}{2\sqrt{3}}$	$\frac{-1}{2\sqrt{6}}$	$\frac{1}{2\sqrt{3}}$	$\frac{1}{2\sqrt{6}}$	·	$\frac{-\sqrt{3}}{2\sqrt{2}}$	·	$\frac{-1}{2\sqrt{6}}$
	Γ_8	·	·	·	·	·	·	·	·	$\frac{1}{3}$	·	$\frac{1}{6}$	$\frac{-1}{6}$	$\frac{-1}{2\sqrt{6}}$	$\frac{-1}{4\sqrt{3}}$	$\frac{1}{2\sqrt{6}}$	$\frac{1}{4\sqrt{3}}$	$\frac{-\sqrt{3}}{2\sqrt{2}}$	$\frac{\sqrt{3}}{4}$	$\frac{-1}{2\sqrt{6}}$	$\frac{1}{4\sqrt{3}}$
$(^1E)\ ^2T_2$	Γ_7	·	·	·	·	·	·	·	·	$\frac{1}{3\sqrt{2}}$	·	$\frac{-1}{3\sqrt{2}}$	$\frac{1}{3\sqrt{2}}$	$\frac{-1}{\sqrt{3}}$	$\frac{-1}{\sqrt{6}}$	·	·	·	·	·	$\frac{-1}{\sqrt{6}}$
	Γ_8	·	·	·	·	·	·	·	·	$\frac{-1}{3}$	·	$\frac{-1}{6}$	$\frac{1}{6}$	$\frac{-1}{\sqrt{6}}$	$\frac{-1}{2\sqrt{3}}$	·	·	·	·	$\frac{-1}{\sqrt{6}}$	$\frac{1}{2\sqrt{3}}$

Figure AI-2d

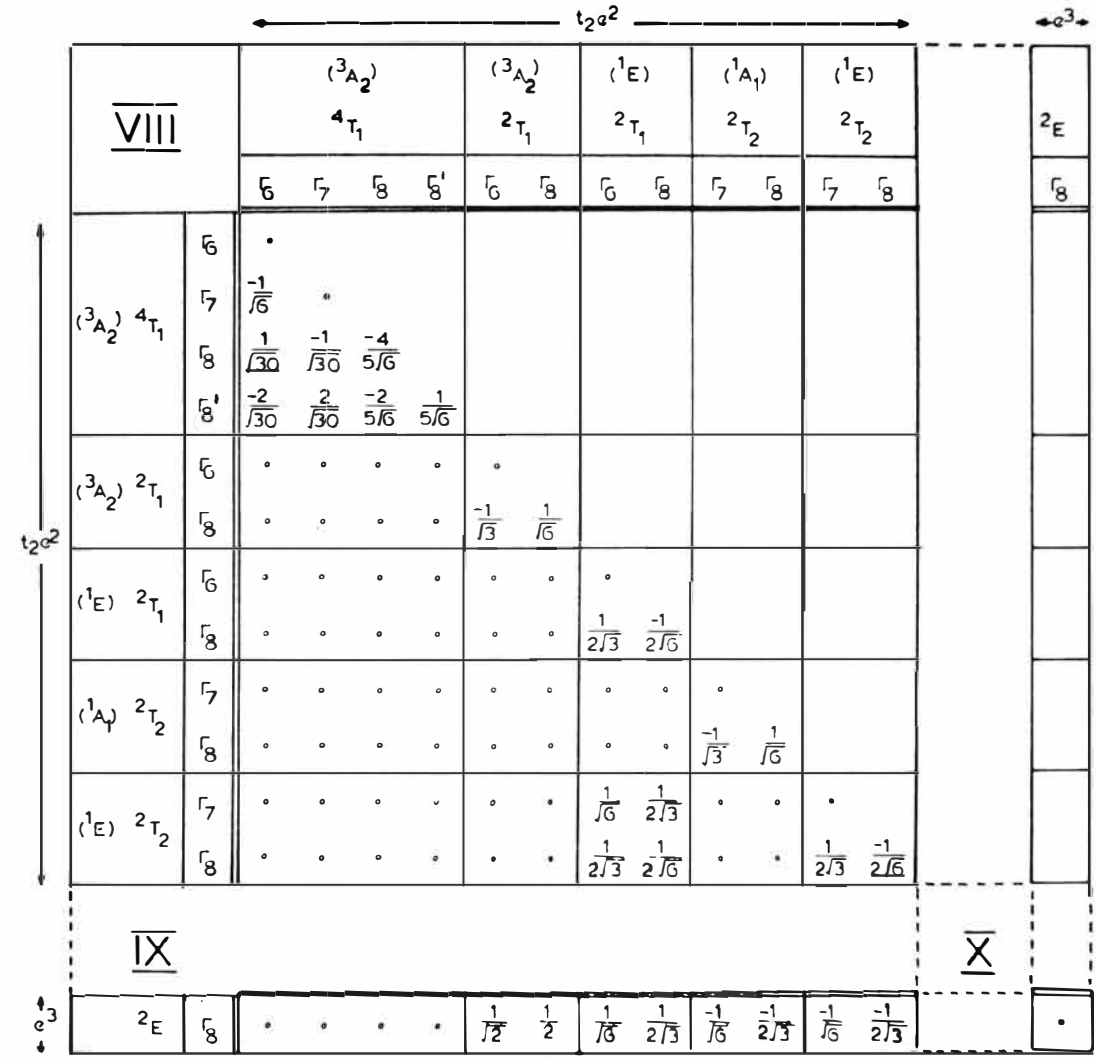
t2e2
e3
VIII
IX
X
(3A2) 4T1
(3A2) 2T1
(1E) 2T1
(1A1) 2T2
(1E) 2T2
2E
Γ6 Γ7 Γ8 Γ8'
Γ6 Γ8
Γ7 Γ8
Γ7 Γ8
Γ8
(3A2) 4T1
(3A2) 2T1
(1E) 2T1
(1A1) 2T2
(1E) 2T2
2E
Γ6
Γ7
Γ8
Γ8'
Γ6
Γ8
Γ6
Γ8
Γ7
Γ8
Γ7
Γ8
Γ8
-1/√6
1/√30 -1/√30 -4/5√6
-2/√30 2/√30 -2/5√6 1/5√6
-1/√3 1/√6
1/2√3 -1/2√6
-1/√3 1/√6
1/√6 1/2√3
1/2√3 1/2√6
-1/√3 1/√6
-1/√6 1/2√3
1/2√3 -1/2√6
1/√2 1/2
1/√6 1/2√3
-1/√6 -1/2√3
-1/√6 -1/2√3

Figure AI-2e

Figure AI-3a

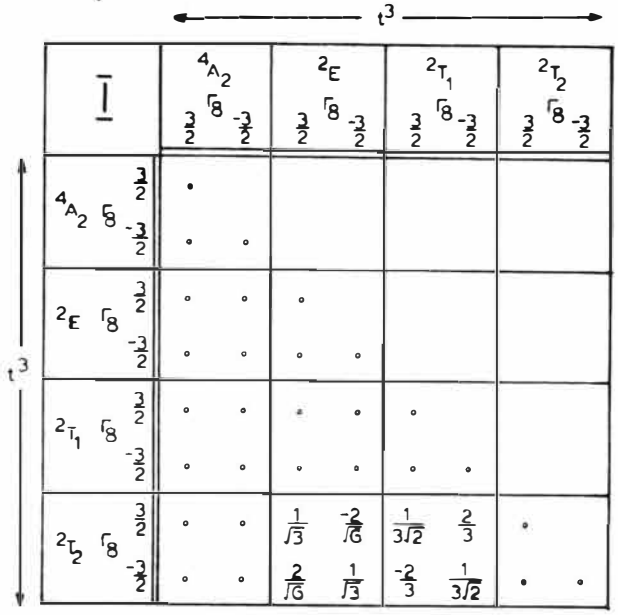

I	$^4A_2$ Γ_8 $\frac{3}{2}$	$^4A_2$ Γ_8 $-\frac{3}{2}$	^2E Γ_8 $\frac{3}{2}$	^2E Γ_8 $-\frac{3}{2}$	$^2T_1$ Γ_8 $\frac{3}{2}$	$^2T_1$ Γ_8 $-\frac{3}{2}$	$^2T_2$ Γ_8 $\frac{3}{2}$	$^2T_2$ Γ_8 $-\frac{3}{2}$
$^4A_2$ Γ_8 $\frac{3}{2}$	•							
$^4A_2$ Γ_8 $-\frac{3}{2}$	∘	∘						
^2E Γ_8 $\frac{3}{2}$	∘	∘	∘					
^2E Γ_8 $-\frac{3}{2}$	∘	∘	∘	∘				
$^2T_1$ Γ_8 $\frac{3}{2}$	∘	∘	∘	∘	∘			
$^2T_1$ Γ_8 $-\frac{3}{2}$	∘	∘	∘	∘	∘	∘		
$^2T_2$ Γ_8 $\frac{3}{2}$	∘	∘	$\frac{1}{\sqrt{3}}$	$\frac{-2}{\sqrt{6}}$	$\frac{1}{3\sqrt{2}}$	$\frac{2}{3}$	•	
$^2T_2$ Γ_8 $-\frac{3}{2}$	∘	∘	$\frac{2}{\sqrt{6}}$	$\frac{1}{\sqrt{3}}$	$\frac{-2}{3}$	$\frac{1}{3\sqrt{2}}$	•	•

Figure AI-3b

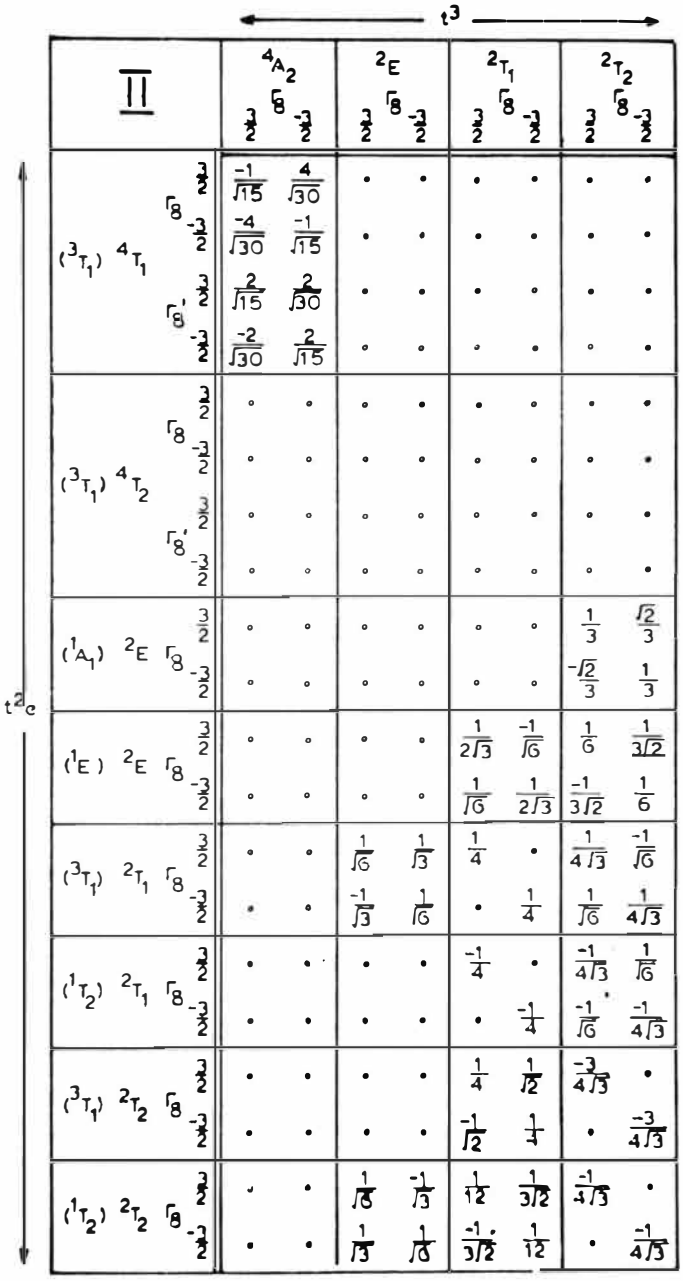

II	$^4A_2$ Γ_8 $\frac{3}{2}$	$^4A_2$ Γ_8 $-\frac{3}{2}$	^2E Γ_8 $\frac{3}{2}$	^2E Γ_8 $-\frac{3}{2}$	$^2T_1$ Γ_8 $\frac{3}{2}$	$^2T_1$ Γ_8 $-\frac{3}{2}$	$^2T_2$ Γ_8 $\frac{3}{2}$	$^2T_2$ Γ_8 $-\frac{3}{2}$
$(^3T_1)$ $^4T_1$ Γ_8 $\frac{3}{2}$	$\frac{-1}{\sqrt{15}}$	$\frac{4}{\sqrt{30}}$	•	•	•	•	•	•
$(^3T_1)$ $^4T_1$ Γ_8 $-\frac{3}{2}$	$\frac{-4}{\sqrt{30}}$	$\frac{-1}{\sqrt{15}}$	•	•	•	•	•	•
$(^3T_1)$ $^4T_1$ Γ_8' $\frac{3}{2}$	$\frac{2}{\sqrt{15}}$	$\frac{2}{\sqrt{30}}$	•	•	•	•	•	•
$(^3T_1)$ $^4T_1$ Γ_8' $-\frac{3}{2}$	$\frac{-2}{\sqrt{30}}$	$\frac{2}{\sqrt{15}}$	∘	∘	∘	∘	∘	∘
$(^3T_1)$ $^4T_2$ Γ_8 $\frac{3}{2}$	∘	∘	∘	∘	∘	∘	∘	∘
$(^3T_1)$ $^4T_2$ Γ_8 $-\frac{3}{2}$	∘	∘	∘	∘	∘	∘	∘	∘
$(^3T_1)$ $^4T_2$ Γ_8' $\frac{3}{2}$	∘	∘	∘	∘	∘	∘	∘	∘
$(^3T_1)$ $^4T_2$ Γ_8' $-\frac{3}{2}$	∘	∘	∘	∘	∘	∘	∘	∘
$(^1A_1)$ ^2E Γ_8 $\frac{3}{2}$	∘	∘	∘	∘	∘	∘	$\frac{1}{3}$	$\frac{\sqrt{2}}{3}$
$(^1A_1)$ ^2E Γ_8 $-\frac{3}{2}$	∘	∘	∘	∘	∘	∘	$\frac{-\sqrt{2}}{3}$	$\frac{1}{3}$
(^1E) ^2E Γ_8 $\frac{3}{2}$	∘	∘	∘	∘	$\frac{1}{2\sqrt{3}}$	$\frac{-1}{\sqrt{6}}$	$\frac{1}{6}$	$\frac{1}{3\sqrt{2}}$
(^1E) ^2E Γ_8 $-\frac{3}{2}$	∘	∘	∘	∘	$\frac{1}{\sqrt{6}}$	$\frac{1}{2\sqrt{3}}$	$\frac{-1}{3\sqrt{2}}$	$\frac{1}{6}$
$(^3T_1)$ $^2T_1$ Γ_8 $\frac{3}{2}$	∘	∘	$\frac{1}{\sqrt{6}}$	$\frac{1}{\sqrt{3}}$	$\frac{1}{4}$	•	$\frac{1}{4\sqrt{3}}$	$\frac{-1}{\sqrt{6}}$
$(^3T_1)$ $^2T_1$ Γ_8 $-\frac{3}{2}$	•	∘	$\frac{-1}{\sqrt{3}}$	$\frac{1}{\sqrt{6}}$	•	$\frac{1}{4}$	$\frac{1}{\sqrt{6}}$	$\frac{1}{4\sqrt{3}}$
$(^1T_2)$ $^2T_1$ Γ_8 $\frac{3}{2}$	•	•	•	•	$\frac{-1}{4}$	•	$\frac{-1}{4\sqrt{3}}$	$\frac{1}{\sqrt{6}}$
$(^1T_2)$ $^2T_1$ Γ_8 $-\frac{3}{2}$	•	•	•	•	•	$\frac{-1}{4}$	$\frac{-1}{\sqrt{6}}$	$\frac{-1}{4\sqrt{3}}$
$(^3T_1)$ $^2T_2$ Γ_8 $\frac{3}{2}$	•	•	•	•	$\frac{1}{4}$	$\frac{1}{\sqrt{2}}$	$\frac{-3}{4\sqrt{3}}$	•
$(^3T_1)$ $^2T_2$ Γ_8 $-\frac{3}{2}$	•	•	•	•	$\frac{-1}{\sqrt{2}}$	$\frac{1}{4}$	•	$\frac{-3}{4\sqrt{3}}$
$(^1T_2)$ $^2T_2$ Γ_8 $\frac{3}{2}$	•	•	$\frac{1}{\sqrt{6}}$	$\frac{-1}{\sqrt{3}}$	$\frac{1}{12}$	$\frac{1}{3\sqrt{2}}$	$\frac{-1}{4\sqrt{3}}$	•
$(^1T_2)$ $^2T_2$ Γ_8 $-\frac{3}{2}$	•	•	$\frac{1}{\sqrt{3}}$	$\frac{1}{\sqrt{6}}$	$\frac{-1}{3\sqrt{2}}$	$\frac{1}{12}$	•	$\frac{-1}{4\sqrt{3}}$

t^2a →

$\overline{V}$	$(^3T_1)\ ^4T_1$				$(^3T_1)\ ^4T_2$				$(^1A_1)\ ^2E$		$(^1E)\ ^2E$		$(^3T_1)\ ^2T_1$		$(^1T_2)\ ^2T_1$		$(^3T_1)\ ^2T_2$		$(^1T_2)\ ^2T_2$	
	Γ_8		Γ_8'		Γ_8		Γ_8'		Γ_8		Γ_8		Γ_8		Γ_8		Γ_8		Γ_8	
	$\frac{3}{2}$	$-\frac{3}{2}$	$\frac{3}{2}$	$-\frac{3}{2}$	$\frac{3}{2}$	$-\frac{3}{2}$	$\frac{3}{2}$	$-\frac{3}{2}$	$\frac{3}{2}$	$-\frac{3}{2}$	$\frac{3}{2}$	$-\frac{3}{2}$	$\frac{3}{2}$	$-\frac{3}{2}$	$\frac{3}{2}$	$-\frac{3}{2}$	$\frac{3}{2}$	$-\frac{3}{2}$	$\frac{3}{2}$	$-\frac{3}{2}$
$(^3T_1)\ ^4T_1\ \Gamma_8\ \frac{3}{2}$	$\frac{2}{5\sqrt{6}}$																			
$\Gamma_8\ -\frac{3}{2}$	•	$\frac{2}{5\sqrt{6}}$																		
$\Gamma_8'\ \frac{3}{2}$	$\frac{1}{5\sqrt{6}}$	$\frac{-1}{2\sqrt{3}}$	$\frac{1}{10\sqrt{6}}$																	
$\Gamma_8'\ -\frac{3}{2}$	$\frac{1}{2\sqrt{3}}$	$\frac{1}{5\sqrt{6}}$	•	$\frac{1}{10\sqrt{6}}$																
$(^3T_1)\ ^4T_2\ \Gamma_8\ \frac{3}{2}$	$\frac{1}{5\sqrt{6}}$	$\frac{2}{5\sqrt{3}}$	$\frac{3}{5\sqrt{6}}$	$\frac{-\sqrt{3}}{10}$	$\frac{2}{5\sqrt{6}}$															
$\Gamma_8\ -\frac{3}{2}$	$\frac{-2}{5\sqrt{3}}$	$\frac{1}{5\sqrt{6}}$	$\frac{\sqrt{3}}{10}$	$\frac{3}{5\sqrt{6}}$	•	$\frac{2}{5\sqrt{6}}$														
$\Gamma_8'\ \frac{3}{2}$	$\frac{3}{5\sqrt{6}}$	$\frac{-\sqrt{3}}{10}$	$\frac{-7}{10\sqrt{6}}$	$\frac{-2}{5\sqrt{3}}$	$\frac{1}{5\sqrt{6}}$	$\frac{1}{2\sqrt{3}}$	$\frac{1}{10\sqrt{6}}$													
$\Gamma_8'\ -\frac{3}{2}$	$\frac{\sqrt{3}}{10}$	$\frac{3}{5\sqrt{6}}$	$\frac{2}{5\sqrt{3}}$	$\frac{-7}{10\sqrt{6}}$	$\frac{-1}{2\sqrt{3}}$	$\frac{1}{5\sqrt{6}}$	•	$\frac{1}{10\sqrt{6}}$												
$(^1A_1)\ ^2E\ \Gamma_8\ \frac{3}{2}$	•	•	•	•	•	•	•	•	•											
$\Gamma_8\ -\frac{3}{2}$	•	•	•	•	•	•	•	•	•	•										
$(^1E)\ ^2E\ \Gamma_8\ \frac{3}{2}$	•	•	•	•	•	•	•	•	•	•	•									
$\Gamma_8\ -\frac{3}{2}$	•	•	•	•	•	•	•	•	•	•	•	•								
$(^3T_1)\ ^2T_1\ \Gamma_8\ \frac{3}{2}$	•	•	•	•	•	•	•	•	•	•	•	•	$\frac{-1}{2\sqrt{6}}$							
$\Gamma_8\ -\frac{3}{2}$	•	•	•	•	•	•	•	•	•	•	•	•	•	$\frac{-1}{2\sqrt{6}}$						
$(^1T_2)\ ^2T_1\ \Gamma_8\ \frac{3}{2}$	•	•	•	•	•	•	•	•	$\frac{\sqrt{2}}{3}$	$\frac{2}{3}$	$\frac{-1}{3\sqrt{2}}$	$\frac{-1}{3}$	•	•	$\frac{1}{2\sqrt{6}}$					
$\Gamma_8\ -\frac{3}{2}$	•	•	•	•	•	•	•	•	$\frac{-2}{3}$	$\frac{\sqrt{2}}{3}$	$\frac{1}{3}$	$\frac{-1}{3\sqrt{2}}$	•	•	•	$\frac{1}{2\sqrt{6}}$				
$(^3T_1)\ ^2T_2\ \Gamma_8\ \frac{3}{2}$	•	•	•	•	•	•	•	•	•	•	•	•	$\frac{1}{2\sqrt{6}}$	$\frac{1}{\sqrt{3}}$	•	•	$\frac{-1}{2\sqrt{6}}$			
$\Gamma_8\ -\frac{3}{2}$	•	•	•	•	•	•	•	•	•	•	•	•	$\frac{-1}{\sqrt{3}}$	$\frac{1}{2\sqrt{6}}$	•	•	•	$\frac{-1}{2\sqrt{6}}$		
$(^1T_2)\ ^2T_2\ \Gamma_8\ \frac{3}{2}$	•	•	•	•	•	•	•	•	$\frac{\sqrt{2}}{3}$	$\frac{-2}{3}$	$\frac{1}{3\sqrt{2}}$	$\frac{-1}{3}$	•	•	$\frac{-1}{2\sqrt{6}}$	$\frac{-1}{3}$	•	•	$\frac{1}{2\sqrt{6}}$	
$\Gamma_8\ -\frac{3}{2}$	•	•	•	•	•	•	•	•	$\frac{2}{3}$	$\frac{\sqrt{2}}{3}$	$\frac{1}{3}$	$\frac{1}{3\sqrt{2}}$	•	•	$\frac{1}{3}$	$\frac{-1}{2\sqrt{6}}$	•	•	•	$\frac{1}{2\sqrt{6}}$

t^2a ↑

Figure AI-3c


VI
t^2e
tc^2
$(^3T_1)\ ^4T_1$
$(^3T_1)\ ^4T_2$
$(^1A_1)\ ^2E$
$(^1E)\ ^2E$
$(^3T_1)\ ^2T_1$
$(^1T_2)\ ^2T_1$
$(^3T_1)\ ^2T_2$
$(^1T_2)\ ^2T_2$
Γ_8 Γ_8'
$\frac{3}{2}$ $-\frac{3}{2}$
$(^3A_2)\ ^4T_1$
$(^3A_2)\ ^2T_1\ \Gamma_8$
$(^1E)\ ^2T_1\ \Gamma_8$
$(^1A_1)\ ^2T_2\ \Gamma_8$
$(^1E)\ ^2T_2\ \Gamma_8$

Figure AI-3d

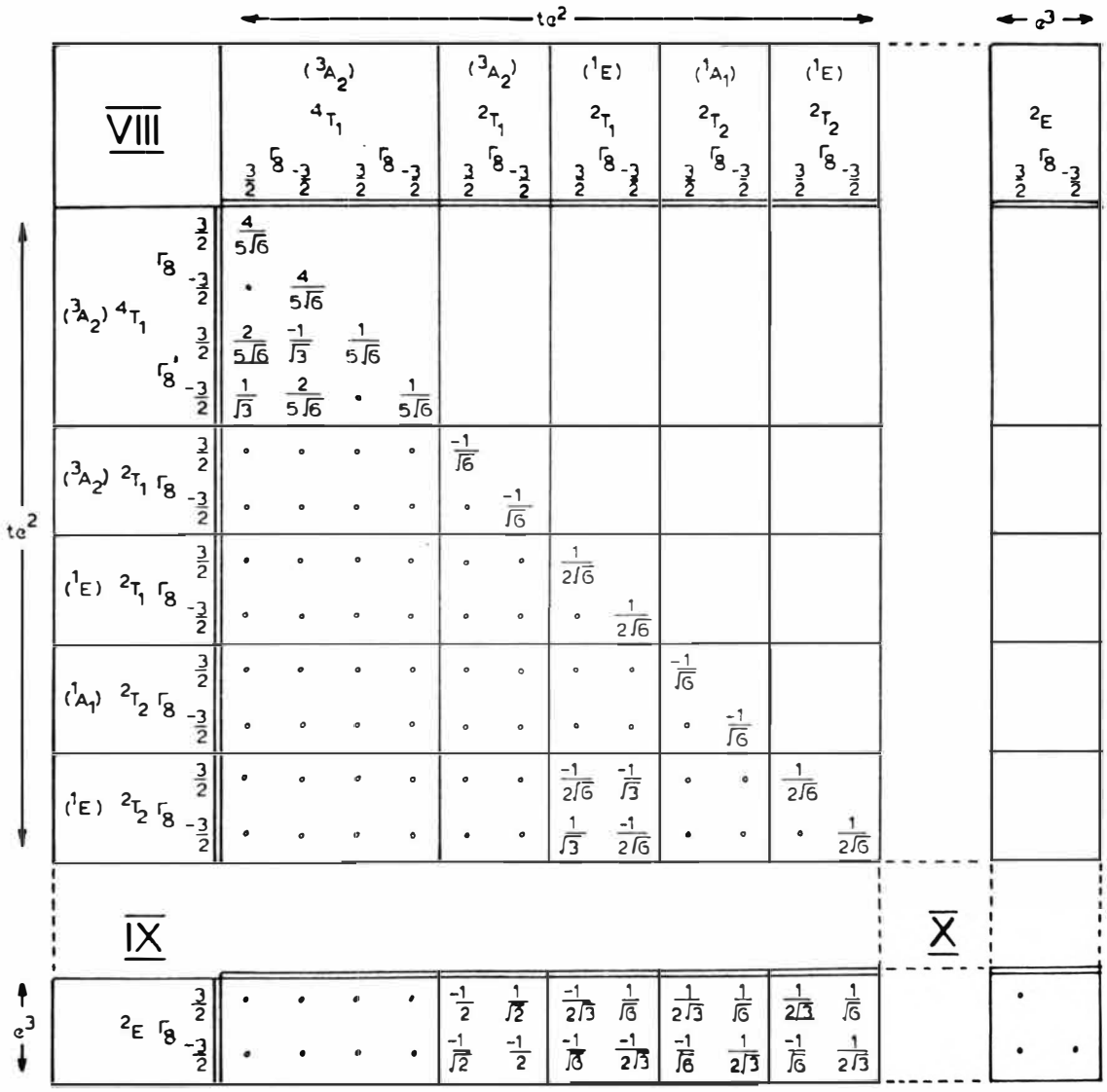
t2^2
e^3
VIII
IX
X
(3A2) 4T1 Γ8 3/2
(3A2) 4T1 Γ8 -3/2
(3A2) 4T1 Γ8' 3/2
(3A2) 4T1 Γ8' -3/2
(3A2) 2T1 Γ8 3/2
(3A2) 2T1 Γ8 -3/2
(1E) 2T1 Γ8 3/2
(1E) 2T1 Γ8 -3/2
(1A1) 2T2 Γ8 3/2
(1A1) 2T2 Γ8 -3/2
(1E) 2T2 Γ8 3/2
(1E) 2T2 Γ8 -3/2
2E Γ8 3/2
2E Γ8 -3/2
4/5√6
4/5√6
2/5√6
-1/√3
1/5√6
1/√3
2/5√6
1/5√6
-1/√6
-1/√6
1/2√6
1/2√6
-1/√6
-1/√6
-1/2√6
-1/√3
1/√3
-1/2√6
1/2√6
-1/2
1/√2
-1/√2
-1/2
-1/2√3
1/√6
-1/√6
-1/2√3
1/2√3
-1/√6
1/√6
1/2√3
-1/√6
1/√6
1/2√3

Figure AI-3e

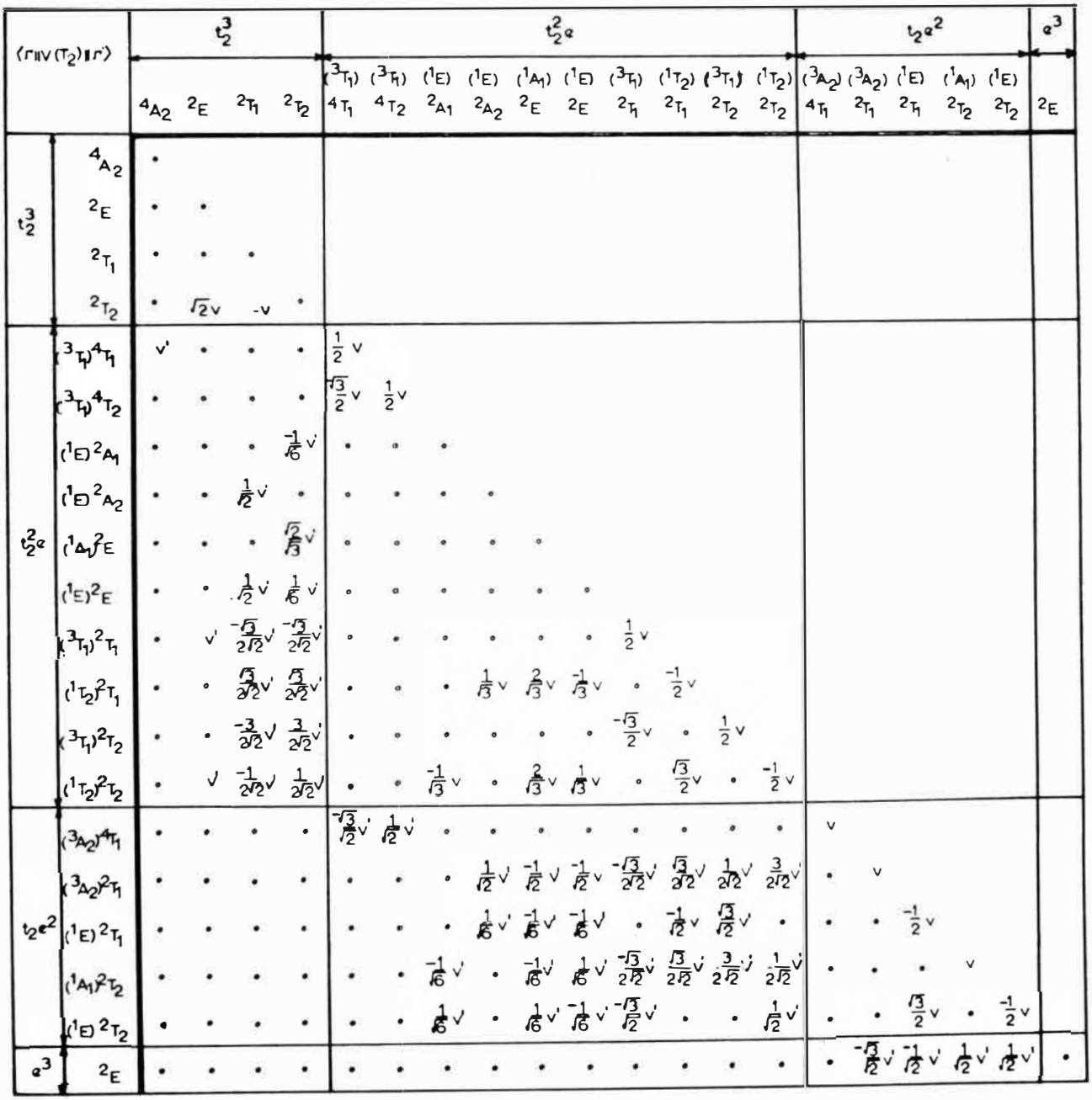
⟨Γ‖V(T2)‖Γ'⟩
t2^3
t2^2e
t2e^2
e^3
4A2
2E
2T1
2T2
(3T1)4T1
(3T1)4T2
(1E)2A1
(1E)2A2
(1A1)2E
(1E)2E
(3T1)2T1
(1T2)2T1
(3T1)2T2
(1T2)2T2
(3A2)4T1
(3A2)2T1
(1E)2T1
(1A1)2T2
(1E)2T2
2E

Figure AI-4

APPENDIX II

Matrix Elements of the Zeeman Interaction between states of the $3d^3(3d^7)$ Configuration

The matrix elements of the components of the Zeeman operator (kL+2S) are listed separately for each operator L_z, S_z, L_x and S_x. The matrix elements of L_y and S_y are pure complex but have the same magnitude as those of L_x and S_x and only differ by the factor $\pm i$. Because of their increased dimension, the matrices are listed in a more compact form than those in Appendix I. The terms in the summation in eqn (2.18) are listed according to their spin multiplicity. (Doublets have 2S+1 = 2 while quartets have 2S+1 = 4.)

Those for the L_z and L_x operators are pure complex and need only be multiplied by the required reduced matrix element, which is also complex, from among those tabulated in Figure AII-3. As can be seen, the states of the $3d^3(3d^7)$ configuration are also characterised by their $t_{2g}^m e_g^n$ configuration which determines what parameters (k and k') are to be associated with the particular matrix element. Elements between the same configuration are to be multiplied by ik (the factor i is omitted from the Figure) while those differing in one t_{2g} and one e_g electron are to be multiplied by ik'. Those differing by more than one e_g electron are identically zero. These relations follow from the fact that the Zeeman operator is a one-electron operator.

In contrast, matrix elements of S_z and S_x are real and only link states of the same $t_{2g}^m e_g^n$ configuration. These elements are given in their final form.

The z-component of the Zeeman operator (kL_z+2S_z) has non-zero matrix elements between states of the same trigonal symmetry as given below:

$$<\tau'\alpha'^{2S+1}\chi_r'\Gamma_n'\gamma_4^{+}\pm\tfrac{1}{2}|L_z|\tau\alpha^{2S+1}\chi_r\Gamma_n\gamma_4^{+}\pm\tfrac{1}{2}>$$

$$<\tau'\alpha'^{2S+1}\chi_r'\Gamma_n'\gamma_{5,6}^{+}\pm\tfrac{3}{2}|L_z|\tau\alpha^{2S+1}\chi_r\Gamma_n\gamma_{5,6}^{+}\pm\tfrac{3}{2}>$$

$$<\tau'\alpha'^{2S+1}\chi_r'\Gamma_n'\gamma_{5,6}^{+}\pm\tfrac{3}{2}|L_z|\tau\alpha^{2S+1}\chi_r\Gamma_n\gamma_{5,6}^{+}\mp\tfrac{3}{2}>$$

and

$$<\tau\alpha^{2S+1}\chi_r\Gamma_n'\gamma_4^{+}\pm\tfrac{1}{2}|S_z|\tau\alpha^{2S+1}\chi_r\Gamma_n\gamma_4^{+}\pm\tfrac{1}{2}>$$

$$<\tau\alpha^{2S+1}\chi_r\Gamma_n'\gamma_{5,6}^{+}\pm\tfrac{3}{2}|S_z|\tau\alpha^{2S+1}\chi_r\Gamma_n\gamma_{5,6}^{+}\pm\tfrac{3}{2}>$$

$$<\tau\alpha^{2S+1}\chi_r\Gamma_n'\gamma_{5,6}^{+}\pm\tfrac{3}{2}|S_z|\tau\alpha^{2S+1}\chi_r\Gamma_n\gamma_{5,6}^{+}\mp\tfrac{3}{2}>$$

Thus, there are three submatrices for states of $\gamma_4^{+}(+\frac{1}{2})$, $\gamma_4^{+}(-\frac{1}{2})$ and $\gamma_{5,6}(\pm\frac{3}{2})$ symmetries with dimensions of 39, 39 and 42. The matrix elements are evaluated only for $\gamma_4^{+}(+\frac{1}{2})$ and $\gamma_{5,6}(\pm\frac{3}{2})$ states as for the trigonal crystal-field operator. Elements between $\gamma_4^{+}(-\frac{1}{2})$ states are given by:

$$<\tau'\alpha'^{2S+1}\chi_r'\Gamma_n'\gamma_4^{+}+\tfrac{1}{2}|L_z|\tau\alpha^{2S+1}\chi_r\Gamma_n\gamma_4^{+}+\tfrac{1}{2}>$$

$$= -<\tau'\alpha'^{2S+1}\chi_r'\Gamma_n'\gamma_4^{+}-\tfrac{1}{2}|L_z|\tau\alpha^{2S+1}\chi_r\Gamma_n\gamma_4^{+}-\tfrac{1}{2}>$$

and

$$\langle \tau\alpha^{2S+1}\chi_r\Gamma_n'\gamma_4^{+}+\tfrac{1}{2}|S_z|\tau\alpha^{2S+1}\chi_r\Gamma_n\gamma_4^{+}+\tfrac{1}{2}\rangle$$

$$= -\langle \tau\alpha^{2S+1}\chi_r\Gamma_n'\gamma_4^{+}-\tfrac{1}{2}|S_z|\tau\alpha^{2S+1}\chi_r\Gamma_n\gamma_4^{+}-\tfrac{1}{2}\rangle$$

The matrix elements of L_z between $\gamma_4^{+}(+\frac{1}{2})$ and $\gamma_{5,6}^{+}(\pm\frac{3}{2})$ doublet states are given in Figures AII-1a and -1b, while those between $\gamma_4^{+}(+\frac{1}{2})$ and $\gamma_{5,6}^{+}(\pm\frac{3}{2})$ quartet states are given in Figures AII-1c and -1d. These are pure complex and need to be multiplied by a factor i together with the appropriate matrix element given in Figure AII-3. The matrix elements of S_z between $\gamma_4^{+}(+\frac{1}{2})$ and $\gamma_{5,6}^{+}(\pm\frac{3}{2})$ doublet states are given in Figures AII-2a and -2b, while those between $\gamma_4^{+}(+\frac{1}{2})$ and $\gamma_{5,6}^{+}(\pm\frac{3}{2})$ quartet states are listed in Figures AII-2c and -2d.

The x-component of the Zeeman operator (kL_x+2S_x) has non-zero matrix elements between states of the same and differing trigonal symmetries as given below:

$$\langle \tau'\alpha'^{2S+1}\chi_r'\Gamma_n'\gamma_4^{+}\pm\tfrac{1}{2}|L_x|\tau\alpha^{2S+1}\chi_r\Gamma_n\gamma_4^{+}\mp\tfrac{1}{2}\rangle$$

$$\langle \tau'\alpha'^{2S+1}\chi_r'\Gamma_n'\gamma_{5,6}^{+}\pm\tfrac{3}{2}|L_x|\tau\alpha^{2S+1}\chi_r\Gamma_n\gamma_4^{+}\pm\tfrac{1}{2}\rangle$$

$$\langle \tau'\alpha'^{2S+1}\chi_r'\Gamma_n'\gamma_{5,6}^{+}\pm\tfrac{3}{2}|L_x|\tau\alpha^{2S+1}\chi_r\Gamma_n\gamma_4^{+}\mp\tfrac{1}{2}\rangle$$

and

$$\langle \tau\alpha^{2S+1}\chi_r\Gamma_n'\gamma_4^{+}\pm\tfrac{1}{2}|S_x|\tau\alpha^{2S+1}\chi_r\Gamma_n\gamma_4^{+}\mp\tfrac{1}{2}\rangle$$

$$\langle \tau\alpha^{2S+1}\chi_r\Gamma_n'\gamma_{5,6}^{+}\pm\tfrac{3}{2}|S_x|\tau\alpha^{2S+1}\chi_r\Gamma_n\gamma_4^{+}\pm\tfrac{1}{2}\rangle$$

$$\langle \tau\alpha^{2S+1}\chi_r\Gamma_n'\gamma_{5,6}^{+}\pm\tfrac{3}{2}|S_x|\tau\alpha^{2S+1}\chi_r\Gamma_n\gamma_4^{+}\mp\tfrac{1}{2}\rangle$$

All other matrix elements are identically zero. The matrix elements of L_x between $\gamma_4^+(\pm\frac{1}{2})$ and $\gamma_{5,6}^+(\pm\frac{3}{2})$ doublet states are given in Figures AII-4a and -4b; those between $\gamma_4^+(\pm\frac{1}{2})$ and $\gamma_{5,6}^+(\pm\frac{3}{2})$ quartet states are given in Figures AII-4c and -4d. The matrix elements of S_x between $\gamma_4^+(\pm\frac{1}{2})$ and $\gamma_{5,6}^+(\pm\frac{3}{2})$ doublet states are given in Figures AII-5a and -5b while those between corresponding quartet states are listed in Figures AII-5c and -5d.

The matrix elements of L_y and S_y are simply related to those of L_x and S_x and may be generated by multiplying the sub-blocks of the 120-dimension matrix as outlined below:

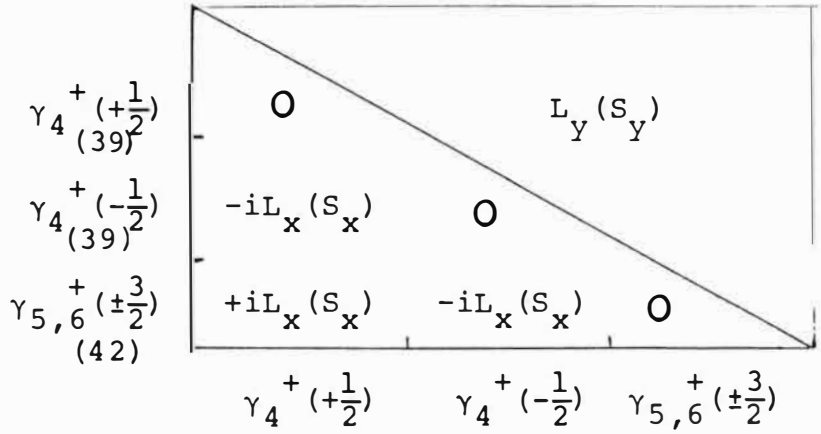

To obtain Zeeman splittings of the trigonal crystal-field split levels, the matrices (kL_z+2S_z) and (kL_x+2S_x) are superimposed on the energy matrices used in the crystal field fit. The summed matrices are then diagonalised. The energy matrices, evaluated between $\gamma_4^+(+\frac{1}{2})$ states may be duplicated to give the elements between $\gamma_4^+(-\frac{1}{2})$ states and placed on the diagonal blocks of the 120-dimension matrix together with those between $\gamma_{5,6}^+(\pm\frac{3}{2})$ states. The g shifts are then simply given by the magnetic field splitting of the $\gamma_4^+(\pm\frac{1}{2})$ or $\gamma_{5,6}^+(\pm\frac{3}{2})$ states. Alternatively, since the γ_4^+ and

$\gamma_{5,6}^{+}$ trigonal states are not mixed by a magnetic field parallel to the c-axis, the $g_{\parallel}$ values may be evaluated without diagonalising the full 120-dimension energy matrix. By separately diagonalising the $\gamma_4^{+}(+\frac{1}{2})$ and $\gamma_{5,6}^{+}(\pm\frac{3}{2})$ sub-blocks the $g_{\parallel}$ shift of the γ_4^{+} levels is given by twice the shift of the $\gamma_4^{+}(+\frac{1}{2})$ level under an applied field, while the $g_{\parallel}$ shift for $\gamma_{5,6}^{+}(\pm\frac{3}{2})$ levels is simply their separation, as above.

γ_4		$^2A_1$	$^2A_2$	^2E	$^2T_1$		$^2T_2$	
		Γ_6	Γ_7	Γ_8	Γ_6	Γ_8	Γ_7	Γ_8
$^2A_1$	Γ_6	·	·	·	$\frac{-1}{\sqrt{3}}$	$\frac{\sqrt{2}}{\sqrt{3}}$	·	·
$^2A_2$	Γ_7		·	·	·	·	$\frac{-1}{\sqrt{3}}$	$\frac{\sqrt{2}}{\sqrt{3}}$
^2E	Γ_8			·	$\frac{1}{\sqrt{3}}$	$\frac{1}{\sqrt{6}}$	$\frac{1}{\sqrt{3}}$	$\frac{1}{\sqrt{6}}$
$^2T_1$	Γ_6				$\frac{-\sqrt{2}}{3}$	$\frac{-1}{3}$	·	$\frac{1}{\sqrt{3}}$
	Γ_8					$\frac{-1}{3\sqrt{2}}$	$\frac{1}{\sqrt{3}}$	$\frac{-1}{\sqrt{6}}$
$^2T_2$	Γ_7						$\frac{\sqrt{2}}{3}$	$\frac{1}{3}$
	Γ_8							$\frac{1}{3\sqrt{2}}$

Figure AII-1a

$\gamma_{5,6}$		$^2E\,\Gamma_8$		$^2T_1\,\Gamma_8$		$^2T_2\,\Gamma_8$	
		$\frac{3}{2}$	$\frac{-3}{2}$	$\frac{3}{2}$	$\frac{-3}{2}$	$\frac{3}{2}$	$\frac{-3}{2}$
$^2E\,\Gamma_8$	$\frac{3}{2}$	·	·	$\frac{-1}{\sqrt{6}}$	$\frac{-1}{\sqrt{3}}$	$\frac{5}{3\sqrt{6}}$	$\frac{-1}{3\sqrt{3}}$
	$\frac{-3}{2}$		·	$\frac{-1}{\sqrt{3}}$	$\frac{1}{\sqrt{6}}$	$\frac{-1}{3\sqrt{3}}$	$\frac{-5}{3\sqrt{6}}$
$^2T_1\,\Gamma_8$	$\frac{3}{2}$			$\frac{-1}{\sqrt{2}}$	·	$\frac{-1}{3\sqrt{6}}$	$\frac{2}{3\sqrt{3}}$
	$\frac{-3}{2}$				$\frac{1}{\sqrt{2}}$	$\frac{2}{3\sqrt{3}}$	$\frac{1}{3\sqrt{6}}$
$^2T_2\,\Gamma_8$	$\frac{3}{2}$					$\frac{-7}{9\sqrt{2}}$	$\frac{-4}{9}$
	$\frac{-3}{2}$						$\frac{7}{9\sqrt{2}}$

Figure AII-1b

γ_4		$^4A_2$		$^4T_1$			$^4T_2$			
		Γ_8	Γ_6	Γ_7	Γ_8	Γ_8'	Γ_6	Γ_7	Γ_8	Γ_8'
$^4A_2$	Γ_8	·	·	·	·	·	$\frac{1}{\sqrt{3}}$	$\frac{1}{\sqrt{3}}$	$\frac{1}{\sqrt{15}}$	$\frac{-2}{\sqrt{15}}$
	Γ_6		$\frac{1}{3\sqrt{2}}$	·	$\frac{-\sqrt{5}}{3\sqrt{2}}$	·	$\frac{-1}{\sqrt{6}}$	·	$\frac{-1}{\sqrt{30}}$	$\frac{2}{\sqrt{30}}$
$^4T_1$	Γ_7			$\frac{1}{3\sqrt{2}}$	$\frac{-1}{\sqrt{10}}$	$\frac{-4}{3\sqrt{10}}$	·	$\frac{1}{\sqrt{6}}$	$\frac{1}{\sqrt{30}}$	$\frac{-2}{\sqrt{30}}$
	Γ_8				$\frac{-\sqrt{2}}{15}$	$\frac{-\sqrt{2}}{5}$	$\frac{-1}{\sqrt{30}}$	$\frac{-1}{\sqrt{30}}$	$\frac{4}{5\sqrt{6}}$	$\frac{2}{5\sqrt{6}}$
	Γ_8'					$\frac{7}{15\sqrt{2}}$	$\frac{2}{\sqrt{30}}$	$\frac{2}{\sqrt{30}}$	$\frac{2}{5\sqrt{6}}$	$\frac{1}{5\sqrt{6}}$
	Γ_6						$\frac{-1}{3\sqrt{2}}$	·	$\frac{-1}{\sqrt{10}}$	$\frac{-4}{3\sqrt{10}}$
$^4T_2$	Γ_7							$\frac{-1}{3\sqrt{2}}$	$\frac{\sqrt{5}}{3\sqrt{2}}$	·
	Γ_8								$\frac{\sqrt{2}}{15}$	$\frac{\sqrt{2}}{5}$
	Γ_8'									$\frac{-7}{15\sqrt{2}}$

Figure AII-1c

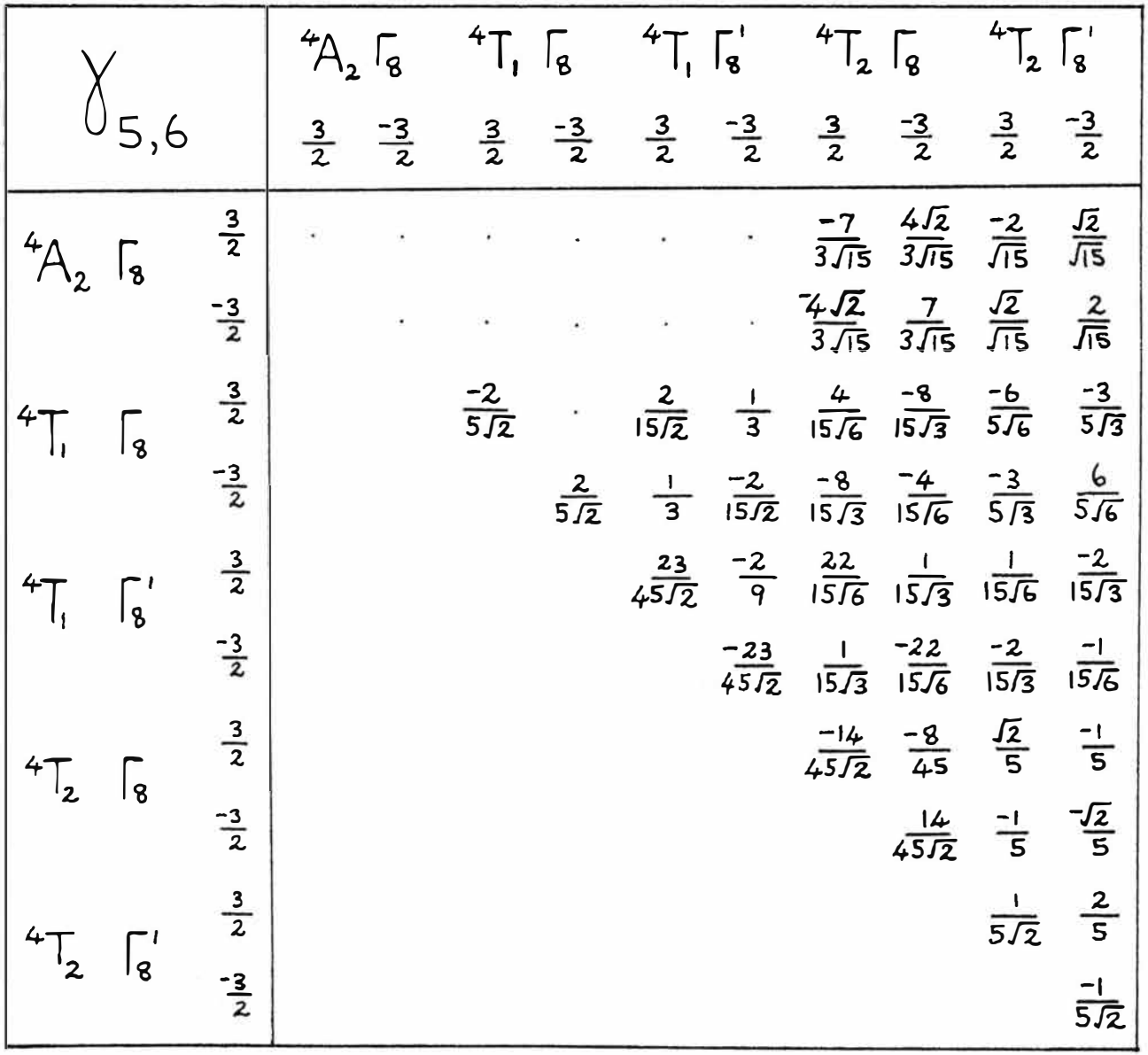

$\gamma_{5,6}$		$^4A_2\ \Gamma_8$		$^4T_1\ \Gamma_8$		$^4T_1\ \Gamma_8'$		$^4T_2\ \Gamma_8$		$^4T_2\ \Gamma_8'$	
		$\frac{3}{2}$	$\frac{-3}{2}$	$\frac{3}{2}$	$\frac{-3}{2}$	$\frac{3}{2}$	$\frac{-3}{2}$	$\frac{3}{2}$	$\frac{-3}{2}$	$\frac{3}{2}$	$\frac{-3}{2}$
$^4A_2\ \Gamma_8$	$\frac{3}{2}$	·	·	·	·	·	·	$\frac{-7}{3\sqrt{15}}$	$\frac{4\sqrt{2}}{3\sqrt{15}}$	$\frac{-2}{\sqrt{15}}$	$\frac{\sqrt{2}}{\sqrt{15}}$
	$\frac{-3}{2}$		·	·	·	·	·	$\frac{-4\sqrt{2}}{3\sqrt{15}}$	$\frac{7}{3\sqrt{15}}$	$\frac{\sqrt{2}}{\sqrt{15}}$	$\frac{2}{\sqrt{15}}$
$^4T_1\ \Gamma_8$	$\frac{3}{2}$		$\frac{-2}{5\sqrt{2}}$	·	$\frac{2}{15\sqrt{2}}$	$\frac{1}{3}$	$\frac{4}{15\sqrt{6}}$	$\frac{-8}{15\sqrt{3}}$	$\frac{-6}{5\sqrt{6}}$	$\frac{-3}{5\sqrt{3}}$	
	$\frac{-3}{2}$			$\frac{2}{5\sqrt{2}}$	$\frac{1}{3}$	$\frac{-2}{15\sqrt{2}}$	$\frac{-8}{15\sqrt{3}}$	$\frac{-4}{15\sqrt{6}}$	$\frac{-3}{5\sqrt{3}}$	$\frac{6}{5\sqrt{6}}$	
$^4T_1\ \Gamma_8'$	$\frac{3}{2}$				$\frac{23}{45\sqrt{2}}$	$\frac{-2}{9}$	$\frac{22}{15\sqrt{6}}$	$\frac{1}{15\sqrt{3}}$	$\frac{1}{15\sqrt{6}}$	$\frac{-2}{15\sqrt{3}}$	
	$\frac{-3}{2}$					$\frac{-23}{45\sqrt{2}}$	$\frac{1}{15\sqrt{3}}$	$\frac{-22}{15\sqrt{6}}$	$\frac{-2}{15\sqrt{3}}$	$\frac{-1}{15\sqrt{6}}$	
$^4T_2\ \Gamma_8$	$\frac{3}{2}$						$\frac{-14}{45\sqrt{2}}$	$\frac{-8}{45}$	$\frac{\sqrt{2}}{5}$	$\frac{-1}{5}$	
	$\frac{-3}{2}$							$\frac{14}{45\sqrt{2}}$	$\frac{-1}{5}$	$\frac{-\sqrt{2}}{5}$	
$^4T_2\ \Gamma_8'$	$\frac{3}{2}$								$\frac{1}{5\sqrt{2}}$	$\frac{2}{5}$	
	$\frac{-3}{2}$									$\frac{-1}{5\sqrt{2}}$	

Figure AII-1d

γ_4		$^2A_1$ Γ_6	$^2A_2$ Γ_7	^2E Γ_8	$^2T_1$ Γ_6	$^2T_1$ Γ_8	$^2T_2$ Γ_7	$^2T_2$ Γ_8
$^2A_1$	Γ_6	$\frac{1}{2}$	·	·	·	·	·	·
$^2A_2$	Γ_7		$\frac{1}{2}$	·	·	·	·	·
^2E	Γ_8			$\frac{-1}{2}$	·	·	·	·
$^2T_1$	Γ_6				$\frac{-1}{6}$	$\frac{-\sqrt{2}}{3}$	·	·
	Γ_8					$\frac{1}{6}$	·	·
$^2T_2$	Γ_7						$\frac{-1}{6}$	$\frac{-\sqrt{2}}{3}$
	Γ_8							$\frac{1}{6}$

Figure AII-2a

$\gamma_{5,6}$		$^2E\ \Gamma_8$ $\frac{3}{2}$	$^2E\ \Gamma_8$ $\frac{-3}{2}$	$^2T_1\ \Gamma_8$ $\frac{3}{2}$	$^2T_1\ \Gamma_8$ $\frac{-3}{2}$	$^2T_2\ \Gamma_8$ $\frac{3}{2}$	$^2T_2\ \Gamma_8$ $\frac{-3}{2}$
^2E	Γ_8 $\frac{3}{2}$	$\frac{-1}{6}$	$\frac{\sqrt{2}}{3}$	·	·	·	·
	$\frac{-3}{2}$		$\frac{1}{6}$	·	·	·	·
$^2T_1$	Γ_8 $\frac{3}{2}$			$\frac{1}{2}$	·	·	·
	$\frac{-3}{2}$				$\frac{-1}{2}$	·	·
$^2T_2$	Γ_8 $\frac{3}{2}$					$\frac{-7}{18}$	$\frac{-4}{9\sqrt{2}}$
	$\frac{-3}{2}$						$\frac{7}{18}$

Figure AII-2b

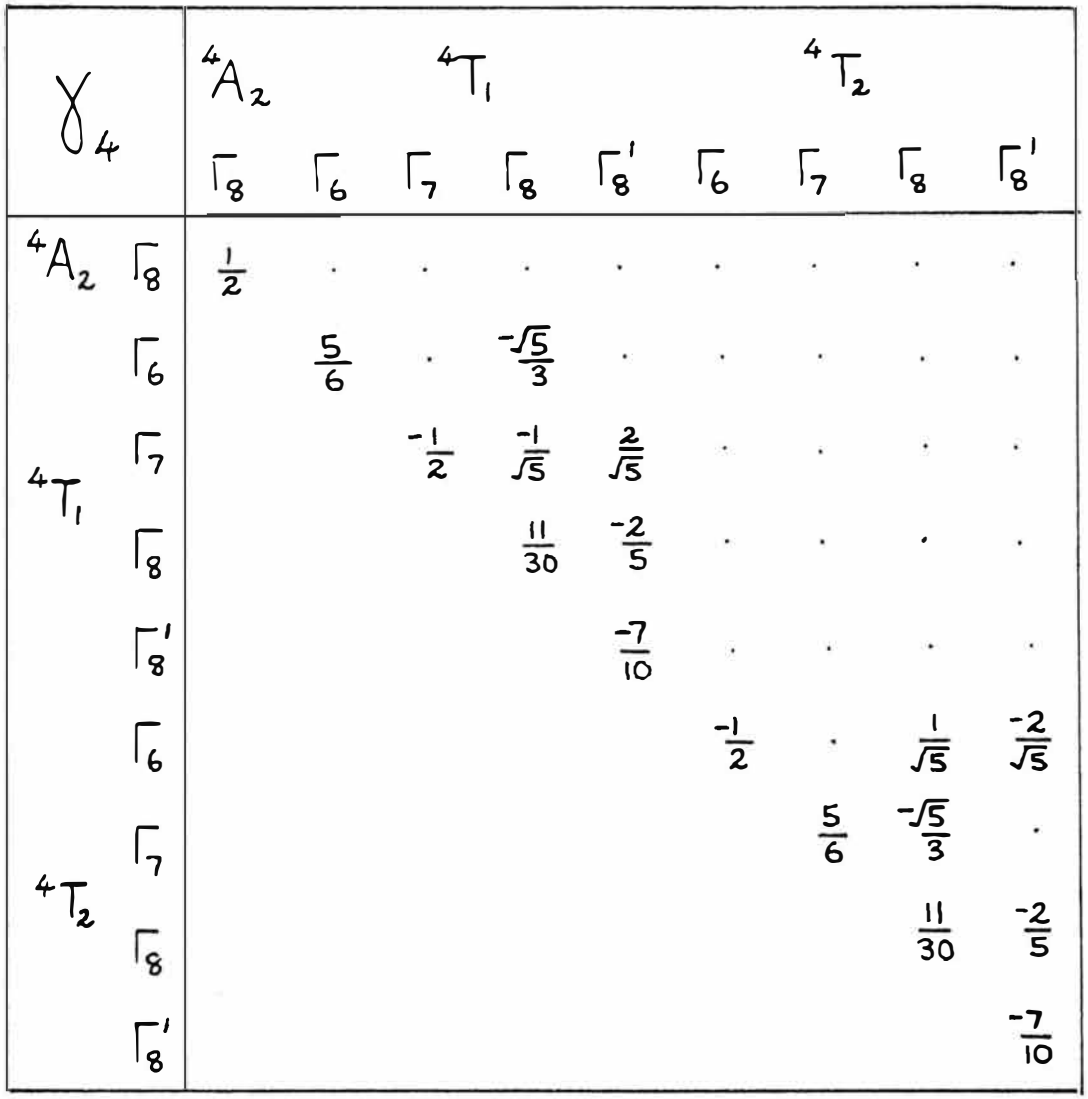

γ_4		$^4A_2$	$^4T_1$				$^4T_2$			
		Γ_8	Γ_6	Γ_7	Γ_8	Γ_8'	Γ_6	Γ_7	Γ_8	Γ_8'
$^4A_2$	Γ_8	$\frac{1}{2}$	·	·	·	·	·	·	·	·
	Γ_6		$\frac{5}{6}$	·	$\frac{-\sqrt{5}}{3}$	·	·	·	·	·
$^4T_1$	Γ_7			$\frac{-1}{2}$	$\frac{-1}{\sqrt{5}}$	$\frac{2}{\sqrt{5}}$	·	·	·	·
	Γ_8				$\frac{11}{30}$	$\frac{-2}{5}$	·	·	·	·
	Γ_8'					$\frac{-7}{10}$	·	·	·	·
$^4T_2$	Γ_6						$\frac{-1}{2}$	·	$\frac{1}{\sqrt{5}}$	$\frac{-2}{\sqrt{5}}$
	Γ_7							$\frac{5}{6}$	$\frac{-\sqrt{5}}{3}$	·
	Γ_8								$\frac{11}{30}$	$\frac{-2}{5}$
	Γ_8'									$\frac{-7}{10}$

Figure AII-2c

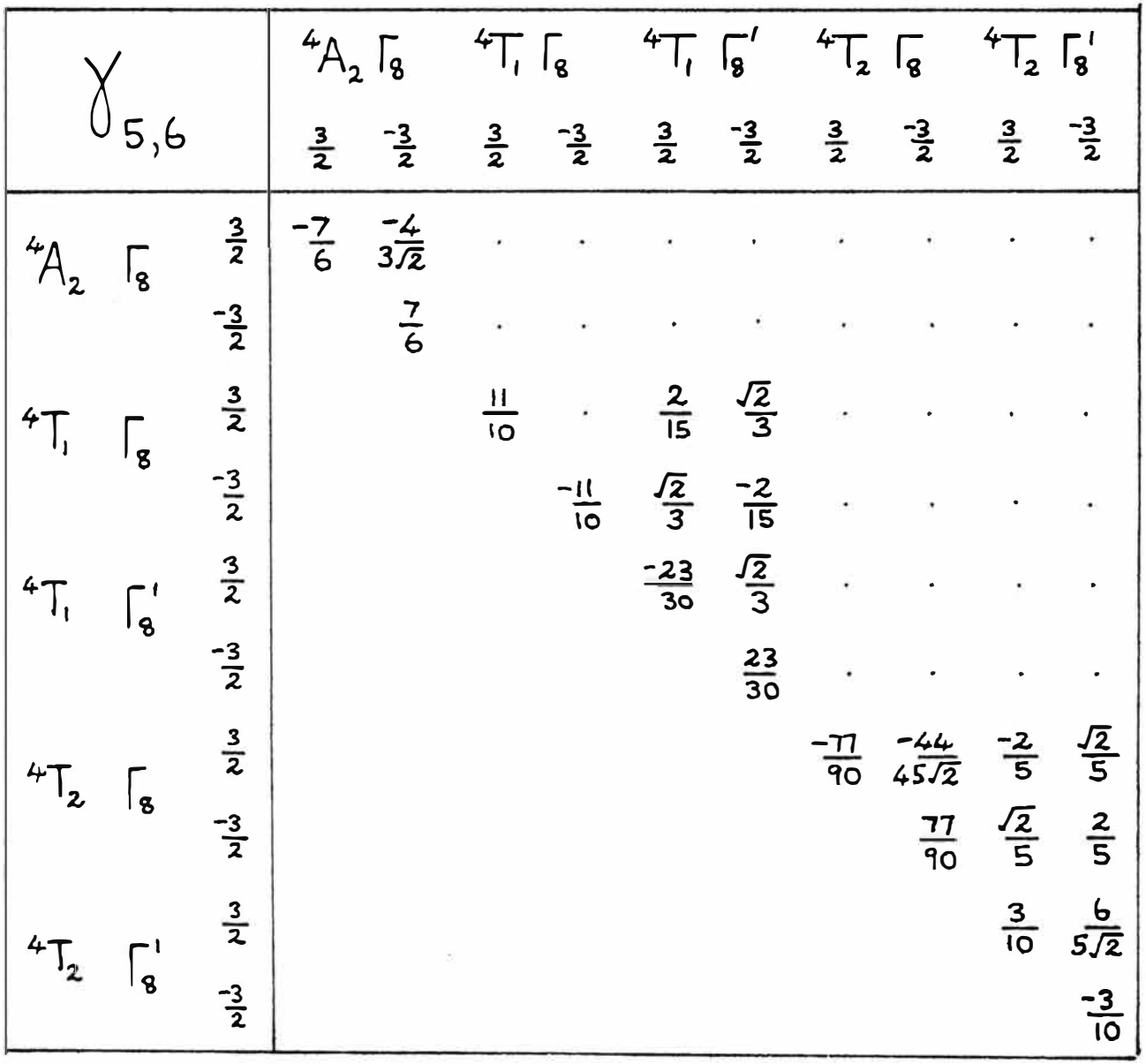

$\gamma_{5,6}$			$^4A_2\ \Gamma_8$		$^4T_1\ \Gamma_8$		$^4T_1\ \Gamma_8'$		$^4T_2\ \Gamma_8$		$^4T_2\ \Gamma_8'$	
			$\frac{3}{2}$	$\frac{-3}{2}$	$\frac{3}{2}$	$\frac{-3}{2}$	$\frac{3}{2}$	$\frac{-3}{2}$	$\frac{3}{2}$	$\frac{-3}{2}$	$\frac{3}{2}$	$\frac{-3}{2}$
$^4A_2$	Γ_8	$\frac{3}{2}$	$\frac{-7}{6}$	$\frac{-4}{3\sqrt{2}}$	·	·	·	·	·	·	·	·
		$\frac{-3}{2}$		$\frac{7}{6}$	·	·	·	·	·	·	·	·
$^4T_1$	Γ_8	$\frac{3}{2}$			$\frac{11}{10}$	·	$\frac{2}{15}$	$\frac{\sqrt{2}}{3}$	·	·	·	·
		$\frac{-3}{2}$				$\frac{-11}{10}$	$\frac{\sqrt{2}}{3}$	$\frac{-2}{15}$	·	·	·	·
$^4T_1$	Γ_8'	$\frac{3}{2}$					$\frac{-23}{30}$	$\frac{\sqrt{2}}{3}$	·	·	·	·
		$\frac{-3}{2}$						$\frac{23}{30}$	·	·	·	·
$^4T_2$	Γ_8	$\frac{3}{2}$							$\frac{-77}{90}$	$\frac{-44}{45\sqrt{2}}$	$\frac{-2}{5}$	$\frac{\sqrt{2}}{5}$
		$\frac{-3}{2}$								$\frac{77}{90}$	$\frac{\sqrt{2}}{5}$	$\frac{2}{5}$
$^4T_2$	Γ_8'	$\frac{3}{2}$									$\frac{3}{10}$	$\frac{6}{5\sqrt{2}}$
		$\frac{-3}{2}$										$\frac{-3}{10}$

Figure AII-2d

		t_2^3				t_2^2e										t_2e^2					e^3
		$^4A_2$	^2E	$^2T_1$	$^2T_2$	$(^3T_1)\,^4T_1$	$(^3T_1)\,^4T_2$	$(^1E)\,^2A_1$	$(^1E)\,^2A_2$	$(^1A)\,^2E$	$(^1E)\,^2E$	$(^3T_1)\,^2T_1$	$(^3T_1)\,^2T_1$	$(^3T_1)\,^2T_2$	$(^1T_2)\,^2T_2$	$(^3A_2)\,^4T_1$	$(^3A_2)\,^2T_1$	$(^1E)\,^2T_1$	$(^1A_1)\,^2T_2$	$(^1E)\,^2T_2$	^2E
t_2^3	$^4A_2$	•																			
	^2E	•	•																		
	$^2T_1$	•	$\sqrt{2}K$	K																	
	$^2T_2$	◦	◦	◦	K																
t_2^2e	$(^3T_1)\,^4T_1$	•	•	•	◦	$\frac{1}{2}K$															
	$(^3T_1)\,^4T_2$	K'	•	•	◦	$\frac{\sqrt{3}}{2}K$	$\frac{-1}{2}K$														
	$(^1E)\,^2A_1$	•	•	$\frac{-1}{\sqrt{2}}K'$	◦	◦	◦	◦													
	$(^1E)\,^2A_2$	•	•	◦	$\frac{1}{\sqrt{6}}K'$	◦	◦	◦	◦												
	$(^1A)\,^2E$	•	•	◦	$\frac{\sqrt{2}}{\sqrt{3}}K'$	◦	◦	◦	◦	◦											
	$(^1E)\,^2E$	•	•	$\frac{-1}{\sqrt{2}}K'$	$\frac{-1}{\sqrt{6}}K'$	◦	◦	◦	◦	◦	◦										
	$(^3T_1)\,^2T_1$	•	◦	$\frac{-3}{2\sqrt{2}}K'$	$\frac{3}{2\sqrt{2}}K'$	◦	◦	◦	◦	◦	◦	$\frac{1}{2}K$									
	$(^1T_2)\,^2T_1$	•	K'	$\frac{-1}{2\sqrt{2}}K'$	$\frac{1}{2\sqrt{2}}K'$	◦	◦	$-K$	◦	◦	$-K$	•	$\frac{-1}{2}K$								
	$(^3T_1)\,^2T_2$	•	K'	$\frac{-\sqrt{3}}{2\sqrt{2}}K'$	$\frac{\sqrt{3}}{2\sqrt{2}}K'$	◦	◦	◦	◦	◦	•	$\frac{\sqrt{3}}{2}K$	◦	$\frac{-1}{2}K$							
	$(^1T_2)\,^2T_2$	•	•	$\frac{\sqrt{3}}{2\sqrt{2}}K'$	$\frac{-\sqrt{3}}{2\sqrt{2}}K'$	◦	◦	◦	K	•	K	◦	$\frac{-\sqrt{3}}{2}K$	•	$\frac{1}{2}K$						
t_2e^2	$(^3A_2)\,^4T_1$	•	•	•	•	$\frac{-1}{\sqrt{2}}K'$	$\frac{\sqrt{3}}{\sqrt{2}}K'$	◦	◦	◦	◦	•	•	•	•	$-K$					
	$(^3A_2)\,^2T_1$	•	•	•	•	◦	◦	$\frac{1}{\sqrt{2}}K'$	•	$\frac{1}{\sqrt{2}}K'$	$\frac{-1}{\sqrt{2}}K'$	$\frac{-1}{2\sqrt{2}}K'$	$\frac{-3}{2\sqrt{2}}K'$	$\frac{\sqrt{3}}{2\sqrt{2}}K'$	$\frac{-\sqrt{3}}{2\sqrt{2}}K'$	•	$-K$				
	$(^1E)\,^2T_1$	•	•	•	•	◦	◦	$\frac{-1}{\sqrt{6}}K'$	•	$\frac{-1}{\sqrt{6}}K'$	$\frac{1}{\sqrt{6}}K'$	$\frac{\sqrt{3}}{\sqrt{2}}K'$	•	•	$\frac{-1}{\sqrt{2}}K'$	•	•	$\frac{1}{2}K$			
	$(^1A_1)\,^2T_2$	•	•	•	•	◦	◦	•	$\frac{-1}{\sqrt{6}}K'$	$\frac{1}{\sqrt{6}}K'$	$\frac{1}{\sqrt{6}}K'$	$\frac{-3}{2\sqrt{2}}K'$	$\frac{-1}{2\sqrt{2}}K'$	$\frac{-\sqrt{3}}{2\sqrt{2}}K'$	$\frac{\sqrt{3}}{2\sqrt{2}}K'$	•	•	•	K		
	$(^1E)\,^2T_2$	•	•	•	•	•	•	•	$\frac{-1}{\sqrt{6}}K'$	$\frac{1}{\sqrt{6}}K'$	$\frac{1}{\sqrt{6}}K'$	•	$\frac{1}{\sqrt{2}}K'$	$\frac{\sqrt{3}}{\sqrt{2}}K'$	•	•	•	$\frac{\sqrt{3}}{2}K$	•	$\frac{-1}{2}K$	
e^3	^2E	•	•	•	•	•	•	•	•	•	•	•	•	•	•	•	$\frac{-\sqrt{3}}{\sqrt{2}}K'$	$\frac{1}{\sqrt{2}}K'$	$\frac{1}{\sqrt{2}}K'$	$\frac{-1}{\sqrt{2}}K'$	•

Figure AII-3

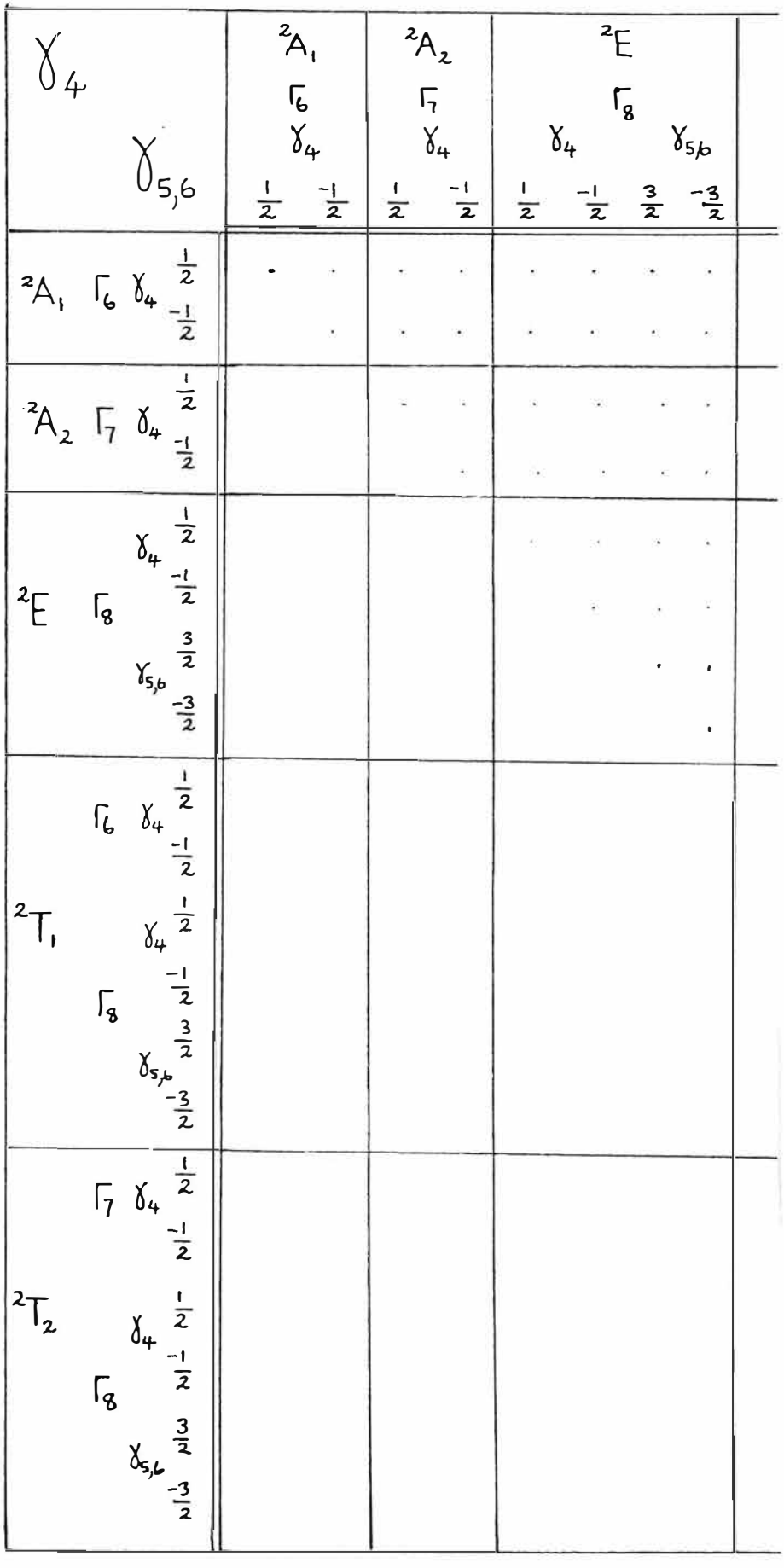

Figure AII-4a

Figure AII-4b

	$^2\Gamma_1$						$^2\Gamma_2$					
	Γ_6			Γ_8			Γ_7			Γ_8		
	γ_4		γ_4		$\gamma_{5,6}$		γ_4		γ_4		$\gamma_{5,6}$	
	$\frac{1}{2}$	$\frac{-1}{2}$	$\frac{1}{2}$	$\frac{-1}{2}$	$\frac{3}{2}$	$\frac{-3}{2}$	$\frac{1}{2}$	$\frac{-1}{2}$	$\frac{1}{2}$	$\frac{-1}{2}$	$\frac{3}{2}$	$\frac{-3}{2}$
	·	$\frac{-1}{3}$	·	$\frac{-1}{3\sqrt{2}}$	$\frac{1}{\sqrt{6}}$	·	·	·	·	·	·	·
	$\frac{-1}{3}$	·	$\frac{-1}{3\sqrt{2}}$	·	·	$\frac{-1}{\sqrt{6}}$	·	·	·	·	·	·
	·	·	·	·	·	·	·	$\frac{1}{3}$	·	$\frac{1}{3\sqrt{2}}$	$\frac{-1}{3\sqrt{6}}$	$\frac{2}{3\sqrt{3}}$
	·	·	·	·	·	·	$\frac{1}{3}$	·	$\frac{1}{3\sqrt{2}}$	·	$\frac{2}{3\sqrt{3}}$	$\frac{1}{3\sqrt{6}}$
	·	$\frac{-1}{6}$	·	$\frac{1}{3\sqrt{2}}$	·	$\frac{-1}{2\sqrt{3}}$	·	$\frac{1}{6}$	·	$\frac{-1}{3\sqrt{2}}$	$\frac{-2}{3\sqrt{6}}$	$\frac{-1}{6\sqrt{3}}$
	$\frac{-1}{6}$	·	$\frac{1}{3\sqrt{2}}$	·	$\frac{-1}{2\sqrt{3}}$	·	$\frac{1}{6}$	·	$\frac{-1}{3\sqrt{2}}$	·	$\frac{-1}{6\sqrt{3}}$	$\frac{2}{3\sqrt{6}}$
	$\frac{1}{2\sqrt{3}}$	·	·	$\frac{-1}{2\sqrt{3}}$	·	·	$\frac{-1}{6\sqrt{3}}$	$\frac{2}{3\sqrt{6}}$	$\frac{-2}{3\sqrt{6}}$	$\frac{-1}{6\sqrt{3}}$	·	·
	·	$\frac{-1}{2\sqrt{3}}$	$\frac{-1}{2\sqrt{3}}$	·	·	·	$\frac{2}{3\sqrt{6}}$	$\frac{1}{6\sqrt{3}}$	$\frac{-1}{6\sqrt{3}}$	$\frac{2}{3\sqrt{6}}$	·	·
	·	$\frac{-2}{3\sqrt{6}}$	·	$\frac{1}{6\sqrt{3}}$	$\frac{-1}{6}$	·	·	·	·	$\frac{-1}{6}$	$\frac{1}{2\sqrt{3}}$	·
		·	$\frac{1}{6\sqrt{3}}$	·	·	$\frac{1}{6}$	·	·	$\frac{-1}{6}$	·	·	$\frac{-1}{2\sqrt{3}}$
			·	$\frac{2}{3\sqrt{6}}$	$\frac{1}{3\sqrt{2}}$	·	·	$\frac{1}{6}$	·	·	$\frac{1}{3\sqrt{6}}$	$\frac{1}{3\sqrt{3}}$
				·	·	$\frac{-1}{3\sqrt{2}}$	$\frac{1}{6}$	·	·	·	$\frac{1}{3\sqrt{3}}$	$\frac{-1}{3\sqrt{6}}$
					·	·	$\frac{-1}{6\sqrt{3}}$	$\frac{2}{3\sqrt{6}}$	$\frac{1}{3\sqrt{6}}$	$\frac{1}{3\sqrt{3}}$	·	·
						·	$\frac{2}{3\sqrt{6}}$	$\frac{1}{6\sqrt{3}}$	$\frac{1}{3\sqrt{3}}$	$\frac{-1}{3\sqrt{6}}$	·	·
							·	$\frac{-2}{3\sqrt{6}}$	·	$\frac{1}{6\sqrt{3}}$	$\frac{-1}{18}$	$\frac{\sqrt{2}}{9}$
							·	·	$\frac{1}{6\sqrt{3}}$	·	$\frac{\sqrt{2}}{9}$	$\frac{1}{18}$
								·	·	$\frac{2}{3\sqrt{6}}$	$\frac{1}{9\sqrt{2}}$	$\frac{-2}{9}$
									·	·	$\frac{-2}{9}$	$\frac{-1}{9\sqrt{2}}$
											·	·
												·

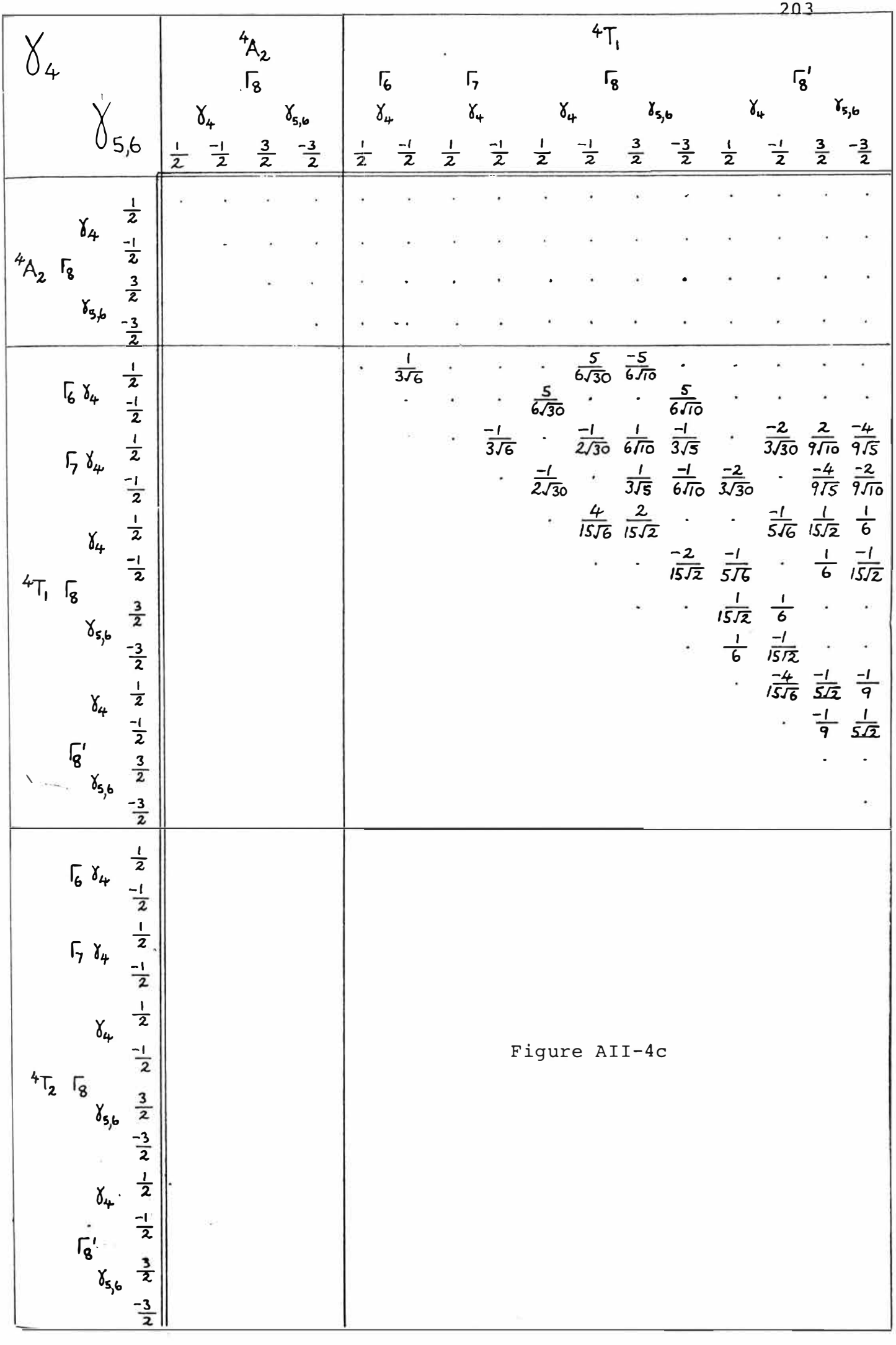

Figure AII-4c

Γ_8'		$^4T_2$											
		Γ_6		Γ_7		Γ_8				Γ_8'			
$\gamma_{5,6}$		γ_4		γ_4		γ_4		$\gamma_{5,6}$		γ_4		$\gamma_{5,6}$	
$\frac{3}{2}$	$\frac{-3}{2}$	$\frac{1}{2}$	$\frac{-1}{2}$	$\frac{1}{2}$	$\frac{-1}{2}$	$\frac{1}{2}$	$\frac{-1}{2}$	$\frac{3}{2}$	$\frac{-3}{2}$	$\frac{1}{2}$	$\frac{-1}{2}$	$\frac{3}{2}$	$\frac{-3}{2}$
.	.	.	$\frac{-1}{6}$	.	$\frac{1}{6}$	.	$\frac{2}{3\sqrt{5}}$	$\frac{1}{3\sqrt{15}}$	$\frac{-4}{3\sqrt{10}}$	.	$\frac{1}{3\sqrt{5}}$	$\frac{1}{\sqrt{15}}$	$\frac{1}{\sqrt{30}}$
.	.	$\frac{-1}{6}$	.	$\frac{1}{6}$	.	$\frac{2}{3\sqrt{5}}$	.	$\frac{-4}{3\sqrt{30}}$	$\frac{-1}{3\sqrt{15}}$	$\frac{1}{3\sqrt{5}}$	.	$\frac{1}{\sqrt{30}}$	$\frac{-1}{\sqrt{15}}$
.	.	$\frac{1}{2\sqrt{3}}$	.	$\frac{-1}{6\sqrt{3}}$	$\frac{2}{3\sqrt{6}}$	$\frac{1}{3\sqrt{15}}$	$\frac{-4}{3\sqrt{30}}$	.	.	$\frac{1}{\sqrt{15}}$	$\frac{1}{\sqrt{30}}$	.	.
.	.	.	$\frac{-1}{2\sqrt{3}}$	$\frac{2}{3\sqrt{6}}$	$\frac{1}{6\sqrt{3}}$	$\frac{-4}{3\sqrt{30}}$	$\frac{-1}{3\sqrt{15}}$	.	.	$\frac{1}{\sqrt{30}}$	$\frac{-1}{\sqrt{15}}$	.	.
.	.	.	$\frac{-1}{3\sqrt{2}}$	.	.	.	$\frac{1}{6\sqrt{10}}$	$\frac{-1}{2\sqrt{30}}$	.	.	$\frac{-1}{3\sqrt{10}}$	$\frac{1}{\sqrt{30}}$	.
.	.	$\frac{-1}{3\sqrt{2}}$	.	.	.	$\frac{1}{6\sqrt{10}}$	.	.	$\frac{1}{2\sqrt{30}}$	$\frac{-1}{3\sqrt{10}}$	.	.	$\frac{-1}{\sqrt{30}}$
$\frac{2}{9\sqrt{10}}$	$\frac{-4}{9\sqrt{5}}$	.	.	.	$\frac{-1}{3\sqrt{2}}$	.	$\frac{1}{6\sqrt{10}}$	$\frac{-1}{6\sqrt{30}}$	$\frac{1}{3\sqrt{15}}$	.	$\frac{-1}{3\sqrt{10}}$	$\frac{1}{3\sqrt{30}}$	$\frac{-2}{3\sqrt{15}}$
$\frac{-4}{9\sqrt{5}}$	$\frac{-2}{9\sqrt{10}}$	.	.	$\frac{-1}{3\sqrt{2}}$	.	$\frac{1}{6\sqrt{10}}$	.	$\frac{1}{3\sqrt{15}}$	$\frac{1}{6\sqrt{30}}$	$\frac{-1}{3\sqrt{10}}$	.	$\frac{-2}{3\sqrt{15}}$	$\frac{-1}{3\sqrt{30}}$
$\frac{1}{15\sqrt{2}}$	$\frac{1}{6}$	.	$\frac{1}{6\sqrt{10}}$	.	$\frac{-1}{6\sqrt{10}}$	.	.	$\frac{-4}{15\sqrt{6}}$	$\frac{-4}{15\sqrt{3}}$	.	$\frac{1}{3\sqrt{2}}$	$\frac{1}{5\sqrt{6}}$	$\frac{-3}{10\sqrt{3}}$
$\frac{1}{6}$	$\frac{-1}{15\sqrt{2}}$	$\frac{1}{6\sqrt{10}}$	.	$\frac{-1}{6\sqrt{10}}$	.	.	.	$\frac{-4}{15\sqrt{3}}$	$\frac{4}{15\sqrt{6}}$	$\frac{1}{3\sqrt{2}}$	.	$\frac{-3}{10\sqrt{3}}$	$\frac{1}{5\sqrt{6}}$
.	.	$\frac{-1}{2\sqrt{30}}$	.	$\frac{1}{6\sqrt{30}}$	$\frac{-1}{3\sqrt{15}}$	$\frac{-4}{15\sqrt{6}}$	$\frac{-4}{15\sqrt{3}}$	.	.	$\frac{1}{5\sqrt{6}}$	$\frac{-3}{10\sqrt{3}}$	.	.
.	.	.	$\frac{1}{2\sqrt{30}}$	$\frac{-1}{3\sqrt{15}}$	$\frac{-1}{6\sqrt{30}}$	$\frac{-4}{15\sqrt{3}}$	$\frac{4}{15\sqrt{6}}$	.	.	$\frac{-3}{10\sqrt{3}}$	$\frac{-1}{5\sqrt{6}}$	.	.
$\frac{-1}{5\sqrt{2}}$	$\frac{-1}{9}$	.	$\frac{-1}{3\sqrt{10}}$	.	$\frac{1}{3\sqrt{10}}$	.	$\frac{-1}{3\sqrt{2}}$	$\frac{-7}{15\sqrt{6}}$	$\frac{1}{30\sqrt{3}}$	.	.	$\frac{-1}{15\sqrt{6}}$	$\frac{-1}{15\sqrt{3}}$
$\frac{-1}{9}$	$\frac{1}{5\sqrt{2}}$	$\frac{-1}{3\sqrt{10}}$	.	$\frac{1}{3\sqrt{10}}$	.	$\frac{-1}{3\sqrt{2}}$	.	$\frac{1}{30\sqrt{3}}$	$\frac{7}{15\sqrt{6}}$	.	.	$\frac{-1}{15\sqrt{3}}$	$\frac{1}{15\sqrt{6}}$
.	.	$\frac{1}{\sqrt{30}}$	.	$\frac{-1}{3\sqrt{30}}$	$\frac{2}{3\sqrt{15}}$	$\frac{-7}{15\sqrt{6}}$	$\frac{1}{30\sqrt{3}}$	.	.	$\frac{-1}{15\sqrt{6}}$	$\frac{-1}{15\sqrt{3}}$	.	.
	.	.	$\frac{-1}{\sqrt{30}}$	$\frac{2}{3\sqrt{15}}$	$\frac{1}{3\sqrt{30}}$	$\frac{1}{30\sqrt{3}}$	$\frac{7}{15\sqrt{6}}$	.	.	$\frac{-1}{15\sqrt{3}}$	$\frac{1}{15\sqrt{6}}$	.	.
		.	$\frac{-1}{3\sqrt{6}}$	.	.	.	$\frac{1}{2\sqrt{30}}$	$\frac{-1}{2\sqrt{10}}$	.	.	$\frac{2}{3\sqrt{30}}$	$\frac{-2}{3\sqrt{10}}$	.
			.	.	.	$\frac{1}{2\sqrt{30}}$	.	.	$\frac{1}{2\sqrt{10}}$	$\frac{2}{3\sqrt{30}}$	.	.	$\frac{2}{3\sqrt{10}}$
				.	$\frac{1}{3\sqrt{6}}$	.	$\frac{5}{6\sqrt{30}}$	$\frac{-5}{18\sqrt{10}}$	$\frac{\sqrt{5}}{9}$	.	.	.	.
				.	.	$\frac{5}{6\sqrt{30}}$	.	$\frac{\sqrt{5}}{9}$	$\frac{5}{18\sqrt{10}}$	.	.	.	.
						.	$\frac{4}{15\sqrt{6}}$	$\frac{\sqrt{2}}{45}$	$\frac{-4}{45}$	.	$\frac{-1}{5\sqrt{6}}$	$\frac{-1}{5\sqrt{2}}$	$\frac{-1}{10}$
							.	$\frac{-4}{45}$	$\frac{-\sqrt{2}}{45}$	$\frac{-1}{5\sqrt{6}}$	.	$\frac{-1}{10}$	$\frac{1}{5\sqrt{2}}$
								.	.	$\frac{-1}{5\sqrt{2}}$	$\frac{-1}{10}$	.	.
									.	$\frac{-1}{10}$	$\frac{1}{5\sqrt{2}}$	.	.
										.	$\frac{-4}{15\sqrt{6}}$	$\frac{1}{15\sqrt{2}}$	$\frac{1}{5}$
											.	$\frac{1}{5}$	$\frac{-1}{15\sqrt{2}}$
												.	.
													.

Figure AII-4d

Figure AII-5a

γ_4 / $\gamma_{5,6}$			$^2A_1$ Γ_6 γ_4		$^2A_2$ Γ_7 γ_4		^2E Γ_8			
							γ_4		$\gamma_{5,6}$	
			$\frac{1}{2}$	$\frac{-1}{2}$	$\frac{1}{2}$	$\frac{-1}{2}$	$\frac{1}{2}$	$\frac{-1}{2}$	$\frac{3}{2}$	$\frac{-3}{2}$
$^2A_1$ Γ_6	γ_4	$\frac{1}{2}$		$\frac{1}{2}$						
		$\frac{-1}{2}$								
$^2A_2$ Γ_7	γ_4	$\frac{1}{2}$				$\frac{-1}{2}$				
		$\frac{-1}{2}$								
^2E Γ_8	γ_4	$\frac{1}{2}$							$\frac{1}{2\sqrt{3}}$	$\frac{1}{\sqrt{6}}$
		$\frac{-1}{2}$							$\frac{1}{\sqrt{6}}$	$\frac{-1}{2\sqrt{3}}$
	$\gamma_{5,6}$	$\frac{3}{2}$								
		$\frac{-3}{2}$								
$^2T_1$ Γ_6	γ_4	$\frac{1}{2}$								
		$\frac{-1}{2}$								
Γ_8	γ_4	$\frac{1}{2}$								
		$\frac{-1}{2}$								
	$\gamma_{5,6}$	$\frac{3}{2}$								
		$\frac{-3}{2}$								
$^2T_2$ Γ_7	γ_4	$\frac{1}{2}$								
		$\frac{-1}{2}$								
Γ_8	γ_4	$\frac{1}{2}$								
		$\frac{1}{2}$								
	$\gamma_{5,6}$	$\frac{3}{2}$								
		$\frac{-3}{2}$								

Figure AII-5b

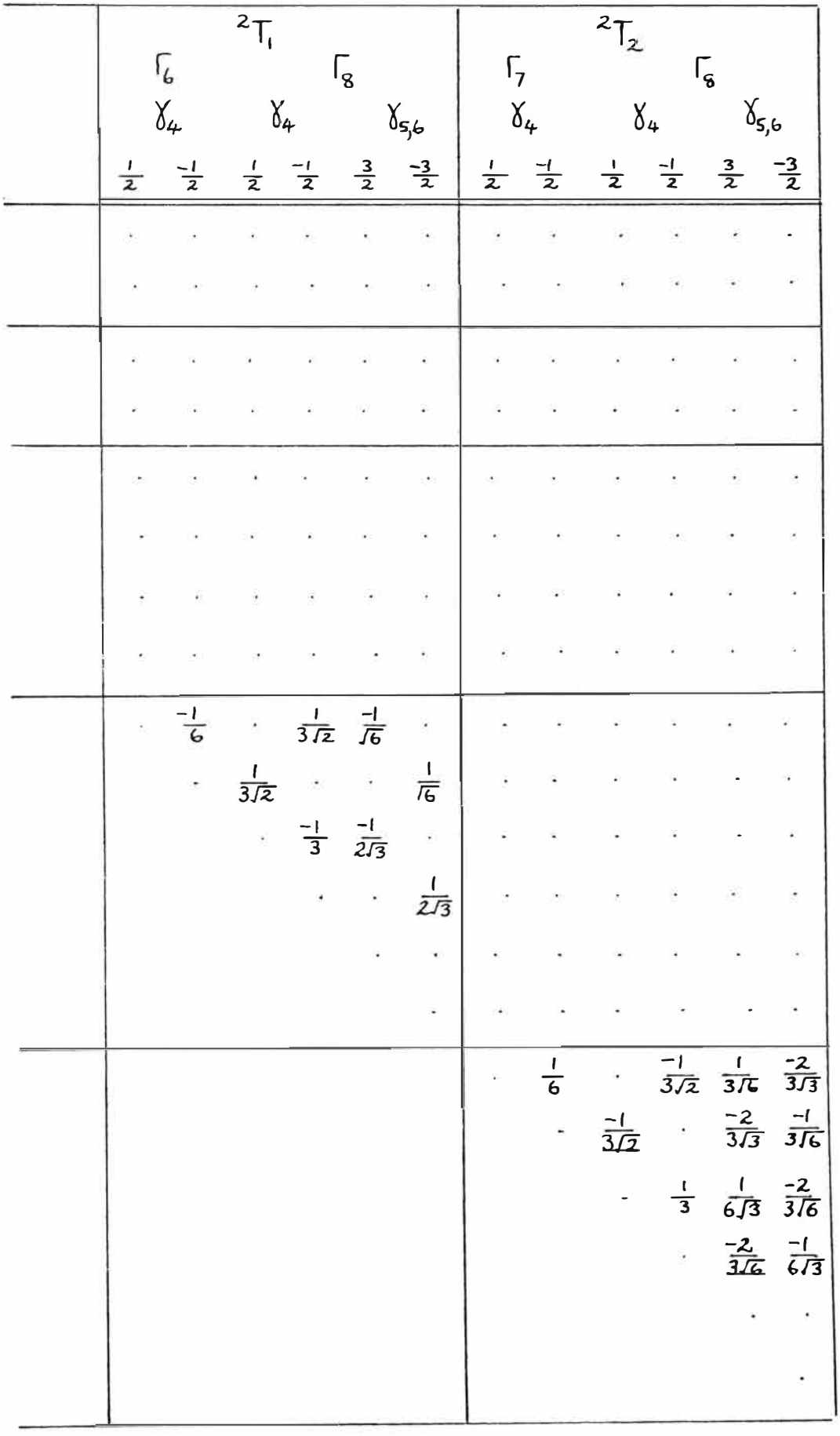

γ_4 / $\gamma_{5,6}$		$^4A_2$ Γ_8				$^4T_1$ Γ_6				$^4T_1$ Γ_7				$^4T_1$ Γ_8				$^4T_1$ Γ_8'			
		γ_4		$\gamma_{5,6}$		γ_4				γ_4				γ_4		$\gamma_{5,6}$		γ_4		$\gamma_{5,6}$	
		$\frac{1}{2}$	$\frac{-1}{2}$	$\frac{3}{2}$	$\frac{-3}{2}$	$\frac{1}{2}$	$\frac{-1}{2}$	$\frac{1}{2}$	$\frac{-1}{2}$	$\frac{1}{2}$	$\frac{-1}{2}$	$\frac{3}{2}$	$\frac{-3}{2}$	$\frac{1}{2}$	$\frac{-1}{2}$	$\frac{3}{2}$	$\frac{-3}{2}$	$\frac{1}{2}$	$\frac{-1}{2}$	$\frac{3}{2}$	$\frac{-3}{2}$
$^4A_2$ Γ_8 γ_4	$\frac{1}{2}$	·	1	$\frac{1}{2\sqrt{3}}$	$\frac{-2}{\sqrt{6}}$	·	·	·	·	·	·	·	·	·	·	·	·	·	·	·	·
	$\frac{-1}{2}$		·	$\frac{-2}{\sqrt{6}}$	$\frac{-1}{2\sqrt{3}}$	·	·	·	·	·	·	·	·	·	·	·	·	·	·	·	·
$\gamma_{5,6}$	$\frac{3}{2}$			·	·	·	·	·	·	·	·	·	·	·	·	·	·	·	·	·	·
	$\frac{-3}{2}$				·	·	·	·	·	·	·	·	·	·	·	·	·	·	·	·	·
Γ_6 γ_4	$\frac{1}{2}$					·	$\frac{5}{6}$	·	·	·	·	$\frac{\sqrt{5}}{6}$	$\frac{-\sqrt{5}}{2\sqrt{3}}$	·	·	·	·	·	·	·	·
	$\frac{-1}{2}$						·	·	·	$\frac{\sqrt{5}}{6}$	·	·	$\frac{\sqrt{5}}{2\sqrt{3}}$	·	·	·	·	·	·	·	·
Γ_7 γ_4	$\frac{1}{2}$							·	$\frac{1}{2}$	·	$\frac{-1}{2\sqrt{5}}$	$\frac{1}{2\sqrt{15}}$	$\frac{-2}{\sqrt{30}}$	·	$\frac{1}{\sqrt{5}}$	$\frac{-1}{\sqrt{15}}$	$\frac{4}{\sqrt{30}}$				
	$\frac{-1}{2}$							·	·	$\frac{-1}{2\sqrt{5}}$	·	$\frac{-2}{\sqrt{30}}$	$\frac{-1}{2\sqrt{15}}$	$\frac{1}{\sqrt{5}}$	·	$\frac{4}{\sqrt{30}}$	$\frac{1}{\sqrt{15}}$				
γ_4	$\frac{1}{2}$									·	$\frac{-11}{15}$	$\frac{-11}{10\sqrt{3}}$	·	·	$\frac{-1}{5}$	$\frac{1}{5\sqrt{3}}$	$\frac{1}{\sqrt{6}}$				
	$\frac{-1}{2}$										·	·	$\frac{11}{10\sqrt{3}}$	$\frac{-1}{5}$	·	$\frac{1}{\sqrt{6}}$	$\frac{-1}{5\sqrt{3}}$				
$^4T_1$ Γ_8 $\gamma_{5,6}$	$\frac{3}{2}$											·	·	$\frac{1}{5\sqrt{3}}$	$\frac{1}{\sqrt{6}}$	·	·				
	$\frac{-3}{2}$												·	$\frac{1}{\sqrt{6}}$	$\frac{-1}{5\sqrt{3}}$	·	·				
γ_4	$\frac{1}{2}$													·	$\frac{4}{10}$	$\frac{11}{10\sqrt{3}}$	$\frac{1}{\sqrt{6}}$				
	$\frac{-1}{2}$														·	$\frac{1}{\sqrt{6}}$	$\frac{-11}{10\sqrt{3}}$				
Γ_8' $\gamma_{5,6}$	$\frac{3}{2}$															·	·				
	$\frac{-3}{2}$																·				
Γ_6 γ_4	$\frac{1}{2}$																				
	$\frac{-1}{2}$																				
Γ_7 γ_4	$\frac{1}{2}$																				
	$\frac{-1}{2}$																				
γ_4	$\frac{1}{2}$																				
	$\frac{-1}{2}$																				
$^4T_2$ Γ_8 $\gamma_{5,6}$	$\frac{3}{2}$																				
	$\frac{-3}{2}$																				
γ_4	$\frac{1}{2}$																				
	$\frac{-1}{2}$																				
Γ_8' $\gamma_{5,6}$	$\frac{3}{2}$																				
	$\frac{-3}{2}$																				

Figure AII-5c

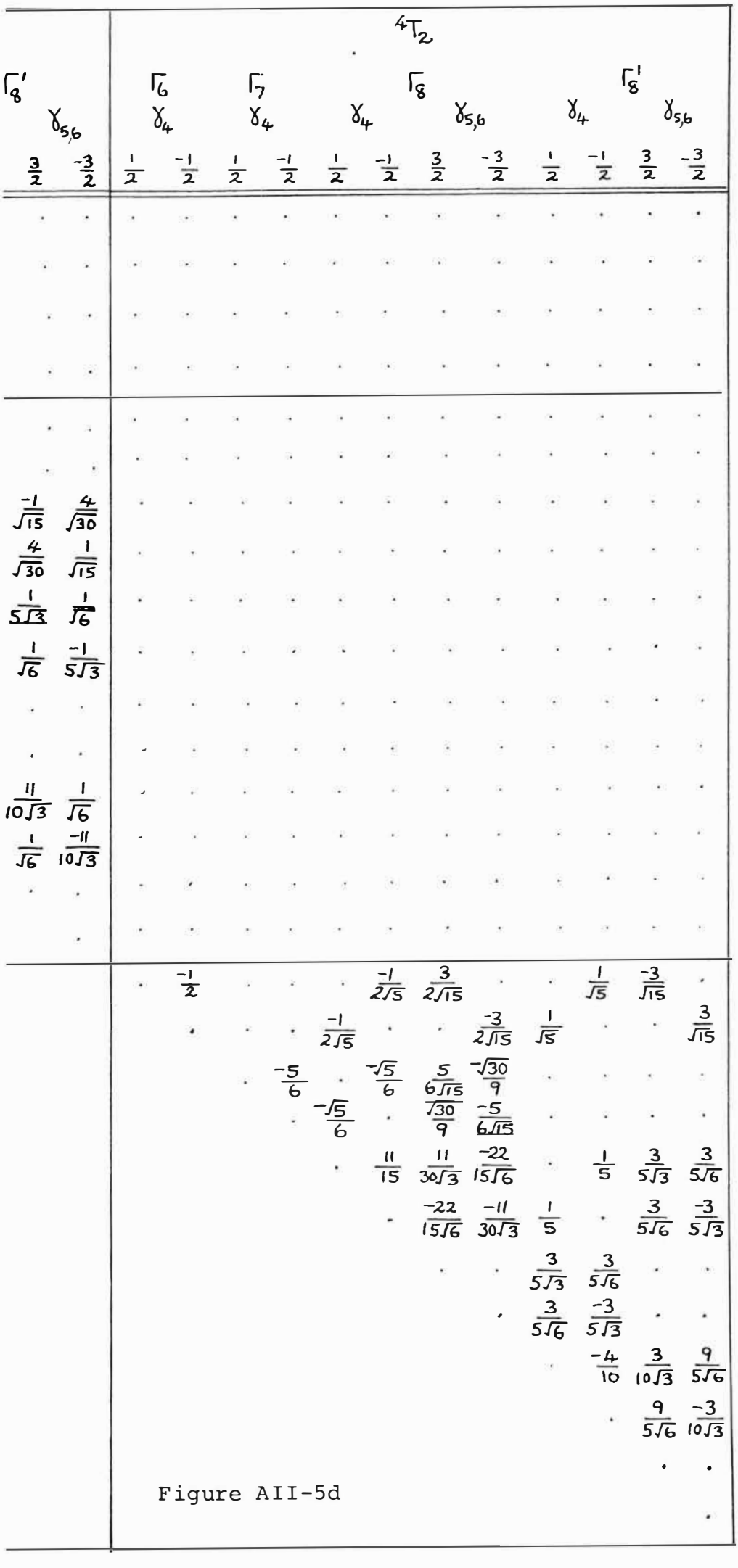

Figure AII-5d

APPENDIX III

Required Matrix Elements of the Operator S_x describing the Molecular Field Appropriate to A.F.M. $CoCl_2$

The non-zero matrix elements of the above operator are evaluated between the six lowest Kramers doublets of $CoCl_2$ and listed below. Each element is labelled $\langle i|op|j\rangle$ i,j = 0,11 where the unperturbed states are characterised by the following energies:

$\|11\rangle, \|10\rangle$: (1115.1 cm^{-1})	$\|5\rangle, \|4\rangle$: (548.8 cm^{-1})
$\|9\rangle, \|8\rangle$: (991.2 cm^{-1})	$\|3\rangle, \|2\rangle$: (216.8 cm^{-1})
$\|7\rangle, \|6\rangle$: (965.3 cm^{-1})	$\|1\rangle, \|0\rangle$: (0.0 cm^{-1})

S_x

$\langle 10\|$	$\|11\rangle$	=	0.12556471	$\langle 3\|$	$\|6\rangle$	=	0.17484382
$\langle 9\|$	$\|11\rangle$	=	0.59047497	$\langle 3\|$	$\|5\rangle$	=	0.03440351
$\langle 9\|$	$\|10\rangle$	=	0.55554330	$\langle 3\|$	$\|4\rangle$	=	0.38718838
$\langle 8\|$	$\|11\rangle$	=	0.55554330	$\langle 2\|$	$\|11\rangle$	=	-0.30923448
$\langle 8\|$	$\|10\rangle$	=	-0.59047497	$\langle 2\|$	$\|10\rangle$	=	0.04584111
$\langle 7\|$	$\|10\rangle$	=	0.30527594	$\langle 2\|$	$\|7\rangle$	=	0.17484382
$\langle 7\|$	$\|9\rangle$	=	-0.50165561	$\langle 2\|$	$\|6\rangle$	=	0.21792022
$\langle 7\|$	$\|8\rangle$	=	0.62327124	$\langle 2\|$	$\|5\rangle$	=	-0.38718838
$\langle 6\|$	$\|11\rangle$	=	0.30527594	$\langle 2\|$	$\|4\rangle$	=	0.03440351
$\langle 6\|$	$\|9\rangle$	=	0.62327124	$\langle 1\|$	$\|11\rangle$	=	-0.01054126
$\langle 6\|$	$\|8\rangle$	=	0.50165561	$\langle 1\|$	$\|9\rangle$	=	0.08558177
$\langle 6\|$	$\|7\rangle$	=	0.72533331	$\langle 1\|$	$\|8\rangle$	=	0.05458017
$\langle 5\|$	$\|11\rangle$	=	-0.17086950	$\langle 1\|$	$\|7\rangle$	=	-0.03890570
$\langle 5\|$	$\|9\rangle$	=	0.47231672	$\langle 1\|$	$\|4\rangle$	=	0.14458305

<5|	|8>	=	0.19462245	<1|	|3>	=	-0.00492336
<5|	|7>	=	-0.28272781	<1|	|2>	=	-0.76577296
<4|	|10>	=	-0.17086950	<0|	|10>	=	-0.01054126
<4|	|9>	=	-0.19462245	<0|	|9>	=	-0.05458015
<4|	|8>	=	0.47231672	<0|	|8>	=	0.08558177
<4|	|6>	=	-0.28272781	<0|	|6>	=	-0.03890570
<4|	|5>	=	-0.78632716	<0|	|5>	=	0.14458305
<3|	|11>	=	-0.04584113	<0|	|3>	=	0.76577296
<3|	|10>	=	-0.30923449	<0|	|2>	=	-0.00492335
<3|	|7>	=	-0.21792021	<0|	|1>	=	0.93143059

with $\langle i|S_X|j\rangle = \langle j|S_X|i\rangle$ i,j = 0,11

APPENDIX IV

Required Matrix Elements of the Operators S_Z, S_X, S_Y, L_Z and L_X Appropriate to $CdCl_2(Co^{2+})$:5 wt.%

The non-zero matrix elements of the above operators are evaluated between the six lowest Kramers doublets of $CdCl_2(Co^{2+})$:5 wt.% and listed below. Each element is labelled $\langle i|op|j\rangle$ where i,j = 0,11 and the unperturbed states are characterised by the following energies:

$\|11\rangle, \|10\rangle$: (1088.3 cm^{-1})	$\|5\rangle, \|4\rangle$: (495.2 cm^{-1})
$\|9\rangle, \|8\rangle$: (948.3 cm^{-1})	$\|3\rangle, \|2\rangle$: (225.2 cm^{-1})
$\|7\rangle, \|6\rangle$: (920.2 cm^{-1})	$\|1\rangle, \|0\rangle$: (0.0 cm^{-1})

(i) S_Z

$\langle 11\|$	$\|11\rangle$	=	1.24325942	$\langle 3\|$	$\|9\rangle$	=	-0.00859904
$\langle 10\|$	$\|10\rangle$	=	-1.24325942	$\langle 3\|$	$\|8\rangle$	=	0.39148466
$\langle 9\|$	$\|9\rangle$	=	0.57881755	$\langle 3\|$	$\|3\rangle$	=	-1.31319482
$\langle 8\|$	$\|9\rangle$	=	0.32362169	$\langle 2\|$	$\|9\rangle$	=	0.39148482
$\langle 8\|$	$\|8\rangle$	=	-0.57881755	$\langle 2\|$	$\|8\rangle$	=	0.00859829
$\langle 7\|$	$\|11\rangle$	=	-0.59619370	$\langle 2\|$	$\|3\rangle$	=	0.06659990
$\langle 7\|$	$\|7\rangle$	=	0.00675629	$\langle 2\|$	$\|2\rangle$	=	1.31319483
$\langle 6\|$	$\|10\rangle$	=	0.59619370	$\langle 1\|$	$\|10\rangle$	=	-0.05714106
$\langle 6\|$	$\|6\rangle$	=	-0.00675629	$\langle 1\|$	$\|6\rangle$	=	-0.02755611
$\langle 5\|$	$\|10\rangle$	=	-0.17756836	$\langle 1\|$	$\|5\rangle$	=	-0.65375251
$\langle 5\|$	$\|6\rangle$	=	-0.70500895	$\langle 1\|$	$\|1\rangle$	=	0.62203842
$\langle 5\|$	$\|5\rangle$	=	0.62982713	$\langle 0\|$	$\|11\rangle$	=	0.05714106
$\langle 4\|$	$\|11\rangle$	=	0.17756836	$\langle 0\|$	$\|7\rangle$	=	0.02755611
$\langle 4\|$	$\|7\rangle$	=	0.70500895	$\langle 0\|$	$\|4\rangle$	=	0.65375251
$\langle 4\|$	$\|4\rangle$	=	-0.62982713	$\langle 0\|$	$\|0\rangle$	=	-0.62203842

with $\langle i|S_Z|j\rangle = \langle j|S_Z|i\rangle$ i,j = 0,11

ERRATUM:

APPENDIX IV(ii) on p.212 should appear on p.217 as APPENDIX V(ii) and vice-versa.

(ii) S_X

<10|	|11>	=	0.21267288	<3|	|6>	=	0.26014295
<9|	|11>	=	0.49105234	<3|	|5>	=	0.03870102
<9|	|10>	=	0.60680948	<3|	|4>	=	0.51225003
<8|	|11>	=	0.60680948	<2|	|11>	=	-0.37065222
<8|	|10>	=	-0.49105234	<2|	|10>	=	0.06799637
<7|	|10>	=	0.3827296	<2|	|7>	=	0.26014295
<7|	|9>	=	-0.53562128	<2|	|6>	=	0.22101638
<7|	|8>	=	0.56385881	<2|	|5>	=	-0.51225003
<6|	|11>	=	0.38027296	<2|	|4>	=	0.03870102
<6|	|9>	=	0.56385881	<1|	|11>	=	-0.00276370
<6|	|8>	=	0.53562128	<1|	|9>	=	0.04804253
<6|	|7>	=	0.67377264	<1|	|8>	=	0.04662430
<5|	|11>	=	-0.17152771	<1|	|7>	=	-0.02633274
<5|	|9>	=	0.45932628	<1|	|4>	=	0.26640467
<5|	|8>	=	0.18786878	<1|	|3>	=	-0.00134329
<5|	|7>	=	-0.23035578	<1|	|2>	=	-0.70420404
<4|	|10>	=	-0.17152771	<0|	|10>	=	-0.00276370
<4|	|9>	=	-0.18786878	<0|	|9>	=	-0.04662436
<4|	|8>	=	0.45932628	<0|	|8>	=	0.04804253
<4|	|6>	=	-0.23035578	<0|	|6>	=	-0.02633274
<4|	|5>	=	-0.77457546	<0|	|5>	=	0.26640467
<3|	|11>	=	-0.06799638	<0|	|3>	=	0.70420404
<3|	|10>	=	-0.37065222	<0|	|2>	=	-0.00134329
<3|	|7>	=	-0.22101638	<0|	|1>	=	0.88395957

with $\langle i|S_X|j\rangle = \langle j|S_X|i\rangle \quad i,j = 0,11.$

(iii) S_Y

Since all the matrix elements of S_Y are pure complex the factor (i) is omitted from the listing below. Upper and lower triangle elements are related by the expression:

$$\langle i|S_Y|j\rangle = -\langle j|S_Y|i\rangle \qquad i,j = 0,11$$

Further, the magnitude of the matrix elements of S_X and S_Y are related such that:

$$\langle i|S_Y|j\rangle = \pm\langle i|S_X|j\rangle \qquad i,j = 0,11$$

$$\langle 10|S_Y|11\rangle = -\langle 10|S_X|11\rangle \qquad \langle 3|S_Y|6\rangle = -\langle 3|S_X|6\rangle$$
$$\langle 9| \ |11\rangle = \langle 9| \ |11\rangle \qquad \langle 3| \ |5\rangle = -\langle 3| \ |5\rangle$$
$$\langle 9| \ |10\rangle = -\langle 9| \ |10\rangle \qquad \langle 3| \ |4\rangle = \langle 3| \ |4\rangle$$
$$\langle 8| \ |11\rangle = \langle 8| \ |11\rangle \qquad \langle 2| \ |11\rangle = \langle 2| \ |11\rangle$$
$$\langle 8| \ |10\rangle = -\langle 8| \ |10\rangle \qquad \langle 2| \ |10\rangle = -\langle 2| \ |10\rangle$$
$$\langle 7| \ |10\rangle = \langle 7| \ |10\rangle \qquad \langle 2| \ |7\rangle = \langle 2| \ |7\rangle$$
$$\langle 7| \ |9\rangle = -\langle 7| \ |9\rangle \qquad \langle 2| \ |6\rangle = -\langle 2| \ |6\rangle$$
$$\langle 7| \ |8\rangle = -\langle 7| \ |8\rangle \qquad \langle 2| \ |5\rangle = -\langle 2| \ |5\rangle$$
$$\langle 6| \ |11\rangle = -\langle 6| \ |11\rangle \qquad \langle 2| \ |4\rangle = \langle 2| \ |4\rangle$$
$$\langle 6| \ |9\rangle = \langle 6| \ |9\rangle \qquad \langle 1| \ |11\rangle = -\langle 1| \ |11\rangle$$
$$\langle 6| \ |8\rangle = \langle 6| \ |8\rangle \qquad \langle 1| \ |9\rangle = \langle 1| \ |9\rangle$$
$$\langle 6| \ |7\rangle = -\langle 6| \ |7\rangle \qquad \langle 1| \ |8\rangle = \langle 1| \ |8\rangle$$
$$\langle 5| \ |11\rangle = -\langle 5| \ |11\rangle \qquad \langle 1| \ |7\rangle = -\langle 1| \ |7\rangle$$
$$\langle 5| \ |9\rangle = \langle 5| \ |9\rangle \qquad \langle 1| \ |4\rangle = -\langle 1| \ |4\rangle$$
$$\langle 5| \ |8\rangle = \langle 5| \ |8\rangle \qquad \langle 1| \ |3\rangle = \langle 1| \ |3\rangle$$
$$\langle 5| \ |7\rangle = -\langle 5| \ |7\rangle \qquad \langle 1| \ |2\rangle = \langle 1| \ |2\rangle$$
$$\langle 4| \ |10\rangle = \langle 4| \ |10\rangle \qquad \langle 0| \ |10\rangle = \langle 0| \ |10\rangle$$
$$\langle 4| \ |9\rangle = -\langle 4| \ |9\rangle \qquad \langle 0| \ |9\rangle = -\langle 0| \ |9\rangle$$

<4|	|8>	=	-<4| |8>	<0|	|8>	=	-<0| |8>
<4|	|6>	=	<4| |6>	<0|	|6>	=	<0| |6>
<4|	|5>	=	<4| |5>	<0|	|5>	=	<0| |5>
<3|	|11>	=	<3| |11>	<0|	|3>	=	-<0| |3>
<3|	|10>	=	-<3| |10>	<0|	|2>	=	-<0| |2>
<3|	|7>	=	<3| |7>	<0|	|1>	=	<0| |1>

(iv) L_Z

<11|	|11>	=	0.97564993	<3|	|9>	=	-0.29191790
<10|	|10>	=	-0.97564993	<3|	|8>	=	0.59547678
<9|	|9>	=	-0.60364463	<3|	|3>	=	-0.10709016
<8|	|9>	=	-0.68305150	<2|	|9>	=	0.59547655
<8|	|8>	=	0.60364440	<2|	|8>	=	0.29191810
<7|	|11>	=	0.44761957	<2|	|3>	=	0.10285054
<7|	|7>	=	0.08864505	<2|	|2>	=	0.10709039
<6|	|10>	=	-0.44761957	<1|	|10>	=	-0.02274269
<6|	|6>	=	-0.08864505	<1|	|6>	=	-0.12864270
<5|	|10>	=	-0.30125780	<1|	|5>	=	-0.93002649
<5|	|6>	=	-0.89998834	<1|	|1>	=	0.26953579
<5|	|5>	=	0.19768293	<0|	|11>	=	0.02274269
<4|	|11>	=	0.30125780	<0|	|7>	=	0.12864270
<4|	|7>	=	0.89998834	<0|	|4>	=	0.93002649
<4|	|4>	=	-0.19768293	<0|	|0>	=	-0.26953579

with $\langle i|L_Z|j\rangle = \langle j|L_Z|i\rangle \quad i,j = 0,11$

(v) L_X

<10|	|11>	=	-0.22299736	<3|	|6>	=	0.44755062
<9|	|11>	=	-0.19790479	<3|	|5>	=	0.15639738
<9|	|10>	=	-0.24945380	<3|	|4>	=	-0.54339626
<8|	|11>	=	-0.24945347	<2|	|11>	=	-0.82453922
<8|	|10>	=	0.19790481	<2|	|10>	=	0.00397183
<7|	|10>	=	-0.39648872	<2|	|7>	=	0.44855039
<7|	|9>	=	0.19016406	<2|	|6>	=	-0.12838565
<7|	|8>	=	-0.59651404	<2|	|5>	=	0.54339632
<6|	|11>	=	-0.39648872	<2|	|4>	=	0.15639763
<6|	|9>	=	-0.59651386	<1|	|11>	=	0.12617766
<6|	|8>	=	-0.19016397	<1|	|9>	=	0.45021715
<6|	|7>	=	-0.52224624	<1|	|8>	=	0.08284435
<5|	|11>	=	-0.00514126	<1|	|7>	=	0.22774223
<5|	|9>	=	0.61951263	<1|	|4>	=	0.56000754
<5|	|8>	=	0.11626496	<1|	|3>	=	0.01867173
<5|	|7>	=	-0.38853639	<1|	|2>	=	-0.86966299
<4|	|10>	=	-0.00514126	<0|	|10>	=	0.12617766
<4|	|9>	=	-0.11626514	<0|	|9>	=	-0.08284400
<4|	|8>	=	0.61951257	<0|	|8>	=	0.45021714
<4|	|6>	=	-0.38853639	<0|	|6>	=	0.22774223
<4|	|5>	=	0.05679602	<0|	|5>	=	0.56000755
<3|	|11>	=	-0.00397175	<0|	|3>	=	0.86966304
<3|	|10>	=	-0.82453922	<0|	|2>	=	0.01867191
<3|	|7>	=	0.12838560	<0|	|1>	=	0.69398632

APPENDIX V

Required Matrix Elements of the Operators S_Z, S_X and S_Y Appropriate to $CdBr_2(Co^{2+})$:5 wt.%

The non-zero matrix elements of the above operators are evaluated between the six lowest Kramers doublets of $CdBr_2(Co^{2+})$:5 wt.% and listed below. Each element is labelled $\langle i|op|j\rangle$ where i,j = 0,11 and the unperturbed states are characterised by the following energies:

|11>,|10>	: (993.5 cm^{-1})	|5>,|4>	: (394.4 cm^{-1})
|9>, |8>	: (892.0 cm^{-1})	|3>,|2>	: (279.7 cm^{-1})
|7>, |6>	: (887.0 cm^{-1})	|1>,|0>	: (0.0 cm^{-1})

(i) S_Z

<11|	|11>	=	1.06339274	<3|	|9>	=	-0.03346069
<10|	|10>	=	-1.06339274	<3|	|8>	=	0.45238908
<9|	|9>	=	0.66749984	<3|	|3>	=	-1.21772690
<8|	|9>	=	0.36842981	<2|	|9>	=	0.45238908
<8|	|8>	=	-0.66749984	<2|	|8>	=	0.03346068
<7|	|11>	=	-0.75716801	<2|	|3>	=	0.05385152
<7|	|7>	=	0.13731313	<2|	|2>	=	1.21772690
<6|	|10>	=	0.75716801	<1|	|10>	=	-0.03509619
<6|	|6>	=	-0.13731313	<1|	|6>	=	0.00115379
<5|	|10>	=	-0.26010275	<1|	|5>	=	-0.71766777
<5|	|6>	=	-0.61453051	<1|	|1>	=	0.71200474
<5|	|5>	=	0.48982707	<0|	|11>	=	0.03509619
<4|	|11>	=	0.26010275	<0|	|7>	=	-0.00115379
<4|	|7>	=	0.61453051	<0|	|4>	=	0.71766777
<4|	|4>	=	-0.48982707	<0|	|0>	=	-0.71200474

ERRATUM:

APPENDIX V(ii) on p.217 should appear on p.212 as APPENDIX IV(ii) and vice-versa.

(ii) S_X

<10|	|11>	=	0.12002605	<3|	|6>	=	0.18203578
<9|	|11>	=	0.59068905	<3|	|5>	=	0.03986753
<9|	|10>	=	0.55086121	<3|	|4>	=	0.40907006
<8|	|11>	=	0.55086133	<2|	|11>	=	-0.31584805
<8|	|10>	=	-0.59068907	<2|	|10>	=	0.04255474
<7|	|10>	=	0.30128502	<2|	|7>	=	0.18203602
<7|	|9>	=	-0.49060455	<2|	|6>	=	0.23499231
<7|	|8>	=	0.62208411	<2|	|5>	=	-0.40906998
<6|	|11>	=	0.30128502	<2|	|4>	=	0.03986772
<6|	|9>	=	0.62208418	<1|	|11>	=	-0.00770830
<6|	|8>	=	0.49060445	<1|	|9>	=	0.08449319
<6|	|7>	=	0.73833467	<1|	|8>	=	0.06014996
<5|	|11>	=	-0.16392334	<1|	|7>	=	-0.03452030
<5|	|9>	=	0.47600983	<1|	|4>	=	0.18026786
<5|	|8>	=	0.20269520	<1|	|3>	=	-0.00479401
<5|	|7>	=	-0.27473530	<1|	|2>	=	-0.75006798
<4|	|10>	=	-0.16392334	<0|	|10>	=	-0.00770830
<4|	|9>	=	-0.20269503	<0|	|9>	=	-0.06014967
<4|	|8>	=	0.47600983	<0|	|8>	=	0.08449319
<4|	|6>	=	-0.27473530	<0|	|6>	=	-0.03452030
<4|	|5>	=	-0.78362851	<0|	|5>	=	0.18026786
<3|	|11>	=	-0.04255498	<0|	|3>	=	0.75006801
<3|	|10>	=	-0.31584827	<0|	|2>	=	-0.00479398
<3|	|7>	=	-0.23499921	<0|	|1>	=	0.92058131

with $\langle i|S_X|j\rangle = \langle j|S_X|i\rangle \quad i,j = 0,11$

(iii) S_Y

The matrix elements of S_Y are related to those of S_X by expressions identical to the ones listed in Appendix IV.

APPENDIX VI

Publications

An account of the work appearing in Chapters II and IV of this thesis has been published in

The Physical Review B Oct. 1 (1975)

in collaboration with G.D. Jones, K. Zdansky and J.H. Christie and is shown overleaf.

Some results have been previously reported at the 3rd and 4th New Zealand Science of Materials Conferences at the Universities of Canterbury (Dec. 10-14, 1973) and Auckland (Dec. 10-12, 1975). Abstracts of these papers have also been included.

3RD NEW ZEALAND SCIENCE OF MATERIALS CONFERENCE
10-14 DEC., 1973 AT THE UNIVERSITY OF CANTERBURY

LOW LYING ENERGY LEVELS OF THE Co^{2+} ION IN A TRIGONAL CRYSTAL FIELD

Ivan Johnstone, John Christie, Karel Zdansky
Physics Department
University of Canterbury

In a trigonal environment the Co^{2+} ion possesses six doubly-degenerate low-lying energy levels with a total splitting of approximately 1000 cm^{-1}. The transitions between the lowest and the other five states have been measured using laser Raman spectroscopy for the crystal hosts $CdBr_2$, $CdCl_2$, $MnCl_2$ and $CoCl_2$. Polarisation measurements are consistent with earlier symmetry assignments given to these transitions. A calculation of the possible energy states for such $(3d)^7$ electrons using the strong crystal field approach of Tanabe and Kamimura is in close agreement with our experiments. Zeeman splittings obtained by an analogous method have provided a useful background to planned Zeeman-Raman experiments and valuable support to our crystal field fittings where the appropriate g-values are already known.

4TH NEW ZEALAND SCIENCE OF MATERIALS CONFERENCE

10-12 DEC., 1975 AT THE UNIVERSITY OF AUCKLAND

INFRARED STUDIES OF EXCHANGE COUPLED COBALT IONS IN CADMIUM CHLORIDE CRYSTALS

G.D. Jones and I.W. Johnstone
Department of Physics
University of Canterbury
Christchurch.

Divalent cobalt ions can be readily doped into cadmium chloride crystals and the spectra of these ions can be observed in the 500 to 1000 cm^{-1} infrared region. The spectra comprise electronic lines of both isolated cobalt ions and cobalt ion pairs, together with their vibronic sidebands. The electronic lines of the cobalt ion pairs are identified by their quadratic dependence on the cobalt ion concentration and largely occur on the high frequency side of the electronic lines of the single cobalt ions. The number, and frequencies of these pair lines can be interpreted on the basis of adjacent single cobalt ions coupled by a Heisenberg exchange interaction $-2JS_1 \cdot S_2$. If the wavefunctions determined by a crystal field analysis of the single cobalt ion spectra are used in the construction of the wavefunctios of the cobalt ion pairs, satisfactory agreement can be obtained using a purely isotropic exchange interaction. If a spin Hamiltonian analysis of the cobalt ion levels is adopted it is necessary to include anisotropic exchange to interpret the spectra. Particular features of these cobalt ion pairs in the far infrared will also be discussed.